The generation of few-cycle laser pulses and their application in strong field physics

im Fachbereich Physik
der Freien Universität Berlin
eingereichte Dissertation

von

Achut Giree

2018

This work was performed at the research and development department of Amplitude Systèmes, France and within the division for Attosecond Physics at the Max-Born-Institute, within the framework of European Industrial Doctorate (EID) program JMAP (Joint Max-Born-Institute Amplitude Phd Program) under the supervision of Prof. Marc J. J. Vrakking.

Erstgutachter: Prof. Dr. Marc J. J. Vrakking (Betreuer)
Zweitgutachter: Prof. Dr. Jens Limpert

Date of defense: 16.02.2018

Contents

1 Introduction

1.1 Motivation and objective

Light sources, in particular lasers, have found a variety of applications over the past half-century. The major application domains are manufacturing industries for processes like cutting, welding, drilling, marking etc., medical fields such as ophthalmology, dentistry, dermatology etc., and scientific areas such as spectroscopy, remote sensing, range finding, atmospheric research, astrophysics and many others. These applications have triggered the innovative development of laser systems demanding improved output characteristics at low cost, small footprint and high efficiency. Outstanding high power, ultrafast laser sources developed in the last decades have continuously found new applications too. In this way, the development of high performance laser systems and their potential applications form a closed-loop as schematically shown in Fig. 1.1.

The output characteristics of a laser system are often specified with respect to its application. A wide variety of lasers are available that emit coherent radiation in continuous-wave or pulsed mode in the spectral range from x-ray to the far-infrared. Output powers up to the kilowatt-level and pulse energies up to several megajoules are possible. Pulses with only a few optical cycles are routinely generated in laboratories. In addition, the possibility of tuning the central wavelength over a wide spectral range has extended the areas of applications further. Among others, the rapid development of ultrafast lasers with high

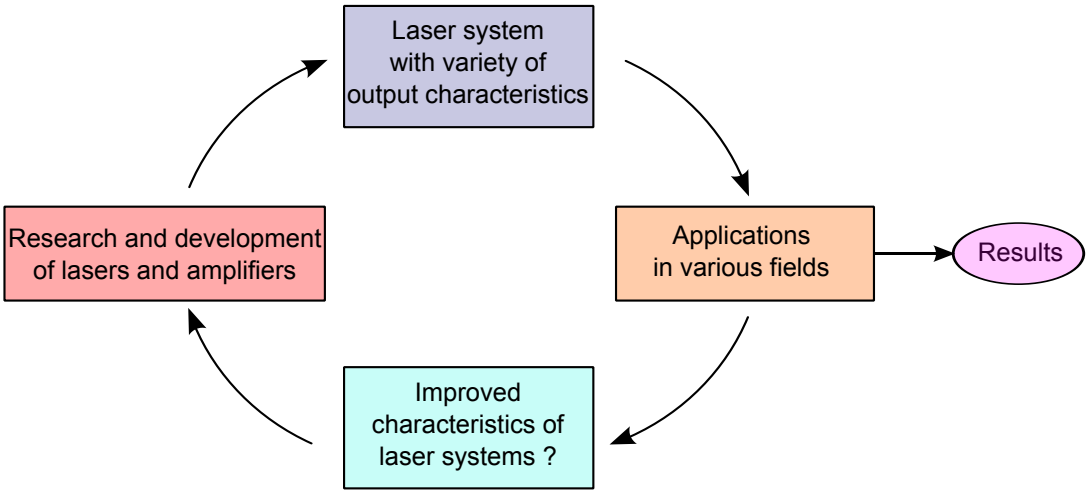

Figure 1.1: Schematic picture of the interrelationship between laser development and applications.

peak power and very short pulses during the last two decades has revolutionized various industrial and scientific applications.

Ultrafast lasers are mostly based on mode-locking [1] techniques, generating picosecond or femtosecond pulses with pulse energies up to a few tens of microjoules. Among others, mode-locked Ti:Sapphire oscillators are capable of producing pulses as short as 5 fs [2] with several nanojoules pulse energies. But the low peak power of such pulses is not enough for many applications, for example in strong field physics where the electric field of the laser has to be comparable to the atomic field strength. The techniques of chirped pulse amplification [3] and optical parametric chirped pulse amplification [4] allow a scaling of the peak power. High peak power, ultrashort pulses have two-fold advantages. On the one hand, very short pulse durations down to a single optical cycle offer high temporal resolution, which is extremely useful to study ultrafast processes in atoms and molecules. On the other hand, high peak intensities correspond to strong electromagnetic fields which approach the binding Coulomb field inside atoms and can lead to various nonlinear and strong field phenomena, such as high harmonic generation and the generation of attosecond pulses [5].

High harmonic generation refers to an emission of extreme ultraviolet (XUV) radiation, which occurs when energetic, ultrashort pulses are focused onto a gas target. The process is described by a semiclassical three-step model, in which the strong electric field of the ultrashort pulses is able to detach an electron from an atom by tunnel ionization ('ionization'), the detached electron is accelerated in the laser field ('acceleration'), and finally the accelerated electron hits the parent atom when it returns leading to the recombination of the electron with the parent atom ('recombination'). The recombination results in the emission of high energy photons corresponding to high harmonics of the incoming laser frequency (note that during the return of the electron to the parent ion, the electron may also scatter and there will be no emission of photons in this case). As the ionization processes occur efficiently only for a short time around the maximum of the electric field, the XUV photons are generated in short bursts around a zero crossing of the electric field with a duration that is a small fraction of the optical cycle of the driver laser. This leads to the generation of attosecond pulse trains, with two pulses per optical cycle [5]. The generation of isolated attosecond pulses can be achieved by effectively limiting the number of optical cycles at the fundamental frequency that produce XUV photons [6]. Therefore, ultrashort pulses with only a few optical cycles within the envelope, which are often referred to as few-cycle pulses, and with stable carrier envelope phase (the phase between the peak of the envelope of the pulse and the nearest maximum of the carrier wave) are necessary for the generation of isolated attosecond pulses. The parameters of the attosecond pulse trains and isolated attosecond pulses are largely determined by the characteristics of the ultrashort pulses. Beside the above-mentioned characteristics, focusablity of ultrashort pulses is another important parameter, which mainly depends upon the output beam quality and the spatiotemporal properties.

Attosecond pulses in the XUV wavelength range and ultrashort pulses in the near-infrared (NIR) wavelength range have been widely used in attosecond two-color (XUV+NIR) pump-probe experiments (see Ref. [7] and references therein). In these experiments, an

XUV (or NIR) pump pulse triggers atomic or molecular dynamics e.g. by photoionization/excitation of atoms or molecules, and the dynamics are probed by a NIR (or XUV) pulse. The charged particles after photoionization are detected using various detectors such as time-of-flight spectrometers, velocity map imaging spectrometers, and electron-ion coincidence detectors, so-called 'reaction microscopes'. Coincidence measurements (i.e. the detected ions and electrons belong to the same parent atom or molecule) can provide 3D momentum vectors of both electrons and ions in coincidence, supplying more insight into the ionization process. The technique is also known as COLTRIMS (COLd Target Recoil Ion Momentum Spectroscopy). For unambiguous identification of electrons and their ionic partners, the number of ionization events per pulse has to be limited to $\ll 1$, on average. This demands laser pulses at a high repetition rate $\gg 10\,\mathrm{kHz}$ in order to speed up the data acquisition and accordingly to increase the signal-to-noise ratio. In addition, the low photon flux of high harmonic sources (due to the low conversion efficiency) can be compensated by increasing the pulse repetition rate.

Therefore, a table-top laser system generating carrier envelope phase-stable few-cycle pulses with millijoule-level pulse energy at a pulse repetition rate $> 100\,\mathrm{kHz}$ and a high spatiotemporal quality would be ideal for many applications in attosecond science [8, 9]. Indeed, in the last decade carrier envelope phase-stable, energetic few-cycle pulses in the near-infrared and mid-infrared spectral range have not only advanced the study of ultrafast dynamics via strong field ionization and pump-probe spectroscopy but have also boosted the development of attosecond science. However, the pulse repetition rate has been limited to a few kHz.

State-of-the-art few-cycle laser systems are mostly available in the near-infrared spectral range due to well-established laser technologies. Various schemes based on nonlinear pulse compression and optical parametric chirped pulse amplification (OPCPA) have been utilized to generate high peak power, few-cycle pulses in the last decades, which are briefly reviewed and schematically shown in Fig. 1.2, dividing them into two categories as follows.

Nonlinear compression of laser amplifiers: As previously mentioned, mode-locked Ti:Sapphire oscillators can directly deliver 5 fs pulses. However, Ti:Sapphire amplifiers do not support few-cycle pulses due to gain narrowing effects. High energy, high peak power pulses with sub-30 fs pulse duration have been achieved with table-top Ti:Sapphire based laser systems and are widely used in various scientific research areas. The generation of few-cycle pulses has largely relied on spectral broadening in a hollow-core fiber and subsequent chirp compensation with chirped-mirrors [10, 11]. This approach has been successful and is dominantly used in scientific laboratories, in particular for the generation of attosecond pulse trains and isolated attosecond pulses. Despite supporting sub-two cycle, carrier envelope phase-stable pulses with several millijoule pulse energies [12, 13], this scheme suffers from high transmission losses in the hollow fiber. Moreover, thermo-optical effects in Ti:Sapphire amplifiers have limited the pulse repetition rate to a few kHz, and accordingly an average power of a few tens of watts before nonlinear pulse compression.

Recently, nonlinear compression of Yb-doped fiber amplifiers has been considered as an alternative to generate high power few-cycle pulses at high repetition rates. This approach

uses gas-filled wave-guide capillaries for the spectral broadening of narrow band pulses from amplifiers (often in multiple stages) and chirped mirrors for chirp compensation. Sub-10 fs pulses with 216 W average power at a pulse repetition rate of 1.27 MHz have recently been achieved [14]. However, carrier envelope phase (CEP) stability has not been demonstrated yet.

Optical parametric amplification of broadband oscillator/supercontinuum: As an alternative to nonlinear compression, optical parametric amplification of broadband pulses from Ti:Sapphire oscillators has received an increasing interest [15–17]. This approach utilizes a nonlinear wave mixing process, where a nonlinear crystal is used to transfer energy from energetic pump pulses to weak seed pulses achieving very high gain. The pump pulses are typically produced by conventional laser amplification of either the same or a different oscillator. Ytterbium-based laser amplifiers based on different technologies such as fiber, thin-disk and Innoslab are often used as pump laser. Advantages of the parametric amplification technique include a broad amplification bandwidth [18], allowing the amplification of few-cycle pulses, and highly reduced thermal effects compared to Ti:Sapphire

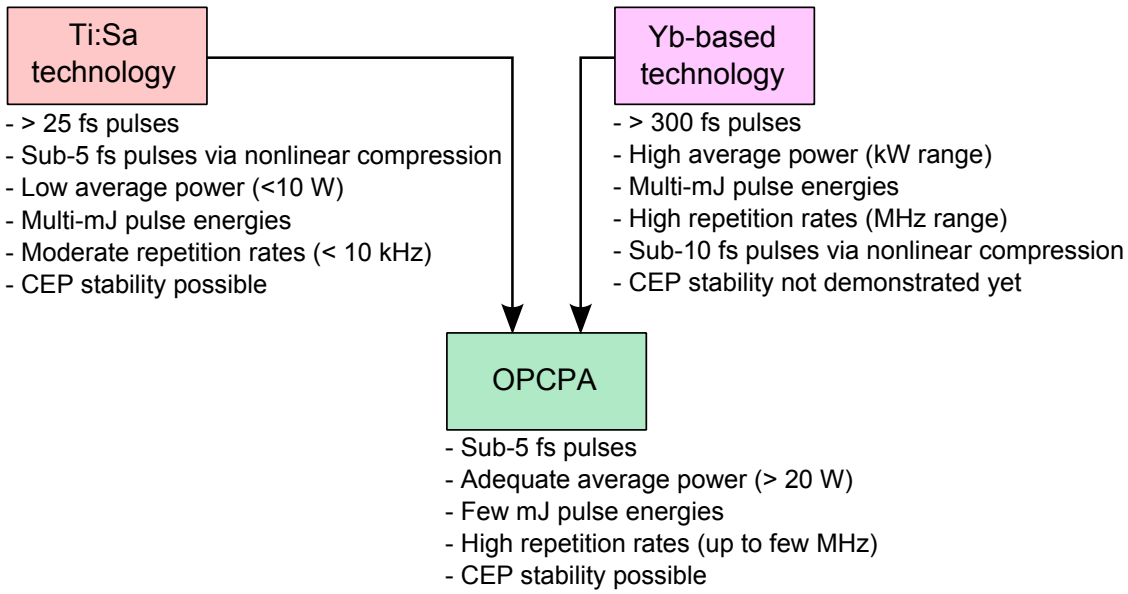

Figure 1.2: Schematic picture of schemes that have been utilized for the generation of few-cycle pulses. The output parameters indicated in the figure are typical performance values. Ultrashort pulses with > 25 fs pulse duration has been achieved with Ti:Sa amplifiers, while typical average power and pulse repetition rates are limited to < 10 W and < 10 kHz respectively. Yb-based technology is known for high pulse repetition rates in MHz range, and high average output power upto a few kilowatts is possible, but not standard. Multi-mJ pulse energies have been achieved with Yb-based amplifiers but at limited pulse repetition rates (not in MHz range). Both Ti:Sa and Yb-based technologies have been combined with the optical parametric chirped pulse amplification (OPCPA) technique which is most suitable for the amplification of high average power, carrier envelope phase (CEP) stabilized few-cycle pulses at high repetition rates.

amplifiers. Therefore, this scheme is scalable to high energy and high pulse repetition rate (i.e. high average power), only limited by the available pump laser. In addition, stability of the carrier envelope phase of the seed pulses is preserved during amplification. Many advantages of the optical parametric amplification technique are due to the fact that energy is not stored in the crystal, in contrast with laser amplifiers, where the energy is stored in a gain medium and non-radiative transitions dissipate a part of the stored energy as heat, ultimately leading to detrimental thermal effects. However, in an optical parametric amplifier, there are strong requirements on the pump laser because most of the characteristics of the pump pulses are transferred to the amplified seed pulses. Additional challenges of this scheme include parasitic nonlinear effects and temporal synchronization of the seed and the pump.

Instead of a broadband Ti:Sapphire oscillator, supercontinuum generated in a hollow fiber, or white light generated in a nonlinear medium have also been utilized as a seed in optical parametric amplification, generating few-cycle pulses after compression [19–22]. Because the seed and the pump pulses can in principle be derived from the same laser, this approach of seed generation has been extensively used, in particular for seed spectral ranges different from that of Ti:Sapphire lasers.

The above-mentioned two approaches i.e. nonlinear pulse compression and parametric amplification, schematically summarized in Fig. 1.2 clearly indicate that there are two strategies one can follow up to now. On the one hand, one can work with the well-established Ti:Sapphire technology that offers high pulse energies, few-cycle pulses (via nonlinear compression) and the possibility of CEP stability, but at modest average output power and moderate repetition rates ($< 10\,\mathrm{kHz}$). High average power and high repetition rates are possible with Yb-based laser systems, but at the expense of pulse duration and CEP stability. Even though, pulse duration can be reduced by nonlinear compression, CEP stability has not been achieved yet. However, one can use the OPCPA technique that combines the high average power and high repetition rates offered by Yb-based technology with the broadband pulses and CEP stability offered by Ti:Sapphire technology. In that respect, OPCPA is an attractive technique to generate CEP-stable, high energy few-cycle pulses at high repetition rates. Indeed, there have been significant efforts to scale the pulse energy and the pulse repetition rate of few-cycle laser systems based on OPCPA in recent years [15–17,23]. This is of high significance in attosecond science, due to the fact that XUV pump - IR probe experiments could be performed at high repetition rates with attosecond time resolution and at the same time, with enhanced signal-to-noise ratio. Furthermore, an increase in pulse energy in optical parametric chirped pulse amplifiers (OPCPAs) will eventually lead to XUV pump - XUV probe experiments, which is, however, feasible with currently available OPCPA-based laser systems only at the expense of a very significant reduction of the repetition rate.

The development of the high repetition rate OPCPA-based laser source at the Max-Born-Institute that is discussed in this thesis is largely aimed for attosecond experiments, which utilize an electron-ion coincidence detector ('reaction microscope') [23]. As discussed earlier, the high repetition rate is essential for such experiments. Therefore, an OPCPA

system generating CEP-stable, few-cycle pulses at high repetition rates in the near-infrared spectral range has been developed, where a broadband Ti:Sapphire oscillator and Yb-doped fiber amplifier were used as seed and pump laser respectively. The laser source has already been used for some strong field ionization experiments [24]. In order to utilize the laser for high harmonic generation and to generate attosecond pulses, there are two important aspects that need to be addressed. On the one hand, scaling of the pulse energy of the few-cycle pulses is necessary. On the other hand, good spatiotemporal quality, and accordingly good focusability of the pulses has to be ensured, which is crucial, in particular at high repetition rates, due to the limited pulse energy. In the beginning of the project related to this thesis, the few-cycle laser system had limited output pulse energy (12 µJ at a pulse repetition rate of 400 kHz) due to the limited pump pulse energy available from fiber amplifiers. Therefore, most of the work focused on the energy scaling of the pump lasers, which can be used for pumping OPCPAs, and the spatiotemporal characteristics of few-cycle pulses that are amplified by the OPCPA technique. Note that energy scaling of the few-cycle laser system has recently been carried out by using thin-disk amplifiers as a pump laser, producing CEP-stable, sub-7 fs pulses with 190 µJ pulse energy at a pulse repetition rate of 100 kHz [25].

1.2 Project description and thesis outline

The work presented in this thesis was performed within the framework of the European Industrial Doctorate (EID) program JMAP (Joint Max-Born-Institute Amplitude Phd Program). The main collaborators were the Max-Born-Institute, Berlin (MBI) and Amplitude Technologies, Paris (AT). In addition, there were three associated partners: Amplitude Systèmes, Bordeaux (AS), Freie Universität Berlin, and University of Geneva. With an objective of research and development of high power laser sources for the development of attosecond and strong-field science, JMAP was structured in four different research projects. One of the projects was the development of high repetition rate optical parametric amplifiers, which are useful to perform strong-field physics and attosecond experiments at MBI as described earlier. The PhD program spanned a time duration of approximately three years, during which half of the time had to be spent at Amplitude Systèmes and the other half at the Max-Born-Institute. Considering the nature of the project, the research activities presented here did not evolve in a monotonous way but form a group of slightly different scientific works that are related to each other and to the laser development based on the OPCPA technique. This thesis brings all the activities together. With regards to the activities at the industrial partner, it should be mentioned that the work did not primarily target the development of novel techniques, but rather focused on the further development and use of a couple of existing techniques, in order to extend the range of output laser parameters and make the lasers more reliable, as a commercial product would require.

The thesis is organized as follows. Chapter 2 presents the necessary theoretical background ranging from the fundamentals of lasers and amplifiers to the generation and amplification of ultrashort pulses. The nonlinear optics of ultrashort pulses, in particu-

lar second-order and third-order nonlinear interactions in a transparent optical medium that are relevant to this work are reviewed. In addition, nonlinear propagation of ultrashort pulses in optical fibers is briefly discussed from the point of view of nonlinear pulse compression.

The first part of this work was dedicated to the development of pump lasers aiming to achieve a pulse energy $> 1\,\mathrm{mJ}$ at a pulse repetition rate $> 100\,\mathrm{kHz}$. The laser development was carried out at the research and development department of Amplitude Systèmes, Bordeaux. The design and characterization of a high repetition rate, high energy, sub-picosecond laser is presented in chapter 3. A passively mode-locked fiber oscillator was amplified in a diode-pumped, Yb:YAG-based thin-disk regenerative amplifier, using the chirped pulse amplification technique. Sub-picosecond pulses with $>1.6\,\mathrm{mJ}$ energy were generated at a pulse repetition rate of 10 kHz. Keeping the pulse energy at millijoule-level, the repetition rate could be increased to 25 kHz. In addition, an average power of 35 W was obtained at 100 kHz with a close to diffraction-limited beam quality. Second and third harmonic generation of these pulses in beta barium borate (BBO) crystals was demonstrated at different pulse repetition rates with high conversion efficiencies and a good beam quality, which demonstrates that the laser is highly suitable for pumping OPCPA in the visible and near-infrared. Additionally, nonlinear compression of the sub-picosecond pulses was performed in an air-filled hollow-core Kagome fiber generating a broad spectrum that supports sub-100 fs pulses with $>50\,\mu\mathrm{J}$ energy. Pulses as short as 130 fs were obtained after dispersion compensation. These pulses at a pulse repetition rate of $>10\,\mathrm{kHz}$ are highly suitable for high harmonic generation.

The second part of this work focused on spatiotemporal characterization of the pulses that are amplified in OPCPAs. Recently, spatiotemporal couplings in OPCPAs [26,27] have been studied and the distortions in the amplified signal are emphasized, which are inherent to the amplifier geometry and known since the introduction of the technique [28]. The systematic study of these issues in a high repetition rate OPCPA is of high interest for the applications in strong field physics and attosecond science, and is numerically performed in this work. The results and analysis are presented in chapter 4. A numerical code called Sisyfos [29] was utilized to simulate optical parametric amplifiers. Spatiotemporal distortions in OPCPAs were systematically studied for a wide range of design parameters and under different amplification conditions. The impacts of gain saturation and back conversion from the signal beam to the pump beam were analyzed for different phase-matching geometries. The simulation results indicate that high conversion efficiencies come at the expense of high spatiotemporal distortions. For BBO-based noncollinear OPCPAs pumped with picosecond pulses in the near-infrared spectral range, conversion efficiencies have to be $<20\,\%$ without strong back conversion if degradation of the pulses is to be minimized.

The last part of this work concentrates on one of the applications of few-cycle pulses in strong field physics: electron interferometry. Strong field ionization experiments performed by using the OPCPA-based, high repetition rate, few-cycle laser source developed at the Max-Born-Institute [24] and corresponding numerical calculations led to an electron interferometry experiment using near-infrared pump and probe pulses. A proof-of-principle interferometric pump-probe experiment was carried out during this work (using a different

laser system producing few-cycle near-infrared laser pulses) with the aim of characterizing bound states of strong-field excited argon. Chapter 5 presents the experimental details and the analysis of the experimental results, which are complemented by a set of numerical calculations based on solution of the time-dependent Schrödinger equation. Finally, chapter 6 provides a summary and outlook.

2 Theoretical background

As previously discussed in the introduction, sources of high energy, few-cycle laser pulses have found numerous applications in strong field physics and attosecond science. As most of the work in this thesis focuses on the generation of few-cycle laser pulses, this chapter discusses the basic theoretical background of laser physics and nonlinear optics that underlie the routes to generate ultrashort laser pulses with high energy and high average power. Since a thorough theoretical description of lasers and nonlinear optics can be found in a number of textbooks and reviews, the aim of the chapter is to bring only those topics into discussion, which are relevant to the experimental/numerical work presented in the following chapters.

At first, a brief introduction to laser physics, including laser oscillators and amplifiers is provided, along with a discussion about the generation and amplification of laser pulses. Then, the limitations in the amplification of ultrashort pulses are reviewed. Next, second-order nonlinear processes for frequency conversion and parametric amplification are described in detail. In addition, the third-order optical nonlinearities that may impose a limitation in the amplification of high peak power pulses are introduced. Finally, the nonlinear propagation of laser pulses in optical fibers is presented from the point of view of nonlinear pulse compression. The chapter is mainly based on Refs. [30–33].

2.1 Fundamentals of lasers

Laser is an acronym that stands for 'Light Amplification by Stimulated Emission of Radiation'. The concept of stimulated emission was introduced by Einstein in the early 20^{th} century while studying a collection of atoms in the form of a gas in thermal equilibrium within a confined cavity that radiates electromagnetic radiation according to the law of a blackbody radiator. Several radiative transitions can occur between the two energy levels that represent an ideal atomic system and each transition is characterized by a rate or coefficient, widely known as the Einstein coefficients.

In order to discuss the Einstein coefficients, let us consider a system with two nondegenerate energy levels E_1 and E_2, with populations N_1 and N_2 respectively. A transition from level 1 to 2 and vice versa is possible either by absorbing or emitting a photon respectively, with an energy given by $h\nu = E_2 - E_1$, where ν is the frequency of the photon and h is Planck's constant. There exist three types of interaction between an electromagnetic field and the atomic system: absorption, spontaneous emission and stimulated emission, as indicated in Fig. 2.1.

If electromagnetic radiation characterized by energy density $\rho(\nu)d\nu$, within a bandwidth $d\nu$ interacts with the system, originally in its ground state E_1, part of the radiation can

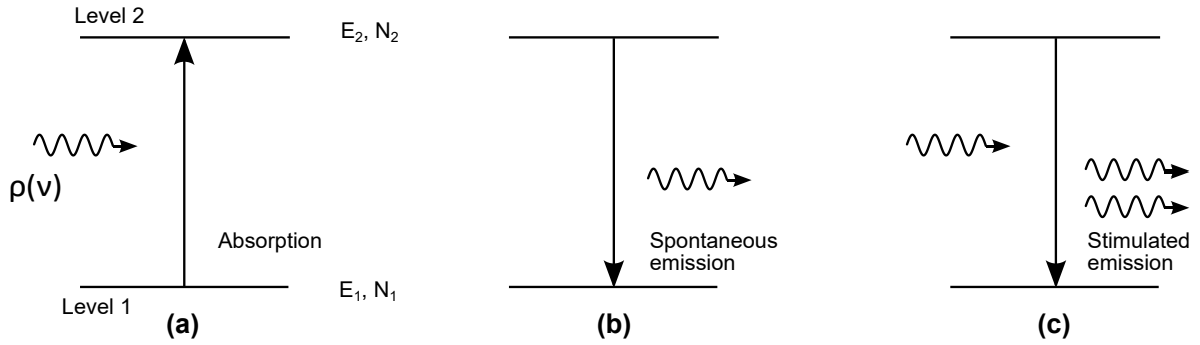

Figure 2.1: Sketch of (a) absorption, (b) spontaneous emission, and (c) stimulated emission transitions that can occur in the interaction of electromagnetic fields and a simple two-level atomic system. Adapted from Ref. [34].

be absorbed promoting the system to the excited state E_2. When the system is in the upper energy level it can spontaneously decay to the lower level emitting a photon with frequency $h\nu = E_2 - E_1$. This is called spontaneous emission. The emission can also take place induced by electromagnetic radiation with the appropriate frequency ν, and this is called stimulated emission. Unlike spontaneous emission, which is incoherent and can occur without the presence of an electromagnetic field, stimulated emission is a coherent process, only occurs in the presence of a stimulating field and has the same polarization, spectral and directional characteristics as the stimulating field. The population of the lower level is depleted due to absorption, and that of the upper level is depleted by spontaneous and stimulated emission.

Assuming that the total number of atoms in the two levels is constant ($N_{tot} = N_1 + N_2$), the rate of change of lower and upper level populations can be expressed, by combining absorption, spontaneous emission and stimulated emission as,

$$\frac{dN_1}{dt} = -\frac{dN_2}{dt} = B_{21}\rho(\nu)N_2 - B_{12}\rho(\nu)N_1 + A_{21}N_2. \tag{2.1}$$

where B_{21}, B_{12} and A_{21} are the Einstein coefficients. The factors $B_{21}\rho(\nu)$ and $B_{12}\rho(\nu)$ refer to the probabilities per unit frequency that transitions are induced by the electromagnetic field. The reciprocal of A_{21} corresponds to the lifetime for spontaneous emission from the upper energy level. Under steady state conditions, $dN_1/dt = dN_2/dt = 0$ and therefore, Eq. 2.1 becomes,

$$B_{12}\rho(\nu)N_1 = A_{21}N_2 + B_{21}\rho(\nu)N_2. \tag{2.2}$$

For an atomic system in thermal equilibrium at temperature T, the populations of the energy levels follow a Boltzmann distribution and the relative population is given by,

$$\frac{N_2}{N_1} = \frac{g_2}{g_1}\exp\left(-\frac{E_2 - E_1}{kT}\right), \tag{2.3}$$

where g_1 and g_2 are the degeneracy of the lower and upper energy levels respectively. Note

that $g_1 = g_2 = 1$ for the atomic system considered in Fig. 2.1. In thermal equilibrium at any temperature $T > 0$, the ratio is always less than unity for $E_2 > E_1$, given that $g_2/g_1 \leq 1$.

If Eqs. 2.2 and 2.3 are combined to derive an expression for $\rho(\nu)$ and if this expression is compared with Planck's law for the electromagnetic radiation emitted by a blackbody in thermal equilibrium, relations between the Einstein coefficients are obtained as [30],

$$\frac{A_{21}}{B_{21}} = \frac{8\pi\nu^2 h\nu}{c^3}, \text{ and } B_{21} = \frac{g_1 B_{12}}{g_2}, \tag{2.4}$$

where c is the speed of light. This shows that for a given degeneracy of the energy levels and for a given lifetime of the upper energy level, one can compute all the Einstein coefficients.

The stimulated emission process implies that light can be amplified. This is possible only if the rate of stimulated emission is higher than that of absorption. For that to happen, the population of the upper level must be bigger than that of the lower level as it will be described in the next subsection. In fact, $N_2 > \frac{g_2}{g_1} N_1$ is an essential condition for amplification, known as population inversion. But according to the Boltzmann distribution, N_2 is always less than N_1 at thermal equilibrium, which rules out the possibility of population inversion. However, inversion can be achieved by pumping or exciting the atoms from the ground state to a higher energy level.

Absorption and gain

The two-level atomic system considered in the previous section assumes that the energy gap between the levels is infinitely sharp. In reality, excited states have a finite radiative lifetime, and as a result the transition has a finite linewidth, the so-called natural linewidth with a lineshape given by a Lorentzian function. In addition, there are a number of line broadening mechanisms that contribute to the broadening of the transition linewidth, leading to different lineshapes. In general, the transition lineshape is a convolution between the natural lineshape and the lineshape due to the broadening mechanism, and is an important factor in defining the bandwidth of a laser pulse in combination with the longitudinal cavity modes [see section 2.2].

The two-level atomic system can be extended further by considering a finite transition linewidth so that the spectral distribution of atoms per unit frequency e.g. in the upper laser level can be written as,

$$N(\nu) = \zeta(\nu) N_2, \tag{2.5}$$

where $\zeta(\nu)$ is called the atomic lineshape function, which depends on the line broadening mechanisms.

Let us consider a beam with an intensity per unit frequency $I(\nu)$ at frequency ν i.e. an energy density per unit frequency given by $\rho(\nu) = I(\nu)/c$ that travels through a thin absorbing medium of thickness dz. Assuming that the medium is characterized by a simple two-level system, there are three possible interactions between the beam and the material, namely absorption, spontaneous emission and stimulated emission. The number of

transitions per unit volume per unit time corresponding to absorption is given by,

$$n_1 \rho(\nu) d\nu B_{12} \zeta(\nu) = n_1 B_{12} \zeta(\nu) I/c. \tag{2.6}$$

where n_1 is the total number of atoms per unit volume in the lower energy level, and I is the intensity given by $I = I(\nu)d\nu$. Similarly, the number of transitions per unit volume per unit time corresponding to spontaneous emission and stimulated emission are given by $n_2 A_{21}\zeta(\nu)$ and $n_2 B_{21}\zeta(\nu)I/c$ respectively, with n_2 as the total number of atoms per unit volume in the upper energy level. When the beam travels through the thin medium with cross-sectional area dA, the amount of energy per unit time added to the beam is given by [32],

$$[I(z+dz) - I(z)]dA = [n_2 B_{21}\zeta(\nu)I/c - n_1 B_{12}\zeta(\nu)I/c]h\nu dA dz. \tag{2.7}$$

The contribution due to spontaneous emission in the direction of the incident beam is assumed to be negligible since the spontaneous emission is radiated in all directions. After some rearrangements and using Eq. 2.4, Equation 2.7 becomes,

$$\frac{dI}{dz} = B_{21}\zeta(\nu)\frac{h\nu}{c} I(n_2 - \frac{g_2}{g_1} n_1). \tag{2.8}$$

The solution to Eq. 2.8 is,

$$I = I_0 \exp\left[B_{21}\zeta(\nu)\frac{h\nu}{c}(n_2 - \frac{g_2}{g_1} n_1) z\right], \tag{2.9}$$

where I_0 is the intensity at $z = 0$. Equation 2.9 can be expressed in the form of $I(z) = I_0 \exp[g_0(\nu)z]$ with $g_0(\nu)$ as a small-signal gain coefficient, which can be written as,

$$g_0(\nu) = B_{21}\zeta(\nu)\frac{h\nu}{c}(n_2 - \frac{g_2}{g_1} n_1) = \sigma_{21}(\nu)\Delta n. \tag{2.10}$$

The factor $B_{21}\zeta(\nu)h\nu/c = \sigma_{21}(\nu)$ represents the cross section for radiative transitions from the upper to the lower energy level, and is called the stimulated emission cross section. Δn is the population difference per unit volume and represents the population inversion if $\Delta n > 0$. Equation 2.9 shows that the intensity of the radiation increases exponentially during propagation for $n_2 > n_1 g_2/g_1$. Indeed, this is an essential condition for optical amplification, implying that there should be more atoms in the upper energy level than in the lower level. In addition, for $n_2 < n_1 g_2/g_1$ the intensity of the beam decreases due to absorption.

Furthermore, the small-signal gain coefficient varies with stimulated emission cross section, which depends on the lineshape function. As mentioned before, the lineshapes are determined by line broadening mechanisms that are mainly classified into two categories: homogenous and inhomogeneous.

In homogeneous line broadening, each atom has the same response to the applied radiation and has the same probability function for a transition within the linewidth of the energy

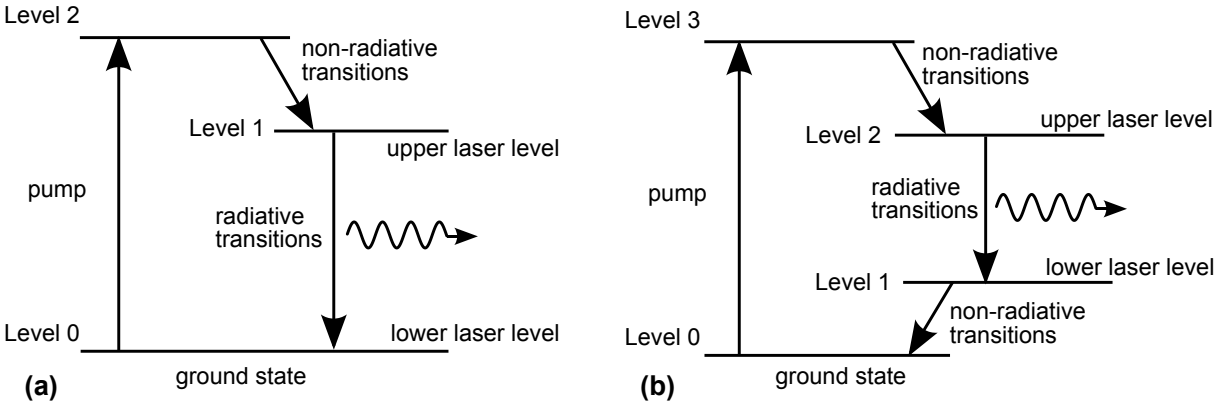

Figure 2.2: Level schemes for a (a) three-level and a (b) four-level laser. Taken from Ref. [34].

level. For sufficiently strong radiation, the atomic transitions saturate uniformly throughout the linewidth. Several mechanisms such as lifetime broadening, collision broadening and thermal broadening lead to homogeneously broadened atomic lineshapes. The lifetime broadening occurs due to the radiative lifetime for spontaneous emission or fluorescence processes. Collision between the atoms within the gain medium disturbs the radiative processes in a random way, resulting in line broadening. Collision broadening occurs in a gas medium at high pressures and it is also called pressure broadening. In addition, thermal vibrations of the lattice surrounding the active ions in a solid material introduce broadening. All of these homogeneous broadening mechanisms lead to a Lorentzian lineshape.

In inhomogeneous line broadening, atoms have frequency responses at different center frequencies, thereby leading to a broader transition lineshape compared to the broadening due to individual atoms. Only those atoms with resonant frequencies close to the frequency of the applied radiation take part in the interaction. Therefore, saturation in the case of a strong signal occurs only in a narrow frequency window. Doppler broadening is one of the inhomogeneous broadening mechanisms, which occurs due to the Doppler shift of resonance frequencies of randomly moving atoms. The resulting lineshape is Gaussian. In addition, line broadening due to crystal inhomogeneities or defects is also inhomogeneous. For the details of broadening mechanisms, see Ref. [31].

Three-level and four-level laser schemes

In order to achieve population inversion, atoms from the lower energy level have to be raised or pumped to the upper energy level. The pumping techniques in real laser systems, together with absorption and emission processes encounter a complex structure of energy levels of gain media. Despite the many-level energy diagram of laser materials, laser systems can mainly be classified into two categories: three-level and four-level systems. The level schemes for a three-level and four-level lasers are shown in Fig. 2.2 [34].

In a three-level scheme, absorption of pump photons raises atoms from the ground state (level 0) to level 2. Most of the excited atoms are transferred into the upper laser level

1 by non-radiative transitions (transitions that do not involve emission or absorption of photons), dissipating energy as heat. The excited atoms return to the ground state by emitting photons (radiative transitions). The radiative transitions occur via both spontaneous and stimulated emission. The latter process is responsible for the laser radiation. It is necessary that the rate of non-radiative transitions from level 2 to 1 is faster than the rate of spontaneous emission from level 2, and from level 1 to the ground state. This implies that the lifetime of level 1 should be large compared to the relaxation time of the 2-to-1 transitions. A level with relatively long lifetime is called a metastable level. Since the lower laser level (ground state) is highly populated, more than half of the atoms in the ground state should be pumped to the upper laser level (1) for population inversion to occur. If the lower laser level is close to the ground state such that there exists population at the operating temperature, the system is said to be quasi-three level.

There exists another three-level scheme (not shown in the sketch) mainly in gas lasers, where the upper energy level of the three levels is the upper laser level. The non-radiative transitions occur from the lower laser level to the ground state.

In a four-level scheme, the lower laser level is not the ground state, rather it is situated above the ground state with a relaxation time fast compared to the lifetime of the laser transition (τ_{21}). The lower laser level is much above the ground state such that its thermal population is negligible and the population inversion can be achieved with a small pump power, and lower pump rate compared to a three-level laser. The transitions between the energy levels 3 and 2, and between levels 1 and 0 are mostly non-radiative and the energy is dissipated as heat.

Gain saturation

Note that population inversion is not sufficient for laser operation. The inverted upper laser level has to be depleted efficiently by stimulated emission. This implies that the gain should exceed the losses in the laser medium. In principle, the condition gain>loss can be achieved if the product of the small-signal gain and the length of the laser medium is sufficiently high. This is fulfilled, in practice, by creating a positive feedback with an optical cavity or resonator in such a way that the radiation passes multiple times through the gain medium (essentially increasing the length of the laser medium). Then, the intensity of the laser radiation increases exponentially until the gain saturates. After gain saturation, the gain increases linearly. If I is an intensity at a point z within the gain medium, the equation for the power density can be written as,

$$\frac{dI}{dz} = (g - \alpha)I, \tag{2.11}$$

where α is a loss coefficient. g is the saturated gain coefficient defined as [30],

$$g = \frac{g_0}{1 + I/I_s}. \tag{2.12}$$

The saturation intensity I_s is the intensity at which the gain coefficient is reduced by 1/2. By solving the differential equation 2.11, one can get $I(z) = I(0)\exp[(g-\alpha)z]$ with $I(0)$ as the intensity at $z = 0$.

Altogether, there are three essential elements in a laser: the gain medium, the pump and the resonator. The gain medium stores the energy provided by the pump and the resonator determines the spatial and directional characteristics of the laser.

Laser resonator

A laser resonator typically consists of mirrors placed at the ends of a gain medium. The configuration not only increases the effective length of the gain medium but also introduces boundary conditions for the electromagnetic fields oscillating between the mirrors. Within the resonator, a standing-wave pattern is established with each standing wave having a different oscillation frequency. The standing waves are known as longitudinal modes. Similarly, an optical resonator has transverse modes that are distinguished based on the electromagnetic field distribution in a plane perpendicular to the direction of laser propagation. A number of transverse resonator modes can cover the transverse cross section of the gain medium. For a given transverse mode, there can be a number of longitudinal modes that differ in oscillation frequency. The spectral characteristics of a laser is determined by the longitudinal modes, where the bandwidth set by the atomic transitions may cover a very large number of longitudinal modes, whereas the spatial characteristics of a laser such as the beam diameter and beam divergence, and the energy distribution are determined by transverse modes.

The transverse mode of a laser with a Gaussian intensity profile is called the 'fundamental mode'. Higher-order modes correspond approximately to the fundamental mode modulated by polynomial functions of the transverse coordinates x and y. The intensity profile of a Gaussian beam is given by,

$$I(x,y) = I_0 \exp\left[\frac{-2(x^2+y^2)}{w^2}\right], \tag{2.13}$$

where w is the beam radius corresponding to a radial distance at which intensity is decreased to $1/e^2$ of its maximum value I_0. During the propagation of the Gaussian beam, the distribution acquires a minimum beam radius w_0 (known as beam waist) with planar wavefront. At a distance z from the beam waist, the beam radius is given as,

$$w(z) = w_0\sqrt{1+\left(\frac{\lambda z}{\pi w_0^2}\right)^2}, \tag{2.14}$$

where λ is the laser wavelength. The half divergence angle for the fundamental mode can be obtained as,

$$\theta = \lim_{z\to\infty}\frac{w(z)}{z} = \frac{\lambda}{\pi w_0}. \tag{2.15}$$

If the fundamental mode of the laser is not a perfect Gaussian, a factor (also known as beam quality factor or beam propagation factor) M^2 is included in the expression of the beam divergence according to,

$$\theta' = M^2 \frac{\lambda}{\pi w_0'}, \tag{2.16}$$

where θ' and w_0' refer to the half-divergence angle and the beam waist of the beam that is not diffraction-limited. This implies that the M^2 factor is 1 for a Gaussian beam. For beams which are not diffraction-limited, the M^2 factor is always larger than 1.

A calculation of the round-trip propagation of a laser beam through various optical components within a resonator provides an expression for the beam size and the radius of curvature of a particular transverse mode at each position within the resonator. The calculation is often performed using an ABCD matrix formalism, where the effect of an optical component on the linear propagation of a laser beam can be represented by an ABCD matrix or ray matrix. The ABCD matrix is a 2×2 matrix defined under the paraxial approximation i.e. it is assumed that all light rays propagate at a very small angle δ with respect to the optical axis of the system such that $\sin\delta \approx \tan\delta \approx \delta$. The matrix can be used to calculate the influence of the optical component on the incoming ray position r and the propagation angle δ with respect to the propagation axis leading to an outgoing ray position r' and propagation angle δ' according to,

$$\begin{bmatrix} r' \\ \delta' \end{bmatrix} = \begin{bmatrix} A & B \\ C & D \end{bmatrix} \begin{bmatrix} r \\ \delta \end{bmatrix} \tag{2.17}$$

For the propagation of a Gaussian beam, a complex q-parameter, which provides information about the beam radius and the radius of curvature of the wavefronts (R) is used and given by,

$$\frac{1}{q} = -i\frac{\lambda}{\pi w^2} + \frac{1}{R}. \tag{2.18}$$

An optical element, represented by an ABCD matrix modifies the q-parameter according to,

$$q' = \frac{Aq + B}{Cq + D}. \tag{2.19}$$

Since any optical resonator can be represented by a set of ABCD matrices, the characteristics of the beam inside the cavity can be calculated at each position inside the resonator. This is extremely useful to design an optical resonator, where one needs to decide the beam size at specific optical components (e.g. in the gain medium) beforehand. The details about optical resonators, including the longitudinal and the transverse modes can be found in Refs. [30, 32].

2.2 Pulsed lasers

Pulsed lasers emit radiation in the form of optical pulses rather than in a continuous-mode. An optical pulse is characterized by various parameters such as pulse duration, pulse energy, pulse repetition rate, spectral bandwidth and central emission wavelength. For plane waves, the electric field associated with optical pulses propagating along the z-direction can be written as,

$$E(z,t) = \frac{1}{2}A(z,t)\exp[i(k_0 z - \omega_0 t)] + c.c., \tag{2.20}$$

where $A(z,t)$ represents the pulse envelope, k_0 is the wave vector at center frequency ω_0, and c.c. stands for complex conjugate. The electric field can also be expressed in terms of its Fourier components according to,

$$E(z,t) = \frac{1}{2\pi}\int_{-\infty}^{\infty} E(z,\omega)\exp(-i\omega t)d\omega, \tag{2.21}$$

where

$$E(z,\omega) = \int_{-\infty}^{\infty} E(z,t)\exp(i\omega t)dt, \tag{2.22}$$

The spectral intensity $S(\omega)$ and the spectral phase $\varphi(\omega)$ at a given position can be calculated as,

$$S(\omega) \propto |E(\omega)|^2, \tag{2.23}$$

$$\varphi(\omega) = Arg[E(\omega)]. \tag{2.24}$$

Due to the properties of Fourier transformation, there exists a relation between the temporal and spectral width of a pulse. The relation is called time bandwidth product and given by,

$$\Delta\nu\Delta\tau \geq K, \tag{2.25}$$

where $\Delta\nu$ and $\Delta\tau$ are the spectral and temporal widths, expressed as full width at half maximum (FWHM), and K is a constant. The value of K depends upon the pulse shape, for example, K is 0.441 for a Gaussian pulse and 0.315 for a hyperbolic secant square pulse.

Ultrashort pulses

Optical pulses are said to be ultrashort if the pulse duration is on the order of femtoseconds or picoseconds. It is clear from the time-bandwidth relation that the generation of ultrashort pulses requires a broad bandwidth. For example, a Gaussian pulse with a duration of 25 fs needs a spectrum with FWHM bandwidth of 17.64 THz i.e. 37.66 nm at a center wavelength of 800 nm, compared to 0.441 THz (0.94 nm at a center wavelength of 800 nm) for a pulse with FWHM pulse duration of 1 ps.

Ultrashort pulses with only a few optical cycles under the pulse envelope are often called few-cycle pulses. In that case, the carrier envelope phase, i.e. the phase between the peak of

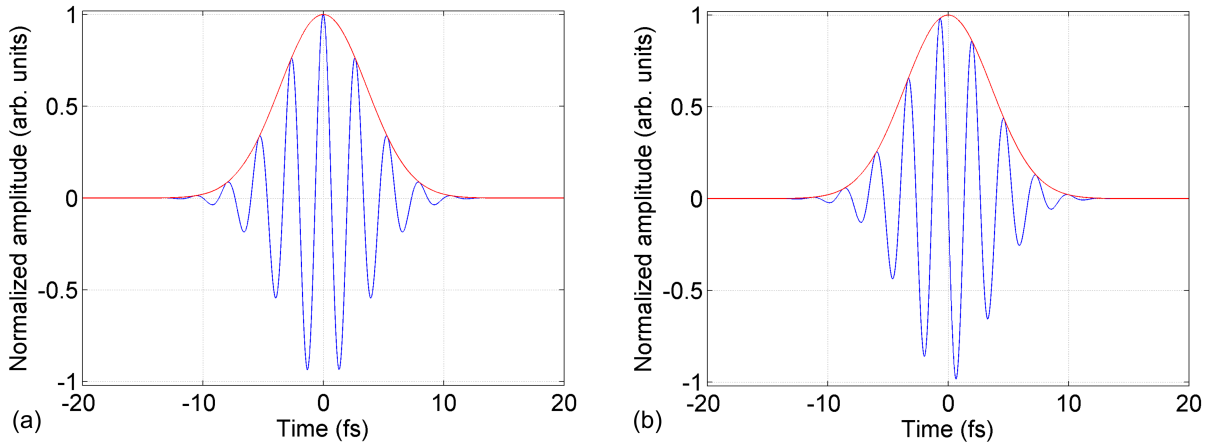

Figure 2.3: Calculated electric field of a Gaussian-shaped few-cycle pulse with a carrier envelope phase (a) $\phi = 0$, and (b) $\phi = \pi/2$. The blue curves correspond to the electric field whereas the red curves are the pulse envelopes.

the envelope of the pulse and the nearest maximum of the carrier wave has to be considered as well. Few-cycle pulses of 6 fs duration (FWHM) with carrier envelope phases of $\phi_0 = 0$ and $\phi_0 = \pi/2$ are shown in Fig. 2.3. It is clearly visible that the strength of the electric field at time $t = 0$ is significantly different for the two pulses (see blue curves).

Dispersion

When an optical pulse propagates through a dispersive medium, the characteristics of the pulse are altered. In particular, the spectral phase is modified due to the frequency dependent refractive index of the medium. After propagation through a transparent medium of length L that introduces a spectral phase $\varphi(\omega)$, the optical pulse in the spectral domain can be written as,

$$E(L,\omega) = E(0,\omega)\exp[i\varphi(\omega)] = E(0,\omega)\exp[ik(\omega)L], \tag{2.26}$$

where $k(\omega)$ is the frequency-dependent propagation wave vector in the medium that has the frequency-dependent refractive index $n(\omega)$.

$$k(\omega) = \frac{\omega}{c}n(\omega). \tag{2.27}$$

In order to describe the influence of dispersion on the pulse duration, the spectral phase can be expressed as a Taylor expansion around a central frequency ω_0 [35],

$$\varphi(\omega) = \varphi_0 + \left.\frac{\partial\varphi}{\partial\omega}\right|_{\omega_0}(\omega-\omega_0) + \frac{1}{2}\left.\frac{\partial^2\varphi}{\partial\omega^2}\right|_{\omega_0}(\omega-\omega_0)^2 + \frac{1}{6}\left.\frac{\partial^3\varphi}{\partial\omega^3}\right|_{\omega_0}(\omega-\omega_0)^3 + ..., \tag{2.28}$$

where φ_0 is the zero-order phase given by,

$$\varphi_0 = k_0 L, \tag{2.29}$$

which is the carrier envelope phase as introduced earlier. It doesn't have any influence on the pulse propagation but changes the carrier envelope phase. This is due to the fact that the phase velocity of the carrier wave and the group velocity of the pulse envelope can be different during the propagation of a pulse in a transparent optical medium. The first derivative in the second term of the right hand side of Eq. 2.28 is known as group delay (t_g), which can be written as,

$$t_g = \frac{\partial \varphi}{\partial \omega} = L\frac{\partial k}{\partial \omega} = \frac{L}{v_g}, \tag{2.30}$$

with v_g as group velocity of the pulse envelope. The group delay introduces a time delay of the pulse and doesn't influence the pulse duration either. The second-order derivative in the third term of the right hand side of Eq. 2.28 is known as group delay dispersion (GDD), which alters the pulse duration. The second-order dispersion (φ_2) can be written as,

$$\varphi_2 = \frac{\partial^2 \varphi}{\partial \omega^2} = L\frac{\partial^2 k}{\partial \omega^2}, \tag{2.31}$$

where $\frac{\partial^2 k}{\partial \omega^2}$ is known as the group velocity dispersion (GVD). In some cases, the second-order dispersion is expressed as the derivative of the group delay with respect to wavelength according to,

$$\varphi_2' = \frac{\partial}{\partial \lambda}\left(\frac{\partial \varphi}{\partial \omega}\right) = -\frac{2\pi c}{\lambda^2}\frac{\partial^2 \varphi}{\partial \omega^2}, \tag{2.32}$$

with the basic unit of s/m. The basic units of GDD and GVD are s^2 and s^2/m. If the pulse is initially Fourier-transform limited and the GDD>0, the low frequency components travel faster than high frequency components and the dispersion is known as normal (or positive) dispersion. Similarly, GDD<0 refers to anomalous (or negative) dispersion, and describes a situation where the lower frequency components move slower. The third-order derivative in the fourth term of the right hand side of Eq. 2.28 is called third-order dispersion (TOD), which alters not only the pulse duration but also the pulse shape during propagation.

Generation of ultrashort pulses

The longitudinal modes of a laser resonator are amplified if the modes lie within the spectral region where the gain of the laser medium is higher than the resonator losses. For an optical resonator of length L, the frequency spacing between the longitudinal modes is given by $\Delta\nu_m = mc/2nL$ (i.e. $\Delta\lambda_m = m\lambda^2/2nL$), with n as the refractive index of the medium inside the resonator and m an integer [Fig. 2.4(a)]. For a gain bandwidth $\Delta\nu_L$ of the laser medium [Fig. 2.4(b)], only a limited number of longitudinal modes falls within the gain profile, which is determined by the net gain i.e. the difference between the gain

and the resonator losses. If N is the number of modes that overlap with the gain profile and the gain exceeds the losses,

$$(N-1)\frac{c}{2nL} = \Delta\nu_L. \tag{2.33}$$

This situation is schematically shown in Fig. 2.4(c).

Since a decrease in the resonator length increases the mode spacing and vice versa, the number of longitudinal modes within the gain bandwidth changes accordingly. Similarly, a broad gain bandwidth incorporates a large number of longitudinal modes, which is essential for the generation of ultrashort pulses.

If there are many longitudinal modes oscillating independently in the resonator with randomly distributed phases, the laser output in the time domain will have the characteristic of noise i.e. intensity fluctuations over time. But modes with a fixed phase relationship with respect to each other lead to a well-defined output in the time domain in the form of a short pulse [Fig. 2.4(d) and (e)]. The laser is then said to be phase-locked or mode-locked. There are several ways of maintaining a fixed phase relation between the modes and the process in general is known as mode-locking. Indeed, mode-locking has been established as a technique to generate ultrashort pulses, and few-cycle pulses have been directly generated from an oscillator. The discussion of various mode-locking techniques, which can be found elsewhere [30, 35] is beyond the scope of the thesis.

2.3 Laser pulse amplification

Laser oscillators are capable of producing short pulses but with low pulse energies i.e. with low peak power. But many applications of pulsed lasers need high energy and high peak power or high peak intensities, for example, experiments in strong field physics.

Amplification of laser pulses can be explained using the same concept as laser operation, namely the creation of population inversion and stimulated emission within a gain medium. In a laser oscillator the photons generated by spontaneous emission are amplified as long as the gain exceeds the losses while in a laser amplifier seed pulses from an oscillator extract the energy stored in the gain medium.

2.3.1 Amplification parameters

For the amplification of a single laser pulse, the pulse energy (E), the fluence (J- energy per unit area) and the small signal gain coefficient (g_0) are the most important parameters to consider. The relation between these parameters in a gain medium of length L can be written as [30],

$$\frac{J_{sto}}{J_{sat}} = g_0 L, \tag{2.34}$$

with

$$J_{sto} = h\nu\Delta nL, \tag{2.35}$$

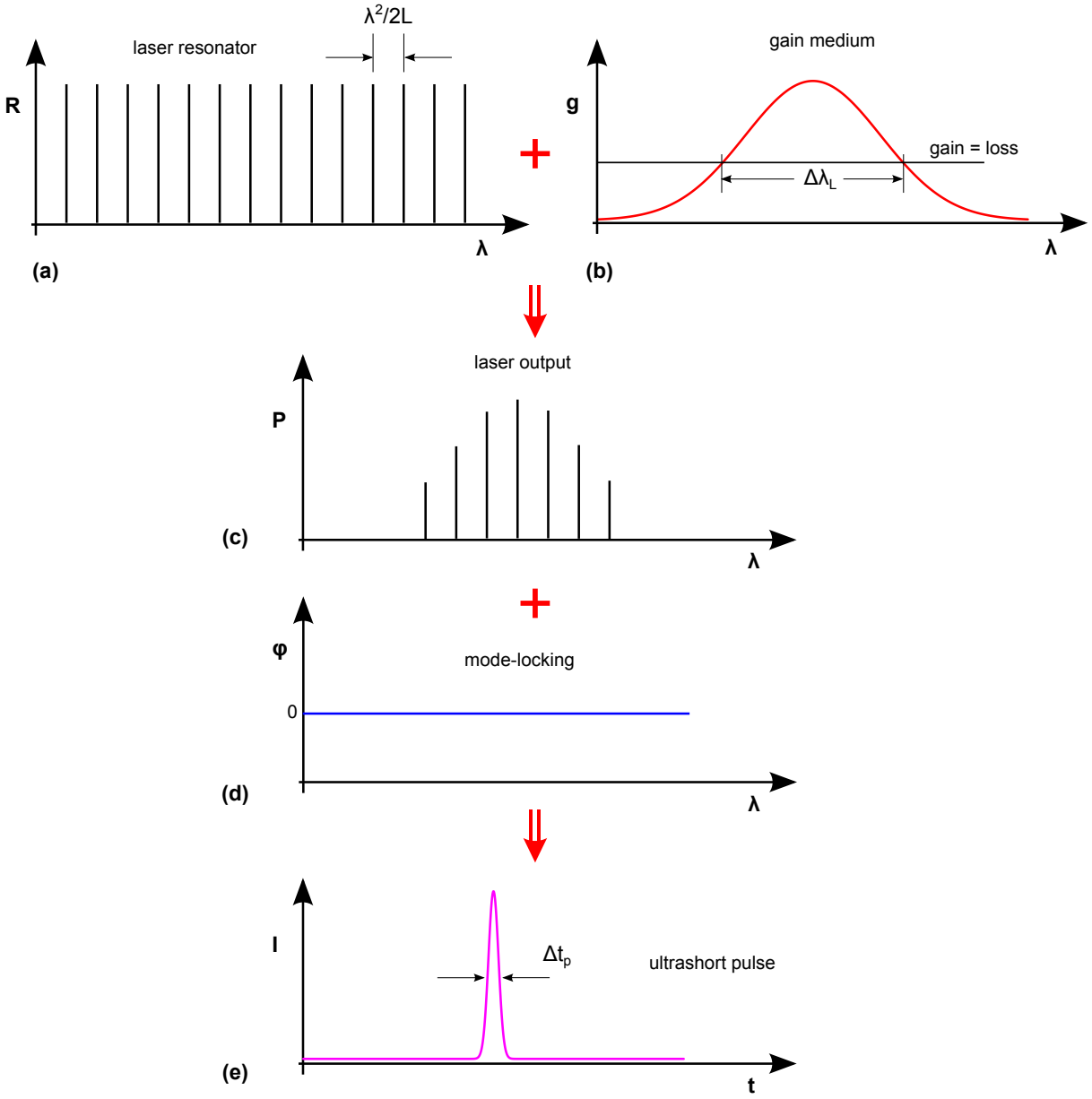

Figure 2.4: Schematic picture of the process of generating ultrashort pulses from a laser oscillator (adapted from Ref. [30]). The combination of the longitudinal modes of an optical resonator (a), the gain profile of the laser medium (b), and the net gain determines the number of modes oscillating in a laser cavity (c). If the modes are locked in phase as shown by the constant phase line in panel (d), there is an ultrashort pulse in the time domain with a FWHM pulse duration defined by Δt_p (e).

$$J_{sat} = h\nu/\sigma_{21}, \tag{2.36}$$

where J_{sto} is the stored energy per unit area in the gain medium, J_{sat} is the saturation fluence, h is Planck's constant, ν is the laser frequency, Δn is the population difference per unit volume [see Eq. 2.10], and σ_{21} is the stimulated emission cross section of the gain medium. The evolution of the fluence within the gain medium for a low seed energy is given by,

$$\frac{dJ}{dz} = g_0 J. \tag{2.37}$$

The solution of Eq. 2.37 provides an expression for the output pulse energy in terms of the saturation fluence and the stored fluence,

$$E_{out} = E_{in} \exp(g_0 L) = E_{in} \exp\left(\frac{J_{sto}}{J_{sat}}\right). \tag{2.38}$$

This implies that the output energy increases exponentially over the length of the laser medium.

For a large seed energy i.e. $J_{in} \approx J_{sat}$, the evolution of the energy density is described by,

$$\frac{dJ}{dz} = g_0 J_{sat}, \tag{2.39}$$

and the solution can be written as,

$$E_{out} = E_{in} g_0 L. \tag{2.40}$$

This means that the increase in energy is linear.

The amplification in the intermediate range of seed energy is given by the Franz-Nodvik equation as,

$$J_{out} = J_{sat} \ln\left[\exp\left(\frac{J_{sto}}{J_{sat}}\right)\left\{\exp\left(\frac{J_{in}}{J_{sat}}\right) - 1\right\} + 1\right]. \tag{2.41}$$

The gain and extraction efficiency of the amplifier can be calculated by J_{out}/J_{in} and $(J_{out} - J_{in})/J_{sto}$ respectively. As an example, the evolution of the gain and the extraction efficiency as a function of J_{in}/J_{sat} is shown in Fig. 2.5.

This shows that the saturation fluence is an important parameter for amplification. Solid state gain media have higher saturation fluence than gases and liquids [36], which leads to low gain. Therefore, in solid state laser amplifiers, multiple passes of the seed pulses through the gain medium are necessary in order to increase the extraction efficiency. This is possible by using amplifier architectures, widely known as multipass and regenerative amplifiers. In a multipass amplifier, seed pulses pass through the gain medium several times, which is geometrically arranged by folding the seed beam using highly-reflective mirrors. A regenerative amplifier can be considered as a particular type of multipass amplifier, where multiple passes of the seed pulses through the gain medium are achieved in an optical resonator or cavity with low losses in which the gain medium is located. Injection of the seed and ejection of the amplified pulses are realized through optical switching. The main

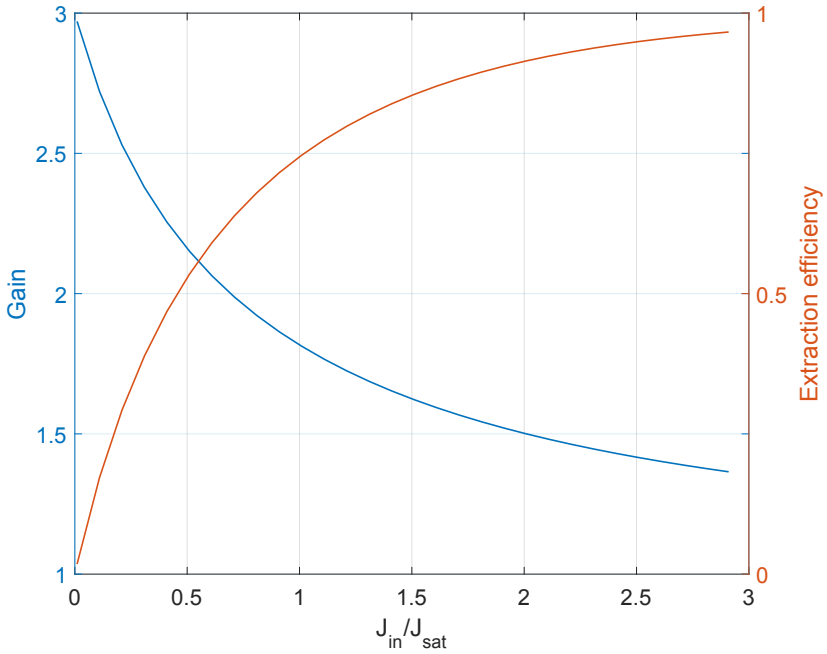

Figure 2.5: Evolution of the gain and extraction efficiency as a function of J_{in}/J_{sat}, calculated using the Franz-Nodvik equation 2.41 for a small signal gain of 3. As can be seen, high gain comes at the cost of extraction efficiency and vice versa.

advantage of a regenerative amplifier is that the amplification is almost independent of the single pass gain and the spatial properties of the amplified beam are largely determined by the resonator, independently of the seed beam. The setup of a multipass amplifier is typically simpler than that of regenerative amplifiers but highly sensitive to misalignment. In the case of high power amplifiers, it is common to utilize both architectures, where a regenerative amplifier is used to obtain high gain and a multipass amplifier is used to boost the output of the regenerative amplifier, achieving high extraction efficiency. The following section briefly reviews the regenerative amplification technique, which is utilized to build a high power, high energy ultrafast amplifier, described in section 3.4.

2.3.2 Regenerative amplifier

A typical regenerative amplifier consists of an optical resonator, an optical switch to couple the beam in and out of the cavity, and an optical arrangement to separate the seed and the amplified pulses. The optical arrangement is similar to an optical isolator and the optical switch consists of a polarizer, a quarter-wave plate, and a Pockels cell driven by a quarter-wave high voltage (see appendix for the details about optical isolators and Pockels cells). The amplification occurs in an optical resonator similar to an oscillator. Unlike the laser resonator where a pulse oscillates inside the cavity and only a part of the energy leaks out of an end mirror or output coupler during each round trip, the seed pulses are coupled into the resonator of the regenerative amplifier and are trapped inside the cavity for a certain

period of time for amplification. Inside the cavity, the seed pulses pass through the gain medium several times extracting the energy that is stored by optical pumping. The pulses are ejected out of the cavity once amplified.

The operation of a regenerative amplifier can be described by dividing it into three phases [30]: pump, amplification and cavity dump. During the pump phase, the high voltage to the Pockels cell is switched off, and the energy is stored in the gain medium. In the amplification phase, a seed pulse is trapped inside the cavity by applying the high voltage to the Pockels cell. The seed pulse circulating inside the cavity is amplified during a certain number of round trips. In the case of a continuous-wave pump, pumping is present even in the amplification phase. Once the energy of the circulating pulse reaches a maximum, the high voltage to the Pockels cell is switched off, ejecting the pulse out of the cavity. This is called cavity dumping.

The main advantage of the regenerative amplifier is that the spatial profile of the amplified pulses is determined by the transverse spatial modes supported by the resonator which is typically close to the diffraction-limit. In addition, a high amplification factor can be achieved despite the low single-pass gain by choosing the appropriate number of round trips of the pulses inside the cavity. However, the gain dynamics can be complex depending upon control parameters such as pulse repetition rate, upper state lifetime of the gain material, number of round trips etc. In a CW-pumped regenerative amplifier operating at a pulse repetition rate higher than the reciprocal of the upper state lifetime, the amplification of a subsequent pulse is significantly affected due to the gain depletion by the current pulse [37]. This may induce instability of the output pulse energy of the amplified pulse train. Such instabilities are represented by a bifurcation diagram showing variations in pulse energy e.g. period doubling and chaotic behaviour [37]. Period doubling is the simplest bifurcation, which refers to a situation in which every second pulse has the same pulse energy, and chaotic behaviour refers to the fluctuations of the pulse energy of subsequent pulses, where the output pulse energies can not be predicted. These behaviours have been reported in the literature in experiments as well as simulations [37–43]. The gain dynamics and the associated bifurcation characteristics of a Yb:YAG thin-disk regenerative amplifier are briefly discussed as follows.

The evolution of the intracavity pulses, the high voltage signal applied to Pockels cell, and the gain are schematically shown in Fig. 2.6 (not to scale) for the case of a CW-pumped regenerative amplifier. The amplification time window is defined by t_G (also called gate length) whereas the repetition rate of the amplified pulses is given by dumping period t_D. Therefore, the number of round trips is given by the round-trip time t_R and the gate length. Note that if the pump source is pulsed and the time between consecutive amplified pulses in the train is much longer than the lifetime i.e. $t_D \gg \tau_L$, any surviving population in the upper laser level after pulse amplification will decay before a new pump pulse, and a new amplification cycle begins. At every new amplification cycle, there is no population inversion from the previous cycle and the gain starts from zero. This implies that there will be no influence of gain depletion from one amplification cycle to other. When the pulse repetition rate is on the order of the reciprocal of the lifetime of the upper laser level, CW pump sources are used and the extraction of the stored energy happens before the

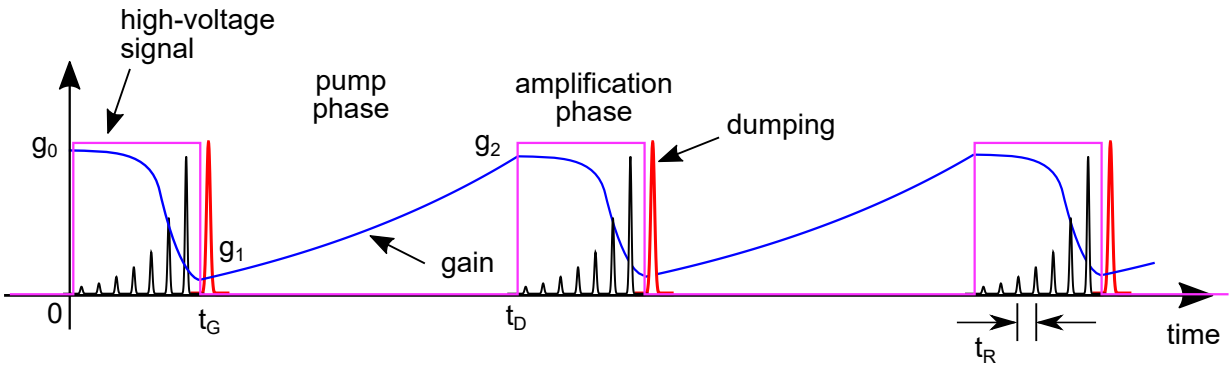

Figure 2.6: Schematic picture of the three phases of regenerative amplification. The high voltage signal determines the amplification time window or gate length (t_G) and the dumping period (t_D). In the amplification phase, the intracavity pulses (black line) separated with a round-trip time t_R extract the stored energy and the gain decreases (blue line). The switching of the high voltage signal to zero dumps the amplified pulse out of the cavity (red line). g_1 and g_2 refer to the initial and final gain values in the pump phase. Adapted from Ref. [38].

population inversion saturates. Therefore, the residual inversion from a previous cycle will affect the stored energy and accordingly the initial gain in the next amplification cycle. As a result, energy of the amplified pulses may vary from cycle to cycle. The variations may get worse when the pulse repetition rate further increases, beyond the reciprocal of the lifetime of the upper laser level. In addition, the number of round trips influences the gain depletion within an amplification cycle, affecting the initial gain for the subsequent cycle and the corresponding amplified pulse energy.

The evolution of the gain and the intracavity pulse energy can be described by rate equations [38], which are different for the pump and the amplification phase. During the pump phase, there is no lasing and the gain varies according to [38],

$$\frac{dg}{dt} = \frac{g_0 - g}{\tau_L}, \tag{2.42}$$

where g_0 and τ_L are the small signal gain and the lifetime of the upper laser level. Note that the small signal gain is proportional to the absorbed pump power [44]. Given the initial gain g_1 at $t = t_G$, Eq. 2.42 can be solved analytically and the solution can be written as,

$$g = g_0 + (g_1 - g_0) \exp\left[-\frac{(t - t_G)}{\tau_L}\right]. \tag{2.43}$$

Then, the gain g_2 at $t = t_D$ is given by,

$$g_2 = g_0 + (g_1 - g_0) \exp\left[-\frac{(t_D - t_G)}{\tau_L}\right]. \tag{2.44}$$

In the amplification phase, the gain is reduced by stimulated emission thereby increasing

Table 2.1: Parameters for the simulation of bifurcation characteristics of a Yb:YAG regenerative amplifier.

Parameter	Value
Center wavelength	1030 nm
Emission cross section	$2.1 \times 10^{-20}\,\mathrm{cm}^2$
Absorption cross section	$0.1 \times 10^{-20}\,\mathrm{cm}^2$
Upper state lifetime	1 ms
Saturation fluence	$8.78\,\mathrm{J/cm}^2$
Laser beam waist radius	1 mm
Seed pulse energy	200 pJ
Cavity losses	0.02
Cavity round-trip time	15 ns
Small signal gain	0.3

the intracavity pulse energy. Therefore, an additional term corresponding to amplification has to be included in Eq. 2.42 and the evolution of the gain is governed by [38],

$$\frac{dg}{dt} = \frac{g_0 - g}{\tau_L} - \frac{gE}{E_{\mathrm{sat}} t_R}, \tag{2.45}$$

and the variation of the intracavity energy E is given by,

$$\frac{dE}{dt} = \frac{E}{t_R}(g_0 - l), \tag{2.46}$$

where E_{sat} and l are the saturation energy (the energy for which the gain is reduced to half of its initial value) and cavity losses respectively. Equations 2.45 and 2.46 have to be solved numerically because analytical solutions are not possible. The boundary conditions are given by $g(t_D) = g_2$ and $E(t_D) = E_s$, with the energy of the seed pulse E_s. For a given set of parameters as shown in Tab. 2.1, Eqs. 2.45 and 2.46 were solved using a fourth-order Runge-Kutta method. More than 300 amplification cycles were considered to ensure that a steady state solution was reached. For a given gate length i.e. number of round trips, the pulse energy of the amplified output pulse was recorded for the last 10 amplification cycles so that the pulse instabilities can be observed if there are any. The calculation was repeated for a set of gate lengths. The output pulse energies are plotted as a function of gate length as shown in Fig. 2.7, which is known as a bifurcation diagram. It is clearly visible that the bifurcation occurs around the gate length of 2.1 µs, where every second pulse has the same pulse energy. Beyond the gate length of 2.5 µs, the chaotic regime occurs, where the pulse energy of the many consecutive pulses fluctuates in an unpredictable way.

It is known that the bifurcation occurs for pulse repetition rates higher than the reciprocal of the upper state lifetime [38]. In addition, bifurcation characteristics depend upon the absorbed pump power (i.e. small-signal gain) for a given number of round trips. For details, see Refs. [37, 39, 41].

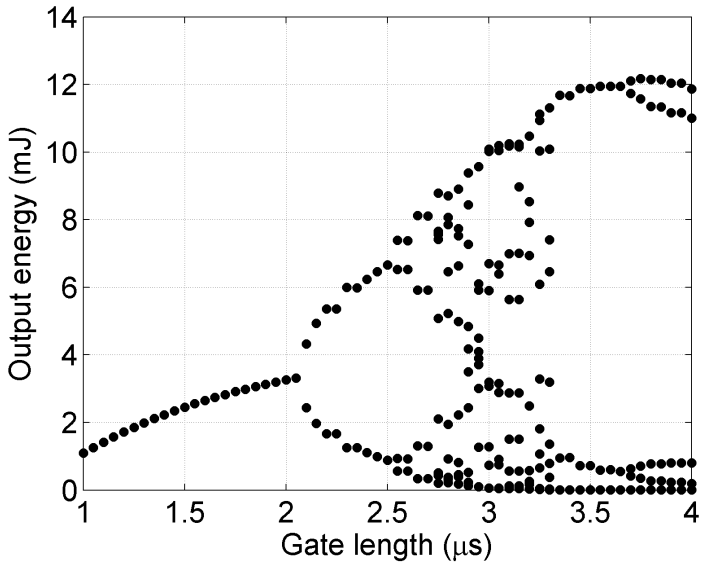

Figure 2.7: Calculated bifurcation diagram with respect to the gate length for a given set of parameters shown in Tab. 2.1. At each gate length, 10 consecutive pulse energies are displayed. The regime of single, double and unpredictable pulse energies are clearly visible.

2.3.3 Amplification of ultrashort pulses

For the amplification of ultrashort pulses, handling the large bandwidth and high peak intensities is crucial. The gain bandwidth of the amplification medium has to be broad enough to preserve the seed bandwidth during amplification. Since the gain profile of the laser transition is not spectrally flat, the frequencies of the seed spectrum that fall at the center of the gain profile experience higher gain compared to the other frequencies. As a result, the spectral bandwidth of the amplified pulses is much narrower than that of the seed pulses. The effect is widely known as gain narrowing.

In addition, the high peak power of ultrashort pulses may induce nonlinear effects during propagation through the gain medium and optical components. One of the dominant nonlinear effects is the Kerr effect, which occurs due to an intensity dependent refractive index of the medium when a beam with high intensity is propagated. The change in refractive index can be expressed to first order by the equation,

$$n = n_0 + n_2 I, \tag{2.47}$$

where n_0 is the linear and n_2 is the nonlinear refractive index, and I is the intensity of the beam. The corresponding propagation phase for a medium of length L can be written as,

$$\varphi = \frac{2\pi}{\lambda}(n_0 + n_2 I)L. \tag{2.48}$$

When ultrashort pulses with high peak intensity propagate through the medium, the

change in refractive index and the corresponding phase depend upon the intensity profile and affect both the spatial and spectral characteristics of the pulses. In the spatial domain, the high intensity beam undergoes self-focusing whereas in the spectral domain, the spectrum of the pulses is broadened by self-phase modulation [the optical Kerr effect, self-focusing and self-phase modulation are briefly discussed in section 2.5.1].

The nonlinear phase introduced due to the Kerr effect, and in general by nonlinear propagation of ultrashort pulses in an amplifier is quantified by a parameter, the so-called B-integral. It is defined by the equation,

$$B = \frac{2\pi}{\lambda} \int n_2 I(t,z) dz, \tag{2.49}$$

where $n_2 I(t,z)$ accounts for the change in refractive index due to the pulse intensity $I(t,z)$ at a position z along the propagation direction and λ is the laser wavelength. The B-integral value during amplification is typically kept < 1 rad in order to avoid nonlinear effects.

In order to limit the B-integral value, the intensity of ultrashort pulses has to be reduced during amplification. This can be realized in principle, by increasing the beam sizes. However, the increase in the beam size is often limited e.g. by the transverse size of the gain medium. An elegant technique was introduced by Strickland and Mourou [3], known as chirped pulse amplification. The pulses are temporally stretched prior to amplification using dispersive elements and compressed afterwards by compensating the dispersion equivalent to that introduced by the stretcher. The technique enabled the development of high energy and high peak power ultrafast lasers. Modern high power laser amplifiers are almost always based on the chirped-pulse amplification technique in which the stretcher and compressor are key components to manipulate the spectral phase of the pulses.

Stretcher

The pulse duration of ultrashort pulses can be increased by introducing dispersion i.e. by changing the spectral phase, which is typically achieved with dispersive bulk materials, or with a special arrangement of optical components such as gratings, prisms, and chirped mirrors. The ultrashort pulses in modern laser systems are mostly stretched by using grating stretchers, chirped-fiber Bragg gratings, and chirped-volume Bragg gratings [45–47].

In particular, the chirped-fiber Bragg grating (CFBG) allows a conventional large grating stretcher to be replaced by a short fiber, which can be integrated in an all-fiber oscillator leading to a compact seed source (except for the case of ultrabroadband pulses, given the limited bandwidth (typically < 30 nm) supported by the CFBG [48]). The Bragg gratings are written inside the core of an optical fiber with an aperiodic modulation of the refractive index over a certain length. For the incident radiation to be reflected from the grating, the Bragg condition, which includes both energy and momentum conservation is to be fulfilled. The momentum conservation implies that the sum of the wave vector of the incident wave and the grating wave vector is equal to the diffracted wave vector. Since the diffracted wave vector is equal and opposite to the incident wave vector, the momentum conservation can

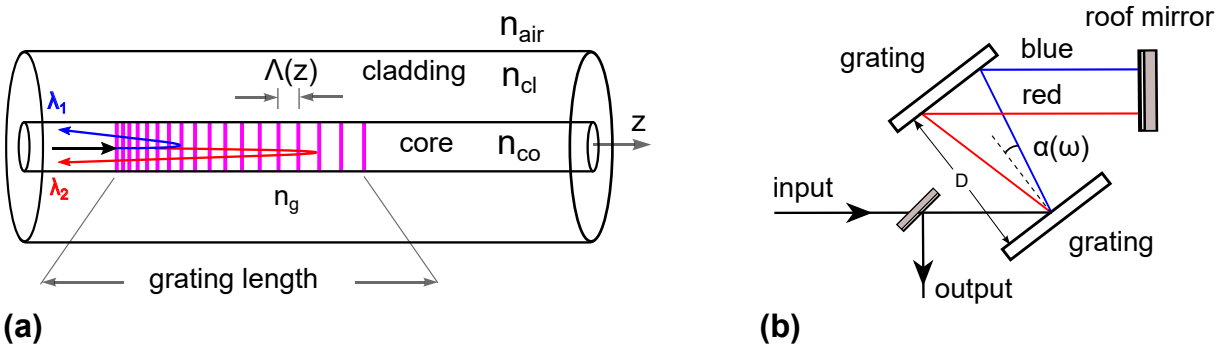

Figure 2.8: (a) Sketch of a chirped-fiber Bragg grating. n_g, n_{air}, n_{cl} and n_{co} are the refractive indices of the grating, air, the fiber-cladding and the fiber-core respectively. Λ is the grating period, which varies along the propagation direction z. λ_1 and λ_2 correspond to shorter and longer wavelengths within the input spectrum. (b) Schematic layout of a Treacy-type grating pair compressor.

be expressed as,

$$2\left(\frac{2\pi n_g}{\lambda_B}\right) = \frac{2\pi}{\Lambda}, \tag{2.50}$$

where n_g and Λ are the effective refractive index of the grating and the grating period respectively. λ_B is the reflected wavelength, known as Bragg wavelength and is given by $2n_g\Lambda$ [cf. Eq. 2.50]. As schematically shown in Fig. 2.8(a), the grating period varies along the fiber length and the Bragg wavelength accordingly as well. This means different wavelengths are reflected at different positions within the grating and the grating is said to be chirped. The wavelength-dependent group delay offered by such a CFBG can provide both positive and negative dispersion depending on the periodicity of the index modulation. For ultrashort pulses, the reflectivity and the group delay have to be optimized for a broad spectral range. In addition, it is important to have low insertion loss, and to minimize the ripples in the group delay. For optimal dispersion compensation in chirped-pulse amplification, the phase function has to be matched with that of the compressor.

The choice of a stretcher depends on the required stretch factor, which is determined in such a way that the nonlinear phase shift accumulated during the amplification is kept small (B-integral value < 1).

Compressor

After amplification, the chirp introduced by the stretcher has to be reversed in order to obtain short pulses. The dispersion introduced by the CFBG stretcher can be compensated by a grating pair compressor, which is widely used in high energy and high power laser systems based on the chirped-pulse amplification technique.

In 1969, E. Treacy introduced an arrangement of two gratings that can provide negative dispersion [49]. The schematic of the grating pair compressor is shown in Fig. 2.8(b). The beam is angularly dispersed by the first grating and the second grating is used to

compensate the angular dispersion, introducing spatial chirp i.e. the central frequency varies as a function of position within the beam profile. The spatially chirped beam is then reflected backwards by an end mirror. The second pass through the pair of gratings removes the spatial chirp. The amount of negative dispersion depends on the distance between the gratings and their groove density. The second and third order dispersion coefficients of a Treacy-type grating pair, as introduced before, are given by [50],

$$GDD = \frac{-\lambda^3 D}{2\pi c^2 d^2 \cos^3 \alpha}, \tag{2.51}$$

$$TOD = \frac{3\lambda^4 D}{4\pi^2 c^3 d^2 \cos^3 \alpha}\left(1 + \frac{\lambda \sin \alpha}{d \cos^2 \alpha}\right), \tag{2.52}$$

where α is the angle of diffraction at a given wavelength λ [see Fig. 2.8(b)], D is the separation of the gratings measured parallel to their surface normals and d is the spacing of the grating rulings.

Thermal effects

Chirped pulse amplifiers have been very successful in scaling the peak power of ultrashort pulses. However, high energy, short pulses have mostly been achieved at a pulse repetition rate $< 10\,\text{kHz}$. Scaling the repetition rate while keeping the pulse energy high (i.e. high average power) is limited by thermal effects that arise due to the heat deposited within the gain medium.

There are several mechanisms that cause a deposition of heat in an optically pumped gain medium. The non-radiative transitions described in section 2.1 are the main source of heat load. This source is quantified by a parameter, known as quantum defect. The quantum defect is given by the difference in photon energies between the pump and the laser. It is also defined as the fractional difference of photon energies between the pump and the laser according to,

$$QD = \frac{E_p - E_l}{E_p} = 1 - \frac{\lambda_p}{\lambda_l}, \tag{2.53}$$

where E_p and E_l are the pump and laser photon energies at pump and laser wavelengths of λ_p and λ_l respectively. Other less important mechanisms such as lifetime quenching, excited-state absorption and cross relaxation are not discussed here and the details can be found in Refs. [30, 51].

In order to remove the heat load in high power amplifiers based on solid state gain media, active cooling of the gain medium is necessary. For efficient cooling, a gain material with high thermal conductivity is preferable. The cooling architecture depends upon the geometry of the gain medium. For example, in the case of end-pumped rod amplifiers, the rod is usually cooled from the edges/side surfaces. This means that heat flows in the radial direction inducing radial temperature gradients. Such a temperature distribution changes

the refractive index of the medium according to,

$$\Delta n(r) = \frac{dn}{dT}\Delta T(r), \tag{2.54}$$

where n is the refractive index of the gain medium, r is the radial coordinate, ΔT is the change in temperature in radial direction, and dn/dT is the thermo-optic coefficient of the gain material. The change in refractive index is higher at the rod center and decreases slowly at positions away from the center and towards the edges. The induced variation of the refractive index effectively creates a thermal lens, introduces wavefront distortions, and can cause focusing of the beam.

In addition, the material expands or contracts when the temperature varies. The tension or compression of the material, which depends upon the coefficient of thermal expansion, may not be uniform in different directions along the material. This induces mechanical stress in the gain medium. Since the area under tension and compression can have different changes in refractive index, the thermally-induced stress creates birefringence. As a result, a linearly polarized beam propagating through the rod undergoes depolarization. Increase in heat load beyond the level where the thermal stress exceeds the tensile strength of the material leads to fracture of the material.

There have been several solutions proposed and utilized to tackle thermal effects in high power amplifiers, reducing the heat load, removing the heat efficiently to reduce temperature gradients, and compensating the thermal-induced optical distortions. Design considerations of high average power laser systems are mainly concentrated on removing the heat efficiently, thereby reducing thermal effects. The techniques utilized to reduce the temperature of the gain medium determine the architecture of a high power laser system, e.g. using different geometries of the laser gain medium such as rod-type, fiber, Innoslab, and thin-disk.

2.4 Second-order nonlinear processes

2.4.1 Wave equation for nonlinear media

An electromagnetic field propagating in any material induces a polarization of the material that can be expanded in a power series of increasing powers of the field. The polarization depends on a property of the material known as electric susceptibility. The polarization induced in the material, $\mathbf{P}(\mathbf{r},t)$ is typically expressed as a sum of linear, $\mathbf{P}_l(\mathbf{r},t)$ and nonlinear, $\mathbf{P}_{nl}(\mathbf{r},t)$ terms given by,

$$\mathbf{P}(\mathbf{r},t) = \mathbf{P}_l(\mathbf{r},t) + \mathbf{P}_{nl}(\mathbf{r},t) = \epsilon_0\chi^{(1)}\mathbf{E}(\mathbf{r},t) + \epsilon_0[\chi^{(2)}\mathbf{E}^2(\mathbf{r},t) + \chi^{(3)}\mathbf{E}^3(\mathbf{r},t) + ...]. \tag{2.55}$$

where $\mathbf{E}(\mathbf{r},t)$ is the electric field with $\mathbf{r}$ as spatial and t as temporal co-ordinates. ϵ_0 corresponds to the permittivity of free space and the $\chi^{(n)}$ are tensors of rank $n+1$, commonly referred as n^{th} order susceptibility. The symbols in bold mean the quantities are vectors,

and $\mathbf{E}^m$ refers to an operation of order m, where m is an integer.

The propagation of electromagnetic waves, that can be derived from the Maxwell equations [33] is represented by,

$$\nabla \times \nabla \times \mathbf{E}(\mathbf{r},t) + \frac{1}{c^2}\frac{\partial^2 \mathbf{E}(\mathbf{r},t)}{\partial t^2} = -\frac{1}{\epsilon_0 c^2}\frac{\partial^2 \mathbf{P}(\mathbf{r},t)}{\partial t^2}, \tag{2.56}$$

This is the most general form of wave equation including nonlinear processes. It can be simplified by reasonable assumptions in order to study specific nonlinear interactions. From vector calculus,

$$\nabla \times \nabla \times \mathbf{E}(\mathbf{r},t) = \nabla(\nabla.\mathbf{E}(\mathbf{r},t)) - \nabla^2 \mathbf{E}(\mathbf{r},t). \tag{2.57}$$

The term $\nabla.\mathbf{E}(\mathbf{r},t)$ vanishes for the linear, isotropic media (without source charge). In nonlinear media, $\nabla.\mathbf{E}(\mathbf{r},t)$ doesn't vanish but is very small and can safely be neglected in many cases [33]. By introducing the linear and nonlinear polarization terms on the right hand side of Eq. 2.56 and substituting the linear polarization by $\epsilon_0\chi^{(1)}\mathbf{E}(\mathbf{r},t)$, the wave equation 2.56 can be simplified to,

$$\nabla^2 \mathbf{E}(\mathbf{r},t) - \frac{\epsilon^{(1)}}{c^2}\frac{\partial^2 \mathbf{E}(\mathbf{r},t)}{\partial t^2} = \frac{1}{\epsilon_0 c^2}\frac{\partial^2 \mathbf{P}_{nl}(\mathbf{r},t)}{\partial t^2}, \tag{2.58}$$

where $\epsilon^{(1)} = 1 + \chi^{(1)}$. The simplified wave equation 2.58 can be used to describe various nonlinear optical interactions. For example, the second-order nonlinear processes such as sum frequency generation (SFG), second harmonic generation (SHG) and difference frequency generation (DFG) are considered if the nonlinear source term contains only the second-order susceptibility ($\chi^{(2)}$) such that $\mathbf{P}_{nl}(\mathbf{r},t) = \epsilon_0\chi^{(2)}\mathbf{E}^2(\mathbf{r},t)$.

If we consider two electric fields of frequency ω_1 and ω_2 interacting in a nonlinear medium to produce a new optical field at the sum frequency $\omega_3 = \omega_1 + \omega_2$, the process is called SFG. Similarly, the interaction is known as DFG if the frequency of the new field is the difference of the input frequencies. The difference between the second-order processes can be clearly visualized in the virtual energy-level diagram that follows the conservation of energy as shown in Fig. 2.9. In SFG, two photons of different frequencies are annihilated to create a new photon with a frequency given by the sum of the input frequencies. SHG is a particular case of SFG where two photons of the same frequency are converted into a photon of twice the input frequency. In DFG, the interaction of two photons at different frequencies creates a photon at the difference frequency. DFG typically occurs when the input fields are of comparable intensities. If the low frequency field is much weaker than the high frequency field, the weak field gets amplified by the DFG process and the phenomenon is known as optical parametric amplification. Even if the low frequency field is not present, there will be two photons created in the DFG by spontaneous two-photon emission from a virtual energy level and the phenomenon is known as parametric fluorescence.

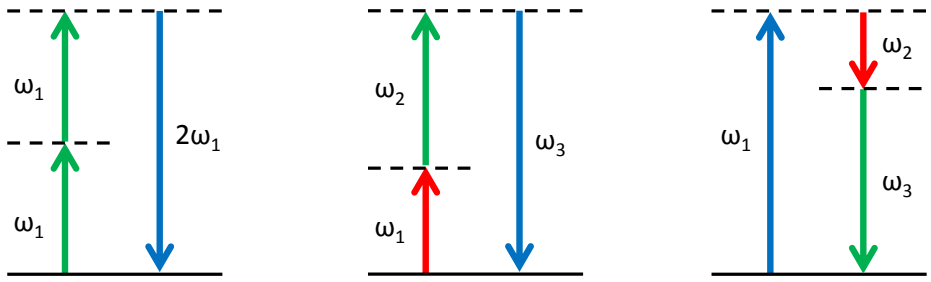

Figure 2.9: Energy-level diagram of second-order nonlinear processes: (a) Second harmonic generation, (b) Sum-frequency generation (SFG) and (c) Difference frequency generation (DFG). Optical parametric amplification is a particular case of DFG where a weak field with lower frequency ω_2 is amplified by a nonlinear interaction with a strong field of higher frequency ω_3.

2.4.2 Sum frequency generation

A simplified representation of a laser electric field that is propagating along the z direction with a propagation wave vector k can be written as,

$$E(z,t) = \frac{1}{2}A(z)\exp\left[i(\omega t - kz)\right] + c.c., \tag{2.59}$$

where the field is quasi-monochromatic with frequency ω and linearly polarized, and the envelope $A(z)$ is separated from the rapid oscillating term. Assuming a lossless nonlinear medium with collimated, quasi-monochromatic, continuous wave input beams and under the slowly varying envelope approximation [$A(z)$ is changing slowly with z compared to the carrier wave i.e. $\frac{\partial^2 A}{\partial z^2} \ll k\frac{\partial A}{\partial z}$], a set of coupled-wave equations that represents the evolution of the amplitudes of the interacting electric fields can be derived. The coupled-wave equations for sum frequency generation are given by [33],

$$\frac{dA_1}{dz} = -i\frac{\omega_1 d_{\text{eff}}}{n_1 c}A_2 A_3 \exp(i\Delta k z), \tag{2.60}$$

$$\frac{dA_2}{dz} = -i\frac{\omega_2 d_{\text{eff}}}{n_2 c}A_1 A_3^* \exp(-i\Delta k z), \tag{2.61}$$

$$\frac{dA_3}{dz} = -i\frac{\omega_3 d_{\text{eff}}}{n_3 c}A_1 A_2^* \exp(-i\Delta k z), \tag{2.62}$$

where A_1, A_2 and A_3 are the electric field amplitudes of the three interacting waves of frequencies ω_1, ω_2 and ω_3 with corresponding refractive indices n_1, n_2 and n_3 respectively. d_{eff} is the effective nonlinear optical coefficient of the medium and c is the speed of light. $\Delta k = k_1 - k_2 - k_3$ is the wave-vector mismatch (also called phase mismatch factor).

An analytical solution of the coupled-wave equation for the sum frequency field is possible within an assumption that the amplitudes A_1 and A_2 are constants. The intensity of the output field I_3 at the frequency ω_3 for a nonlinear medium of length L can then be written

as,

$$I_3 = \frac{2d_{\text{eff}}^2\omega_3^2 I_1 I_2}{n_1 n_2 n_3 \epsilon_0 c^2} L^2 \,\text{sinc}^2\left(\frac{\Delta kL}{2}\right), \tag{2.63}$$

where I_1 and I_2 are the intensities of the input waves, calculated from the field amplitudes as,

$$I(z) = \frac{1}{2} n \epsilon_0 c \left|A(z)\right|^2. \tag{2.64}$$

Equation 2.63 clearly indicates that the efficiency of the frequency mixing process is largely determined by wave-vector mismatch. The efficiency decreases when Δk increases. An efficient mixing of the frequencies requires to fulfill the condition $\Delta k = 0$, which is known as the perfect phase-matching condition. This can be considered as a momentum conservation condition, similar to the energy conservation. Both conditions can be expressed as,

$$\vec{k}_3 = \vec{k}_1 + \vec{k}_2 \tag{2.65}$$

$$\omega_3 = \omega_1 + \omega_2 \tag{2.66}$$

2.4.3 Phase-matching

The perfect phase-matching condition for three collinearly propagating waves ($\omega_1 \leq \omega_2 < \omega_3$) can be written as,

$$\omega_3 n_3 = \omega_1 n_1 + \omega_2 n_2. \tag{2.67}$$

From Eqs. 2.66 and 2.67,

$$n_3 - n_2 = (n_1 - n_2)\frac{\omega_1}{\omega_3}. \tag{2.68}$$

It is clear that for the perfect phase-matching condition, n_2 has to be smaller than both n_3 and n_1, which is not possible in optical materials with normal dispersion (refractive index increases with frequency). Equation 2.68 can be satisfied by utilizing the natural birefringence of uniaxial or biaxial crystals, where the refractive index also depends on the polarization direction of the incident beam. For a given propagation direction, there exist two refractive indices corresponding to two orthogonally polarized beams known as ordinary beam (polarized perpendicular to the plane containing the optical axis of the crystal and the propagation direction) and extraordinary beam (polarized in the plane containing the optical axis of the crystal and the propagation direction). The refractive index of the extraordinary beam varies with the propagation direction with respect to the optical axis of the crystal. Therefore, the perfect phase-matching condition can be obtained by choosing the polarization direction and the direction of propagation appropriately [see Tab. 2.2].

Depending upon the polarization of the lower frequency waves, the phase-matching configuration is often classified into two types: type I and type II. Type I refers to the case where the two lower frequency waves have the same polarization and Type II corresponds to the case where the lower frequency waves are orthogonally polarized. Both configurations

Table 2.2: Phase-matching configurations for uniaxial crystals: o: ordinary beam, e: extraordinary beam, ω_1, ω_2: frequencies of input beams, and ω_3: frequency of output beam ($\omega_1 \leq \omega_2 < \omega_3$).

	Negative uniaxial $n_e < n_o$			Positive uniaxial $n_e > n_o$		
	ω_1	ω_2	ω_3	ω_1	ω_2	ω_3
Type I	o	o	e	e	e	o
Type II	e	o	e	o	e	o

are summarized in Tab. 2.2 in the case of uniaxial crystals. The ordinary and extraordinary beams are represented by o and e respectively.

There are three major approaches to achieve phase-matching in nonlinear crystals as follows:

a) *Critical phase-matching*: This is the most common phase-matching technique utilized in birefringent crystals in which the phase-matching condition is satisfied by selecting an appropriate crystal orientation with respect to the propagation direction for one of the interacting waves and the technique is also known as angular phase-matching.

For a uniaxial crystal, the refractive index of a wave with extraordinary polarization is given by,

$$\frac{1}{n_e^2(\theta)} = \frac{\cos^2\theta}{n_o^2} + \frac{\sin^2\theta}{n_e^2}, \tag{2.69}$$

where $n_e(\theta)$ is the refractive index of the extraordinary polarized beam at an angle θ between the propagation wave vector and the optical axis of the crystal. n_o is the ordinary refractive index, which doesn't depend on θ and n_e is the extraordinary refractive index for $\theta = 90°$, which equals n_o at $\theta = 0°$. The angle θ can be adjusted to obtain the value of $n_e(\theta)$ for which the phase-matching condition is satisfied.

As an example of the sum frequency generation process, where three waves propagate collinearly through a negative uniaxial crystal, the perfect phase-matching condition in Type I phase-matching can be expressed as,

$$\omega_3 n_e(\omega_3, \theta) = \omega_1 n_o(\omega_1) + \omega_2 n_o(\omega_2). \tag{2.70}$$

A major drawback of critical phase-matching is spatial walk-off of the extraordinary polarized beam i.e. the Poynting vector (the vector that defines the rate of energy transfer per unit area) subtends an angle with the propagation wave vector if $\theta \neq 90°$. Due to the walk-off, the interacting waves with ordinary and extraordinary polarization separate from each other after propagating a certain distance within the crystal, resulting in a reduction of the conversion efficiency.

b) *Noncritical phase-matching*: In this technique, the temperature of the birefringent crystal is adjusted, instead of the propagation angle, in order to change the refractive

indices of the interacting waves thereby changing the phase velocities and minimizing the wave-vector mismatch. Therefore, it is also called temperature-controlled phase-matching. While changing the temperature of the crystal, the angle θ is fixed at 90°. As a result, there are no spatial walk-off effects. The term 'noncritical' refers to the fact that this phase-matching approach is relatively insensitive to slight misalignment of the propagating waves.

c) *Quasi-phase-matching*: This approach uses a nonlinear material with spatially modulated nonlinear properties, unlike the homogenous material that is used in other techniques. The phase-matching is mostly achieved by using an alternating sign of the effective nonlinear optical coefficient along the propagation length in periodically poled crystals. In contrast to critical phase-matching, the interacting waves can have the same polarization states, and the approach is sometimes called type 0 phase-matching.

2.4.4 Second harmonic generation

In second harmonic generation, the incident field at frequency ω interacts with a $\chi^{(2)}$ nonlinear medium generating radiation at the second-harmonic frequency 2ω. Similar to the coupled-wave equations for sum frequency generation [Eqs. 2.60, 2.61 and 2.62], the coupled differential equations for the fundamental and second harmonic field can be written as [33],

$$\frac{dA_\omega}{dz} = -i\frac{\omega d_{\text{eff}}}{n_\omega c} A_{2\omega} A_\omega^* \exp(i\Delta k z), \tag{2.71}$$

$$\frac{dA_{2\omega}}{dz} = -i\frac{\omega d_{\text{eff}}}{2n_{2\omega} c} A_\omega^2 \exp(-i\Delta k z), \tag{2.72}$$

where $\Delta k = 2k_\omega - k_{2\omega}$ is the wave-vector mismatch. A_ω and $A_{2\omega}$ are the amplitudes of the fundamental and second-harmonic fields respectively propagating along the z-direction, with corresponding refractive indices of n_ω and $n_{2\omega}$ respectively.

The coupled-wave equations 2.71 and 2.72 can be solved analytically for the intensity of the second-harmonic field $I_{2\omega}$ under an approximation of $A_\omega \approx$ *constant* (undepleted pump approximation) over a crystal length of L. The solution is given by the equation,

$$I_{2\omega}(L) = \frac{2\omega^2 d_{\text{eff}}^2 I_\omega(0)^2}{\epsilon_0 c^3 n^3} L^2 \,\text{sinc}^2\left(\frac{\Delta k L}{2}\right), \tag{2.73}$$

where $I_\omega(0)$ is the intensity of the fundamental field at $z = 0$ and $n = n_\omega \approx n_{2\omega}$. For a given crystal and a given fundamental wavelength, the conversion efficiency depends on the wave-vector mismatch, length of the crystal and the intensity of the fundamental field. The factor $\text{sinc}^2(\Delta k L/2)$ is often called the phase-mismatch factor. An increase in the crystal length increases the phase-mismatch factor and therefore, decreases the conversion efficiency.

For more accurate calculations of the conversion efficiency, pump depletion and real

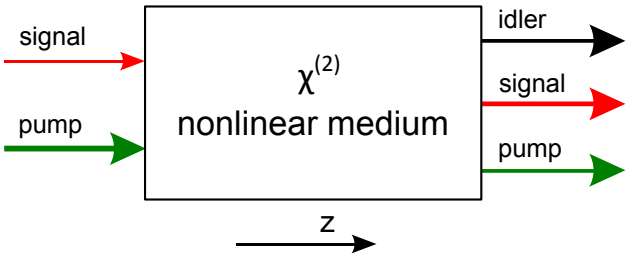

Figure 2.10: Schematic diagram of optical parametric amplification in a nonlinear medium. The signal and pump waves propagating along z direction interact nonlinearly in the medium amplifying the signal wave and generating an idler wave.

beams (instead of plane waves) have to be taken into account. Additional parameters, which influence the second harmonic generation are laser characteristics such as the beam divergence and spectral width, and parameters related to the harmonic generation process such as angular, thermal and spectral sensitivities to the phase-matching condition [30]. For example, a large beam divergence increases the phase-mismatch factor while the perfect phase-matching is only possible over a narrow spectral range. Any variations of the phase-matching angle and temperature of the crystal increase the phase-mismatch factor, limiting the conversion efficiency. The limitations associated with both the laser and harmonic generation parameters are well-understood and the details can be found in Refs. [30, 52].

2.4.5 Optical parametric amplification

Optical parametric amplification (OPA) is a particular case of difference frequency generation where energy of an intense field at a high frequency is transferred to a field with low frequency i.e. the low frequency field is amplified, generating a new field whose frequency is the difference between the frequencies of the two input fields. The high frequency input field is called pump whereas the low frequency input field and the newly generated field are called signal and idler respectively (sometimes signal and idler are interchanged). The energy and momentum conservation for OPA are given by,

$$\omega_p - \omega_s = \omega_i \tag{2.74}$$

$$\vec{k}_p - \vec{k}_s = \vec{k}_i \tag{2.75}$$

The subscripts p, s and i are used for pump, signal and idler respectively.

Coupled-wave equations

If the three waves are propagating along the z-axis in a lossless nonlinear medium with second-order nonlinear susceptibility as schematically shown in Fig. 2.10, the coupled-wave equations for parametric amplification under the slowly varying envelope approximation

can be written as [53],

$$\frac{dA_p}{dz} = -i\frac{\omega_p d_{\text{eff}}}{n_p c} A_s A_i \exp(i\Delta k z), \tag{2.76}$$

$$\frac{dA_s}{dz} = -i\frac{\omega_s d_{\text{eff}}}{n_s c} A_p A_i^* \exp(-i\Delta k z), \tag{2.77}$$

$$\frac{dA_i}{dz} = -i\frac{\omega_i d_{\text{eff}}}{n_i c} A_p A_s^* \exp(-i\Delta k z), \tag{2.78}$$

where $\Delta k = k_p - k_s - k_i$ is the wave-vector mismatch that determines the nonlinear interactions among the pump, signal and idler, and A_n with $n = p$, s and i corresponds to the amplitude of the electric field defined as,

$$E(z,t) = Re\left\{A(z)\exp\left[i(wt - kz)\right]\right\}. \tag{2.79}$$

The analytical solutions of the coupled-wave equations under the assumption of undepleted pump ($A_p \approx constant$) for OPA are available elsewhere [53]. The solutions are briefly discussed here. After a propagation distance of z along the crystal, the solutions for the signal and the idler intensities are given by,

$$I_s(z) = I_s(0)\left[1 + \frac{\Gamma^2}{g^2}\sinh^2(gz)\right], \tag{2.80}$$

$$I_i(z) = I_s(0)\frac{\omega_i}{\omega_s}\frac{\Gamma^2}{g^2}\sinh^2(gz), \tag{2.81}$$

where the small signal gain g is defined as,

$$g = \sqrt{\Gamma^2 - \left(\frac{\Delta k}{2}\right)^2}, \tag{2.82}$$

with Γ as the small signal gain for perfect phase-matching given by,

$$\Gamma^2 = \frac{2\omega_s\omega_i d_{\text{eff}}^2}{c^3\epsilon_0 n_i n_s n_p} I_p. \tag{2.83}$$

The parametric gain G in a crystal of length L is given by,

$$G(L) = \frac{I_s(L)}{I_s(0)} = 1 + \frac{\Gamma^2}{g^2}\sinh^2(gL). \tag{2.84}$$

In the approximation of large parametric gain ($gL \gg 1$), Eq. 2.84 reduces to,

$$G(L) \approx \frac{\Gamma^2}{g^2}\frac{\exp(2gL)}{4}. \tag{2.85}$$

This is the expression for parametric gain in the case of monochromatic waves under the approximation of no depletion of the pump. Despite the restrictive approximations, it provides insight into the factors governing or influencing the parametric gain. Furthermore, if the phase-matching is perfect i.e. $\Delta k = 0$ and $g = \Gamma$, Eq. 2.85 reduces to,

$$G(L) = \frac{1}{4}\exp(2\Gamma L). \tag{2.86}$$

It can be seen from the Eqs. 2.82, 2.83 and 2.84 that the parametric gain mainly depends on the effective nonlinear optical coefficient, the pump intensity, the crystal length and the wave-vector mismatch. The most critical parameter to achieve large parametric gain is the wave-vector mismatch. Once the mismatch reduces to zero, the gain varies exponentially with the effective nonlinear optical coefficient, crystal length and the square root of the pump intensity. This suggests that pump pulses with high peak power and long crystals with large d_{eff} are essential for large parametric gain and/or high conversion efficiency, once the phase-matching condition is satisfied.

So far the interacting waves are assumed to be monochromatic, continuous-wave fields. This can be extended to the interaction of pulses, the electric field of which can be written as,

$$E(z,t) = Re\left\{A(z,t)\exp\left[i(\omega t - kz)\right]\right\}, \tag{2.87}$$

where $A(z,t)$ is the pulse envelope. The nonlinear wave equation, if solved for the electric field of the pulses, provides a new set of coupled-wave nonlinear equations. Compared to the coupled-wave equations in the case of monochromatic waves, additional terms appear which represent dispersion effects. The general coupled-wave equations for ultrashort pulses are given by [54],

$$\frac{dA_p}{dz} + \sum_{n=1}^{\infty}\frac{(-i)^{n-1}}{n!}k^{(n)}\frac{\partial^n A_p}{\partial t^n} = -i\frac{\omega_p d_{\text{eff}}}{n_p c}A_s A_i \exp\left(i\Delta k z\right), \tag{2.88}$$

$$\frac{dA_s}{dz} + \sum_{n=1}^{\infty}\frac{(-i)^{n-1}}{n!}k^{(n)}\frac{\partial^n A_s}{\partial t^n} = -i\frac{\omega_s d_{\text{eff}}}{n_s c}A_p A_i^* \exp\left(-i\Delta k z\right), \tag{2.89}$$

$$\frac{dA_i}{dz} + \sum_{n=1}^{\infty}\frac{(-i)^{n-1}}{n!}k^{(n)}\frac{\partial^n A_i}{\partial t^n} = -i\frac{\omega_i d_{\text{eff}}}{n_i c}A_p A_s^* \exp\left(-i\Delta k z\right), \tag{2.90}$$

where $k^{(n)}$ is the n^{th} order dispersion coefficient described in section 2.2. Different group velocities of the pump, signal and idler as well as group velocity dispersion effects, that appear in the coupled-wave equations via dispersion coefficients, influence the performance of an OPA. The equations can be simplified if the interacting pulses are longer ($\gg$100 fs transform-limited) by approximating the dispersion coefficient to the first order i.e. neglecting the pulse broadening during propagation through the crystal. Unlike the case of monochromatic waves, wave-vector mismatch depends upon frequency which largely determines the phase-matching bandwidth. The analytical solution of the set of Eqs. 2.88, 2.89 and 2.90 is not possible in the general case and it is challenging even in the undepleted

pump approximation. Therefore, the equations have to be solved numerically which will be discussed in chapter 4.

Phase-matching bandwidth

For waves with spectral bandwidth $\Delta\omega$, the wave-vector mismatch can be expressed in a Taylor series (up to second-order terms only) around a central frequency ω_0 as:

$$\begin{aligned}\Delta k = k_p + \left.\frac{\partial k_p}{\partial \omega}\right|_{\omega_{p0}} \Delta\omega_p + \left.\frac{\partial^2 k_p}{\partial \omega^2}\right|_{\omega_{p0}} (\Delta\omega_p)^2 - k_s - \left.\frac{\partial k_s}{\partial \omega}\right|_{\omega_{s0}} \Delta\omega_s \\ - \left.\frac{\partial^2 k_s}{\partial \omega^2}\right|_{\omega_{s0}} (\Delta\omega_s)^2 - k_i - \left.\frac{\partial k_i}{\partial \omega}\right|_{\omega_{i0}} \Delta\omega_i - \left.\frac{\partial^2 k_i}{\partial \omega^2}\right|_{\omega_{i0}} (\Delta\omega_i)^2 - ...\end{aligned} \tag{2.91}$$

If the pump is assumed to be quasimonochromatic ($\Delta\omega_p \approx 0$), $\Delta\omega_s = -\Delta\omega_i$. Excluding the second-order terms in the expansion, Eq. 2.91 becomes,

$$\Delta k = k_p - k_s - k_i - \left(\left.\frac{\partial k_s}{\partial \omega}\right|_{\omega_{s0}} - \left.\frac{\partial k_i}{\partial \omega}\right|_{\omega_{i0}} \right) \Delta\omega_s. \tag{2.92}$$

Assuming a perfect phase-matching at the central frequencies i.e. ($k_p = k_s + k_i$) and using group velocities, the expression for wave-vector mismatch becomes,

$$\Delta k = \left(\frac{1}{v_{gi}} - \frac{1}{v_{gs}} \right) \Delta\omega_s. \tag{2.93}$$

Equation 2.93 refers to a broadband phase-matching condition and indicates that wave-vector mismatch strongly depends upon the difference between the group velocities of the signal (v_{gs}) and the idler (v_{gi}). phase-matching occurs over a broad spectrum when $v_{gs} = v_{gi}$. This is inherently achieved in a degenerate OPA where the central frequency of the pump is twice the central frequency of the signal and the idler has the same spectrum as the signal. Perfect phase-matching up to the first order increases gain bandwidth significantly.

Within the large gain approximation, the full width at half maximum (FWHM) phase-matching bandwidth is given by [55],

$$\Delta\nu = \frac{2\sqrt{\ln 2}}{\pi} \sqrt{\frac{\Gamma}{L}} \frac{1}{\left| \frac{1}{v_{gi}} - \frac{1}{v_{gs}} \right|}. \tag{2.94}$$

This expression shows that the phase-matching bandwidth has a singularity when the OPA is at degeneracy or if the group velocities of the idler and the signal are matched. Under these conditions, the gain bandwidth is maximized and will ultimately be determined by higher-order terms in the expansion of the wave-vector mismatch.

If $v_{gi} = v_{gs}$, Eq. 2.94 has to be extended to include at least the second-order term in the

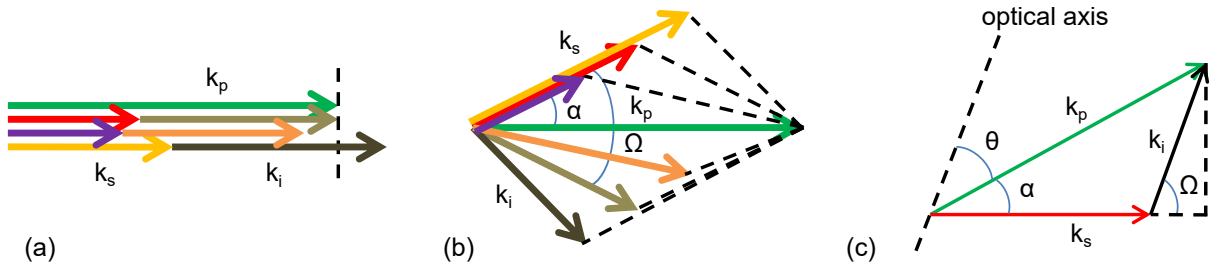

Figure 2.11: Illustration of (a) collinear and (b) noncollinear phase-matching along with the (c) schematic of the noncollinear case. θ: phase-matching angle between the pump wave vector (k_p) and the optical axis of the crystal, α: noncollinear angle between the pump and signal wave vector (k_s), Ω: angle between the signal and the idler wave vector (k_i).

expansion of the wave-vector mismatch. In that case, the gain bandwidth is given by [55],

$$\Delta\nu = \frac{2(\ln 2)^{\frac{1}{4}}}{\pi}\left(\frac{\Gamma}{L}\right)^{\frac{1}{4}}\frac{1}{\sqrt{\left|\frac{\partial^2 k_s}{\partial\omega_s^2}+\frac{\partial^2 k_i}{\partial\omega_i^2}\right|}}. \tag{2.95}$$

In collinear OPA, the propagation direction of the pump and the signal are chosen in order to satisfy phase-matching, which fixes the signal and the idler group velocities. The constant difference in the group velocities ultimately determines the phase-matching and gain bandwidth. When the signal and the idler propagate along the same direction through the crystal with different group velocities, they get quickly separated as a result of which the bandwidth is reduced. A particular configuration where pump and signal propagate at an angle with respect to each other allows group-velocity matching leading to broadband phase-matching. This type of phase-matching geometry, widely known as noncollinear phase-matching, is discussed in the following section.

2.4.6 Noncollinear-phase-matching

As discussed in the previous section, a broad parametric gain bandwidth can only be achieved if the group velocities of the signal and the idler are matched. This can be achieved in a noncollinear configuration in which the pump and the signal propagate at an angle with respect to each other. As a result the projection of the idler group velocity along the signal propagation direction can be chosen so that it matches the group velocity of the signal. The concept, first introduced in optical parametric generation [28], is widely known as noncollinear optical parametric amplification (NOPA).

A schematic of noncollinear phase-matching is shown in Fig. 2.11(c). The orthogonal components of the wave-vector mismatch Δk can be written as,

$$\Delta k_{\parallel} = k_p\cos\alpha - k_s - k_i\cos\Omega, \tag{2.96}$$

$$\Delta k_\perp = k_p \sin\alpha - k_i \sin\Omega, \tag{2.97}$$

where α is the angle between the pump and the signal wave vector, called noncollinear angle and Ω is the angle between the signal and the idler wave vector which varies according to the signal wavelength. For perfect phase-matching, both $\Delta k_\parallel$ and $\Delta k_\perp$ vanish which gives,

$$k_p^2 - 2k_s k_p \cos\alpha + k_s^2 - k_i^2 = 0. \tag{2.98}$$

Let us discuss how one can calculate the phase-matching angle in a negative uniaxial crystal such as BBO in a type I phase-matching configuration for a given set of pump and signal wavelengths, and a given noncollinear angle. In this case, the signal and idler wave vectors can be calculated from the refractive indices for ordinary polarization at their respective wavelengths that are obtained according to conservation of energy. For a given noncollinear angle, Eq. 2.98 can be solved for k_p which then provides a value of the extraordinary refractive index for the pump (n_p) that is necessary to satisfy perfect phase-matching, according to

$$n_p = \frac{k_p c}{\omega_p}. \tag{2.99}$$

where c and ω_p are the speed of light and the pump frequency respectively. Then, the phase-matching angle θ can be calculated by,

$$\frac{1}{n_p^2(\theta)} = \frac{\cos^2\theta}{n_o^2} + \frac{\sin^2\theta}{n_e^2}, \tag{2.100}$$

where n_o and n_e are the ordinary and extraordinary refractive indices at the pump frequency respectively. $n_p(\theta)$ is the refractive index of the extraordinary polarized pump beam that corresponds to perfect phase-matching i.e. $n_p(\theta) = n_p$.

The above-mentioned procedure allows to calculate the phase-matching angle if the noncollinear angle is given, which does not necessarily correspond to the maximum gain bandwidth. In case of broadband phase-matching, a different procedure can be followed to calculate the noncollinear angle and the phase-matching angle. In this case, the spectral bandwidth of the signal pulses has to be taken into account. For this, the wave-vector mismatch in both directions can be expanded in Taylor series around the central frequency up to first order as,

$$\Delta k_\parallel \approx \frac{\partial k_s}{\partial \omega_s}\Delta\omega + \frac{\partial k_i}{\partial \omega_i}\cos\Omega\Delta\omega - k_i \sin\Omega \frac{\partial\Omega}{\partial\omega_i}\Delta\omega, \tag{2.101}$$

$$\Delta k_\perp \approx \frac{\partial k_i}{\partial \omega_i}\sin\Omega\Delta\omega + k_i \cos\Omega \frac{\partial\Omega}{\partial\omega_i}\Delta\omega, \tag{2.102}$$

where the pump is assumed to be quasimonochromatic ($\Delta\omega_p \approx 0$) and $\Delta\omega$ is the spectral bandwidth of the signal which means the spectral bandwidth of the idler $\Delta\omega_i = -\Delta\omega$. Broadband phase-matching implies that $\Delta k_\parallel = 0$ and $\Delta k_\perp = 0$. Under these conditions,

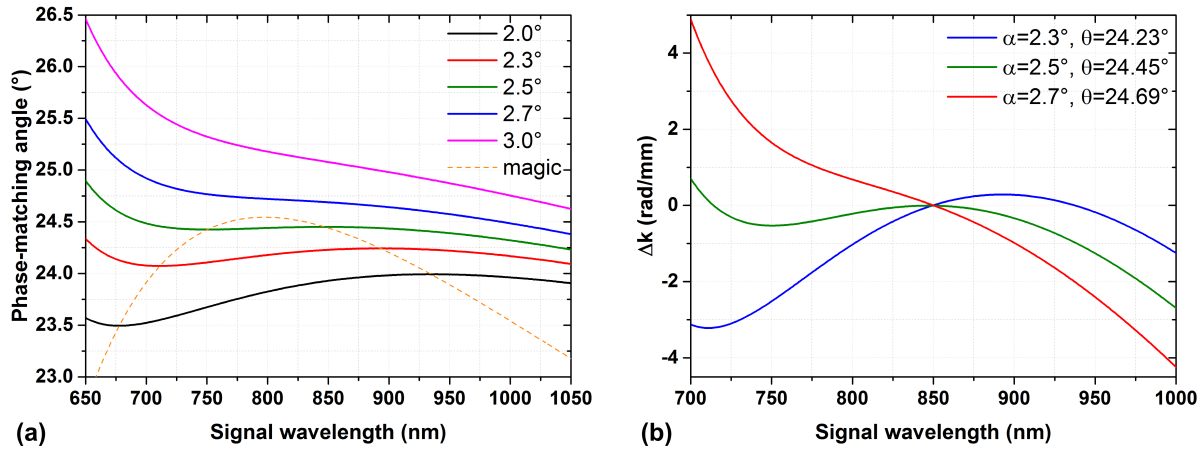

Figure 2.12: (a) Calculated phase-matching angles in a BBO crystal for a broad signal spectrum pumped at 515 nm for different noncollinear angles, including the broadband noncollinear angle corresponding to each signal wavelength (indicated as 'magic' in the legend). (b) Variation of the wave-vector mismatch when the noncollinear angle is detuned from broadband phase-matching.

the solution of Eqs. 2.101 and 2.102 is given by,

$$v_{gs} = v_{gi} \cos \Omega. \tag{2.103}$$

In addition, from the triangular arrangement of the pump, signal and idler wave vectors corresponding to the respective central frequencies as shown in Fig. 2.11(c) for perfect phase-matching, one can write

$$\tan \alpha = \frac{k_i \sin \Omega}{k_s + k_i \cos \Omega}, \tag{2.104}$$

$$k_p \sin \alpha = k_i \sin \Omega. \tag{2.105}$$

where Ω refers to the angle between the signal and the idler wave vector at the corresponding central wavelengths. Equations 2.103 and 2.104 can be solved for the noncollinear angle α if the pump and signal central frequencies are given. The noncollinear angle calculated in this way corresponds to perfect phase-matching up to the first order which leads to a broad gain bandwidth. Note that the noncollinear angle at which the gain bandwidth is maximum is widely referred in the literature as the 'magic angle'. Then, the refractive index at the central frequency of the extraordinary polarized pump n_p, which corresponds to broadband phase-matching can be calculated from Eqs. 2.105 and 2.99. Furthermore, the phase-matching angle θ is found from Eq. 2.100 utilizing $n_p(\theta) = n_p$. The noncollinear angle and the phase-matching angle computed in this way serve as broadband phase-matching angles in the type I configuration based on a uniaxial crystal.

The above-mentioned procedure can be followed to calculate phase-matching angles for any set of pump, signal and idler frequencies. Figure 2.12(a) shows the calculated phase-

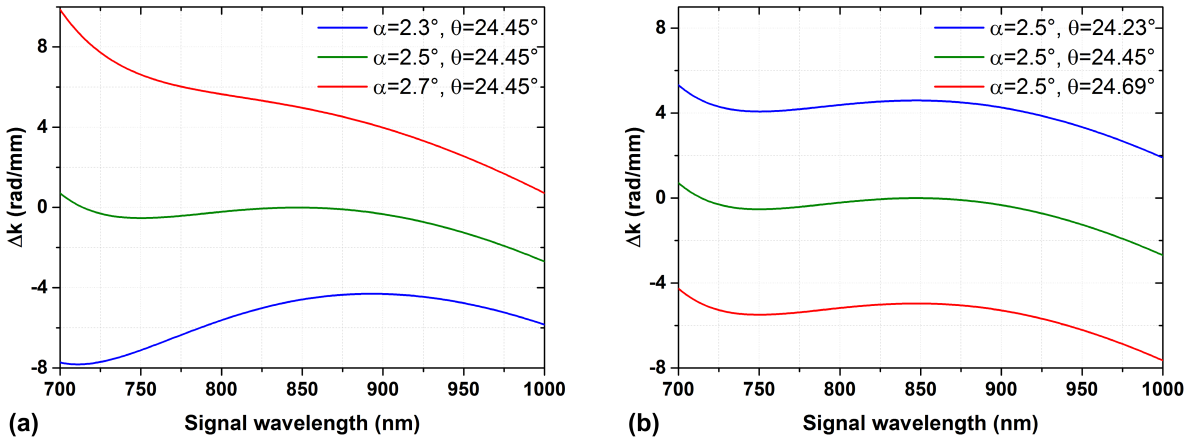

Figure 2.13: Influence of the noncollinear angle and the phase-matching angle on the wave-vector mismatch. (a) Detuning the noncollinear angle keeping the phase-matching angle constant and (b) Detuning the phase-matching angle keeping the noncollinear angle constant.

matching angles in a BBO crystal for a broad range of signal wavelengths pumped at 515 nm for five different noncollinear angles including the magic angle for each signal wavelength [cf. Legend]. For example, broadband phase-matching between 515 nm pump and 850 nm signal corresponds to a noncollinear angle of 2.5° and a phase-matching angle of 24.45° which leads to a broad gain bandwidth in the spectral range from $\sim$ 700 nm to $\sim$ 950 nm.

If the noncollinear angle is detuned from the magic angle (2.5°), the phase-matching is no longer broadband. The phase-matching angle has to be adjusted to achieve perfect phase-matching for a given noncollinear angle at particular pump and signal frequencies. As can be seen clearly in Fig. 2.12(b), detuning introduces wave-vector mismatch and accordingly will reduce the gain bandwidth. Perfect phase-matching is possible only at a particular signal wavelength and the wave-vector mismatch is significantly minimized over a certain range of signal spectrum only if the noncollinear angle is close to the magic angle.

Any detuning that doesn't maintain perfect phase-matching strongly degrades the performance of NOPCPAs. Figure 2.13(a) depicts the effect of detuning the noncollinear angle without maintaining perfect phase-matching. The wave-vector mismatch is significantly changing over the signal spectrum and far away from the broadband phase-matching. This indicates that the gain bandwidth as well as the gain/conversion efficiency drops accordingly. In addition, if the phase-matching angle is slightly detuned from the broadband condition keeping the noncollinear angle fixed at magic angle [Fig. 2.13(b)], the wave-vector mismatch is uniformly moved away from the case of broadband phase-matching. This will decrease the gain/conversion efficiency without affecting the bandwidth.

2.5 Third-order nonlinear processes

This section focuses on third-order nonlinear processes. The third-order nonlinearity is the lowest order nonvanishing nonlinearity for centrosymmetric materials, where all the even-order nonlinear susceptibilities are zero because of symmetry [33]. Excluding the second-order nonlinearity, the expression of the induced polarization given by Eq. 2.55 reduces to,

$$\mathbf{P}(\mathbf{r},t) = \epsilon_0\chi^{(1)}\mathbf{E}(\mathbf{r},t) + \epsilon_0\chi^{(3)}\mathbf{E}^3(\mathbf{r},t), \tag{2.106}$$

Considering an incident scalar electric field propagating along the z-direction,

$$P(z,t) = \epsilon_0\chi^{(1)}E(z,t) + \epsilon_0\chi^{(3)}E^3(z,t). \tag{2.107}$$

If $E(z,t)$ is assumed to be a monochromatic field of frequency ω with an amplitude $A(z)$ such that $E(z,t) = A(z)\cos(\omega t)$, the expression for the induced polarization (Eq. 2.107) reduces to,

$$P(z,t) = \epsilon_0\chi^{(1)}A(z)\cos(\omega t) + \epsilon_0\chi^{(3)}A^3(z)\left[\frac{1}{4}\cos(3\omega t) + \frac{3}{4}\cos(\omega t)\right]. \tag{2.108}$$

The second term in the right hand side of Eq. 2.108 corresponds to the process of third harmonic generation, where an incident field at frequency ω interacts with the nonlinear medium generating a field at frequency 3ω. The third term refers to a nonlinear contribution to the induced polarization at the frequency of the incident field. Therefore, the term describes a nonlinear change in the refractive index that is experienced by the field at frequency ω. Such a nonlinear variation of the refractive index for the incident field because of the intensity of the field itself is known as the optical Kerr effect.

2.5.1 Kerr effect

The Kerr effect is a nonlinear optical effect in which a high intensity light beam modifies the refractive index of the medium through which it propagates. The change in refractive index Δn for the high intensity beam itself is typically expressed as,

$$\Delta n = n_2 I \tag{2.109}$$

where I is the intensity and n_2 is the nonlinear refractive index of the medium. In order to calculate the expression for Δn, let us consider the nonlinear contribution to the induced polarization that is responsible for the nonlinear refractive index (the third term of Eq. 2.108),

$$P_3(z,t) = \frac{3}{4}\epsilon_0\chi^{(3)}A^3(z)\cos(\omega t). \tag{2.110}$$

Using the expressions for the electric field $E(z,t)$ and the nonlinear polarization $P_3(z,t)$ in the wave equation 2.58, where ∇^2 is replaced by d^2/dz^2,

$$\frac{d^2A}{dz^2} - \frac{1}{c^2}\left(\epsilon^{(1)} + \frac{3}{4}\chi^{(3)}|A|^2\right)\frac{d^2A}{dt^2} = 0. \tag{2.111}$$

Equation 2.111 provides an expression for the refractive index as,

$$n = \sqrt{\epsilon^{(1)} + \frac{3}{4}\chi^{(3)}|A|^2} = n_0\sqrt{1 + \frac{3}{4}\frac{\chi^{(3)}|A|^2}{n_0^2}}, \tag{2.112}$$

where n_0 is the linear refractive index such that $n_0^2 = \epsilon^{(1)} = 1 + \chi^{(1)}$. If the expression for the refractive index n is expanded in a Taylor series assuming that the second term within the square root is very small,

$$n \approx n_0\left(1 + \frac{3}{8}\frac{\chi^{(3)}|A|^2}{n_0^2}\right). \tag{2.113}$$

As the intensity of the incident wave can be expressed as,

$$I = \frac{1}{2}c\epsilon n_0|A|^2, \tag{2.114}$$

Equation 2.113 is reduced to,

$$n \approx n_0\left(1 + \frac{3}{4}\frac{\chi^{(3)}I}{c\epsilon_0 n_0^3}\right), \tag{2.115}$$

implying that n_2 is given by,

$$n_2 = \frac{3}{4}\frac{\chi^{(3)}}{\epsilon c n_0^2}. \tag{2.116}$$

The nonlinear effects associated with the optical Kerr effect or the intensity-dependent refractive index such as self-focusing and self-phase modulation are briefly discussed in the following section.

Self-focusing

Self-focusing refers to the focusing of a high intensity beam propagating through a medium due to the beam itself changing the refractive index of the medium. The profile of the refractive index follows the intensity profile of the beam leading to a refractive index gradient in space, and in the case of pulsed lasers, in time. The high intensity part of the beam slows down due to the larger change in the refractive index compared to the low intensity part. This means that the medium acts like a lens (also called Kerr-lens), distorting the wavefronts and focusing the beam. The focusing makes the beam more

intense and therefore, the Kerr-lens stronger. Depending upon the length of the medium, the process continues until the material is ionized. This can ultimately lead to a catastrophic damage of the medium.

The upper limit of the peak power beyond which self-focusing occurs is typically defined as the critical power (P_{cr}) by the equation [35],

$$P_{cr} = \frac{3.77\lambda^2}{8\pi n_0 n_2}, \tag{2.117}$$

Self-phase modulation

Self-phase modulation refers to the modulation of the nonlinear phase of an optical pulse by its intensity via the nonlinear change in the refractive index of the medium. In order to calculate the expression for the nonlinear phase, let us consider the electric field of an optical pulse,

$$E(z,t) = \frac{1}{2}A(z,t)\exp[i(k_0 z - \omega_0 t)] + c.c.. \tag{2.118}$$

The intensity of the pulse $I(z,t)$ is,

$$I(z,t) \propto |A(z,t)|^2, \tag{2.119}$$

and the propagation constant k_0 at center frequency ω_0 is,

$$k_0 = \frac{\omega_0}{c}n(t) = \frac{\omega_0}{c}[n_0 + n_2 I(t)]. \tag{2.120}$$

Then, the expression for the intensity-dependent phase is,

$$\phi(t) = \omega_0 t - \frac{\omega_0}{c}n_0 z - \frac{\omega_0}{c}n_2 I(t) z. \tag{2.121}$$

The third term in Eq. 2.121 corresponds to the intensity-dependent nonlinear phase. As can be seen, the nonlinear phase has the same temporal shape as the intensity. The instantaneous frequency can be written as,

$$\omega(t) = \frac{d\phi(t)}{dt} = \omega_0 - \frac{\omega_0}{c}n_2\frac{dI}{dt}z. \tag{2.122}$$

Therefore, the pulse experiences a frequency shift in the instantaneous frequency given by,

$$\Delta\omega(t) = -\frac{\omega_0}{c}n_2\frac{dI}{dt}z. \tag{2.123}$$

This means that the leading edge of the pulse (rising intensity) introduces a red shift towards the lower frequency range whereas the trailing edge (falling intensity) introduces a blue shift towards the higher frequency range. Indeed, the self-phase modulation generates new frequency components, the spectrum gets broadened and the pulse is chirped. A pair

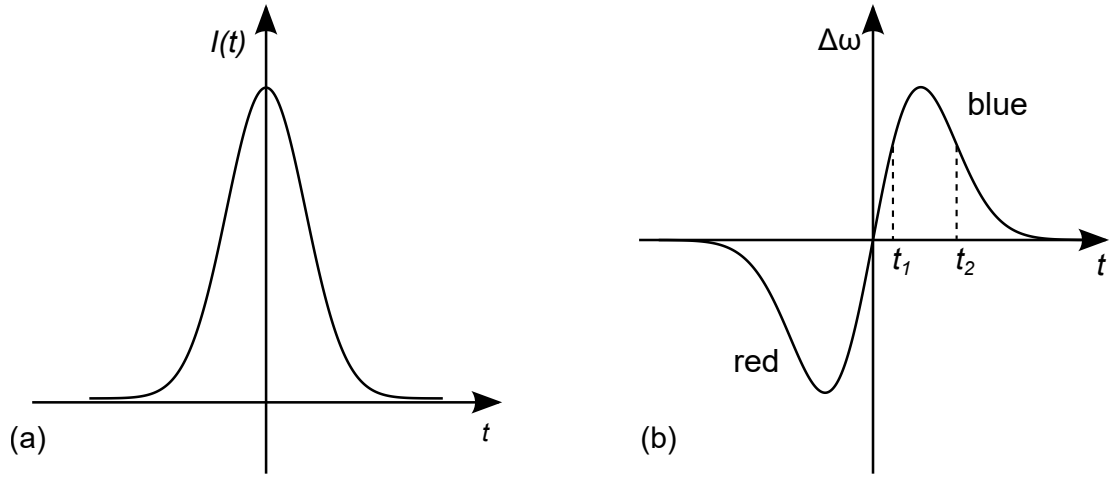

Figure 2.14: (a) Intensity profile of a Gaussian pulse, and (b) the instantaneous change in frequency as a function of time due to the Gaussian pulse propagating through an optically transparent medium (taken from Ref. [34]). On the leading edge of the pulse the frequency is lowered whereas on the trailing edge it is increased, resulting in a broadening of the pulse spectrum.

of equal frequencies will be generated at times t_1 and t_2 as shown in Fig. 2.14. As the phase difference between the components depends upon $(t_2 - t_1)$, constructive interference occurs for $\omega_0 \Delta t = 2\pi m$, with m an integer, and destructive interference occurs for $\omega_0 \Delta t = (2m + 1)\pi$. The interference effects lead to modulations in the output spectrum. As an example, let us consider an ultrashort pulse of 1 ps FWHM duration with a pulse energy of 1 µJ at a central wavelength of 1030 nm propagating through a single mode, solid-core optical fiber with a fundamental mode field diameter of 30 µm. For a fiber length of 5 cm, the spectrum is broadened from 1.56 nm to 16.81 nm as shown in Fig. 2.15. The dispersion is not included in the calculation, assuming that the effect for the 1 ps pulse within the short fiber is negligible. The pulse propagation was simulated in the software 'fiberdesk' (DEMO version 4) [56], considering only self-phase modulation.

2.5.2 Nonlinear pulse propagation in fibers

Let us consider an optical pulse propagating through an optical fiber, which is quasi-monochromatic i.e. the spectral width $\Delta\omega$ is much smaller than the central frequency ω_0 ($\Delta\omega/\omega_0 \ll 1$). The electric field of the pulse, in the slowly varying envelope approximation (the pulse envelope is slowly varying over time relative to the optical cycle), can be written as [57],

$$\mathbf{E}(\mathbf{r}, t) = \frac{1}{2}\hat{x}\{F(x, y)A(z, t)\exp[i(\beta_0 z - \omega_0 t)] + c.c.\}, \tag{2.124}$$

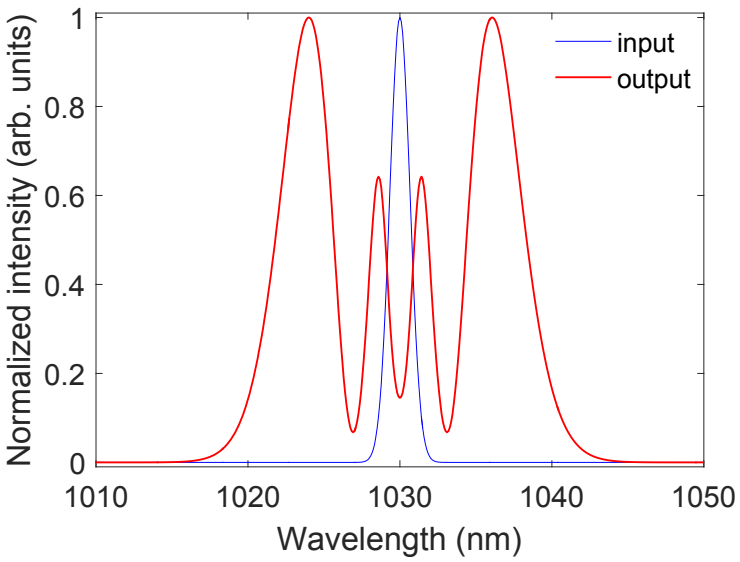

Figure 2.15: Calculated spectrum of an ultrashort pulse of 1 ps FWHM duration at the input and the output of a single mode, solid-core optical fiber with a fundamental mode field diameter of 30 µm and a length of 5 cm. The input pulse energy is 1 µJ and the spectrum is centered at a central wavelength of 1030 nm. The spectral broadening and the modulations in the output spectrum are due to self-phase modulation.

where $\hat{x}$ is the polarization unit vector, $A(z,t)$ is the slowly varying pulse envelope, $F(x,y)$ is the modal distribution of the fiber, and β_0 is the mode-propagation constant[1] at frequency ω_0. Similar to the case of propagation wave vector, $\beta(\omega)$ can be expanded in a Taylor series around ω_0 according to,

$$\beta(\omega) = \beta_0 + \beta_1(\omega - \omega_0) + \frac{1}{2}\beta_2(\omega - \omega_0)^2 + \frac{1}{6}\beta_3(\omega - \omega_0)^3 + ..., \tag{2.125}$$

where β_1 and β_2 correspond to the group velocity and group velocity dispersion of the fiber, and β_3 refers to the third-order dispersion.

The propagation equation for the pulse envelope $A(z,t)$ can be derived from the wave equation 2.58. Considering only the third-order nonlinear polarization, and dispersion terms up to the second-order, the propagation of the pulses is given by the equation,

$$\frac{\partial A}{\partial z} + \frac{\alpha}{2}A + \beta_1\frac{\partial A}{\partial t} + i\frac{\beta_2}{2}\frac{\partial^2 A}{\partial t^2} = i\gamma|A|^2A, \tag{2.126}$$

where the term with attenuation coefficient α includes fiber losses and the terms with β_1 and β_2 represent dispersion effects. The nonlinearity of the fiber is included by the right hand side of the equation with γ known as the nonlinear coefficient of the fiber, which is

[1]The propagation constant of a mode in a fiber is a parameter which describes the evolution of the amplitude and phase of the light with a given frequency along the propagation direction.

defined as,

$$\gamma = \frac{n_2 \omega_0}{c A_{\text{eff}}}, \tag{2.127}$$

with n_2 as the nonlinear refractive index of the fiber core, c the speed of light, and A_{eff} the effective mode area. For a Gaussian mode distribution of mode-field radius w, the effective mode area is given by πw^2.

If a frame of reference moving with the pulse at the group velocity v_g is assumed according to $T = t - z/v_g \equiv t - \beta_1 z$, and the attenuation constant is assumed to be zero, Equation 2.128 can be reduced to [57],

$$i\frac{\partial A}{\partial z} - \frac{\beta_2}{2}\frac{\partial^2 A}{\partial T^2} + \gamma |A|^2 A = 0, \tag{2.128}$$

which describes the propagation of pulses in single-mode fibers and is referred to as the nonlinear Schrödinger equation (NLSE). This is the fundamental equation for the nonlinear propagation of optical pulses in fibers.

Depending upon the initial pulse duration and peak power of the pulse, either the dispersion term or the nonlinear term or both dominates during the pulse propagation through the fiber. Therefore, the nonlinear pulse propagation is often classified into different regimes based on two length scales known as the dispersion length and the nonlinear length. The dispersion length (L_D) is defined as,

$$L_D = \frac{\tau_0^2}{|\beta_2|}, \tag{2.129}$$

where τ_0 is the initial pulse duration. Similarly, the nonlinear length (L_{NL}) is defined as,

$$L_{NL} = \frac{1}{\gamma P_0}, \tag{2.130}$$

where P_0 is the initial peak power of the pulse. Based upon the length of the fiber L, the following four regimes can be encountered.

1. $L \ll L_D$, $L \ll L_{NL}$: The pulse propagates without distortions.
2. $L_D \ll L \ll L_{NL}$: The temporal profile is affected by the dispersion but the nonlinearity doesn't have any influence. The spectrum remains unchanged.
3. $L_D \gg L \gg L_{NL}$: Nonlinearity dominates and the spectrum gets broadened.
4. $L \gg L_D$, $L \gg L_{NL}$: Both nonlinearity and dispersion affect the pulse propagation.

Nonlinear pulse compression

Nonlinear pulse compression refers to a technique of generating very short pulses with high pulse energy/high average power, which is otherwise limited by the available gain bandwidth of ultrafast amplifiers via gain narrowing. It is a two-step process as schematically

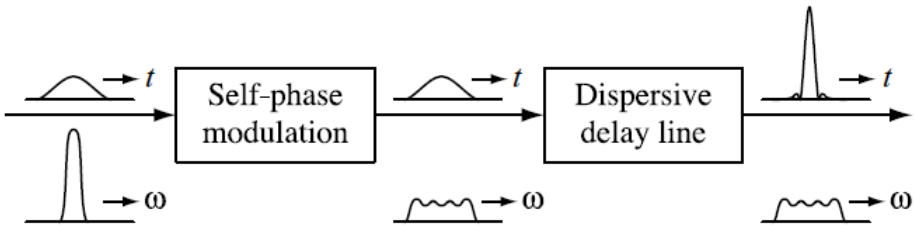

Figure 2.16: Schematic diagram of nonlinear pulse compression along with a sketch of the temporal and spectral profile of the optical pulse (taken from Ref. [35]). The input spectrum is broadened in a nonlinear medium by self-phase modulation. Then, the nonlinear chirp is compensated using a dispersive delay line leading to a compressed pulse.

shown in Fig. 2.16. First, the spectrum of the high energy/high power pulses is broadened in a $\chi^{(3)}$ nonlinear medium with normal dispersion due to self-phase modulation as described earlier. Because of the increased bandwidth, the optical pulses can be compressed in time. This is only possible if the nonlinear chirp acquired by the pulses due to self-phase modulation is compensated. The dispersion compensation, which is the second step of nonlinear pulse compression, is performed by using dispersive elements such as chirped mirrors or grating pairs. Since the nonlinear pulse propagation in a normally dispersive medium introduces positive chirp (up-chirp), a dispersive delay line providing negative chirp leads to the compression of pulses.

Optical fibers or waveguides are often utilized as nonlinear medium due to the fact that the guided-wave geometry ensures that the nonlinear phase shift and thereby the spectral broadening is uniform over the transverse spatial profile. Additionally, the available input pulse energy and peak power determine the characteristics of the nonlinear medium. For low peak power pulses with energy less than a few microjoules, solid core fibers [58, 59] or bulk dielectrics [60] have been used. These are limited by self-focusing when the peak power increases. For example, for fused silica the power is limited to $\sim$4 MW for linearly polarized light. The self-focusing threshold can be increased by using noble gases as nonlinear medium in hollow capillaries. Gas-filled glass fiber capillaries have been widely used for spectral broadening of millijoule-level ultrashort pulses [11, 61]. However, the large core size of capillaries - necessary for low transmission loss - requires high peak power for efficient spectral broadening. Therefore, solid core fibers and gas-filled capillaries are not suitable for sub-picosecond pulses with a pulse energy in the range of 10 µJ to 200 µJ.

Gas-filled hollow-core photonic crystal fibers provide simultaneous reduction of the core size and the transmission loss over a broad bandwidth. In particular, the recent development of hollow-core Kagome-type fibers has enabled pulse compression with moderate pulse energies and at high average power. Kagome-type fibers are based on an inhibited coupling guiding mechanism [62] in which the overlap between the optical field of the core modes and the cladding modes is strongly reduced. This mechanism is different from the photonic bandgap-guiding in which the coupling of the core modes with the cladding is avoided due to the absence of cladding modes at the frequencies and the effective refractive indices of

the core modes.

In recent years, Kagome-type fibers have offered very low loss, broadband transmission, ultra-low dispersion and highly reduced optical field overlap with the surrounding silica material [63–65]. These excellent features have been exploited in several pulse compression experiments [66–72], showing its potential for the compression of sub-picosecond pulses with moderate peak power. Remarkable achievements include a large pulse compression factor of 18 [67], sub-10 fs few-cycle pulses [73] and gigawatt level peak power [70]. It is worth to mention that Kagome-type fibers have been found very useful for ultrashort pulse delivery. These fibers are capable of transporting ultrashort pulses with high average power up to 100 W and pulse durations of 300 fs [74] as well as 600 fs pulses with millijoule-level pulse energies [75]. This is of great importance for fiber-based beam delivery in industries where handling high pulse energy and high average power of ultrashort pulses is challenging.

3 Development of a sub-ps, mJ-level pump laser

As discussed in the introduction, optical parametric chirped-pulse amplification (OPCPA) is the technique of choice for the amplification of few-cycle pulses at high repetition rates, and the scaling of the pulse energy and the average power is limited by the pump lasers. Therefore, a significant part of the thesis was focused on the development of a highly stable, high energy and high average power ultrafast laser in the near-infrared, providing sub-picosecond pulses with millijoule-level pulse energy at a repetition rate $> 100\,\mathrm{kHz}$. The laser development work was carried out at the research and development department of Amplitude Systèmes, Bordeaux, France, and the major goal of the research was to build a compact, highly stable industrial laser rather than the demonstration of cutting-edge laser technology and a state-of-the-art laser system. The development was based on the established laser technology focusing on compactness and stability. For this reason, the reported laser characteristics are not expected to compete with record laser parameters.

Beginning with a brief overview of the limitations in the amplification of high energy, high power ultrafast pulses, this chapter presents a table-top, millijoule class, sub-picosecond industrial laser system at a center wavelength of 1030 nm based on thin-disk technology. The excellent characteristics of the laser have been preserved in the highly efficient frequency conversion, generating second and third harmonic wavelengths, which indicate the suitability of the laser to pump an optical parametric amplifier in the visible and near-infrared spectral range. In addition, the laser source was used in nonlinear pulse compression in a hollow-core Kagome fiber to reduce the pulse duration.

3.1 Background

The primary goal of the laser development work was to scale the pulse energy and average power of ultrafast amplifiers. It has been known for a long time that simultaneous scaling of the pulse energy and the repetition rate (i.e. the average power) of ultrafast laser amplifiers has to overcome twofold limitations. On the one hand, high peak power pulses suffer from nonlinear propagation effects such as self-focusing and self-phase modulation [see chapter 2] during the propagation through optical components including the gain medium. These effects can introduce distortions in the pulses, and in extreme cases, lead to damage of the gain medium and/or other optical components. On the other hand, thermal effects such as thermal lensing and thermal-induced birefringence arising due to the heat generated in the gain medium of the amplifiers, as discussed in chapter 2 limit the average output power. Therefore, simultaneous scaling of the pulse energy and average power of ultrafast lasers requires the management of thermal and nonlinear effects.

There have been extensive studies on the techniques that can be employed to minimize

the impacts of nonlinear and thermal effects. The management techniques ultimately determine the architecture of a laser system. The chirped pulse amplification technique, as discussed in chapter 2, is an elegant solution to avoid optical nonlinearities, whereas the thermal issues are tackled to some extent by using different laser geometries, where the increased surface-to-volume ratio of the gain medium eases the heat removal. Based on the geometry of the laser gain medium, laser architectures are classified into different categories such as rod-type, fiber, Innoslab, thin-disk etc. (see Refs. [76, 77] and references therein for details of these laser geometries). In recent decades, thin-disk technology utilizing Yb:YAG crystal as a gain medium has been very successful for average power scaling of ultrafast laser systems in the near-infrared spectral range, and is considered as a potential technique for scaling the pulse energy [78, 79]. Therefore, this work utilized a thin-disk architecture, which is briefly described in the following section.

3.1.1 Thin-disk geometry

In a thin-disk laser architecture, a doped material of few hundreds micron thickness is used as the active medium. The material is coated for high reflection of the pump and laser wavelengths on the back side, and anti-reflection coated for both on the front side. The disk is then soldered to a heat sink in such a way that the heat flow is approximately along the direction of the laser beam propagation as shown in Fig. 3.1. Since the disk is very thin, the heat is generated close to the surface of the disk and the cooling is efficient, leading to a significantly reduced thermal load. The disk also acts as a reflecting mirror in a laser cavity or amplifier. The main advantage of the thin-disk geometry is that scaling of the average power is possible by increasing the pump beam cross-section, keeping the intracavity intensity constant and without increasing the brightness[1] of the pump diodes. Similarly, the large transverse mode sizes of the laser, compared to the longitudinal extension of the gain medium, helps to minimize nonlinear effects such as self-phase modulation, thus allowing the amplification of high energy and high peak power pulses (unless the pulses have to pass through the gain medium several times, for example, in a regenerative amplifier). However, because of the very thin gain medium, multiple passes of the pump beam through the disk are necessary to achieve a high population inversion, which is typically done with a proper arrangement of folded prisms.

In a thin-disk geometry, the thickness of the gain medium is typically in the range of 100 µm to 400 µm. Despite its importance from the thermal management point of view, the thin gain medium has two major drawbacks: a low pump absorption efficiency and a low single-pass gain. Nevertheless, there have been elegant solutions to these problems. On the one hand, the problem of low pump absorption efficiency is alleviated by using multiple passes of the pump beam. On the other hand, the overall gain of the amplifier is enhanced by using either a regenerative amplifier cavity or a multipass configuration. Modern high power thin-disk amplifiers often consist of a regenerative amplifier, which amplifies weak

[1] The brightness of a laser source is typically defined as the power divided by the product of the mode area at the focal plane and the solid angle in the far-field.

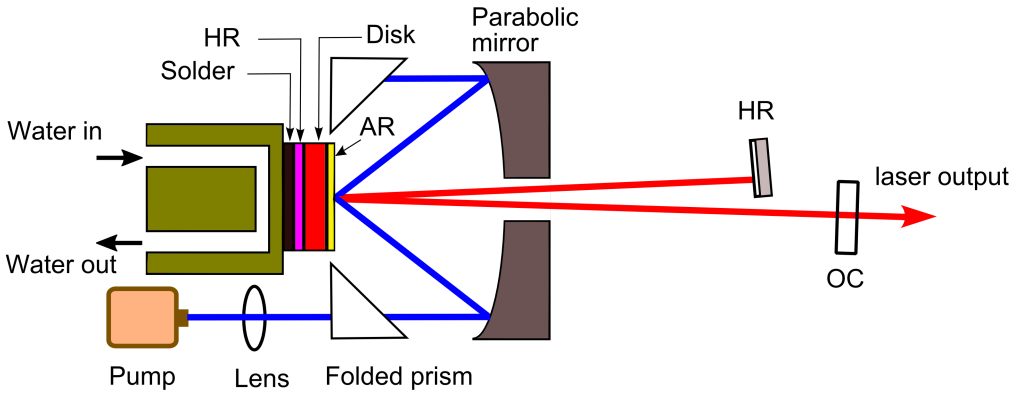

Figure 3.1: Schematic of a thin-disk laser. The front and back surface of the thin-disk are coated for anti-reflection (AR) and high reflection (HR), respectively, of the pump and laser wavelengths. The disk is then soldered to a water-cooled heat sink. The pump beam is imaged into the disk using a parabolic mirror, and multiple passes of the pump beam are realized by using folded prisms. The laser cavity is formed between the highly reflective mirror HR and the partially reflective output coupler OC, through which the laser beam is coupled out of the cavity.

pulses from an oscillator with high gain, and a multipass amplifier in order to boost the output power/pulse energy with high extraction efficiency, as discussed in chapter 2.

More than 2 kW average power and 6.7 mJ pulse energy with a few picoseconds pulse duration at a central wavelength of 1030 nm have recently been achieved in a multipass configuration [80]. Further scaling of both the average power and the pulse energy is mainly hindered by thermal distortions of the disk as well as nonlinear effects due to the high peak intensity. In the near-infrared spectral range, the thin-disk geometry utilizing an Yb:YAG gain medium has been found successful in scaling of the average power and pulse energy of laser amplifiers [78, 81]. The following section briefly reviews the important characteristics of the Yb:YAG as a laser gain medium.

3.1.2 Yb:YAG as gain medium

Ytterbium is used as an active dopant in its trivalent form (Yb^{3+}) in several host materials such as glasses and crystals. Yttrium Aluminum Garnet (YAG, $Y_3Al_5O_{12}$) is one of the most common host materials which, after doping with ytterbium ions, is widely used as gain medium in solid state laser amplifiers.

The energy level structure of the ytterbium ion consists of two manifolds; the ground manifold $^2F_{7/2}$ with four Stark-shifted levels and the excited manifold $^2F_{5/2}$ with three Stark levels, as shown in Fig. 3.2(a). The two manifolds are well-separated and their spectroscopy is simple compared to other rare-earth ions. Figure 3.2(b) shows the absorption and emission cross sections of a Yb:YAG crystal at room temperature. Some of the common absorption- and emission-wavelengths are indicated in the energy level diagram. The main emission peak is around 1030 nm. There are three major absorption peaks around 915 nm, 940 nm and 969 nm which are suitable for diode-pumping. The absorption and emission

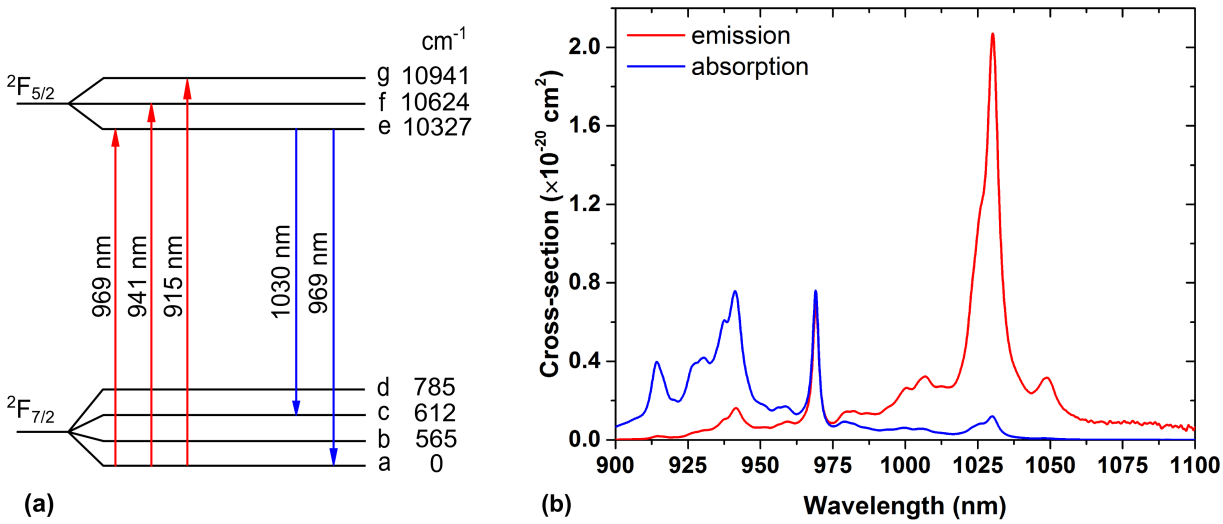

Figure 3.2: (a) Energy level structure of Yb^{3+} at room temperature [82], and (b) typical absorption and emission cross sections of Yb:YAG crystals [83]. The highest emission cross section is at 1030 nm whereas the absorption peaks are at 915 nm, 940 nm and 969 nm. The broad absorption peak around 940 nm is more suitable for diode-pumping due to the reduced constraints on the wavelength stability of the pump diode.

peak at 969 nm arises from the transition between the Stark levels a and e (so-called zero-phonon line due to the fact that there is no phonon involved during the absorption/emission of photons). However, the detailed absorption and emission spectra depend on the temperature and doping concentration due to the fact that the transition linewidths are broadened due to collision broadening. If the temperature decreases, the excitation of the lattice vibrations is reduced resulting in narrower linewidths and larger emission cross sections. Therefore, the absorption and emission cross sections are enhanced significantly at cryogenic temperatures.

Yb:YAG as an active medium has several advantages, and as a result it is widely employed to build solid state lasers and amplifiers in the spectral range around 1 µm. Some of the important reasons behind the choice of Yb:YAG as gain medium, with laser diodes as pump are the followings [84, 85]:

- The electronic structure is relatively simple which eliminates parasitic processes such as excited-state absorption[2] that reduce the gain.
- The quantum defect is low, which reduces thermal effects. For a pump wavelength of 940 nm and laser wavelength of 1030 nm, the quantum defect is only 8.7 %, much lower compared than 24 % in the case of a Nd:YAG laser for the pump and laser wavelengths of 808 nm and 1064 nm respectively.
- The emission spectrum is broad (∼6 nm), which allows the generation and amplifica-

[2]Absorption of photons by atoms or ions in an excited electronic state

tion of sub-picosecond pulses (6 nm corresponds to a Fourier-transform limited pulse duration of 260 fs for a Gaussian pulse).

- The absorption spectrum is broad, in particular around 940 nm, which reduces the constraints on pump diodes. As an example, pump diodes without highly stabilized emission wavelength can be utilized.
- The lifetime of the upper laser level is long (around 1 ms) which allows to store large amounts of energy.
- The host material YAG offers a high thermal conductivity and a high tensile strength[3].
- High doping levels are possible for high gain, which allows the use of short crystals.

Despite the above-mentioned advantages of Yb:YAG crystals as laser gain medium, the population of the lower laser level depends upon the temperature and therefore the material corresponds to a quasi-three level laser at room temperature. For this reason, it requires high pump power densities (>1.5 kW/cm^2) to reduce re-absorption of the laser wavelength. However, high pump power densities are possible due to the availability of high power pump diodes at the absorption bandwidth around 940 nm.

3.2 System block diagram

In this work, the well-established approach of a regenerative amplifier, in combination with the chirped-pulse amplification technique was adopted in order to amplify pulses from a fiber oscillator. The block diagram of the system is shown in Fig. 3.3. The stretched seed pulses from the front-end were amplified in a regenerative amplifier based on a Yb:YAG thin-disk laser architecture, and compressed using a grating compressor. The compressed pulses (at a central wavelength of 1030 nm) were frequency-upconverted in order to achieve radiation at shorter wavelengths (515 nm and 343 nm), which is necessary if the laser is to be used for pumping optical parametric amplifiers [see section 2.4.5] in the visible and near-infrared spectral range. In addition, nonlinear pulse compression was carried out in a Kagome fiber in order to shorten the pulse duration towards 100 fs, which will be useful e.g. to generate high harmonic radiation at high repetition rates.

3.3 Front end

The front end, provided by Amplitude Systèmes was an all-fiber laser system. It consists of a passively mode-locked Yb-doped fiber oscillator, a chirped-fiber Bragg grating stretcher and an Yb-doped fiber pre-amplifier. The stretched pulses at the output of the system directly seed the regenerative amplifier. Such a seed source is compact, highly stable and

[3]The tensile strength is defined as the maximum force per unit area that a material can support without fracture when it is stretched.

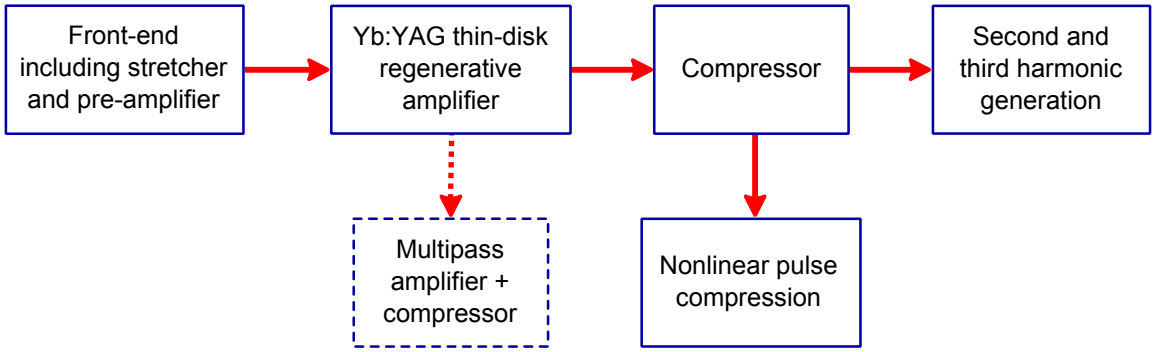

Figure 3.3: Representative block diagram of the laser system developed during this work. The front end, which is provided by Amplitude Systèmes, consists of a fiber oscillator, a stretcher and a fiber pre-amplifier. The output parameters of the front-end are presented in section 3.3. The design and characteristics of the regenerative amplifier developed within this work using a Yb:YAG thin-disk as a gain medium are presented in section 3.4. The amplified pulses are compressed in a grating compressor [section 3.4.6]. The compressed output is characterized at different pulse repetition rates and the results are presented in section 3.5. Second and third harmonic generation of the amplified pulses are reported in section 3.6. In addition, nonlinear compression of the sub-picosecond pulses from the amplifier system are carried out in a Kagome fiber, and is discussed in section 3.7. The dotted block represents a proposed way of scaling the average power of the regenerative amplifier.

alignment-free, and has been widely used in the last decade as a source of sub-picosecond pulses, to seed high energy, high power ultrafast amplifiers.

The nominal output average power of the front end was ∼10 mW at a pulse repetition rate of 40.7 MHz. This corresponds to a pulse energy of 0.25 nJ. The output spectral profile was measured using a spectrometer (AVANTES) with a spectral resolution of 0.06 nm, and is shown in Fig. 3.4. The spectral width is ∼11.8 nm (FWHM). Since the second-order dispersion introduced by the chirped-fiber Bragg grating stretcher was 35 ps/nm, which is equivalent to a group delay dispersion of 19.7 ps^2 at a center wavelength of 1030 nm(see Eq. 2.32), the stretched pulse duration was ∼ 400 ps (the specifications were provided by the company).

3.4 Yb:YAG thin-disk regenerative amplifier

3.4.1 Schematic of the amplifier system

A regenerative amplifier similar to the standard regenerative amplification scheme [86] was built with a thin Yb:YAG disk as gain medium. The schematic of the experimental set up is shown in Fig. 3.5. The output of the front end was collimated by using a lens. The half-wave plate (HWP1) was used to adjust the plane of polarization of the seed pulses. In the Faraday isolator (see Appendix for details) ISO the pulses traveling in the direction from the oscillator to the amplifier are allowed to pass while those coming back in the

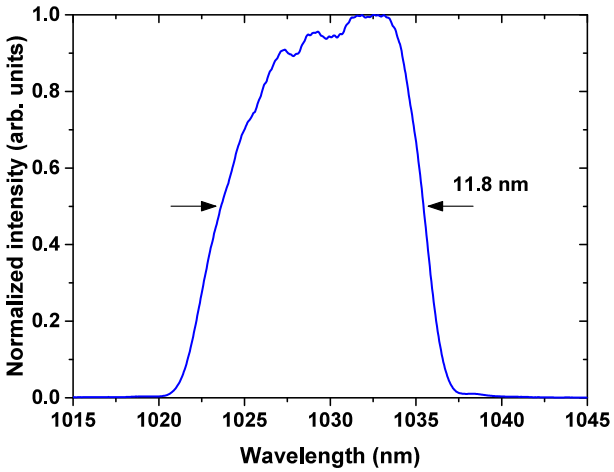

Figure 3.4: Spectral profile at the output of the front-end.

direction of the front-end are rejected.

The combination of a thin-film polarizer (TFP1), a half-wave plate (HWP2) and a Faraday rotator were used to separate the output pulses from the input based on the polarization so that the amplified pulses will not return to the front end. The high-reflective plane mirror PM3 and the high-reflective convex spherical mirror CM5 were used as the end mirrors of the optical cavity (see section 3.4.3 for the design of the cavity). The seed pulses enter into the cavity and the amplified pulses leave the cavity through the thin-film polarizer TFP2. This operation was controlled by an optical switch, which consisted of the combination of the polarizer TFP2, the quarter-wave plate (QWP), the plane mirror PM3 and the Pockels cell PC (see Appendix for details). The Pockels cell had a beta-barium borate (BBO) crystal, with a clear aperture of 4 mm and length of 30 mm. Because of the high damage threshold of the BBO crystal, it is preferred for high average power and high repetition rates.

A thin-disk pump module, which was provided by the Institut für Strahlwerkzeuge (IFSW) Stuttgart, was utilized to mount an Yb:YAG thin-disk that was soldered on a copper mount. The copper mount was cooled with water. The disk was 200 µm thick, with a doping concentration of 7 at.%[4]. The front and rear surfaces of the disk were coated for anti-reflection and high reflection of the pump and laser wavelengths respectively. The pump beam was focused by a parabolic mirror of 32.5 mm focal length onto the thin disk. 24 passes (12 reflections) of the pump beam through the thin-disk were realized by using folded prisms in combination with the parabolic mirror.

The disk was pumped with a laser diode, that delivered a maximum continuous-wave power of 200 W through a single mode fiber with a 600 µm mode field diameter. The emission spectrum was centered at 940 nm, exactly at the broad absorption peak of Yb:YAG. The collimated output of the pump-delivery fiber was imaged onto the disk with a spot size

[4] 'at.%' refers to the atomic percentage of the dopant e.g. ytterbium ions in Yb:YAG which refers to the fraction of yttrium ions Y^{3+} in YAG that have been replaced with ytterbium ions.

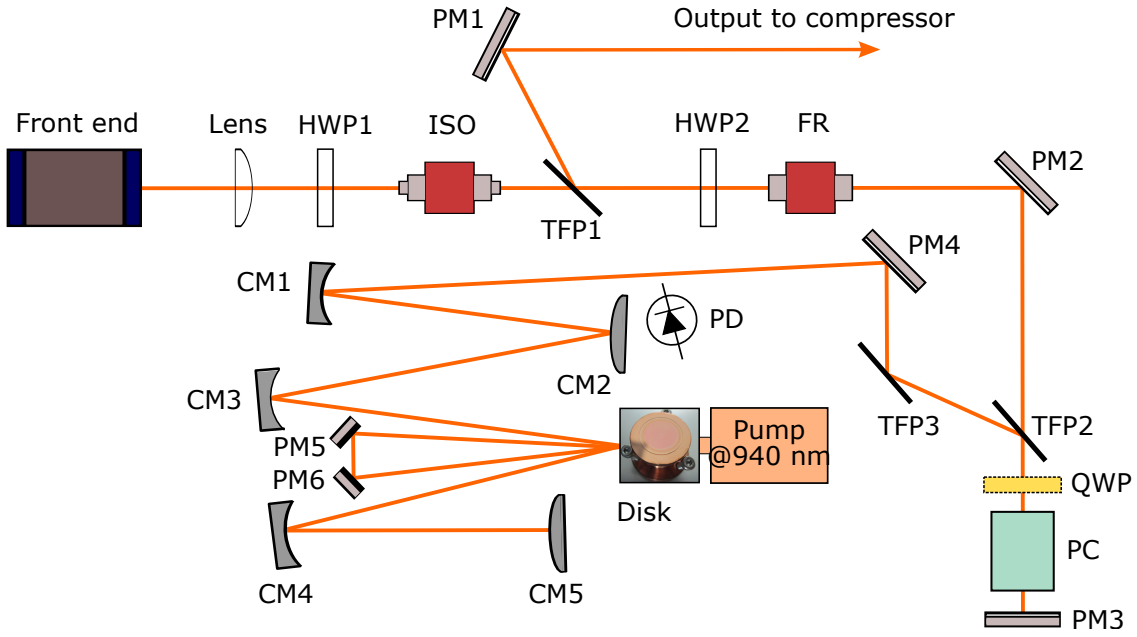

Figure 3.5: Schematic layout of the regenerative amplifier. After collimating the output of the front end by using a lens, a half-wave plate (HWP1) adjusts the plane of polarization. The isolator (ISO) prevents optical feedback from the amplifier to the front end. The combination of a thin-film polarizer (TFP1), a half-wave plate (HWP2) and a Faraday rotator (FR) separates the amplified pulses from the seed pulses based on their polarization. Similarly, the combination of a thin-film polarizer (TFP2), a quarter-wave plate (QWP), a Pockels cell (PC) and a plane mirror (PM3) couples the seed pulses into the cavity and the amplified pulses out of the cavity. The plane mirror PM3 and the curved mirror CM5 are the end mirrors of the cavity. The plane mirrors PM5 and PM6 are used to make a second pass through the disk. The 'Disk' corresponds to a Yb:YAG thin-disk, which is pumped by a laser diode with an emission wavelength of 940 nm. A photodiode (PD) monitors the evolution of the intracavity pulses during the amplification.

of 2.2 mm (full width at $1/e^2$ of peak intensity). This corresponds to a maximum intensity of 5.26 kW/cm^2. For this set of parameters, $\approx 94\,\%$ of the incident pump power was absorbed in 24 passes, which corresponds to a stored fluence of $\sim 0.688\,\mathrm{mJ/cm^2}$ (calculations were performed using the equations given in Ref. [87]). Note that this work focused on experiments rather than numerical analysis of the amplification process considering the fact that similar regenerative amplifier configurations have been extensively studied both experimentally and numerically in the last decades.

3.4.2 Working principle

The working principle of regenerative amplifiers is explained elsewhere [86]. For completeness, the principle is described here with respect to the schematic shown in Fig. 3.5. The amplifier is divided into three blocks based on their roles and the function of each block is summarized as follows.

1. **Separation of input and output pulses**: After passing through the isolator (ISO) [see Appendix], the p-polarized seed pulses pass through the thin-film polarizer TFP1. The half-wave plate HWP2 is adjusted in such a way that the polarization direction of the pulses is rotated by 45° counter-clockwise. Then the Faraday rotator changes the polarization direction by 45° in the clockwise direction. This means that after the Faraday rotator the seed pulses are still p-polarized and can pass through the thin-film polarizer TFP2 entering into the cavity.

   After amplification inside the cavity the pulses are coupled out through the polarizer TFP2 (see the second block for the details). The p-polarized amplified pulses, while propagating back through the Faraday rotator, are rotated by 45° clockwise as before. Then, the polarization state of the amplified pulses after the half-wave plate is changed to s-polarization. In this way, the polarization state of the amplified pulses is orthogonal to that of the input pulses. The amplified pulses are then reflected by the polarizer TFP1 and directed towards the compressor.

2. **Coupling the pulse into and out of the cavity**: When there is no high voltage applied to the Pockels cell, the p-polarized seed pulse, after passing through the polarizer (TFP2), Pockels cell (PC) and quarter-wave plate (QWP), is reflected back by the end mirror (PM3). After going through the quarter-wave plate twice, the polarization plane is rotated by 90°. The s-polarized pulse is then reflected by the thin-film polarizer towards the gain medium. The pulse is returned to the switching elements again after one round trip. If the voltage is kept OFF, the polarization state of the reflected pulse from the end mirror after passing through the quarter-wave plate twice is changed back to p-polarization and the pulse is transmitted through the polarizer. This way, the seed pulse makes only one round trip. However, if the voltage is turned ON so that the Pockels cell acts as a quarter-wave plate, the polarization plane of the returning pulse from the gain medium is the same as the input pulse even after the reflection from the end mirror. This is possible due to the combination of a single reflection and a double pass through the two quarter-wave plates, which altogether act as a full-wave plate and rotate the polarization plane by 180°. Therefore, the s-polarized seed pulse is trapped inside the cavity as long as the quarter-wave voltage signal is ON. During this time, the subsequent p-polarized seed pulses from the front end pass through the switching elements twice keeping the polarization fixed and are ejected out of the cavity without reaching the gain medium. The time during which the high voltage signal is ON defines the amplification window for the trapped seed pulse.

   To eject the pulse out of the cavity after amplification, the voltage is switched back to zero. Then, the polarization plane of the amplified pulse after reflection from the end mirror and passing through the quarter-wave plate is rotated by 90°. The p-polarized amplified pulse passes through the polarizer TFP2 and travels towards the Faraday rotator on the same path via which the seed came in. The thin-film polarizer TFP1 separates the amplified pulse from the input seed pulse because of their different

polarization.

3. **Amplification**: Once the seed pulse is trapped inside the cavity, it passes through the gain medium. The number of passes depends upon the chosen configuration e.g. two in each reflection and four in each round trip. By implementing an additional reflection from the thin-disk within a round trip (using the two plane mirrors PM5 and PM6 in the case of the configuration shown in the schematic 3.5), the number of passes through the gain medium can be doubled (eight in one round trip) keeping the passes through the Pockels cell constant (thus minimizing the losses). This increases the round-trip net gain and ultimately reduces the number of round trips that is necessary to extract the stored energy efficiently. By controlling the number of round trips via the switching time window of the Pockels cell, the maximum possible energy is extracted from the gain medium and the amplified pulse is coupled out of the cavity by switching the quarter-wave voltage signal of the Pockels cell back to zero. The numerical modeling of the laser dynamics of a regenerative amplifier (see Refs. [86, 88–90]) can be utilized to estimate the relevant amplification parameters.

3.4.3 Cavity design

The cavity was designed with the help of an open-source simulation software- *reZonator*. It calculates the beam propagation with the ABCD matrix formalism, as mentioned in chapter 2, where each optical component and the distance between the components are represented by corresponding square matrices. The mode size of the laser at the thin disk was chosen so that the laser modes were matched with the pump beam size. For a pump spot size of 2.2 mm, a laser mode field diameter of 2 mm was chosen at the disk. The position of the switching elements was chosen close to the end mirror of the cavity (PM3 in Fig. 3.5) where the beam is expected to be collimated and the size is big enough to minimize nonlinearities for pulse energies up to few millijoules. The selection of mirrors, the distances between them and the evolution of the beam radius across the cavity are shown in Fig. 3.6. The radii of curvature of the mirrors were selected and the separation distances were adjusted to achieve the pre-defined beam sizes at the disk and Pockels cell, ensuring that the cavity is stable within a certain range (few centimeters) if the actual distances between the components in the experiment differ from the simulated ones.

The B-integral during amplification was estimated by using nonlinear refractive indices and pulse peak intensities for a given laser beam size in the Yb:YAG crystal and in the BBO-based Pockels cell. For the calculation of B-integral, an extreme case was considered such that the pulse energy that will be extracted from the cavity can be as high as 5 mJ (not higher than this since the idea was to achieve a high average power at the same time) and the spectral bandwidth of the intracavity pulses may be significantly reduced due to gain narrowing, let's assume down to ~ 1.4 nm (this assumption was based on the spectral widths that have been achieved experimentally in a similar amplifier configuration). This led to a pulse duration of ~ 50 ps. The nonlinear refractive index was taken to be $7.3 \times 10^{-16}\,\mathrm{cm^2/W}$ for Yb:YAG [91] and $5.1 \times 10^{-16}\,\mathrm{cm^2/W}$ [92] for BBO. For beam ra-

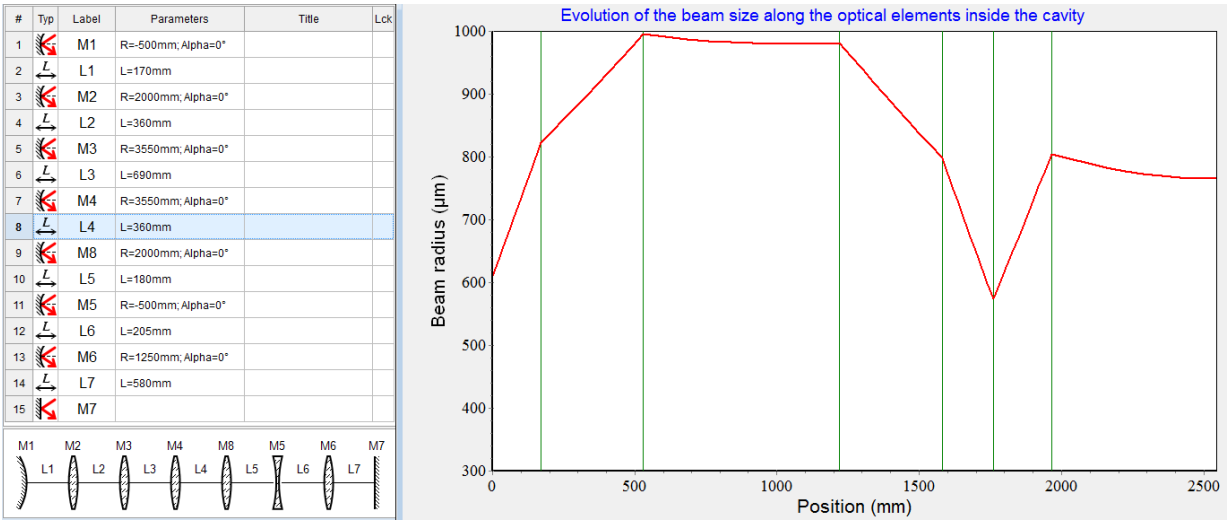

Figure 3.6: Simulation of a regenerative cavity with *reZonator*. The optical components and the separation distances are given in the left side while the beam evolution across the cavity is shown in the right side. Experimental parameters might slightly differ.

dii of 1 mm in the crystal and 750 µm in the Pockels cell [see Fig. 3.6], the accumulated nonlinear phase shift in the cavity i.e. B-integral value per round trip was estimated to be 1.8 rad. In such an extreme case, nonlinear distortions are expected in the spectral as well as spatial profiles.

3.4.4 CW operation

At first, the cavity was operated in continuous-wave (CW) operation to extract the maximum possible power with a diffraction-limited beam. If there are no seed pulses and the high voltage signal of the Pockels cell is switched off, the resonator acts like a CW laser where the quarter-wave plate (QWP) and the polarizer (TFP2), which together work as a variable output coupler, can be adjusted to optimize the output power.

For a pump power of 155 W, 37 W CW power was extracted, which corresponds to an optical-to-optical conversion efficiency[5] of 24 %, including the losses due to switching elements. The beam propagation factor M^2 (see chapter 2) of the output beam was measured to be <1.1 in both axes as shown in Fig. 3.7, which indicates that the beam is close to the diffraction-limit. The measurement was carried out by using a beam profiling CCD camera and software from DataRay Inc.

[5]Optical-to-optical conversion efficiency refers to the efficiency by which the pump power is converted to the laser average power.

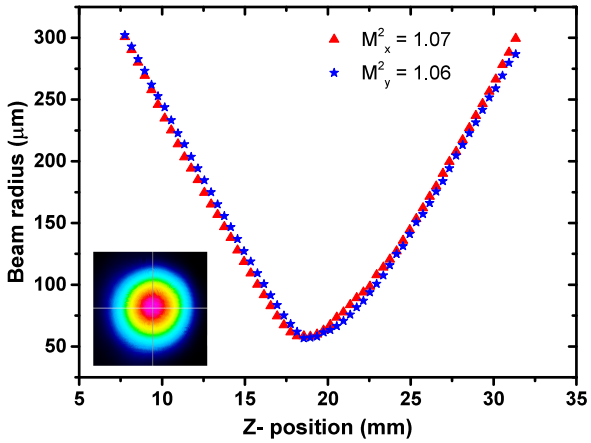

Figure 3.7: M^2 measurement of continuous-wave output of 37 W average power. Inset: near field beam profile.

3.4.5 Pulse amplification

For the amplification of seed pulses, the quarter-wave plate was properly adjusted and a high voltage signal ($\sim$ 3 kV) was applied to the Pockels cell, to operate as a polarization switch as described in section 3.4.2. The seed pulses were aligned into the cavity. The pulse repetition rate of the amplified pulses could be varied from a few kHz up to 300 kHz, only limited by the switching of the Pockels cell. At first, the amplifier was optimized for a repetition rate of 100 kHz to achieve high average power. Figure 3.8 depicts the evolution of the intracavity pulses and the amplified output pulse, measured by a photodiode that was placed behind the curved mirror CM2 [see Fig. 3.5]. The width of the amplification window was set so that maximum possible pulse energy could be achieved from regenerative amplification before the losses overcome the gain.

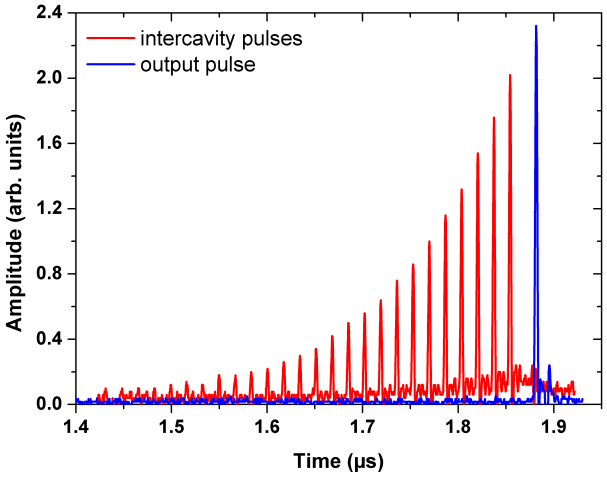

Figure 3.8: Photodiode-trace of the intracavity pulses (red) and the amplified output pulse (blue).

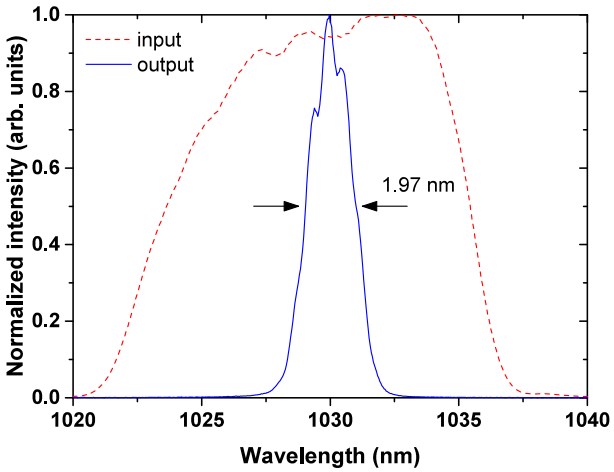

Figure 3.9: (a) Seed spectrum and the amplified output spectrum corresponding to the 39 W average power at a pulse repetition rate of 100 kHz. The output spectrum is significantly narrower than the input seed spectrum due to gain narrowing effect.

A pulse energy of 390 µJ was extracted for a pump power of 180 W, with an output average power of 39 W. This was achieved with 108 cavity round trips corresponding to a 1800 ns wide amplification window. Further increase of the average power was only limited by the available pump power. Because of gain narrowing, the output spectrum was much narrower than the seed spectrum as shown in Fig. 3.9(a). The 11.8 nm wide seed spectrum centered at 1030 nm was reduced to 1.97 nm. Nevertheless, the amplified spectrum supports a Fourier transform-limited pulse duration of 526 fs at FWHM. The output near field beam profile was close to diffraction-limited with a beam propagation factor similar to that of the CW output in both axes.

Next, the pulse repetition rate was changed to 10 kHz to extract a higher pulse energy. For 39 round trips corresponding to 650 ns of amplification, a maximum energy per pulse of 2 mJ was extracted, corresponding to 20 W average power. With this pulse energy, no spectral or spatial distortions were observed. The pulse repetition rate was not decreased further, despite the possibility of extracting more energy from the gain medium at lower repetition rates, as the primary focus was to achieve high average power.

The performance of the amplifier was characterized for four arbitrary pulse repetition rates of 10 kHz, 25 kHz, 50 kHz and 100 kHz, for corresponding amplification time windows of 650 ns, 900 ns, 1500 ns and 1800 ns respectively. Figure 3.10 shows the variation of the average output power as a function of input pump power for the four different repetition rates. At each repetition rate, the input pump power was varied keeping the amplification time window constant. A slope efficiency[6] of 29.5 % was obtained at 100 kHz which decreases to 22.3 % for a repetition rate of 10 kHz. The difference in slope efficiency for different repetition rates was mainly due to the optimization of the number of round trips, which

[6]Slope efficiency is defined as the slope of the curve obtained by plotting the laser output power as a function of the input pump power once the laser starts lasing.

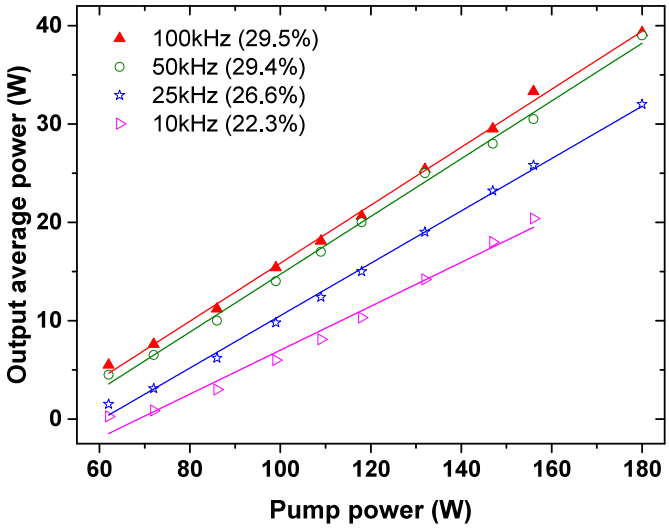

Figure 3.10: Output power as a function of the pump power at four different pulse repetition rates. The slope efficiency at each repetition rate is mentioned in the legend. The relatively lower slope efficiency of Yb:YAG thin-disk regenerative amplifier is attributed to the high threshold pump power due to the fact that Yb:YAG is a quasi-three level gain medium at room temperature. The decrease in slope efficiency for lower repetition rates was due to optimization of the number of round trips, which was necessary to ensure pulse-energy stability as described in the text.

was necessary to ensure pulse-energy stability as described in the following paragraph. This range of slope efficiency is common in thin-disk regenerative amplifiers [39,93], due to the high threshold pump power required to overcome the cavity losses and the high pump intensity necessary to achieve population inversion in quasi-three level gain media.

For a given pump power, the number of round trips at each repetition rate was carefully chosen in order to avoid bifurcations namely period doubling and chaotic behavior as described in chapter 2. For a pump power up to 180 W, bifurcations were not observed at a repetition rate of 100 kHz, however, were visible at lower repetition rates of 10 kHz to 25 kHz. The regime for this behavior was carefully examined by monitoring the pulse energies with a photodiode while varying the pump power for a given number of round trips and vice versa. The stable operation was ensured by adjusting the number of round trips (i.e. the gate length as described in chapter 2) for the maximum pump power, which limited the number of round trips leading to a reduction of the extracted energy and average power. This ultimately led to a reduction of the slope efficiency of the amplifier at lower repetition rates (compare the slope efficiencies shown in Fig. 3.10). Even though there is a possibility to operate such a regenerative amplifier in a stable regime of period doubling [39], no effort was made to operate the amplifier in a bi-stable regime (at half of the possible pulse repetition rate) since the stability of the amplifier was one of the major concerns in order to utilize the amplified output for nonlinear pulse compression and/or for pumping OPCPAs.

The amplified output spectrum at all repetition rates suffered from gain narrowing.

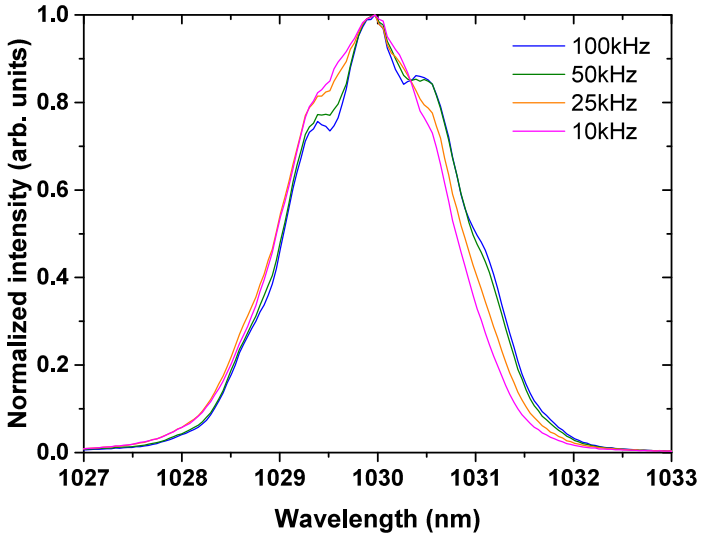

Figure 3.11: Output spectral profiles at four different repetition rates [cf. legend]. In each case, the FWHM spectral bandwidth is reduced to < 2 nm due to gain narrowing, and is much narrower than the spectral width of the seed (11.8 nm). The impact of gain narrowing is slightly larger for lower repetition rates because of the higher gain.

Output spectra for the four different repetition rates are shown in Fig. 3.11. It can be seen that the gain narrowing is relatively stronger for higher gain e.g. in the 10 kHz case. Nevertheless, each spectrum supports sub-picosecond Fourier transform-limited pulses.

3.4.6 Grating compressor

After amplification, the amplified beam was magnified ($\times 1.5$) with a telescope in order to reduce the peak intensity on the gratings. This is important in the case of high energies at lower repetition rates. Then, the pulses were compressed by a single transmission grating in folded configuration. The schematic of the compressor set up is shown in Fig. 3.12. After the telescope, the beam passes through the grating. The diffracted beam is sent back to the grating at the same height by using a retro-reflector(H), where H refers to the horizontal plane. The output beam, which is spatially chirped, is sent to the grating again but at a different height by using the retro-reflector(V), where V refers to the vertical plane. The retro-reflector(H) folds the beam and makes the beam pass a fourth time through the same grating, thereby eliminating angular dispersion and spatial-chirp. As the heights of the incoming and outgoing beams are different, a high-reflective plane mirror (often D-cut mirror) is used to select the compressed output beam. The configuration is equivalent to the grating pair compressor discussed in section 2.

Thanks to the high diffraction efficiency of multilayer dielectric gratings with groove density of 1750 lines/mm, a compressor throughput as high as 80 % was achieved. For the maximum pump power of 190 W, a compressed average power of 35.5 W was obtained at a pulse repetition rate of 100 kHz. The pulse duration was monitored by using an intensity

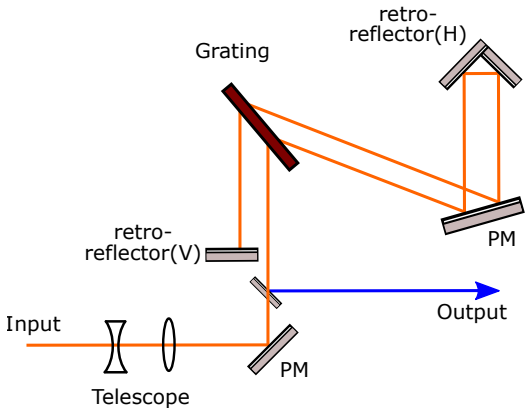

Figure 3.12: Optical layout of the grating compressor utilizing a single grating in folded configuration. Two retro-reflectors (H) and (V) fold the beam in the horizontal and vertical planes respectively so that the beam passes four times through the transmission grating at different positions.

autocorrelator (APE) and the spacing between the grating and the retro-reflector(H) was varied. An optimum separation of 32 cm between the virtual gratings (i.e. the propagation distance between the two passes through the grating via the retro-reflector(H)) compressed the pulses down to 940 fs at FWHM assuming a sech^2 shape as shown in Fig. 3.13(b). This corresponds to a group delay dispersion of 20.2 ps^2 (or 35.8 ps/nm at 1030 nm). However, the 1.88 nm wide output spectrum as shown in Fig. 3.13(a) supports Fourier transform-limited pulse duration of 550 fs. The discrepancy might be due to the mismatch of higher order dispersion coefficients of the CFBG stretcher and the grating compressor. There is a possibility to optimize the compression, reducing the pulse duration close to the Fourier limit if the CFBG stretcher is customized to match the dispersion coefficients of the grating compressor.

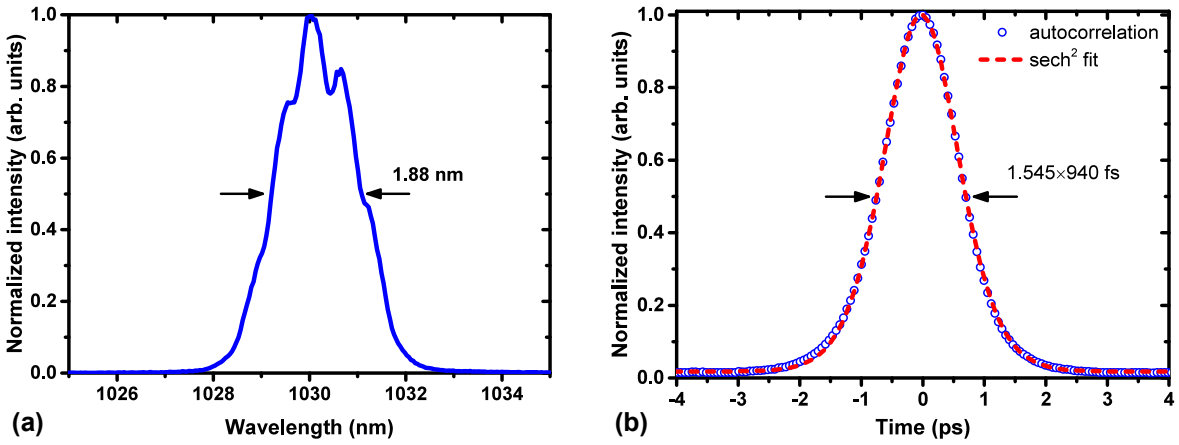

Figure 3.13: (a) Output spectrum and (b) autocorrelation measurement of the compressed pulse with 35.5 W average power at a pulse repetition rate of 100 kHz.

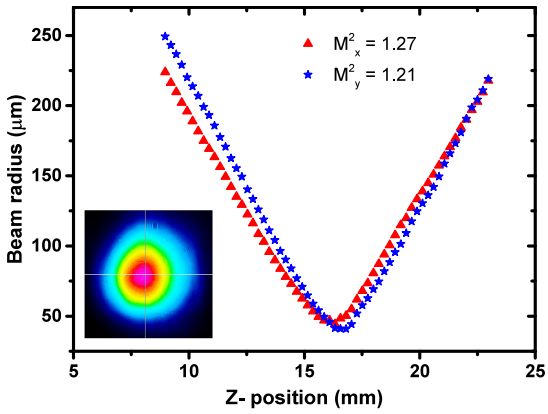

Figure 3.14: M^2 measurement of the compressed output with 35.5 W average power at a pulse repetition rate of 100 kHz. Inset: near field beam profile.

Note that in the case of thin-disk regenerative amplifiers using Yb:YAG crystal as gain medium, the pulse duration of the amplified pulses after the compressor is often in the range of sub-ps to few picoseconds, which is mainly due to the gain narrowing effect arising from the limited gain bandwidth of the Yb-doped gain medium, and the high gain of the amplifier.

The diffraction-limited beam quality offered by the regenerative cavity was preserved after the compression. A beam propagation factor of M^2<1.3 was measured in both axes as shown in Fig. 3.14, along with an excellent near field beam profile.

The performance of the grating compressor at various pulse repetition rates was examined by measuring the output pulse energy, output spectrum, compressed pulse duration and power stability (or average power drift) over a long time. No misalignment or drifts were noticed for several hours while running the amplifier with high average power as well as high energy. The complete characterization of the amplifier system is summarized in the following section.

3.5 Output characteristics

In this section, output characteristics of the laser are presented in detail. Since the stability of the laser is very important if it is used for nonlinear pulse compression or for pumping OPCPA, pulse-to-pulse stability, beam pointing as well as power stability were measured for long periods of time. Variation of the output average power, pulse duration and M^2 parameter as a function of pulse repetition rate were recorded.

Figure 3.15(a) shows the variation of the average power and pulse energy when the pulse repetition rate is changed. As expected, higher pulse energy can be extracted at low repetition rates. For a nominal pump power of 150 W, a pulse energy of 1.6 mJ was obtained at 10 kHz whereas an average power of 28.5 W was achieved at 100 kHz after compression. In order to optimize the average power and pulse energy simultaneously, the

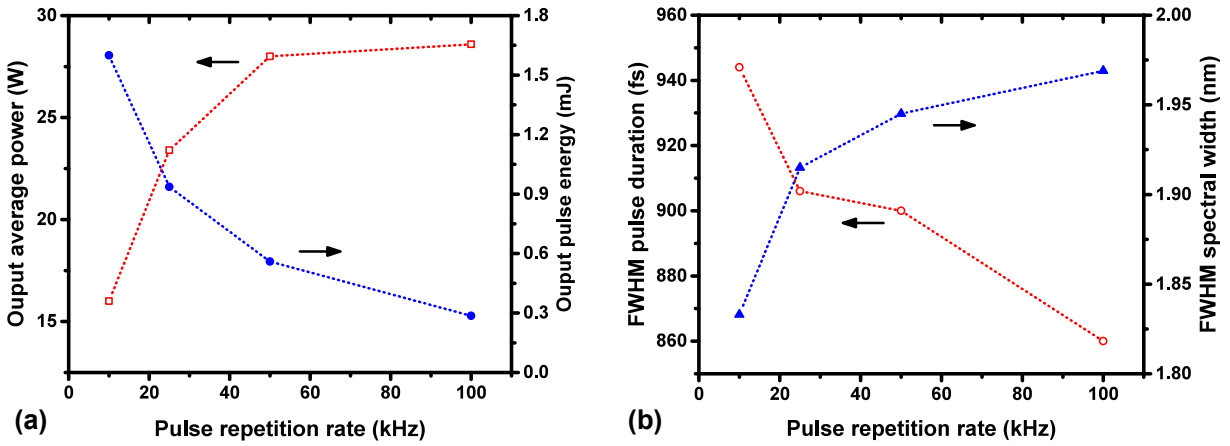

Figure 3.15: Variation of (a) average output power and pulse energy, and (b) pulse duration and spectral width with the pulse repetition rate.

pulse repetition rate was set to a moderate value e.g. 25 kHz at which 0.94 mJ pulses can be obtained after the compressor, corresponding to 23.5 W average power. When the pump power was increased to 180 W, the average power could be increased to 28 W, corresponding to 1.1 mJ energy per pulse.

Despite strong gain narrowing, the amplified spectrum supports sub-picosecond Fourier transform-limited pulses at all repetition rates of interest. Autocorrelation measurements of the compressed pulses indicated that pulse durations were in the range of 850 fs to 950 fs at all repetition rates as shown in Fig. 3.15(b).

Similarly, the beam quality was also monitored over the range of repetition rates. Figure 3.16 shows the M^2 measurement along with the near field beam profile after compression. It can be seen that the beam after the compressor is not far from the diffraction limit and no sign of spatial distortions were observed even for the highest pulse energy, meaning that nonlinear effects seem to play no role. In other words, the B-integral of the amplifier is not significant.

Furthermore, the output power stability (or the power drift) at the highest average power as well as the highest pulse energy were monitored for several hours by measuring the average power after the compressor using a power meter (Ophir, NOVA II). Excellent power stability was recorded at an average power close to 28 W with root mean square deviation less than 0.2 % over 6 hours as shown in Fig. 3.17(a). Similarly, the power drift corresponding to the maximum pulse energy of 1.6 mJ was monitored over 2.5 hours. As can be seen in Fig. 3.17(b), the laser output was very stable with root mean square deviation less than 0.4 %.

In addition to the power stability, beam pointing is a key parameter for many applications. At a pulse repetition rate of 100 kHz, the beam pointing of the laser system was measured by focusing the beam with a lens of 75 mm focal length and by placing a beam profiler CCD camera at the focus. The centroid of the focused beam was monitored over several hours. Figure 3.18 shows a screenshot of the measurement for more than 2 hours.

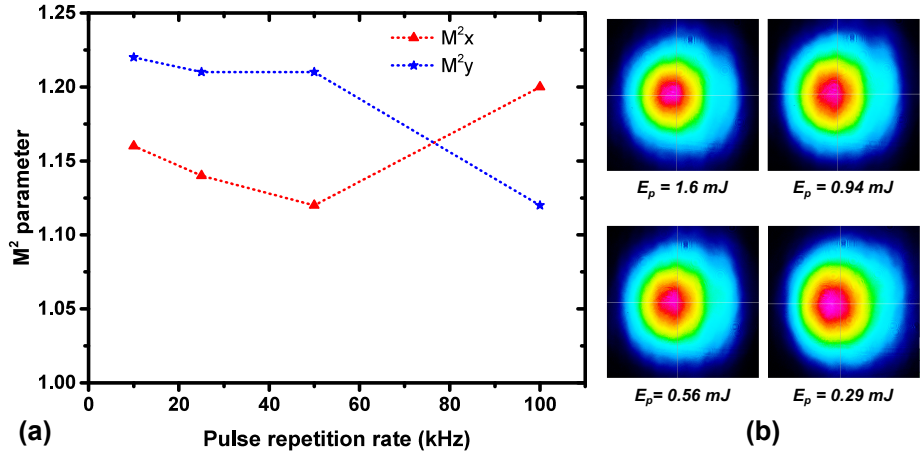

Figure 3.16: Measurement of (a) M^2 parameter and (b) near field beam profiles measured after the compressor at four different repetition rates 10 kHz, 25 kHz, 50 kHz and 100 kHz. The highest pulse energy of 1.6 mJ corresponds to the lowest repetition rate of 10 kHz and so on. Close to diffraction-limited beam qualities were observed in all cases.

The variations of the centroid along both x and y-axes were monitored with respect to a reference point. From the root mean square deviation of 1.35 µm, the pointing stability was characterized by 18 µrad whereas the maximum deviation of 2 µm corresponds to a pointing variation of 26.7 µrad. These values indicate that the pointing stability of the high power beam is not far from values (sub-10 µrad) reported in the literature [93, 94].

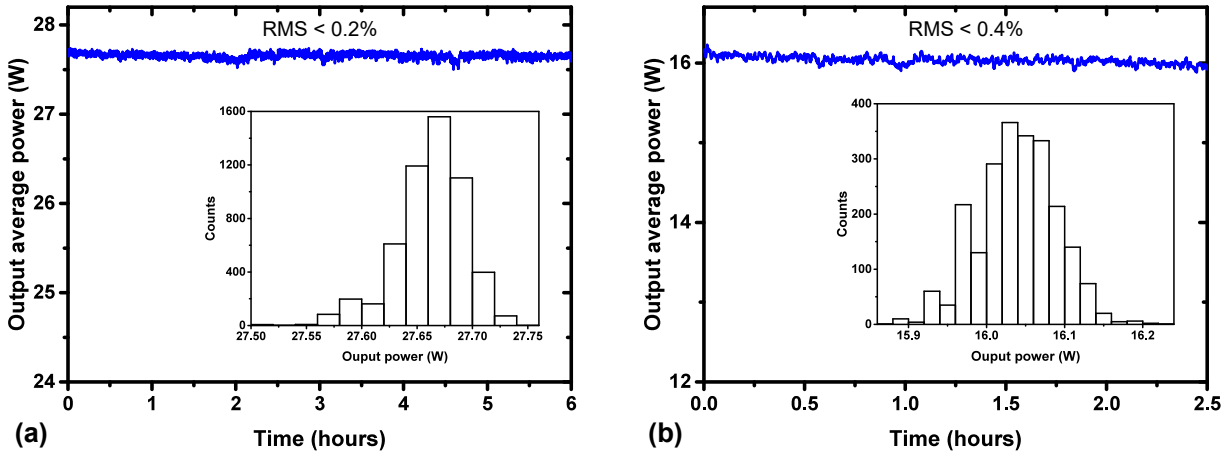

Figure 3.17: Power stability measurement at a pulse repetition rate of (a) 100 kHz and (b) 10 kHz corresponding to high average power and high pulse energy after the compressor respectively.

Another key parameter of the amplified pulses to characterize is the stability from pulse to pulse. This can usually be characterized by monitoring the variation of the peak height or intensity of the pulse with a fast photodiode and an oscilloscope. In this work, a fast photodiode (DET10A from Thorlabs) and a 2.5 GHz, 40 GS/s digital oscilloscope (DPO7254C

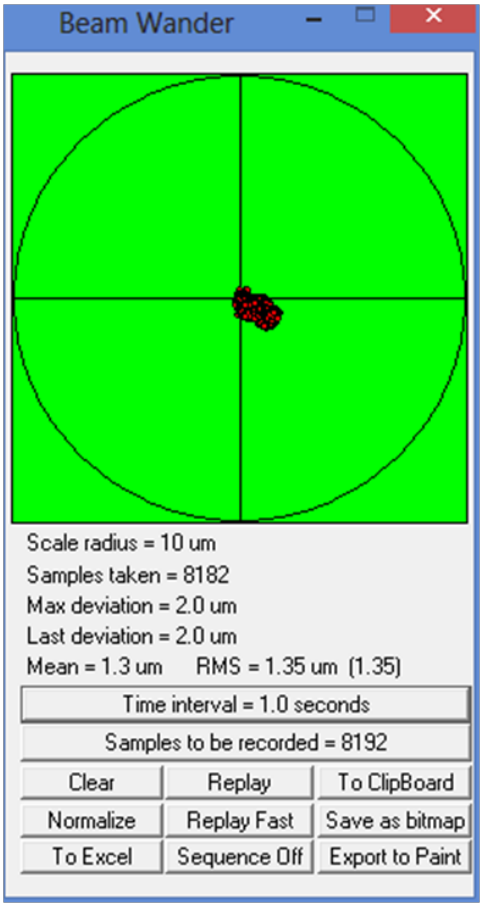

Figure 3.18: Screenshot of the beam pointing measurement with a beam profiling camera from DataRay Inc. The beam with 28 W average power at a pulse repetition rate of 100 kHz was focused with a 75 mm lens.

from Tektronix®) were used to track the maximum amplitude of the pulses in the pulse train. The amplitude variations from shot to shot were measured to be within a root mean square value of 0.9 % which indicates excellent pulse-to-pulse stability. This is comparable to the pulse-to-pulse stability reported in the literature for similar regenerative amplifiers e.g. see Ref. [39].

Finally, the performances of the diode-pumped Yb:YAG thin-disk regenerative amplifiers reported in the literature in recent years have been summarized in Tab. 3.1. Given the limited pump power, the output characteristics of the amplifier is comparable to that of Yb:YAG based thin-disk regenerative amplifiers demonstrated in recent years, where optical-to-optical efficiency <35 % has been achieved with an output spectral bandwidth <2.4 nm. With increased pump power, pulse energy of 30 mJ at a repetition rate of 10 kHz i.e. the average power of 300 W has been demonstrated with regenerative amplification using an Yb:YAG thin-disk as gain medium.

Table 3.1: Performances of diode-pumped Yb:YAG thin-disk regenerative amplifiers reported in recent years. P_{in}: input pump power, E_p: output pulse energy, f_p: pulse repetition rate, $\Delta\lambda$: FWHM spectral bandwidth, $\Delta\tau$: FWHM pulse duration, η: optical-to-optical conversion efficiency, P_{avg}: average output power after the compressor, P_0: peak power, rms: root mean square, na: not available. * refers to the pulse-to-pulse energy fluctuations instead of power drift and ** refers to the power drift measured at an average power of ∼28 W.

Ref.	P_{in} (W)	E_p (mJ)	f_p (kHz)	$\Delta\lambda$ (nm)	$\Delta\tau$ (ps)	η (%)	M^2	Power drift rms(%)	P_{avg} (W)	P_0 (GW)
[95]	172	17	3	2	0.615	29.7	<1.5	0.8*	51	27.6
[39]	274	25	3	1.02	1.6	26	<1.1	0.7*	75	15.6
[96]	280	20	5	1.6	1	35.7	<1.1	0.5	100	20
[78]	640	30	10	1.6	1	47	na	1.5*	300	30
This work	190	0.35	100	1.97	0.94	18.7	<1.25	0.2**	35	0.37
[93]	375	0.8	100	0.8	1.9	21.3	na	na	80	0.42
[97]	370	0.3	300	2.3	0.79	27	<1.35	0.8	100	0.38
[98]	500	0.2	800	2	0.75	32	<1.2	na	160	0.27

3.6 Frequency conversion

The performance of the laser reported in the previous section demonstrates its capability to pump OPCPA systems in the near-infrared and the visible spectral ranges. This requires the generation of low-order harmonics e.g. the second and third harmonic, which is often performed in nonlinear crystals. There are several nonlinear crystals available for harmonic generation. Among others, beta barium borate (BBO) and lithium triborate (LBO) are most commonly used for frequency upconversion of 1 µm-lasers. In this work, BBO was chosen due to its higher nonlinearity compared to LBO and was set up in critical phase-matching (see chapter 2 for details about phase-matching).

3.6.1 Second harmonic generation

For second harmonic generation, BBO was used in type I phase-matching (the configuration in which the polarization of the input fundamental beam is perpendicular to that of the output beam). The crystal was manufactured given the expected phase-matching angle of 23.4° for a conversion of the input laser beam at 1030 nm into 515 nm, according to Eq. 2.70. A half-wave plate and a thin-film polarizer were used in order to regulate the laser power going into the conversion stage as shown in Fig. 3.19. The beam size was decreased to 2.2 mm by using a telescope with demagnification factor of 1.5. For a maximum pulse energy of 1.6 mJ and 1 ps pulse duration, the peak intensity in the crystal was 84.2 GW/cm^2, which is significantly less than the damage threshold (> 200 GW/cm^2 for ~ 1 ps pulses). The polarization plane of the fundamental beam was adjusted by using a half-wave plate before the crystal. In addition, as the crystal cut is never perfect in practice, the angle of the crystal was adjusted to maximize the conversion efficiency. After conversion, the second

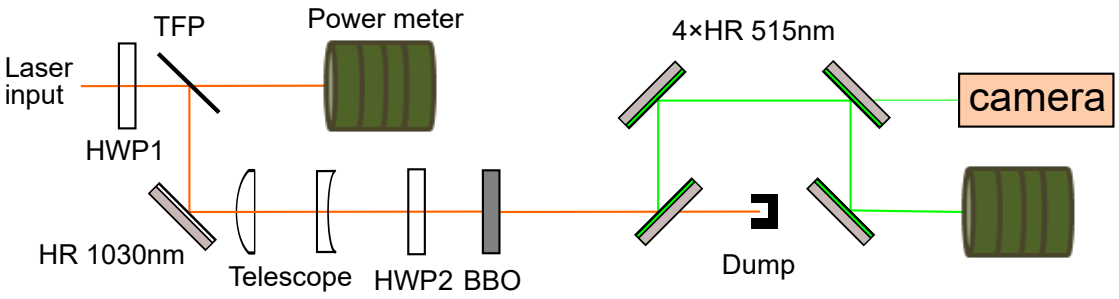

Figure 3.19: Optical layout for second harmonic generation. A part of the s-polarized laser output is reflected from the thin-film polarizer (TFP) depending upon the rotation of the half-wave plate (HWP1), and is used for second harmonic generation. A telescope is used to reduce the beam size and accordingly to increase the intensity. After the conversion in the crystal, the second harmonic beam is separated from the fundamental power using four dichroic mirrors. The spatial profile of the leakage from the third dichroic mirror is recorded using a beam profiler CCD camera. HR: high reflector.

harmonic power was separated from the residual near-infrared (IR) power by using four dichroic mirrors. Leakage from the third mirror was sent to a beam profiler CCD camera to monitor the second harmonic beam.

At first, the beam diameter was set to ∼2.2 mm (full width at $1/e^2$ of peak intensity). For an input average power of 25 W at a pulse repetition rate of 100 kHz, the peak intensity is then around 13.2 GW/cm^2. The length of the BBO crystal was 1.5 mm. The conversion was optimized by adjusting the plane of polarization using the half-wave plate, and the angle of the crystal. The second harmonic power was measured as a function of input IR power as shown in Fig. 3.20(a). A maximum output power of 12.7 W was achieved with a conversion efficiency of 51 %. The beam quality of the input laser beam was almost preserved with an M^2 parameter of ~ 1.3 along both axes as shown in Fig. 3.20(b). Because the conversion is still growing without beam degradation, further increase in second harmonic power with higher conversion efficiency seems possible without compromising the beam quality. This can be achieved by increasing the input intensity as can be seen in Eq. 2.73. Note that increase in crystal length may increase conversion efficiency but only with the expense of phase-mismatch factor, which can degrade other characteristics e.g. the bandwidth of the second harmonic pulses.

Next, the repetition rate of the laser was changed to 50 kHz keeping the beam size and crystal length constant so that the pulse energy and accordingly the peak intensity was almost doubled. As expected, the conversion efficiency was increased and a maximum value of 67 % was achieved with 16 W average power in the second harmonic as shown in Fig. 3.21(a), along with a good near field beam profile. As can be seen clearly, the conversion is still growing but slowing down at higher peak intensities. Nevertheless, a good beam quality close to that of the fundamental beam was observed even at high conversion efficiency, as can be seen in the M^2 measurement of the green beam at 16 W average power (or 320 µJ pulse energy) shown in Fig. 3.21(b).

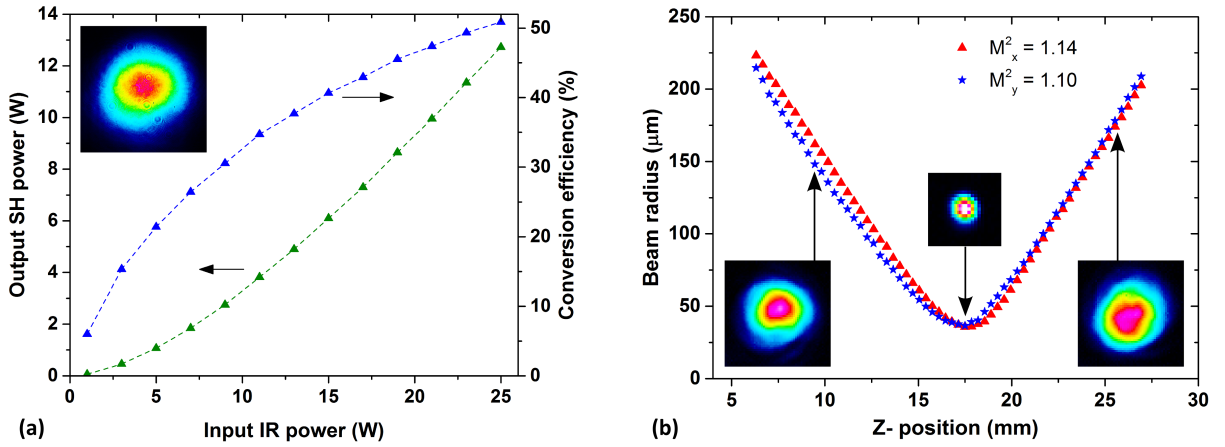

Figure 3.20: Second harmonic generation at a pulse repetition rate of 100 kHz. (a) Evolution of the average second harmonic (SH) power and conversion efficiency as a function of the input IR power [inset: near field beam profile measured at maximum power], and (b) M^2 measurement of 12 W second harmonic beam. A maximum conversion efficiency of 51 % is achieved with an average second harmonic power of 12.7 W. Further increase in conversion efficiency seems possible as the conversion is increasing with increase in the input fundamental power.

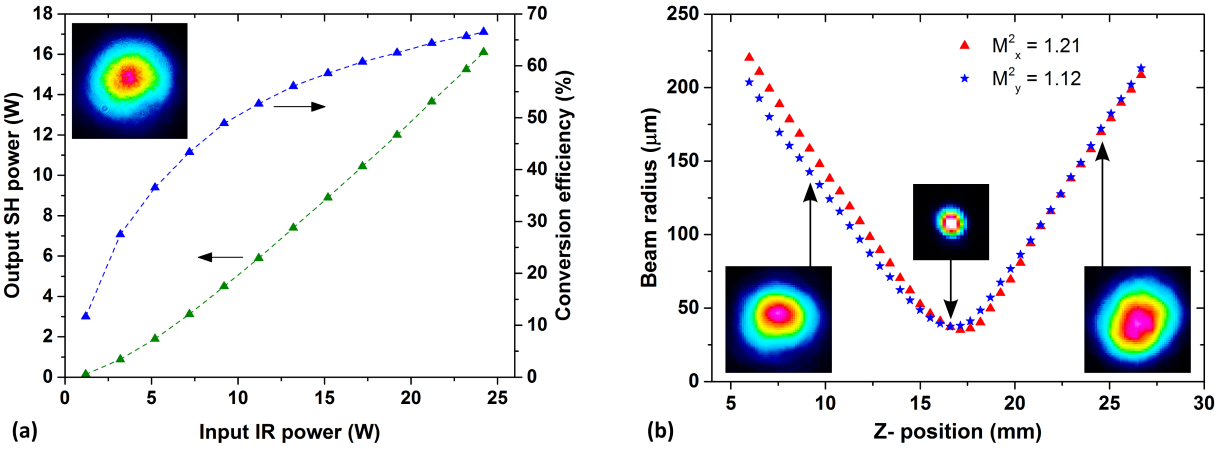

Figure 3.21: Second harmonic generation at a pulse repetition rate of 50 kHz. (a) Variation of the average second harmonic (SH) power and conversion efficiency as a function of the input IR power [inset: near field beam profile measured at maximum power], and (b) M^2 measurement of 16 W second harmonic beam. The decrease in pulse repetition rate from 100 kHz to 50 kHz i.e. increase in intensity by a factor of 2 led to an increase in conversion efficiency from 51 % to 67 %.

A maximum second harmonic power close to 17 W was achieved for an input IR power of 25 W. The average output power of the second harmonic beam was measured for an hour and it is shown in Fig. 3.22. The variation was characterized by a root mean square (RMS) value of 0.7 %, which is comparable to the power drift reported in the literature e.g. RMS value of 0.5 % [16]. The excellent output characteristics of the second harmonic demonstrate

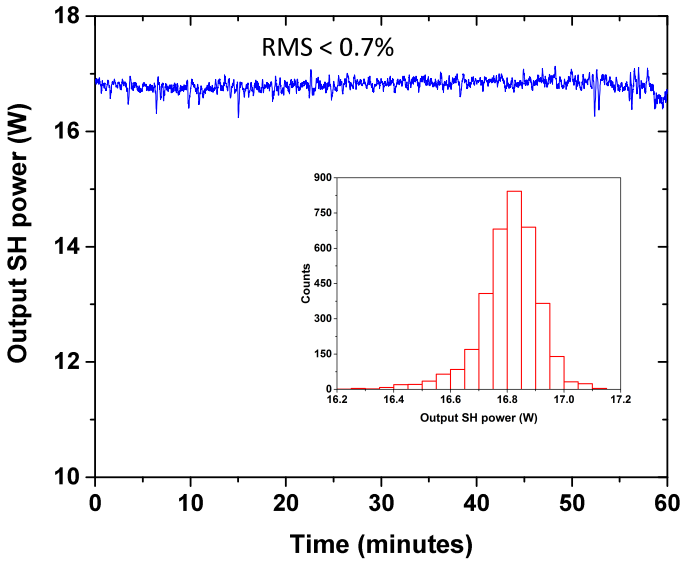

Figure 3.22: Power stability measurement of the second harmonic (SH) beam at a pulse repetition rate of 50 kHz.

that the beam is highly suitable for pumping OPCPA e.g. with a seed spectrum centered around 800 nm.

Finally, the repetition rate was set at 25 kHz in order to study the conversion at higher pulse energies. The IR beam diameter and the crystal length were kept constant at 2.2 mm and 1.5 mm respectively. For an input IR power of 21 W, a second harmonic power of 14.8 W was generated which corresponds to a pulse energy of 590 µJ and a conversion efficiency of 70 %. The second harmonic beam at maximum power had a close to diffraction-limited beam quality as indicated by the measurement of the beam propagation factor shown in Fig. 3.23(b). The evolution of the average second harmonic power and conversion efficiency are shown in Fig. 3.23(a). Compared to the experiments at higher pulse repetition rates, the conversion efficiency is noticeably slowing down beyond 50 % which indicates that further optimization of the conversion without compromising the beam quality is not possible.

The high conversion efficiency of the second harmonic generation of Yb:YAG thin-disk regenerative amplifiers is due to the relatively narrow spectral bandwidth ($\sim$ 2 nm) of the amplified pulses, which implies that phase-matching is achieved over the whole bandwidth. Second harmonic conversion efficiencies around 70 % have recently been reported in the literature [16, 81, 96] for similar regenerative amplifier systems.

3.6.2 Third harmonic generation

Yb-doped laser sources, after upconversion to the third harmonic are useful for pumping OPCPAs in the visible spectral range. Therefore, the output of the thin-disk regenerative amplifier was also converted to the third harmonic by using two BBO crystals. The schematic of the conversion set up is shown in Fig. 3.24. The fundamental beam was converted

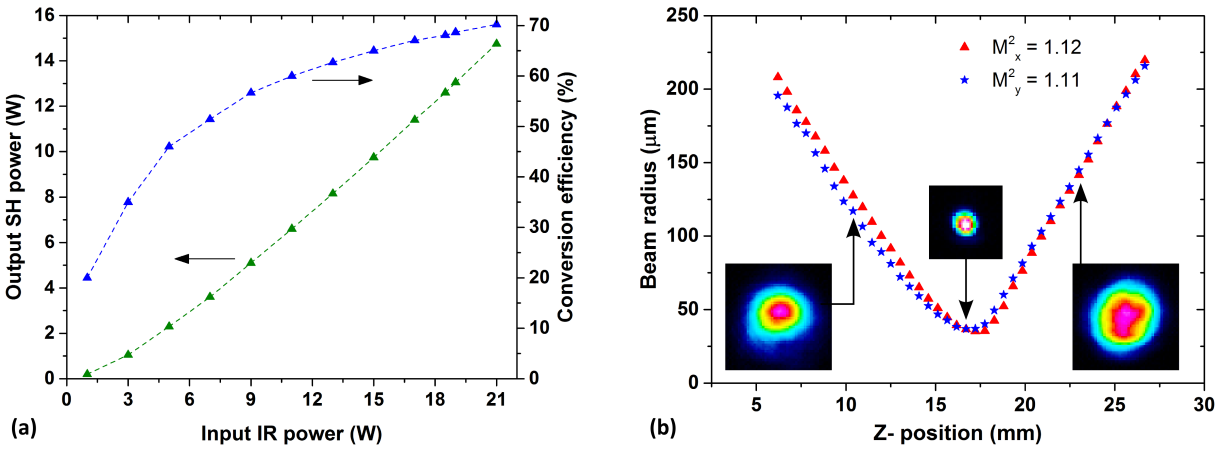

Figure 3.23: Second harmonic generation at a pulse repetition rate of 25 kHz. (a) Variation of the average second harmonic (SH) power and conversion efficiency as a function of the input IR power [inset: near field beam profile measured at maximum power], and (b) M^2 measurement of 14.8 W second harmonic beam. Compared to the conversion at higher pulse repetition rates, the conversion efficiency is increased to 70 %.

to the second harmonic in the crystal BBO1 as described in the previous section. Then, the second harmonic beam interacted with the fundamental beam in the crystal BBO2 via a sum-frequency mixing process, generating the third harmonic beam at a wavelength of 343 nm.

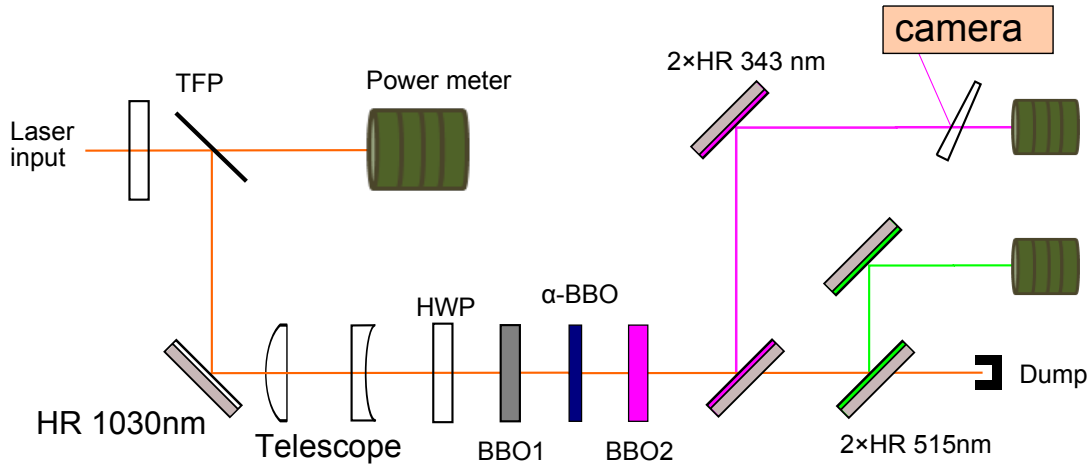

Figure 3.24: Optical layout for third harmonic generation. TFP: thin film polarizer, HWP: half-wave plate, HR: high reflector. BBO1 and BBO2 are BBO crystals for second and third harmonic generation respectively.

As discussed in section 2.4, frequency conversion is an instantaneous process and therefore the fields have to overlap in space and time. Because of the group velocity mismatch during propagation in one crystal, the different frequency components are not overlapped

in time while entering the second crystal. This would lead to a reduced conversion efficiency, or no frequency conversion at all in the worse case, and for that reason, it is necessary to reverse the temporal walk-off between the pulses at the fundamental (1030 nm) and second harmonic (515 nm) wavelengths originating in the first crystal. This was achieved by using an alpha-BBO (α-BaB_2O_4) birefringent crystal, which is a negative uniaxial crystal similar to beta-BBO except for a vanishing second-order nonlinearity due to the centrosymmetry in its crystal structure. The high birefringence of the alpha-BBO crystals make them preferable for the time delay compensation. After the third harmonic generation, two dichroic mirrors that reflect the third harmonic, and transmit the second harmonic and the IR wavelength, were used to separate the third harmonic beam. The reflection from a thin wedge placed after the second dichroic mirror was used to characterize the third harmonic beam. The second harmonic power was also monitored by using two dichroic mirrors that reflect the second harmonic and transmit the IR wavelength whereas the IR power was estimated from the residual power measurement after the thin film polarizer. The sum frequency generation process was carried out in both a type I and type II phase-matching configuration as described in section 2.4.3 in order to optimize the conversion efficiency.

At first, the repetition rate was set to 50 kHz where the maximum average power of the second harmonic was achieved with the 1.5 mm long BBO crystal as described in section 3.6.1. The residual IR beam was p-polarized whereas the second harmonic beam was s-polarized. Therefore, type II phase-matching was utilized for the sum-frequency mixing by using a 1 mm long BBO crystal, generating a third harmonic beam that is polarized in the same plane as the fundamental beam. Phase-matching was achieved with the crystal cut at an angle of 40.1° i.e. the fundamental and the third harmonic beams were propagating at that angle with respect to the crystal axis (extraordinary beams) and the second harmonic beam was propagating along the crystal axis (ordinary beam) [see section 2.4.3]. A 1 mm long α-BBO crystal was found to be optimum for the compensation of the group delay between the IR and second harmonic pulses, which ultimately helped to maximize the conversion efficiency.

For an input IR power of 24 W, an average third harmonic power of 9.5 W was obtained which corresponds to a 39.5 % conversion efficiency. The evolution of the output power and conversion efficiency at the third harmonic wavelength of 343 nm with respect to the input IR power is shown in Fig. 3.25. It can be seen that a maximum conversion efficiency of 41 % was achieved for an input IR power of 19 W. Beyond this input power, the conversion efficiency decreases with increase in input IR power. This can be explained by the coupled-wave equations for sum frequency generation as discussed in section 2.4, where the source term in the nonlinear equations contains both input and output interacting fields [see Eqs. 2.60, 2.61 and 2.62]. This means that when the energy is transferred from the intense input fields to the output during the conversion process, at some point the energy flow is reversed when the output field is intense enough. In particular, this does not happen homogeneously, but rather where the spatiotemporal distribution is most intense, giving rise to distortions in the spatiotemporal distributions and degradation of the peak power. Such a process, often known as back-conversion, can significantly degrade the output beam quality. In this case, the degradation is visible in the near field beam profile at 9.2 W third

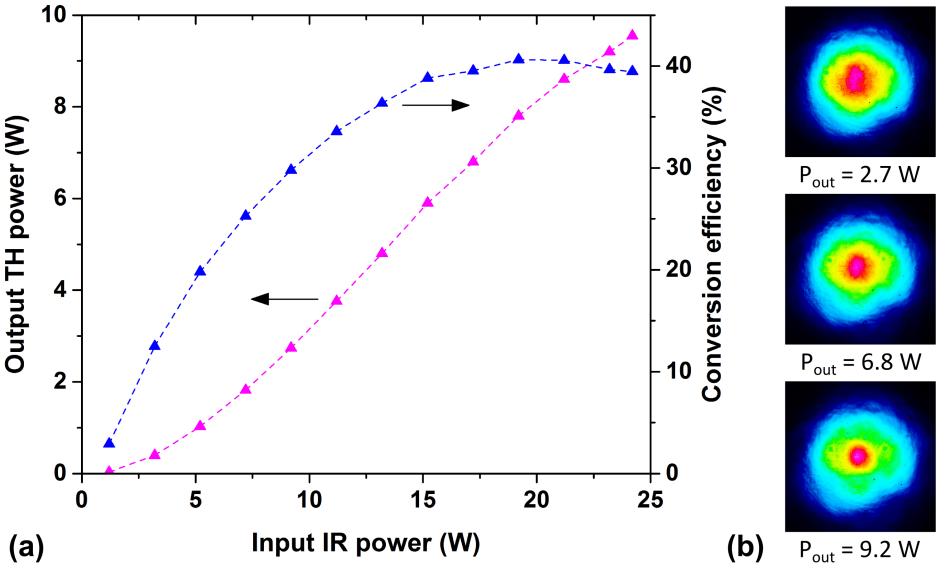

Figure 3.25: Third harmonic generation in type II phase-matching at a pulse repetition rate of 50 kHz. (a) Variation of the average third harmonic (TH) power and conversion efficiency with respect to the input IR power, and (b) near field beam profiles at three different third harmonic average powers. The conversion is slightly saturated and spatial narrowing is visible at high conversion efficiencies, which is mainly due to the non-uniform profile of the IR beam (note the beam profile at 9.2 W third harmonic power).

harmonic power, compared to the beam profiles for lower third harmonic powers as shown in Fig. 3.25(b). In particular, a spatial narrowing of the third harmonic beam occurs, which is mainly due to the non-uniform spatial profile of the IR beam.

Next, the length of the crystals BBO1 and BBO2 were changed to 3 mm and 1.5 mm respectively and the phase-matching configuration in the BBO2 crystal was changed to type I i.e. the fundamental beam and the second harmonic beam were polarized in the same polarization plane. This was accomplished by adjusting the polarization plane of the input beam with a half-wave plate placed before the crystal BBO1 [see Fig. 3.24] so that the IR power was divided into two orthogonal polarization directions during the propagation through the crystal. The s-polarized part of the IR power was converted to second harmonic while the p-polarized part was preserved. That means that after the second harmonic generation, both the fundamental and the second harmonic beams had the same polarization, which interacted in the BBO2 crystal for sum frequency mixing, generating the third harmonic of the fundamental beam. The nonlinear interactions are governed by Eqs. 2.60, 2.61, and 2.60. The second crystal BBO2 was cut at a phase-matching angle of 32.5° for type I, which was adjusted in such a way that the input beams were ordinary (o) and the third harmonic beam was extraordinary (e). As explained in the previous section, a 1.5 mm long alpha-BBO crystal was used for the compensation of the group delay between the IR and second harmonic pulses.

The variation of the third harmonic output power with respect to the input IR power

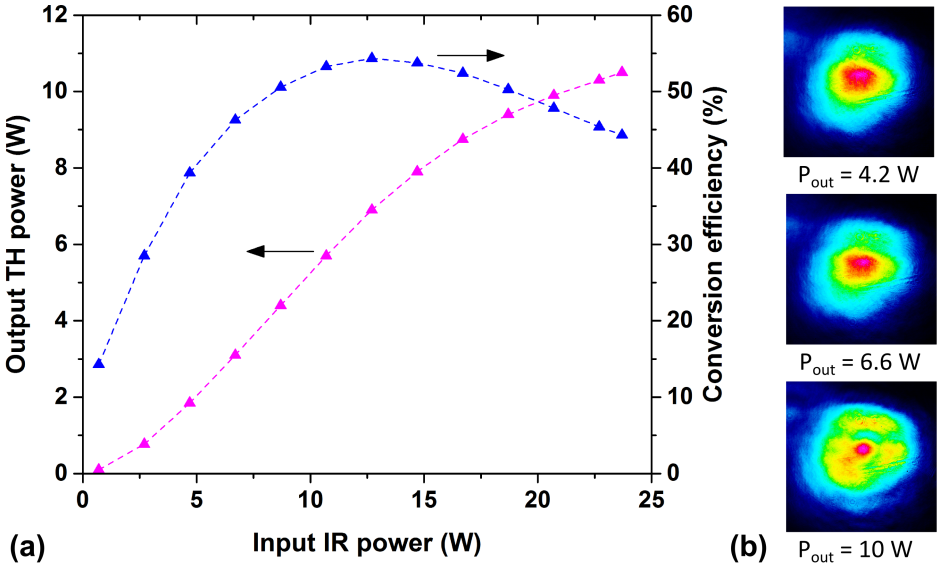

Figure 3.26: Third harmonic generation in type I phase-matching at a pulse repetition rate of 50 kHz. (a) Variation of the average third harmonic (TH) power and conversion efficiency with respect to the input IR power, and (b) near field beam profiles at three different third harmonic average powers. Back-conversion of the third harmonic to IR occurred for higher input average power as can be seen in the evolution of the conversion efficiency. The back-conversion introduced spatial distortions, which are visible in the beam profile at 10 W third harmonic power, compared to the others for lower output powers.

is shown in Fig. 3.26(a), along with the conversion efficiency. For average third harmonic powers higher than 8 W, back-conversion of the third harmonic to the IR beam was observed as clearly visible in the conversion efficiency. The spatial profile of the third harmonic beam at 10 W output power shows some structures compared to that at lower average powers [Fig. 3.26(b)], which is mostly due to the back-conversion. This can be avoided by decreasing either the intensity or the crystal length. Excluding the back-conversion regime, a maximum conversion efficiency of 54 % with an average third harmonic power of 7 W was achieved with type I phase-matching. This implies that type I phase-matching offers more efficient third harmonic generation compared to type II. This is due to the fact that the IR radiation used for the third harmonic generation in the type I configuration has clean spatial and temporal profiles unlike the depleted profiles of the residual IR radiation from the second harmonic stage in the case of a type II configuration.

Finally, the repetition rate was increased to 100 kHz keeping the crystal lengths and the phase-matching configuration constant in order to avoid back-conversion. Indeed, the decrease in pulse energy and thus peak intensity minimized the back-conversion which can be seen in Fig. 3.27(a), both in the evolution of the conversion efficiency and the near field beam profile corresponding to the maximum conversion efficiency (shown in the inset). A third harmonic average power of 13 W was achieved for an input IR power of 24.5 W which corresponds to 53 % conversion efficiency. The M^2 parameter, measured at 11 W third

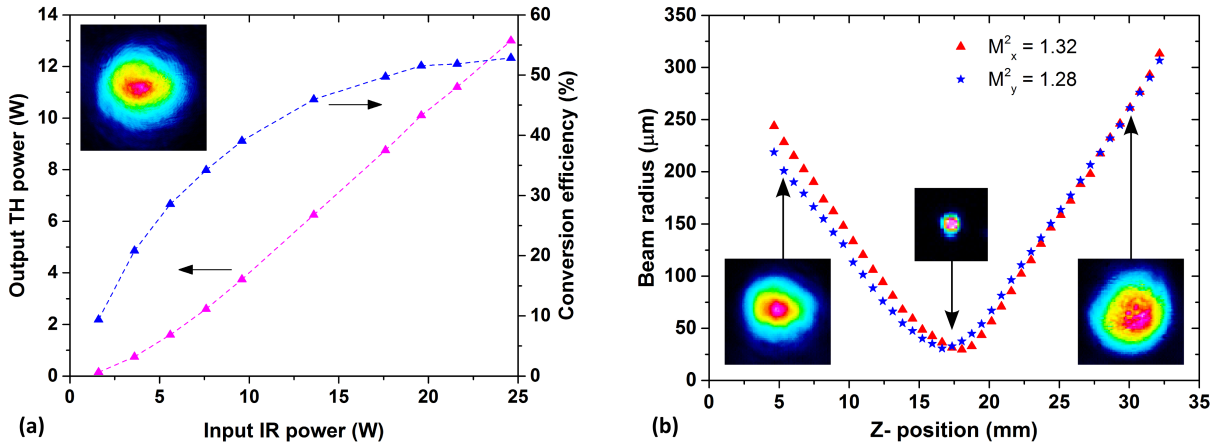

Figure 3.27: Third harmonic generation in type I phase-matching at a pulse repetition rate of 100 kHz. (a) Variation of the average third harmonic (TH) power and conversion efficiency with respect to the input IR power [inset: near field beam profile at maximum conversion efficiency], and (b) M^2 measurement at 11 W third harmonic power. As expected, an increase in pulse repetition rate while keeping all other parameters constant and thus decreasing the peak intensity avoided the saturation and back-conversion significantly. A conversion efficiency as high as 53 % was achieved.

harmonic power and shown in Fig. 3.27(b), indicates that the third harmonic beam was not far from the diffraction limit. The average power of the third-harmonic generation was measured for almost an hour using a power meter (OPHIR). As can be seen in Fig. 3.28, the power drift was characterized by a root mean square value of <0.3 %. There was no significant drift in average power and no misalignment was noticed within the measurement time.

3.7 Pulse compression in Kagome fiber

Laser systems based on Yb-doped fibers and a Yb:YAG gain medium are capable of delivering high average power or high energy but inherently limited to pulse durations >300 fs because of the limited gain bandwidth of the gain medium. The only way to decrease the pulse duration of such systems is external nonlinear pulse compression.

In this work, the pulse compression of sub-picosecond pulses from the Yb:YAG regenerative amplifier was performed in a hypocycloid core Kagome fiber with air in the core at atmospheric pressure. Compressed pulses of $\sim$ 130 fs (FWHM) pulse duration with few tens of microjoules pulse energy were achieved in a simple set up. The characteristics of the Kagome fiber and the results of the pulse compression experiments are presented in the following sections.

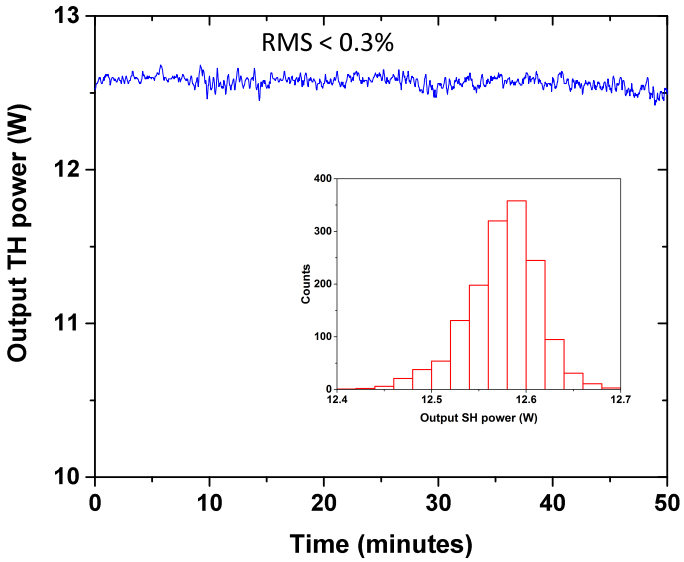

Figure 3.28: Measurement of 12.6 W average third harmonic (TH) power at a pulse repetition rate of 100 kHz for almost an hour. The power drift was measured with a root mean square (RMS) value <0.3 %.

3.7.1 Hypocycloid-core Kagome fiber

All the experiments presented in the following sections were performed in a Kagome-type hollow fiber with a 7-cell core and 3-ring cladding geometry. An image of the fiber cross section is shown in Fig. 3.29(a). The core has diameters of 56 µm and 72 µm for the inner and outer circumscribing cups respectively [Fig. 3.29(b)], resulting a mode-field-diameter of ∼40 µm. The experimentally measured propagation losses and the simulated group velocity dispersion of the fiber in the near-infrared spectral range are shown in Fig. 3.29(c) (taken from Ref. [70]). At a laser wavelength of 1030 nm, the propagation loss is maintained below 50 dB/km with a normal group velocity dispersion of 5.6×10^{-4} ps^2/m. Low transmission loss and low group velocity dispersion essentially maintain high peak power along the fiber length and make it attractive for nonlinear pulse compression.

In this experiment, Kagome fibers of two different lengths- 16 cm and 120 cm were used. The choice of the fiber lengths was motivated by the fact that a high pulse energy can be used with a short piece of fiber while a long nonlinear interaction length can be achieved with a long fiber even for low pulse energy and accordingly with higher average power. As discussed in chapter 2, the influence of group velocity dispersion of the fiber and self-phase modulation on the propagation of pulses can be estimated by calculating the dispersion length and the nonlinear length using Eqs. 2.129 and 2.130 respectively. For an input pulse duration of 900 fs, the dispersion length is 1.45 km, which is far longer than the fiber length. This means that dispersion of the fiber has almost no effect on the pulse propagation. Therefore, self-phase modulation is dominant and only responsible for broadening of the spectrum. This is further clear from the calculation of the nonlinear length of the fiber,

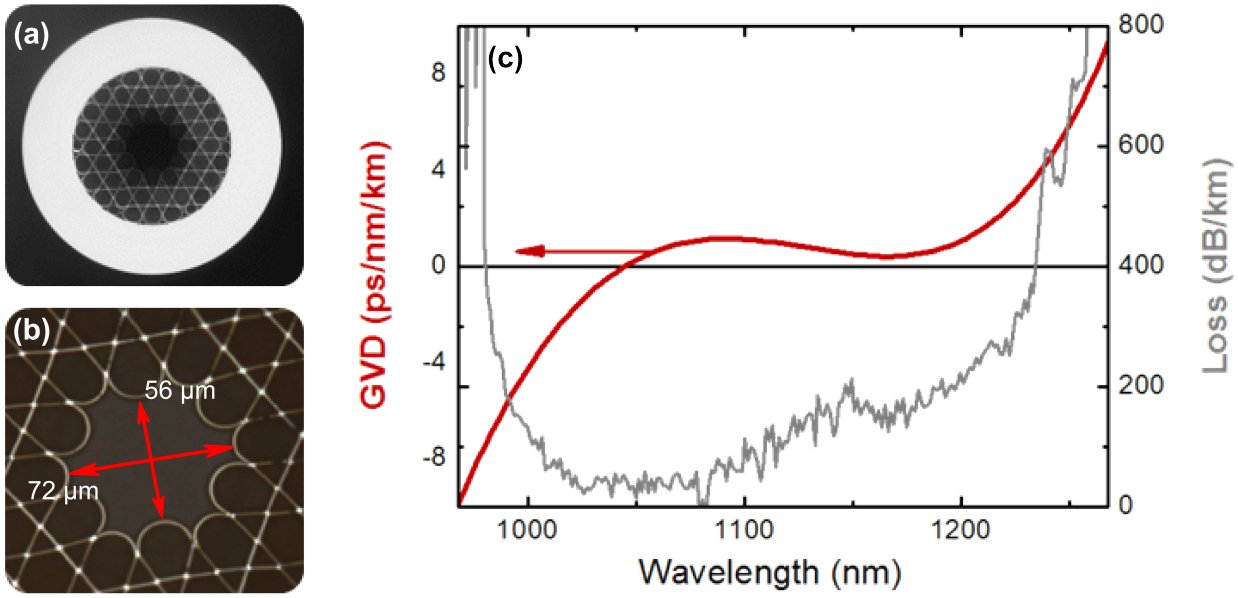

Figure 3.29: (a) Image of the cross section of the hypocycloid-core Kagome fiber, (b) Zoom of the core and (c) group velocity dispersion and transmission loss in the near-infrared spectral range (taken from [70]).

which is ∼0.93 m for a given pulse energy of 100 µJ and a pulse duration of 900 fs at a central wavelength of 1030 nm. Measurements of coupling or transmission efficiency were carried out in the 16 cm long fiber whereas spectral broadening and pulse compression were performed in both fibers. The transmission efficiency including coupling, propagation losses as well as losses in the focusing and collimating lenses was found to be ∼70 % as shown in Fig. 3.30. For this measurement, the fiber was placed in a copper V-groove and input and output powers were measured before the focusing and after the collimating lenses respectively [see Fig. 3.31].

3.7.2 Spectral broadening and dispersion compensation

For the spectral broadening, the sub-picosecond pulses from the regenerative amplifier presented in section 3.4 were coupled, at first, into the 16 cm long Kagome fiber with air inside the core at atmospheric conditions. The repetition rate of the laser was set at 10 kHz, which was chosen so that higher energy, if necessary, can be coupled into the short fiber with relatively low average power (<10 W). This allows simple mounting of the fiber end and helps to maintain high coupling efficiency minimizing instabilities due to heating of the fiber end.

The schematic of the pulse compression setup is shown in Fig. 3.31. The laser output was controlled with a half-wave plate and a thin-film polarizer. The beam was first de-magnified by a telescope and coupled into the fiber by a plano-convex lens. The focal length of the lens was optimized for mode matching, maximizing the transmission efficiency of the fiber.

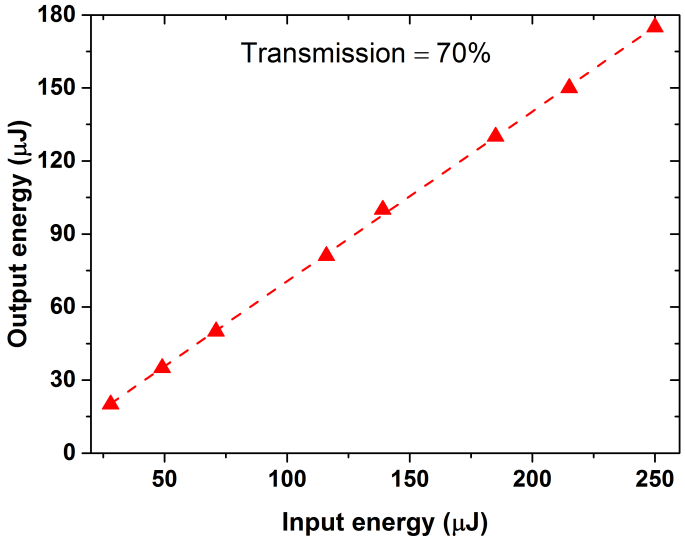

Figure 3.30: Transmission efficiency of the 16 cm long Kagome fiber, including coupling and propagation losses as well as the losses in the focusing and collimating lenses.

The input end of the fiber was fixed in a copper V-groove. The output from the fiber, after collimation by a lens, was sent through a half-wave plate and a polarizing cube in order to select linearly polarized light. At the same time, the residual power was also measured which was used to calculate the polarization extinction ratio.

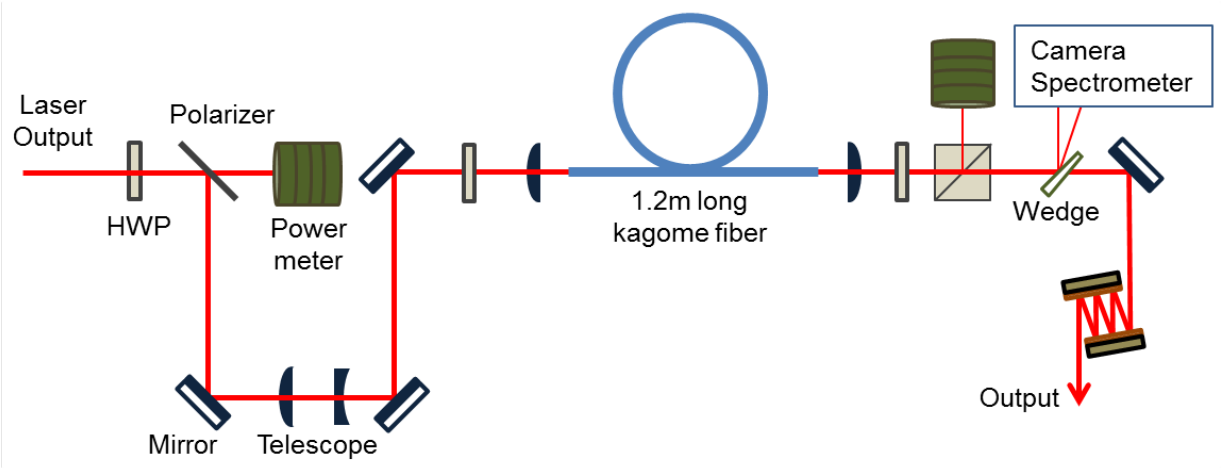

Figure 3.31: Optical layout of nonlinear pulse compression. HWP: half-wave plate

Pulse compression in a 16 cm long fiber

A plano-convex lens of 60 mm focal length was used to couple the beam into the 16 cm long fiber achieving maximum coupling efficiency of ∼80 %. The input energy was increased stepwise and the output spectrum was recorded with a spectrometer. Pulse energy as high

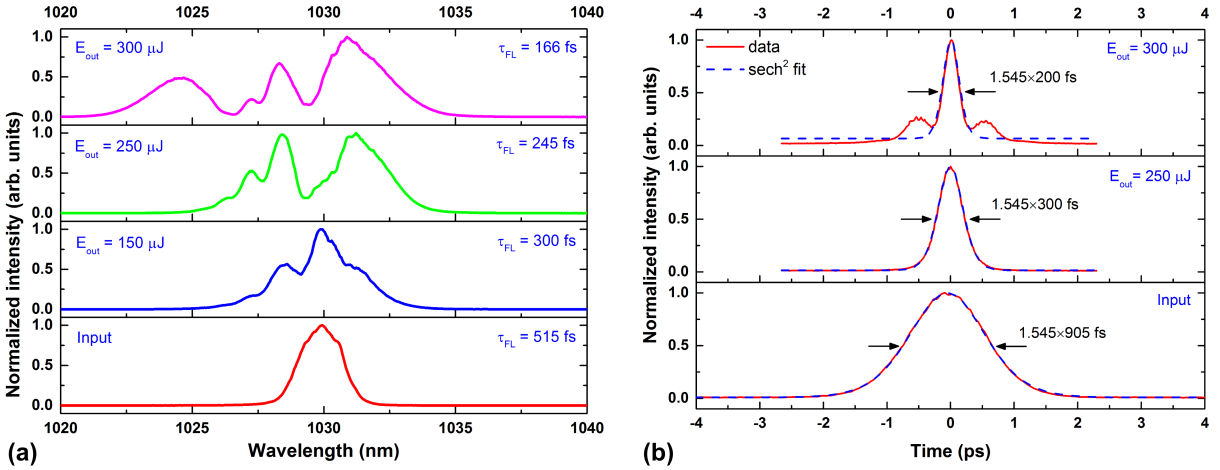

Figure 3.32: (a) Evolution of the spectrum at the output of the 16 cm long Kagome fiber and (b) autocorrelation measurements of the compressed pulses. Side peaks appeared in the pulse profile corresponding to the output pulse energy of 300 µJ and were due to the uncompensated higher-order spectral phase. E_{out} and τ_{FL} refer to the output pulse energies before the compressor and the Fourier transform-limited pulse duration respectively.

as 300 µJ was coupled into the fiber. Beyond this energy, the fundamental mode profile degraded and the spectrum was significantly broadened towards shorter wavelengths. Figure 3.32 shows spectra at three different output pulse energies along with the input spectrum. For the highest pulse energy, the broadened spectrum supports a Fourier transform-limited pulse duration of 166 fs (FWHM). A grating compressor with a transmission grating of 500 lines/mm groove density was used in a folded-configuration to compensate the induced nonlinear phase due to self-phase modulation. Autocorrelation measurements show that the pulses were compressed down to 200 fs for the 300 µJ (uncompressed) pulse energy. Further broadening of the spectrum, necessary to reduce the pulse duration, is only possible by increasing the nonlinear interaction length i.e. either increasing the pulse energy or the length of the fiber. However, a possible increase in the pulse energy was limited by ionization of the air due to the high peak intensity inside the fiber. Therefore, a longer fiber was used in the following experiment.

Pulse compression in a 120 cm long fiber

To increase the spectral broadening further, a 120 cm long fiber was used for the rest of the pulse compression experiments. An overall transmission efficiency of 80 % was achieved with a coupling lens of 60 mm focal length.

At first, spectral broadening was measured at various input pulse energies. Additionally, the output end face of the fiber was imaged onto a CCD camera to monitor the beam profile. The evolution of the output spectrum is shown in Fig. 3.33 along with the near field beam profiles measured at different output pulse energies that are mentioned for each spectrum. The spectrum at an output pulse energy of 60 µJ supports 81 fs Fourier

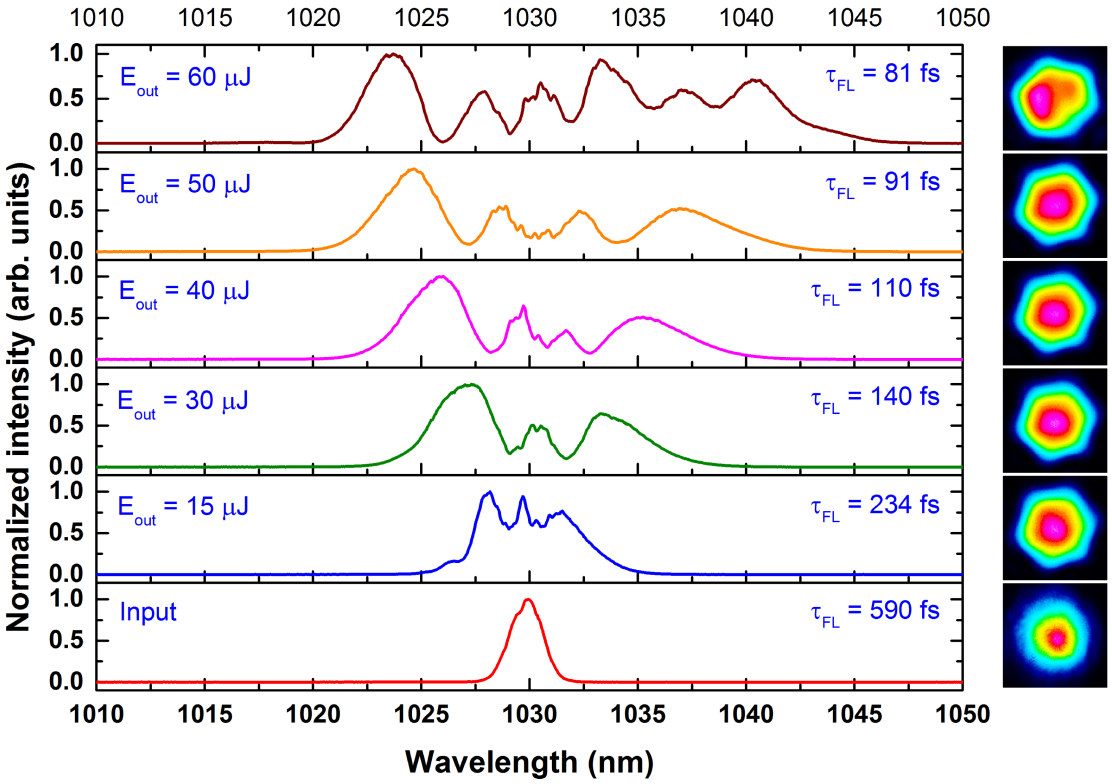

Figure 3.33: Spectral broadening in a 120 cm long Kagome fiber at different pulse energies and the corresponding near field beam profiles. E_{out} and τ_{FL} refer to the output pulse energies before the compressor and the Fourier transform-limited pulse duration respectively.

transform-limited pulses. However, the beam was slightly distorted which might be due to higher-order modes. For pulse energies higher than 60 µJ, strong spectral modulations appeared. Additionally, depolarization losses increased and distortions in the beam got worse. These effects are attributed to coupling between the fundamental mode and higher-order modes during the propagation through the fiber. Indeed, higher-order modes were visible at the reflected output of the polarizer. A detailed study of the mode-coupling is beyond the scope of the thesis.

Nevertheless, the output spectrum at 50 µJ output energy [Fig. 3.34(a)] was broad enough to support 92 fs Fourier transform-limited pulses [Fig. 3.34(b)]. GTI (Gires-Tournois Interferometer) laser mirrors (LAYERTECH) were used to compensate the nonlinear phase introduced by self phase modulation. The available dispersive mirrors had different negative group delay dispersion per bounce such as 250 fs^2, 450 fs^2, 550 fs^2, 900 fs^2 and 10 000 fs^2. A total dispersion of 34.1 ps^2 achieved with multiple bounces on those dispersive mirrors led to compression down to 130 fs as can be seen in the autocorrelation traces shown in Fig. 3.34(c). This corresponds to a compression factor of 7.5, compared to the input pulse shown in the same figure. The compression factor can probably be further improved by using a proper combination of GTI mirrors or using a grating compressor. Note that the

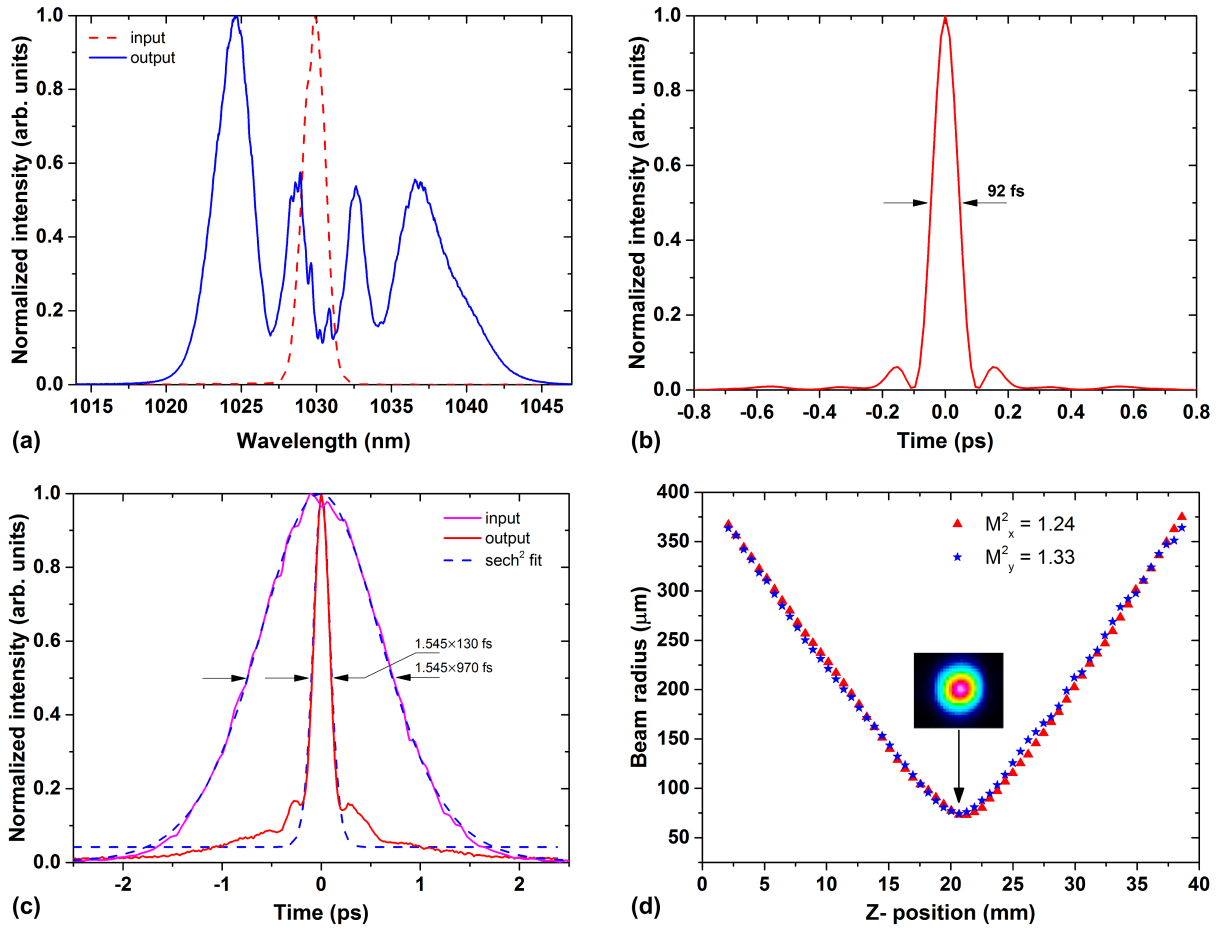

Figure 3.34: (a) Input and output spectrum for 50 µJ pulse energy at the output of the 120 cm long fiber, (b) Fourier transform-limited pulse profile corresponding to the output spectrum, (c) Autocorrelation profiles of the input and the compressed output pulses, and (d) M^2 measurement of the output beam after the compressor.

long pedestal of the compressed pulse is due to uncompensated higher-order dispersion since the GTI mirrors were optimum to compensate the group delay dispersion only. Because of the many bounces required on the GTI mirrors, the throughput of the compression was only ∼70 %. The beam quality was not far from the diffraction limit as can be seen in the M^2 measurement shown in Fig. 3.34(d).

Since most of the pulse compression experiments reported in the literature have used gas-filled Kagome fibers [66–69], relatively larger compression factors (up to 18 [67]) were possible but with increased complexity. Given the simplicity of the set up presented in this thesis, the pulse compression factor of 7.5 is remarkable. These pulses with few tens of microjoules pulse energy and close to 100 fs pulse duration are highly suitable for high harmonic generation, in particular at high repetition rates.

For spectral broadening at higher pulse energies, the peak intensity might be large enough

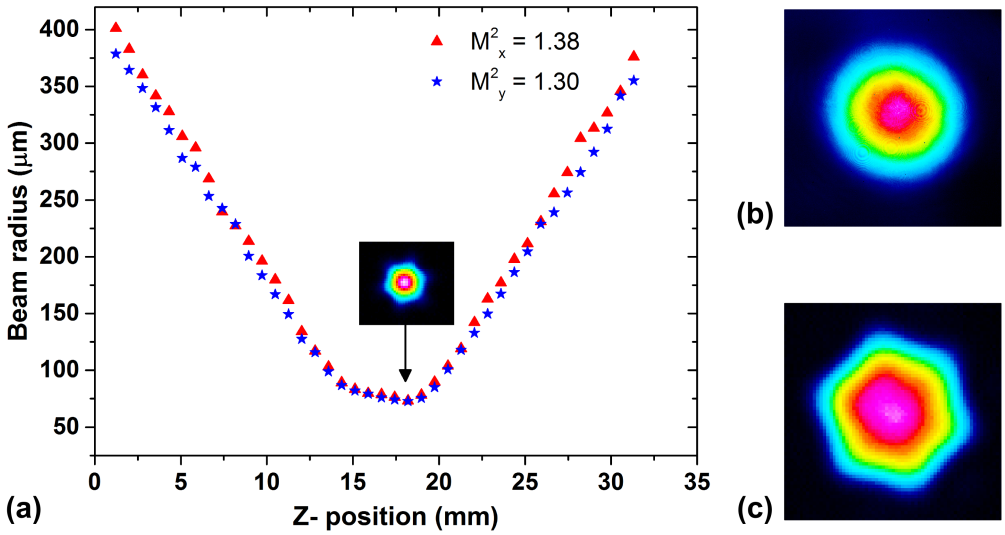

Figure 3.35: (a) M^2 measurement of the output beam with 100 µJ output pulse energy in the case of 1.1 ps input pulses along with the collimated beam profile (b) and the image of the fiber end face (c). Not to scale.

to ionize air inside the fiber which could distort the beam profile and introduce strong spectral modulations. In order to study this, the input pulses were chirped to ∼1.1 ps and the above-mentioned pulse compression experiment was repeated.

For the 1.1 ps input pulses, spectral broadening due to self-phase modulation was observed as before but no distortions were seen in the beam profile up to 100 µJ output pulse energy as clearly observed in the M^2 measurement of the output beam along with the near field beam profiles shown in Fig. 3.35. However, compared to the input pulse the output temporal profile was slightly distorted as shown in Fig. 3.36(a). At the same time, strong spectral modulations that were asymmetric and could not be associated with self-phase modulation appeared in the spectrum [Fig. 3.36(b)]. This may indicate air ionization inside the fiber. Nevertheless, the spectrum supports sub-50 fs transform-limited pulses. Beyond 100 µJ pulse energy inside the fiber, the spectrum was heavily distorted (no effort was made to compress the output pulses) and slight distortions were visible in the beam profile. This indicates that the long nonlinear interaction length or high peak intensity that can cause air ionization might be the cause of the spectral and the spatial distortions.

Finally, the chirped-pulse duration of input pulses was increased to 4 ps. Therefore, for the same peak power pulses with higher energies can be coupled into the fiber without spatial distortions and depolarization losses. The beam profiles as well as the autocorrelation profiles of the output pulses were monitored for various output pulse energies. As expected, more than 200 µJ pulses were coupled inside the fiber without any temporal and spatial distortions. As shown in Fig. 3.37, slight distortions in the temporal profile appeared when the output pulse energy reached 250 µJ. However, no sign of spatial distortions were observed in the beam profiles up to that level of pulse energy. This suggests that high

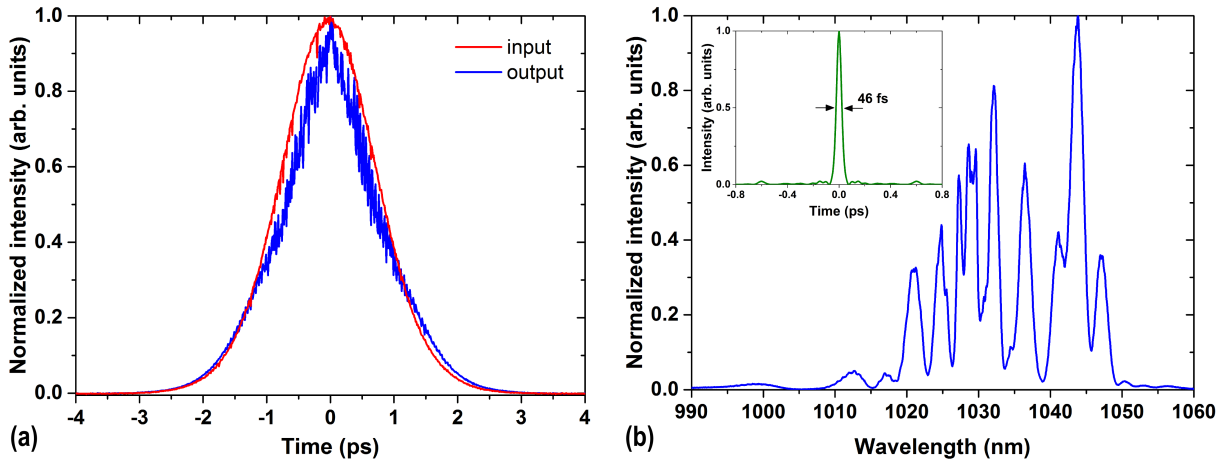

Figure 3.36: (a) Autocorrelation pulse profiles measured before (red) and after (blue) the fiber in the case of 1.1 ps (FWHM) input pulses. (b) Output spectrum for 100 µJ output pulse energy [inset: corresponding Fourier transform-limited pulse profile]. Strong spectral modulations and temporal distortions indicate that the input peak power or peak intensity is too high.

peak power or peak intensity was the limiting factor for scaling the pulse energy with the current experimental configuration and parameters.

In conclusion, scaling of pulse energy beyond 50 µJ in nonlinear pulse compression with air-filled Kagome fiber was hindered by the ionization of air due to the high peak intensity. This leads to distortions in the temporal, spectral or spatial profiles as well as significant depolarization losses. The threshold can be extended further by using a fiber with larger mode field diameter. Instead of air, noble gases such as Argon, Neon etc. with reduced nonlinearity can be used to achieve the spectral broadening that is required to reduce the pulse duration below 100 fs, as it has been demonstrated recently [67].

3.8 Summary

In conclusion, an ultrafast regenerative amplifier based on Yb:YAG thin-disk was built to amplify pulses from a fiber oscillator, generating sub-picosecond pulses with millijoule-level pulse energy. The amplifier was based on chirped-pulse amplification using a chirped-fiber Bragg grating stretcher and a grating compressor. The laser system can be operated at a repetition rate within the range of 10 kHz to 100 kHz. A maximum pulse energy of 2 mJ before compression was achieved at 10 kHz. Similarly, an average power up to 39 W was achieved at a pulse-repetition-rate of 100 kHz. After the compressor, millijoule-level pulses could be extracted at repetition rates as high as 25 kHz with a pulse duration close to 1 ps and a beam profile close to diffraction-limit.

Second and third harmonics of the laser were generated with BBO crystals. In type I phase-matching, a conversion efficiency of 70 % was achieved in the second harmonic whereas 53 % was achieved in the third harmonic. The maximum average power of the

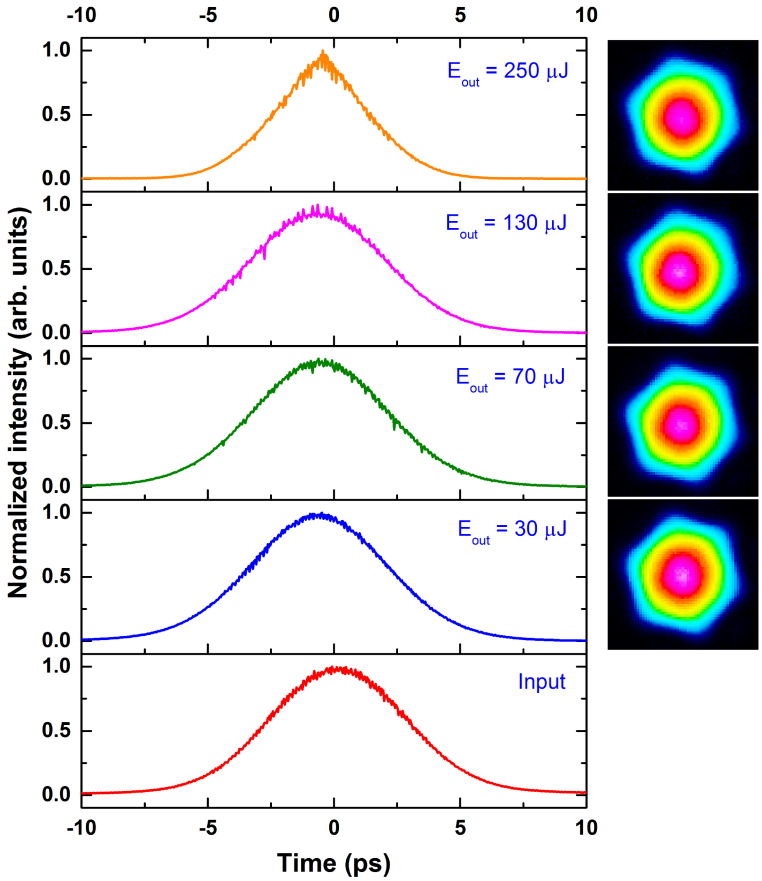

Figure 3.37: Autocorrelation pulse profiles measured at the output of the 120 cm long fiber at different output pulse energies, along with the corresponding near field profiles. The input pulse duration was 4 ps (FWHM). E_{out} refers to the output pulse energy measured before the compressor. At the maximum output pulse energy of 250 µJ, the pulse profile is slightly distorted around the peak but not the beam profile. Note that small amplitude fluctuations are always present in the pulse profiles, which are the measurement artifacts.

second and third harmonic beams were 16 W and 13 W respectively. The beam quality of the near-infrared beam was almost preserved after the frequency upconversion. In addition, excellent average power stability of the second and third harmonic beam demonstrated that the laser source is an ideal candidate for pumping OPCPAs in the visible and near infrared spectral range.

Furthermore, nonlinear compression of the amplified pulses was carried out in a hollow-core Kagome fiber. In a simple pulse compression experiment using Kagome fibers with air inside the core at atmospheric pressure, 900 fs pulses were compressed down to 130 fs with output pulse energy close to 50 µJ. Further shortening of pulses with higher pulse energy was limited by ionization of the air inside the fiber due to the high peak intensity. The pulse energy can be scaled up if a fiber with a larger mode field diameter is used, and further spectral broadening is expected if the fiber is filled with noble gases where

nonlinearity strength can be controlled by changing the gas type and pressure [61].

Scaling of the current laser system towards 100 W average power with millijoule level pulse energy i.e. at a pulse repetition rate of 100 kHz can be envisioned. After the regenerative amplifier, a multipass amplifier based on thin-disk technology can be used as a booster to scale the average power. Such a development will enable high-repetition-rate, few-cycle OPCPA sources with a few hundred microjoules pulse energies and accordingly the generation of high harmonics and isolated attosecond pulses with high photon flux. Indeed, a thin-disk multipass amplifier has been demonstrated with kW-level output average power and few millijoules pulse energy with sub-10 ps pulses [81]. Similarly, 30 mJ, 1.6 ps pulses at 10 kHz repetition rate i.e. with 300 W average power was demonstrated only with a thin-disk regenerative amplifier [78].

4 Numerical simulations of NOPCPA

As previously mentioned in chapter 1, optical parametric amplification (OPA) is an attractive alternative to the nonlinear pulse compression of Ti:Sa amplifiers for the generation of few-cycle pulses at high energy and high pulse repetition rates. This is mainly due to the several advantages offered by OPA in comparison to conventional laser amplifiers [18]. Among others, the thermal load is drastically reduced due to the fact that energy is not stored in the crystal and there are no non-radiative transitions. Therefore, the technique is favorable for the scaling of the average power and pulse repetition rate. Furthermore, scaling of the pulse energy is achieved by stretching the seed pulse before amplification and recompressed after the amplification in a similar way to the chirped-pulse amplification technique [3] in laser amplifiers. The technique, widely known as optical parametric chirped-pulse amplification (OPCPA), can be combined with noncollinear phase-matching [see section 2.4.6]. The noncollinear OPCPA (NOPCPA) allows the direct amplification of few-cycle pulses from a broadband oscillator at high repetition rates.

In recent years several few-cycle laser systems at high repetition rates ($\gg$10 kHz) have been built utilizing the NOPCPA technique [15, 16, 23, 99–102]. Scaling of the pulse energy keeping the repetition rate high (>100 kHz) has received increased interest, in particular, in strong field physics and attosecond science [17]. In strong field physics experiments, the amplified few-cycle pulses has to be focused in order to achieve high intensity and the maximization of the intensity at the target at a high pulse repetition rate is crucial because of the limited pulse energy available. Since the maximum achievable intensity at focus depends on the spatiotemporal quality of the pulses, spatiotemporal characterization of the few-cycle pulses has gained significant interest in recent years (see Ref. [103] and references therein for its importance in applications). In this regard, this chapter mainly focuses on the numerical modeling of noncollinear optical parametric chirped-pulse amplifiers (NOPCPAs) and the study of the spatiotemporal properties of the amplified pulses.

The details about the theory and fundamentals of OPA can be found elsewhere [53, 104, 105]. A brief summary of the fundamentals behind NOPCPA is provided in the previous chapter [see section 2.4.5]. In this chapter, numerical techniques to simulate NOPCPAs are briefly introduced in section 4.1 along with a concise summary of design parameters that are important to consider during the development of NOPCPA [section 4.2]. A NOPCPA system has been numerically modeled and the simulation results are presented in section 4.3. As the main focus of the chapter is on spatiotemporal distortions that may occur in NOPCPAs, the distortions have been studied numerically under different amplification conditions and general guidelines to minimize the distortions are discussed in section 4.4. Note that the results and analysis presented in section 4.4 and a part of the summary [section 4.5] have already been published as an article in 'Optics Express' [106].

4.1 Numerical techniques

As discussed in section 2.4.5, coupled-wave nonlinear equations describe the propagation of interacting waves in OPA. Analytical solutions of these equations are only possible for monochromatic, infinite plane waves in a collinear propagation and take the form of Jacobi elliptical functions [104, 105]. Otherwise, the solutions are derived under several restrictive approximations and assumptions. In many cases, it is important to include diffraction and walk-off effects. Furthermore, third-order nonlinear effects as well as thermal effects are also relevant in some cases. Numerical simulation is the only way to consider all such realistic effects.

There are two commonly used numerical methods to solve the coupled-wave nonlinear equations [29]. One is the split-step method in which the nonlinear medium is divided into sufficiently small steps and, in each step the propagation of the interacting waves is simulated by considering the linear and nonlinear interactions separately. The propagation, considering only linear effects such as losses, dispersion and diffraction is performed in the frequency domain whereas the propagation including only nonlinear processes such as second-order frequency mixing and nonlinear refractive index is carried out in the time domain [54,107,108]. Another is the Fourier-space method, where both linear and nonlinear effects are included simultaneously and the propagation is simulated in frequency domain. Each wave is decomposed into plane wave eigenmodes and the coupled-wave differential equations are solved for eigenmode amplitudes [109, 110]. The numerical code utilized in this work for simulating NOPCPAs is based on the latter approach and is briefly discussed in section 4.3.

4.2 Design considerations

The brief discussion of the fundamentals of OPA and the noncollinear phase-matching in section 2.4.5 clearly highlights its importance to amplify broadband pulses with very high gain. In order to exploit the full potential of the technique, the design requires carefully chosen parameters. In general, the performance of NOPCPAs depends on the characteristics of the pump pulses such as wavelength, pulse duration, pulse energy and peak intensity as well as on the nonlinear interaction determined by the type of nonlinear crystal, crystal length and phase-matching geometry. In this section, some critical parameters are briefly discussed along with a literature review of the guidelines to build broadband NOPCPAs.

Nonlinear crystal

The properties of the nonlinear crystal largely determine the parametric amplification process. The crystal has to satisfy several requirements for NOPCPAs. First of all, it has to be transparent for a wide spectral range covering all interacting waves. A large nonlinear optical coefficient as well as a high damage threshold are essential for high gain/conversion efficiency. In the case of small beam waists of the pump and the signal, large angular acceptance of the crystal is favorable in order to achieve high gain. Most importantly,

the crystal must support broadband phase-matching for the amplification of ultrashort pulses. The broadband phase-matching can be achieved in either a degenerate case or a noncollinear geometry as discussed in section 2.4.5.

Most of these requirements are fulfilled by crystals such as beta barium borate (β-BaB_2O_4, BBO), lithium triborate (LiB_3O_5, LBO), bismuth triborate (BiB_3O_6, BIBO), deuterated potasium dihydrogen phosphate (KD_2PO_4, DKDP) [4, 111–113] etc. in the visible and near infrared spectral range. Periodically poled crystals such as lithium niobate ($LiNbO_3$, PPLN), potasium titanyl phosphate ($KTiOPO_4$, KTP) [100] etc. are also commonly used in the near infrared. In the mid-infrared spectral range, a number of crystals such as Zinc germanium phosphide ($ZnGeP_2$, ZGP), Gallium selenide (GaSe), Silver thiogallate ($AgGaS_2$, AGS), Silver gallium selenide ($AgGaSe_2$, AGSE) [55,114] etc. are available with very wide transparency. For the amplification of broadband pulses centered at 800 nm, BBO is the most suitable crystal due to its high effective nonlinear optical coefficient and capability of supporting broad gain bandwidth, where parasitic effects are minimized for a wide range of signal wavelengths, if a particular phase-matching geometry is chosen [115].

Nonlinear interaction length

It has been discussed in section 2.4.5 that the parametric gain increases exponentially with $\sqrt{I_p} \times L$ which is also called the nonlinear interaction length. Even though longer crystals seem favorable for higher gain, the crystal length has to be chosen carefully for two particular reasons: First, the group-velocity mismatch between the signal and the idler pulses (that eventually reduces the gain bandwidth) introduces temporal walk-off between the pump and the signal pulses while propagating through the crystal. This increases with the crystal length and tends to reduce the conversion efficiency depending upon pulse duration. Next, spatial walk-off effects increase with crystal length and can severely limit the interaction length depending upon the beam sizes and the angle between the interacting beams. This implies that the crystal length has to be optimum in order to minimize the temporal and spatial walk-off and at the same time, to achieve reasonable gain and conversion efficiency.

Thin crystals are always preferred in ultra-broadband amplification in order to reduce phase mismatch ($\Delta k \times L$), thus increasing the gain bandwidth. The lowering of parametric gain due to short propagation distances can be compensated by using a high pump intensity which is only limited by the damage threshold of the crystal. Since the damage threshold decreases with decreasing pulse duration, the combination of the thin crystals and the picosecond pump pulses with high peak intensity is the most appropriate approach to amplify broadband pulses. In addition, thin crystals help to reduce spatial as well as temporal walk-off, otherwise critical for small beams and short pulses respectively. In the case of a noncollinear configuration, thin crystals minimize spatial walk-off due to the geometry.

Gain bandwidth

One of the most striking characteristics of OPA is the broad gain bandwidth which strongly depends on wave-vector mismatch. A few conditions and tricks to obtain/optimize the gain bandwidth (some of which has been discussed earlier) are summarized as follows.

- The degenerate OPA offers a very broad gain bandwidth due to the group velocity-matching of the signal and the idler.
- Noncollinear geometry provides an additional degree of freedom to optimize the gain bandwidth by matching the group-velocities of the signal and the idler thereby avoiding the phase-mismatch up to the first order [28].
- Ultra-broad bandwidth is possible if the phase-mismatch is minimized up to the second order by using angularly dispersed signals [116, 117].
- The use of thin crystals, pumped at high intensity allows optimizing gain bandwidth as discussed in the previous section.
- Multiple pump beams (at either same or different wavelengths) can be utilized to increase the amplification bandwidth [118, 119].

phase-matching geometry

Birefringent phase-matching has been widely used to minimize the wave-vector mismatch. Walk-off of the extraordinary beam away from the optical axis in negative uniaxial crystals is known to limit the conversion efficiency and to degrade the beam quality in the parametric amplification processes. This is critical in the case of long crystals.

In NOPCPAs, walk-off effects can be considerably compensated if the signal beam is positioned on the side to which the pump beam walks off [115] as shown in Fig. 4.1(a), for a negative uniaxial crystal in type I phase-matching. The geometry is often called Poynting vector walk-off compensating (PVWC) or simply walk-off compensating (WOC) geometry. The walk-off compensation significantly improves the beam quality. However, second harmonics of the signal as well as the idler can be phase-matched which introduces modulations in the amplified spectrum and may reduce output signal and idler energies. On the other hand, if the signal beam is positioned on the side from which the pump beam walks away [see Fig. 4.1(b)], the configuration is called non-walk-off compensating (NWOC) geometry or tangential phase-matching. The NWOC geometry, in general, doesn't suffer from parasitic second harmonics and therefore, is preferable for achieving a better output spectrum whereas WOC geometry is favorable for better beam quality [115]. After all, the choice of the phase-matching geometry is based upon the application of the amplified signal/idler.

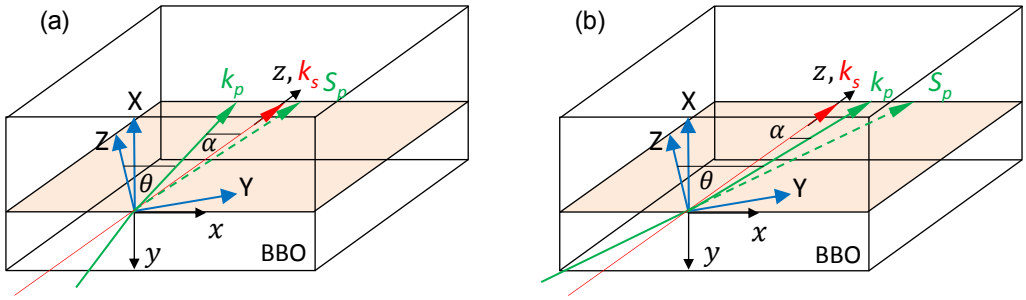

Figure 4.1: Illustration of type I phase-matching geometries in a BBO crystal: (a) walk-off compensating (WOC) geometry and (b) non-walk-off compensating (NWOC) geometry. X, Y, Z: crystal axes of the BBO crystal; x, y, z: Cartesian co-ordinate system used in the calculations; k_s: signal wave vector that is incident perpendicularly to the crystal face, k_p: pump wave vector at an internal angle α with the signal wave vector and at the phase-matching angle θ with the optical axis (Z), and S_p: Poynting vector of the pump. All the vectors that relate to the laser propagation lie in the (Y, Z) or (x, z) plane. Not to scale.

Gain saturation

Equation 2.85 shows that the parametric gain of an optical parametric amplifier in the high-gain approximation grows exponentially. The exponential growth of the signal will stop beyond a certain point because of the limited pump pulse energy available in the nonlinear interaction. Then, a linear growth of the signal continues as long as the pump intensity is higher than that of the signal and the idler. The regime of linear gain is often considered as gain saturation. Beyond this regime, the intensities of the signal and the idler are comparable to the pump intensity and back conversion of the signal and the idler to the pump takes place. The conversion of the signal and the idler to the pump and vice versa continues further which introduces strong modulations in spatial and temporal profiles of the interacting fields. For this reason, strong gain saturation or back conversion may not be useful. Nevertheless, gain saturation improves pulse-to-pulse stability and helps to minimize the spectral narrowing effects by amplifying the wings of the spectrum. The degree of gain saturation depends on several parameters such as pump intensity, crystal length, the effective nonlinear optical coefficient and the ratio of the intensities of the pump and the signal.

Signal-to-pump pulse energy ratio

The ratio of the pulse energy of the input signal to the pump (for given beam sizes and pulse durations) is a critical parameter in NOPCPAs. If the seed energy is low, gain saturates in a longer crystal which limits the gain bandwidth and lowers the extraction efficiency. In the case of higher seed energy, saturation occurs in a shorter crystal resulting in low gain but higher extraction efficiency. In addition, a very low signal-to-pump pulse energy ratio leads to an increased level of superfluorescence. Therefore, it is crucial to find an appropriate ratio in order to optimize the gain, extraction efficiency and if applicable, the

superfluorescence.

The well-known approach for optimization of gain and extraction efficiency is to build multiple amplification stages: the first amplifiers with high gain and a last amplifier with high extraction efficiency. This can be achieved by using a low signal-to-pump pulse energy ratio in the first stage and a high signal-to-pump pulse energy ratio in the second stage. Analytical calculations have shown that a signal-to-pump pulse energy ratio of 10^{-3} in a single stage amplifier ensures high gain and high conversion efficiency simultaneously [120].

Signal-to-pump pulse duration ratio

Because of the instantaneous nature of the parametric amplification process, temporal overlap between the pump and the signal pulses is necessary. This is achieved by proper synchronization of the pulses. The synchronization techniques are typically divided into two categories: active and passive. In active synchronization, the pump and signal sources are actively synchronized using electronics [121, 122] whereas in passive synchronization, signal and the seed for the pump laser are derived from the same source [23]. In addition to synchronization, the ratio between the pump and the signal pulse durations is an important parameter to consider, which influences amplification. This is especially noticeable for Gaussian-shape of the temporal profiles because the pump intensity, varying over time, induces different gain across the pulse.

An optimum signal-to-pump pulse duration ratio is crucial to optimize the amplified spectrum and the pump-to-signal energy conversion efficiency. If the signal-to-pump pulse duration ratio is close to 1, the wings of the spectrum will experience less gain compared to the center leading to spectral narrowing. On the other hand, small signal-to-pump pulse duration ratio decreases the temporal overlap and reduces the pump-to-signal energy conversion efficiency. This has been studied using numerical simulations [54, 118], which suggest that signal-to-pump pulse duration ratio between 0.3 and 0.6 in the case of Gaussian pulses optimizes the effect of spectral narrowing with reasonable conversion efficiency. It should be noted that the optimum ratio strongly depends upon the shape of the temporal profiles, crystal length and pulse durations.

Superfluorescence

Even if an optical parametric amplifier is not seeded with a signal, fields are spontaneously generated at signal and idler frequencies from the downconversion of a pump photon. Such spontaneous photons are referred to as superfluorescence or optical parametric fluorescence. This quantum phenomenon has been studied by using a quantum mechanical model of OPAs [123]. Superfluorescence is an unwanted effect, occurs within the pump pulse and is proportional to the pump intensity. Studies have suggested that it can be suppressed by avoiding very high parametric gain, optimizing the temporal overlap between the pump pulse and the signal pulse, and using tight spatial filtering between the amplification stages [108].

Superfluorescence decreases the energy, stability and coherence of the output signal as

well as degrades the temporal contrast of the compressed pulses. In a multistage amplifier, these effects can significantly be minimized by optimizing the temporal chirp in the seed (i.e. changing the signal-to-pump pulse duration ratio) at each stage [124].

Parasitic effects

As parametric processes are largely determined by phase-matching, second harmonics of the signal as well as the idler can, in principle, be phase-matched with the corresponding fundamentals during the process of parametric amplification. Such effects, one particular type of parasitic effects, may cause unwanted loss of energy and introduce strong modulations in the amplified spectrum [115] which are mainly determined by the phase-matching geometry, the type of nonlinear crystal as well as the pump and signal wavelengths. The corresponding modulations in the spectral phase may influence the pulse compression. In the case of green-pumped BBO crystals in a type I phase-matching configuration, it has been shown that a NWOC geometry is free from parasitic effects for the spectral range below 1129 nm unlike the WOC geometry in which a parasitics-free spectral range exists below 860 nm [115].

Thermal effects

As previously discussed, OPA is known as a potential amplification technique for scaling average power and pulse repetition rate. Due to the absence of energy storage in the nonlinear crystals unlike conventional laser amplifiers, the thermal load is drastically reduced. Most of the OPAs at an early stage of development were limited in output average power and experienced negligible thermal effects. However, in recent years, the rapid development of high average power laser systems that are suitable to pump NOPCPAs allows scaling of the output average power > 100 W [101]. Such high average power NOPCPAs may suffer from heating of the crystal due to the intrinsic absorption of the interacting waves that depends upon the transparency of the crystal in the wavelength range of interest. Indeed, it has recently been experimentally studied in a high power NOPCPA pumped at 515 nm with the amplified spectrum spanning from 700 to 1000 nm and confirmed that the absorption of the idler by the BBO crystal and absorption of coatings at 515 nm is responsible for heating of the crystal [125]. It is expected that the average power scaling of NOPCPAs may be hindered by thermal issues beyond output powers of a few hundreds of watts [126]. Considering the negligible thermal load in low-power NOPCPAs, thermal effects have not been included in the simulations presented in this thesis.

Spatiotemporal distortions

In recent years, spatiotemporal characterization of ultrashort pulses has received an increased interest. For some applications of ultrashort pulses e.g. in strong field physics and attosecond science, couplings between the spatial and temporal coordinates of the electric field is problematic because they may introduce distortions, often leading to pulse broadening and the reduction of peak intensity at focus.

NOPCPAs are susceptible to spatiotemporal couplings, which are an intrinsic property of a noncollinear geometry. The spatiotemporal distortions and their impacts are known since the introduction of the amplification technique [28, 127]. In particular, tilted pulse fronts (i.e. the plane of the maximum intensity of the pulse envelope) of the pump with respect to signal create a tilted gain distribution which leads to spatiotemporal distortions in the amplified signal. The extent of these distortions depends upon several design parameters and amplification conditions which will be discussed in section 4.4 in detail.

4.3 Modeling of NOPCPA system

In this section, a NOPCPA system is numerically modeled and the output characteristics are reported. Direct amplification of few-cycle pulses from an oscillator is possible due to the broad amplification bandwidth offered by noncollinear phase-matching. The choice of nonlinear crystal and the pump laser depends upon the spectrum of the pulses to be amplified. For example, for the amplification of pulses from a broadband oscillator emitting sub-6 fs pulses centered around 800 nm, the second harmonic of Yb-doped lasers around 515 nm is highly suitable to pump a NOPCPA based on BBO. At the Max Born Institute in the last few years, there has been remarkable progress in the development of a NOPCPA based, high repetition rate (>100 kHz), few-cycle laser system [17, 23]. So far, Yb-doped fiber amplifiers have been used as pump lasers which has limited the output energy of the few-cycle pulses to around 10 µJ at repetition rates of 400 kHz or higher. In order to scale up the pulse energy beyond 100 µJ at the output of the NOPCPA system, a new pump laser based on thin-disk technology has recently been installed. The NOPCPA system is currently under development[1]. A brief overview of the multistage NOPCPA system including the seed and the pump laser will be presented in the following section, followed by numerical simulations of the three amplification stages.

All the numerical simulations have been performed utilizing the numerical code, Sisyfos (SImulation SYstem For Optical Science) [29,128]. Prior to this work, this code was already utilized in several works [116, 129–131], verifying its potential to simulate second-order frequency mixing, including the effects of pump depletion, walk-off, dispersion, diffraction, parasitic effects, and thermal effects. The program solves the coupled-wave equations in three dimensions in Fourier space. In the case of parametric amplification, it calculates the complex electric field distribution of the amplified signal, pump and idler beams, as well as parasitic second harmonics of the signal and the idler (optional).

4.3.1 Block diagram

The schematic of the multistage NOPCPA system is shown in Fig. 4.2. An ultrabroadband Ti:Sa oscillator (Venteon, Pulse:One) emits an octave-spanning spectrum supporting

[1] At the end of the thesis writing, the amplification stages have been set up, achieving an output pulse energy of 210 µJ at a repetition rate of 100 kHz. The amplified pulses have been compressed down to ∼ 7 fs using chirped mirrors.

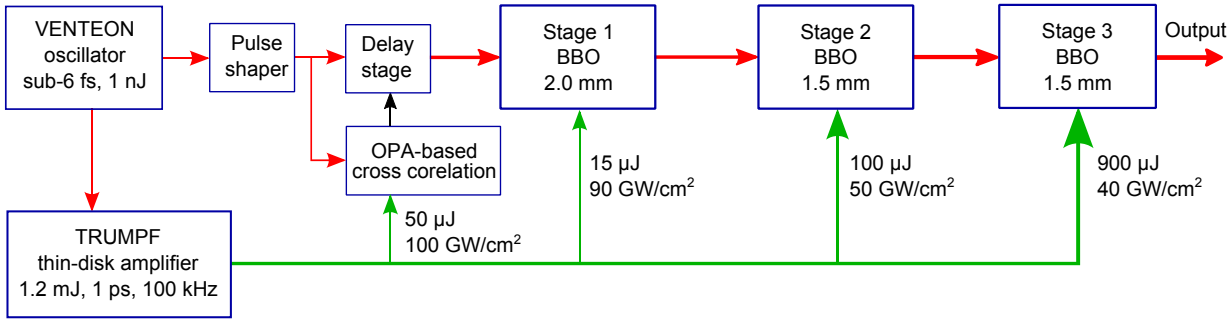

Figure 4.2: Schematic of the NOPCPA system currently under development at the Max-Born-institute. An ultrabroadband oscillator (Venteon, Pulse:One) seeds both the pump and the parametric amplifiers. The delay between the pump and seed pulses is controlled by adjusting a delay stage, which is operated by the control signal that is generated from an additional OPA stage (the scheme is similar to the one described in Ref. [132]). The seed pulses are amplified in three amplification stages based on BBO crystals, which are pumped by a thin-disk amplifier (from TRUMPF Scientific). The amplified pulses are compressed using chirped mirrors (not shown). The pulse compression is optimized with the help of a pulse shaper, compensating higher order dispersion.

sub-6 fs pulses. A portion of the output spectrum around 1030 nm has been used to seed the thin-disk amplifier whereas the rest of the output serves as a seed for the NOPCPA stages. That means the signal and the pump are optically synchronized, also called passive synchronization. A separate OPA stage has been developed in order to characterize and actively control the delay between the seed and the pump pulses [132]. In addition, a spatial light modulator-based pulse shaper (MIIPS Box 640 P, from Biophotonics Solutions Inc.) is used to facilitate the pulse compression by manipulating the spectral phase of the seed pulses.

The pump laser (TRUMPF Scientific) consists of fiber Bragg grating stretcher, several fiber pre-amplifiers and a regenerative amplifier cavity with Yb:YAG thin disk as gain medium. The pulses, compressed by a grating compressor are frequency doubled in a LBO crystal. The output pulses centered at a wavelength of 515 nm have a duration of approx. 1 ps (FWHM), with $\sim$ 1.2 mJ pulse energy at a pulse repetition rate of 100 kHz. This corresponds to an output average power of 120 W at 515 nm. With such a high power, high energy pump laser, the aim is to generate few-cycle pulses with high energy (>100 µJ) at a pulse repetition rate of 100 kHz (>10 W average power). This implies that the laser system offers high peak power and high average power simultaneously.

The output of the pump laser is split into four, out of which the first output is used to pump the delay-control-OPA and the other three pump three different amplification stages as indicated in Fig. 4.2. The details about these amplification stages including the characteristics of the output signal from each stage are discussed in the following sections.

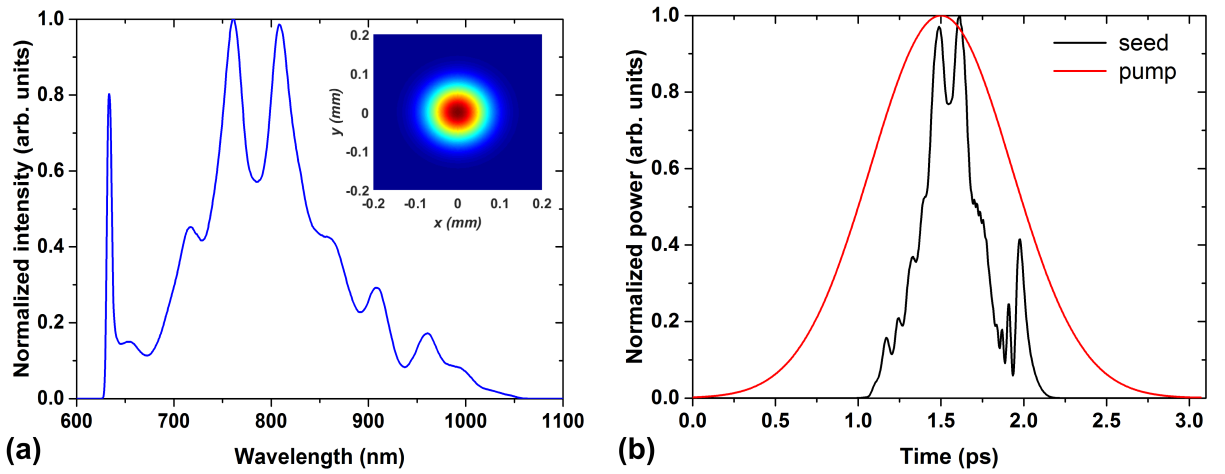

Figure 4.3: (a) Spectrum of the seed, which was measured at the output of the ultrabroadband Ti:Sa oscillator using a spectrometer (Avantes) [inset: calculated beam profile of the seed and pump, assuming a Gaussian shape]. (b) Temporal profiles of the seed and the pump used for the first amplification stage. The pump pulse is assumed to be Gaussian with FWHM pulse duration of 1 ps. The seed pulse is calculated from the measured spectrum and then stretched using group delay dispersion numerically.

4.3.2 First amplification stage

The first amplification stage is based on a 2 mm BBO crystal in type I phase-matching. The effective nonlinear optical coefficient is taken to be 2 pm/V for all interacting beams including parasitic second harmonics. Phase-matching angles are calculated for the pump wavelength of 515 nm and signal center wavelength of 850 nm. Walk-off compensation phase-matching geometry [see Fig. 4.1(a)] has been chosen in order to minimize spatiotemporal couplings in the amplified output signal originated due to spatial walk-off. The broad band phase-matching condition implies that the pump and the signal propagate at an angle of 24.45° and 26.45° with respect to the optical axis of the crystal respectively. Parasitic second harmonics of the signal and the idler have also been included in the simulation.

Figure 4.3(a) shows pulse spectrum at the output of the oscillator that seeds the first amplification stage after stretching. Seed pulses were numerically stretched up to ≈ 600 fs. The pump pulse-shape was assumed to be Gaussian with a pulse duration of 1 ps (Fourier transform-limited) at FWHM which is shown in Fig. 4.3(b) along with the stretched seed pulse. A pump intensity of 90 GW/cm^2 was chosen which corresponds to a beam waist of ~ 100 µm (half width at $1/e^2$ of peak intensity) for a pulse energy of 15 µJ. The spatial profiles of the pump and the signal are assumed to be Gaussian and both have the same beam waists. For completeness, the profile is shown in the inset of Fig. 4.3(a).

According to the calculation, the signal is amplified from 0.3 nJ to 1.331 µJ which corresponds to a gain of 4436 and a pump-to-signal energy conversion efficiency of 8.9 %. The simulation program provides the three-dimensional complex electric field distribution of

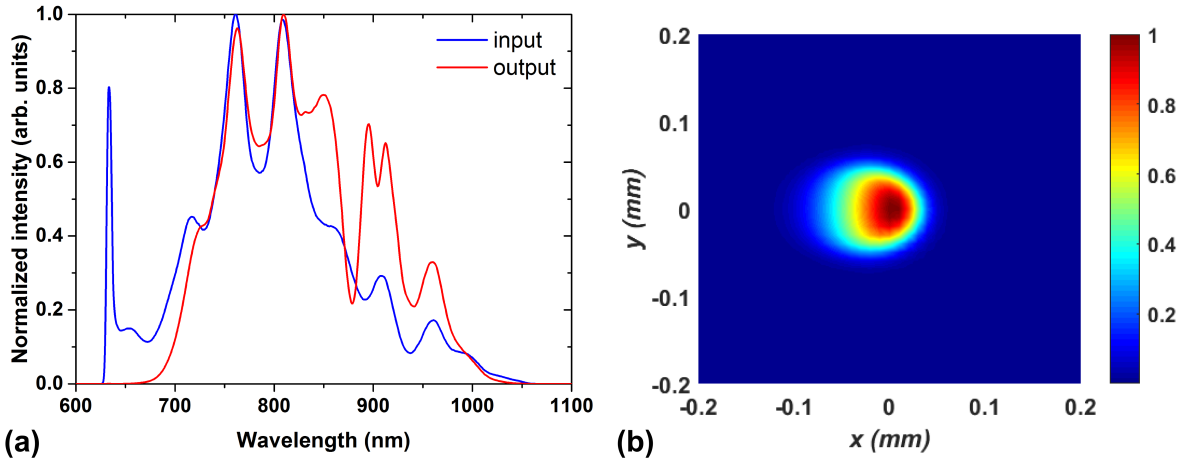

Figure 4.4: (a) Spectrum of the seed and the output signal, and (b) near field profile of the amplified signal in the first amplification stage. A dip in the output spectrum around 880 nm is due to the parasitic second harmonics of the signal. Additionally, the output beam profile shows signs of spatial narrowing.

the output signal from which the amplified output spectrum and beam profile are computed. Figure 4.4(a) shows the input and output spectrum of the signal. A strong dip in the amplified spectrum around 880 nm is attributed to depletion due to parasitic second harmonics of the signal that is inherent to the walk-off compensating geometry. The near field profile of the output signal is shown in Fig. 4.4(b), which suffers from spatial narrowing that is mainly due to the Gaussian shape of the pump beam.

4.3.3 Second amplification stage

The second amplification stage is similar to the first one except that it is seeded with the output from the first stage after magnifying the beam in order to match the beam waists of the seed and the pump in the second stage. The pump pulse energy is increased to 100 µJ which corresponds to a beam waist of $\sim$ 350 µm for a pump intensity of 50 GW/cm^2. In addition, the crystal length is reduced to 1.5 mm to avoid strong gain saturation. The temporal as well as the spatial profiles of the pump are assumed to be Gaussian.

This stage amplifies the signal to 15.28 µJ with a corresponding gain of 11.5 and pump-to-signal energy conversion efficiency of 13.9 %. The average spectrum of the amplified output signal along with input spectrum is shown in Fig. 4.5(a). As can be seen clearly, the whole bandwidth of the input signal is amplified with minimal spectral modulations and enhanced wings of the spectrum. Similarly, the near field profile of the output signal, as shown in Fig. 4.5(b) is slightly asymmetric which is due to the enhancement of the asymmetry present in the seed. In general, the asymmetry in the amplified beam profile is common in NOPCPAs due to noncollinear geometry.

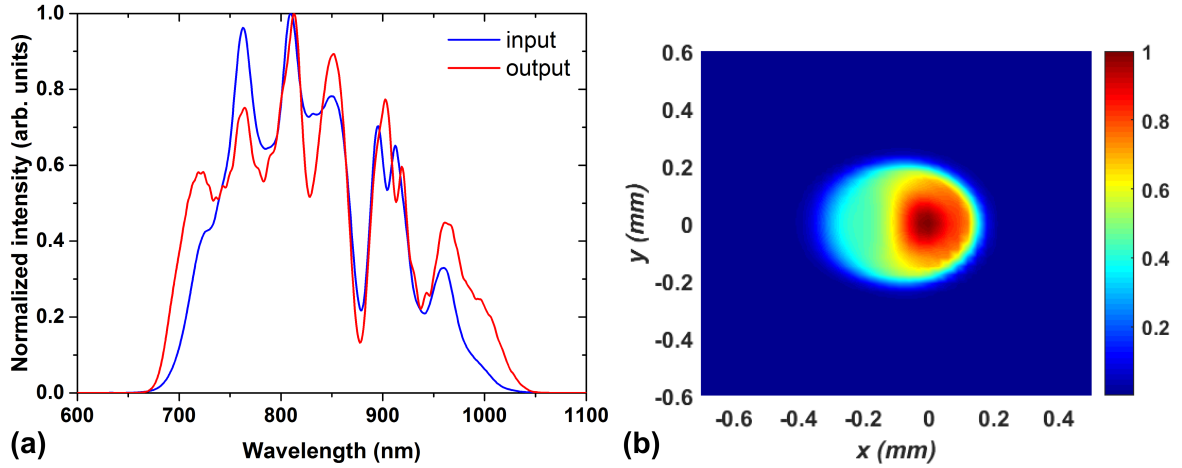

Figure 4.5: (a) Calculated input and output spectrum of the signal, and (b) near field profile of the output signal in the second amplification stage. The whole bandwidth of the seed spectrum is amplified along with the enhancement of the wings.

4.3.4 Third amplification stage

The last amplification stage is designed to extract energy more efficiently with low parametric gain. A 1.5 mm long BBO crystal is pumped at a peak intensity of 40 GW/cm^2 with a pulse energy of 900 µJ, which corresponds to a beam waist of 1150 µm. Because of the larger beam size, spatial walk-off effects are expected to be lower. Therefore, the phase-matching geometry is chosen to be non-walk-off compensating which avoids parasitic effects in the spectral range of interest. Phase-matching and noncollinear angles are calculated for broadband phase-matching as mentioned in the first amplification stage.

A parametric gain of 9.5 is achieved in this stage with pump-to-signal energy conversion efficiency of 14.5 %. The output energy per pulse is 145.4 µJ. The average spectrum of the input and the output signal are shown in Fig. 4.6(a). It can be clearly seen that the full bandwidth has been amplified and no additional spectral modulations are observed. The near field beam profile of the amplified signal, as shown in Fig. 4.6(b) is asymmetric in the opposite direction compared to the input beam profile. This is mainly due to the spatial walk-off effects dominating in the non-walk-off compensating phase-matching geometry.

Note that the second and third amplification stages have similar gain and conversion efficiency. In principle, these stages can be merged and designed as two-stage NOPCPA system. However, the extraction efficiency has to be significantly increased in the last stage, which introduces strong spatiotemporal distortions in the amplified signal and accordingly reduces the maximum achievable peak intensity at focus (see section 4.4).

The output from the third amplification stage has been further characterized by calculating the spectral phase at the center of the near field profile utilizing the complex electric field distribution. First, a third-order polynomial was fitted to the total spectral phase and then the fitted phase was subtracted from the total phase. The residual phase obtained in that way is shown in Fig. 4.7(a) along with the total signal spectrum. The residual phase

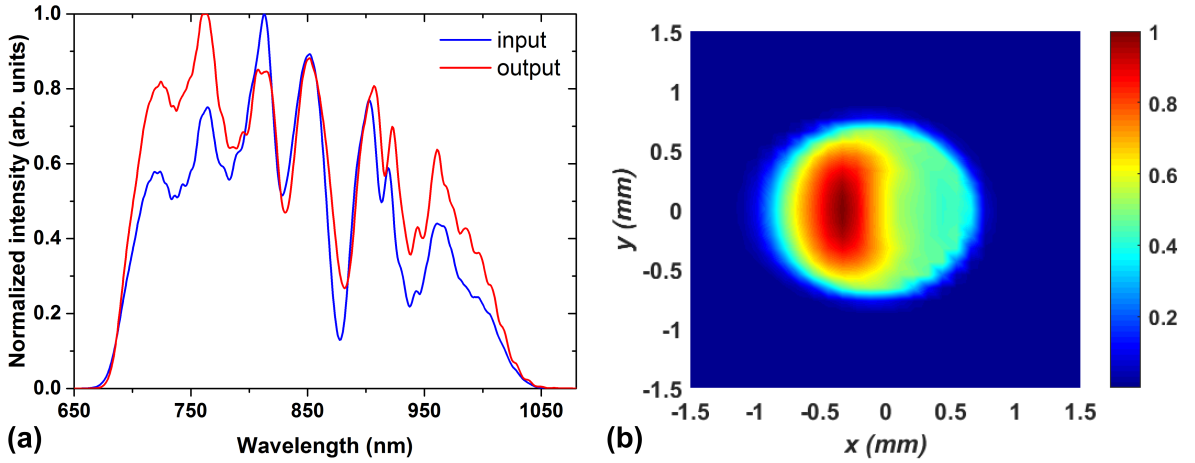

Figure 4.6: (a) Calculated input and output pulse spectrum, and (b) the output near field profile of the signal in the third amplification stage. The full bandwidth of the input signal is amplified in a non-walk-off compensating geometry without additional spectral modulations.

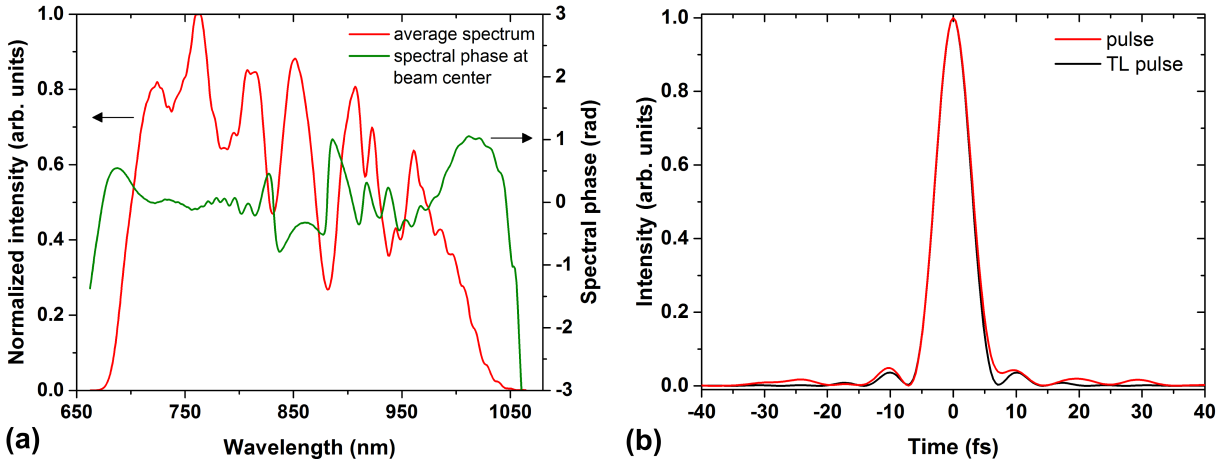

Figure 4.7: (a) Average spectrum of the output signal and the residual spectral phase at the center of the beam profile when the phase up to third order is compensated. (b) Corresponding pulse profile along with the Fourier transform-limited pulse with a duration of 6.3 fs (FWHM). The pedestals present in the transform-limited pulse profile are due to spectral modulations, in particular, narrow features in the spectrum leads to long pedestals. Satellites emerge due to phase jumps and uncompensated spectral phase in general.

refers to the higher-order phase terms that should be compensated in order to achieve Fourier transform-limited pulses. Figure 4.7(b) shows the corresponding pulse profile along with the Fourier-transform limited pulse profile. Pulse pedestals can be clearly seen in the pulse profiles which are due to the modulations in the output spectrum and the corresponding phase-jumps in the residual spectral phase. Nevertheless, the amplified spectrum supports Fourier transform-limited pulse duration of 6.3 fs (FWHM) which contains <3 optical cycles.

Since the numerical program has considered all realistic phenomena in parametric amplification processes and solved the coupled-wave nonlinear equations in three dimensions, the results serve as important guidelines for the development of NOPCPA systems. Above all, the complex field distribution of the amplified signal can directly be used for characterizing spatiotemporal distortions present in the field distribution. Such characterization is particularly important for few-cycle pulses where maximization of the peak intensity with limited pulse energy available at high pulse repetition rate is crucial. A systematic study of spatiotemporal distortions and possible ways to minimize them in NOPCPAs will be the main focus of the following section. The simulation results and analysis presented hereafter have already been published [106].

4.4 Spatiotemporal distortions in NOPCPA

Widely used components in ultrafast optics such as prisms, gratings and lenses all introduce spatiotemporal couplings, i.e. couplings between the spatial and temporal properties of the electromagnetic field [133]. Even the propagation of ultrashort pulses in vacuum may introduce spatiotemporal couplings, due to the wavelength-dependent diffraction of a beam with a finite size [134]. A rigorous theory has recently been developed [135] and several experimental techniques have been implemented to measure first-order spatiotemporal couplings [133]. In the case of NOPCPAs, spatiotemporal couplings naturally occur due to the noncollinear geometry. Since such couplings, often called spatiotemporal distortions or aberrations, degrade the achievable pulse duration and the peak intensity at focus, it is important to address this issue if NOPCPAs are to be used in research fields such as attosecond science, where a high peak intensity needs to be achieved with a limited available pulse energy when one operates at high repetition rates. Pioneering work by Bromage *et al.* [26] demonstrated experimentally that angular dispersion of the amplified signal beam can be eliminated if the NOPA is operated at a particular noncollinear angle, the so-called "magic angle" [136], where the group velocities of the signal and the idler beams are matched, leading to a broad amplification bandwidth. The experimental findings were supported by a simple numerical model. Numerical simulations supported by experimental results reported by Zaukevičius *et al.* [27] pointed out that at the magic angle pulse front tilt is still present, despite the vanishing angular dispersion, and can only be avoided by matching the pulse fronts of the pump and the signal. In that respect, experimental efforts to eliminate the pulse front tilt have been reported in the literature (see for example [137, 138]).

In this section, a detailed numerical study of spatiotemporal distortions in NOPCPAs is presented, utilizing three-dimensional (3D) simulations. The studied NOPCPAs are based on amplification in BBO crystals under type I phase-matching. In all cases the amplifier is pumped at 515 nm and seeded with a broad-band pulse centered at 850 nm. The aim of the study is to characterize the spatiotemporal properties of the amplified field and to find guidelines for optimum amplifier design. It is investigated how spatiotemporal distortions in the amplified beam depend on experimental conditions such as noncollinear angle, pump beam size, phase-matching geometry, pulse front matching, and distortions in the seed beam and how they are related to gain saturation and back conversion. In section 4.4.1, different sources of spatiotemporal distortions in NOPCPAs are briefly reviewed. The numerical tools to characterize the distortions are introduced in section 4.4.2. In section 4.4.3, a single stage NOPCPA is analyzed for different noncollinear angles and beam sizes, and for different phase-matching configurations. Next, the influence of pulse-front matching and gain saturation is analyzed. In particular, the impacts of spectral shaping of the signal pulse and spatial shaping of the pump beam are analyzed in saturated amplifiers. In addition, it is discussed how spatiotemporal distortions from a first amplification stage influence a second amplification stage. Finally, a series of recommendations for the optimal design of a BBO-based NOPCPA are given based on the simulation results.

4.4.1 Background

The origins of spatiotemporal distortions in NOPCPAs have been known since the introduction of the technique [28]. The pulse front of the signal is shaped by the spatiotemporal distribution of the gain, so unless the pulse front of the pump is tilted to match the signal, the signal pulse front will end up being tilted with respect to its propagation direction. The combination of tilted pulse front and temporal chirp also leads to spatial chirp. In addition, phase-matching can contribute to further pulse front tilt through its direct impact on angular dispersion [26]. Detuning the noncollinear angle from the magic angle leads to an angularly dispersed amplified signal beam and accordingly tilts the pulse fronts. The effect is dominant for relatively small beam sizes and large detuning angles.

In addition to these effects, birefringence of the crystal causes spatial walk-off of the extraordinary beam. For example, in BBO under type I phase-matching, the pump beam shifts away from the optical axis. Furthermore, during propagation the pump and the signal beams get separated from each other in the walk-off plane due to the noncollinear configuration. Such spatial walk-off effects, in combination with temporal walk-off due to pump versus signal group-velocity mismatch, introduce additional spatiotemporal couplings. The spatiotemporal couplings due to the combined birefringent and temporal walk-off are present even if the pulse fronts of the pump and the signal are matched (e.g. in collinear amplification).

An analytical study of spatiotemporal distortions in NOPCPAs is difficult, since the coupled-wave equations for three-wave mixing can be solved analytically only under very restrictive assumptions or approximations. Analytical expressions for the analysis of first-order spatiotemporal distortions have been presented in [27]. However, for a complete

study of spatiotemporal distortions under more realistic amplification conditions, numerical methods are indispensable. In this work, the nonlinear coupled-wave equations are solved in three dimensions, which allows studying all possible spatiotemporal distortions in NOPCPAs over a diverse range of parameters.

4.4.2 Numerical model and analysis tools

NOPCPAs are simulated with Sisyfos code as described in section 4.3. After modeling the amplifier, the complex electric field of the amplified signal in three dimensions (x, y and t) is used for post-processing, where x and y refer to the transverse spatial coordinates and t is the time.

For simplicity, the study of spatiotemporal couplings is often limited to the first-order. The definitions for first-order couplings introduced in this section and analyzed in the following one are focused in couplings occurring between the walk-off plane spatial coordinate (taken as the x-coordinate) and time. These results can be easily extended to the orthogonal y-coordinate. As the electric field can be represented in four different domains: (x, t), (x, ω), (k_x, t) and (k_x, ω), where ω and k_x are angular and spatial frequencies, respectively, there are eight possible couplings when both amplitude and phase are considered. They are connected via Fourier transformations [135], and only two of them are independent. From these eight first-order distortions, pulse front tilt, spatial chirp and angular dispersion are most commonly encountered.

The pulse front tilt, which is the angle between the pulse front and the phase front, may be characterized by the slope of the profile in the (x, t) domain,

$$\tan\gamma = c\left(\frac{dt_0}{dx}\right)_{x_0}, \tag{4.1}$$

where γ is the pulse front tilt angle, c is the speed of light, x_0 is the center of the beam profile, and t_0 is the center of gravity of the temporal profile at a particular position. The pulse front tilt can arise from angular dispersion according to [139],

$$\tan\gamma_0 = c\left(\frac{dk_{x0}}{d\omega}\right)_{\omega_0} = -\lambda_0\left(\frac{d\epsilon}{d\lambda}\right)_{\lambda_0}, \tag{4.2}$$

where γ_0 refers to the pulse front tilt angle due to the angular dispersion only. k_{x0} corresponds to the center of gravity of the spatial frequency profile for a particular angular frequency ω, ω_0 is the center frequency and ϵ is the propagation angle of the spectral component λ with respect to the center wavelength λ_0.

Spatial chirp refers to the coupling between spatial and spectral coordinates and can be characterized in the (x, ω) domain by the spatial dispersion $(dx_0/d\omega)_{\omega_0}$ or analogously the frequency gradient $(d\omega_0/dx)_{x_0}$ [140]. If spatial and temporal chirp appear simultaneously, the combined effect of both phenomena induces pulse front tilt even in the absence of angular dispersion. For example, in the case of a field with a Gaussian spectrum and a

Gaussian spatial profile, the overall pulse front tilt is given by [141],

$$\left(\frac{dt_0}{dx}\right)_{x_0} = \left(\frac{dk_{x0}}{d\omega}\right)_{\omega_0} + \left(\frac{d^2\varphi}{d\omega^2}\right)_{\omega_0}\left(\frac{d\omega_0}{dx}\right)_{x_0}, \tag{4.3}$$

where φ refers to the spectral phase.

For the analysis of the simulations presented in this work, the spatiotemporal distortions were divided into two groups: first-order distortions and higher-order distortions. In order to calculate linear distortions, the simulated field in the (x, y, t) domain was transformed to the other domains by Fourier transformation. Then, the slopes of the two-dimensional intensity profiles in the (x, t), (x, ω) and (k_x, ω) were calculated in order to obtain the pulse front tilt, spatial chirp and angular dispersion respectively in the walk-off plane. In principle, this method can be utilized to characterize nonlinear distortions as well, but the quantitative analysis would be cumbersome, with a rapidly increasing number of distortion terms for each expansion order that is included. Therefore, the Strehl ratio (SR) was used as a measure of the extent of both linear and nonlinear spatiotemporal distortions. The Strehl ratio was computed as,

$$SR = \frac{I}{I_0}, \tag{4.4}$$

where I and I_0 are the peak intensities of the output signal beam with and without distortions, respectively at the focal plane of an ideal lens. The procedure to calculate the intensities is as follows: First, the amplified pulses are compressed uniformly across the spatial profile. For this, the spectral phase, $\varphi(x_{max}, y_{max}, \omega)$ was taken as a reference, where (x_{max}, y_{max}) corresponds to the position of maximal intensity within the beam profile. This reference phase was then subtracted at all positions across the beam profile, resulting in a Fourier transform-limited pulse duration at (x_{max}, y_{max}) , but not necessarily at other positions within the beam profile. The distortion-free electric field $E_{df}(x', y', \omega')$ which is by definition separable in (x', y') and ω' , was constructed from the distorted field $E(x, y, \omega)$ by multiplying the position-averaged spectral distribution times the frequency-averaged spatial distribution, while the spectral phase was set to zero at all positions according to,

$$E_{df}(x', y', \omega') = \beta \sum_{\omega} |E(x', y', \omega)| \sum_{x,y} |E(x, y, \omega')|, \tag{4.5}$$

where β is a normalization constant that ensures that both fields have the same energy. Then, both the distorted and the distortion-free field were focused under ideal conditions by solving Kirchoff's integral under the Fraunhofer approximation leading to the peak intensities I and I_0 respectively. The Strehl ratio calculated in this manner [cf. Eq. 4.4] is a measure of the extent of spatiotemporal distortions irrespective of the order. The ratio will be unity for an ideal distortion-free field and decreases if spatiotemporal distortions are present i.e. the stronger the spatiotemporal distortions, the lower the Strehl ratio.

4.4.3 Simulation results and analysis

For all the simulations the nonlinear material considered was BBO under type I phase-matching. The pump pulses had a Gaussian temporal profile with a Fourier transform-limited duration of 1 ps (FWHM) and a central wavelength of 515 nm. The broadband seed pulses had a Fourier transform-limited pulse duration of 10 fs (FWHM), a Gaussian spectral profile, and a central wavelength of 850 nm. They were positively chirped to 600 fs (FWHM), unless specified otherwise. The choice of the initial pulse parameters and the nonlinear material was motivated by widely available Ytterbium-doped amplifiers that are suitable to pump NOPCPAs in the visible and near infrared. Both the pump and seed beam profiles were Gaussian and the beam sizes were matched in all cases. Considering the limited pump pulse energy at high repetition rate, the beam waists (half width at $1/e^2$ of the peak intensity) on the BBO crystal were always <=1 mm.

A. Single stage NOPCPA

First, a single stage NOPCPA was considered. The phase-matching geometry was chosen to be a walk-off compensating (WOC) geometry [see Fig. 4.1(a)], in which the asymmetry in the beam profile of the amplified signal due to birefringent walk-off is minimized [115]. In negative uniaxial crystals ($n_e < n_o$), the Poynting vector of the extraordinary wave subtends an angle with the propagation wave vector, effectively displacing the energy distribution of the field away from the optical axis. The displacement is towards the signal wave in WOC configuration which partially compensates the walk-off effect between the pump and the signal wave due to the noncollinear geometry. Meanwhile in non-walk-off compensating (NWOC) configuration, the Poynting vector of the pump points away from the signal, increasing the spatial walk-off effects [see Fig. 4.1(b)]. In the WOC configuration, second harmonic generation from both the signal and the idler is phase-matched, introducing modulations in the spectra and ultimately reducing the signal and the idler pulse energies. These parasitic effects have been considered in the simulations. In the case of broadband phase-matching, the pump and the signal beams propagate at an angle of 24.45° and 26.95° respectively with respect to the optical axis of the crystal.

For the first simulation, a 2 mm long crystal was pumped at a peak intensity of 40 GW/cm^2. For a beam waist of 500 µm, the pump pulse energy corresponds to 168 µJ. The seed pulse energy was chosen to be 8.4 nJ keeping the ratio of pump to seed pulse energy constant for all simulations. The effective nonlinear optical coefficient of BBO was taken to be 2 pm/V for both the OPA and the parasitic processes. The given set of parameters ensures that the gain is not saturated with 9 % pump-to-signal energy conversion efficiency, which simplifies the analysis. The intensity profiles in different domains are shown in Fig. 4.8. It can be clearly seen that the distortions are almost linear and dominate along the walk-off plane [Figs. 4.8(d) and 4.8(e)] whereas distortions in the orthogonal plane are negligible [Figs. 4.8(b) and 4.8(c)]. Therefore, for the rest of the analysis of first-order distortions the attention is focused on effects arising in the walk-off plane. Note that the dips observed in the spatio-temporal and spatio-spectral profiles correspond to modulations in the spec-

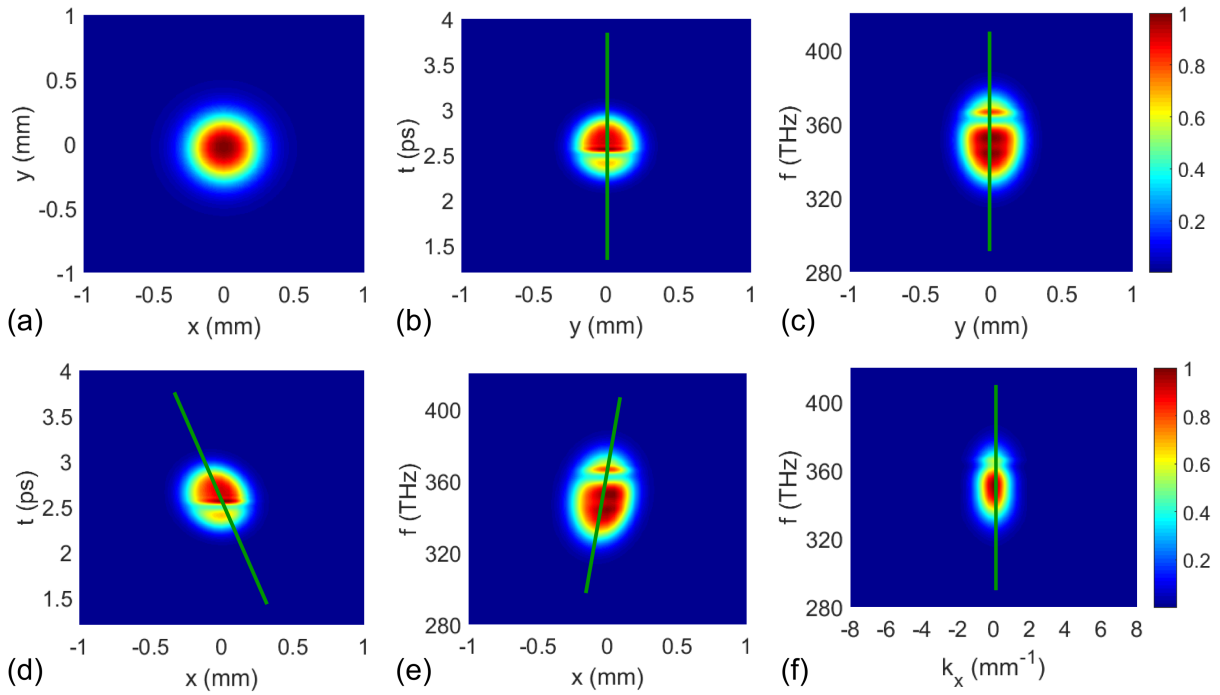

Figure 4.8: Intensity profiles of the output signal from an unsaturated NOPCPA in different domains: (a) y-x (b) t-y (c) f-y (d) t-x (e) f-x, and (f) f-k_x for an input beam waist of 500 µm (half width at $1/e^2$ of peak intensity). The green lines are there to guide the eye. The output energy of the signal is 15.1 µJ (gain = 1800).

trum due to parasitic effects. Since the slopes of the profiles directly reflect the first-order distortions, as explained in section 4.4.2, there is significant pulse front tilt [Fig. 4.8(d)], spatial chirp [Fig. 4.8(e)] and almost no angular dispersion [Fig. 4.8(f)] in the walk-off plane. These results are consistent with the results reported in [27].

Influence of detuning the noncollinear angle

The noncollinear angle was detuned from the magic angle and the above-mentioned calculation was repeated for four different beam waists of 125 µm, 250 µm, 500 µm and 1000 µm. These particular beam sizes were chosen in such a way that the smallest beam is comparable to the physical extension of the pump pulse and in order to cover several experimentally used pump beam sizes [23, 99]. For a peak intensity of 40 GW/cm^2, the pump pulse energies corresponding to the four different beam sizes are 10.5 µJ, 42 µJ, 168 µJ and 672 µJ respectively. In each case, first-order distortions were calculated from the spatiotemporal profiles as explained in section 4.4.2. The impact of detuning the noncollinear angle from the optimum value is shown in Fig. 4.9. Before compression, the overall pulse front tilt is significant in all cases [Fig. 4.9(a)]. After compression, the pulse front tilt decreases dramatically and is fully determined by angular dispersion [compare Figs. 4.9(b) and 4.9(d)]. Spatial chirp dominates for larger beam sizes [Fig. 4.9(c)] which has been discussed in [142].

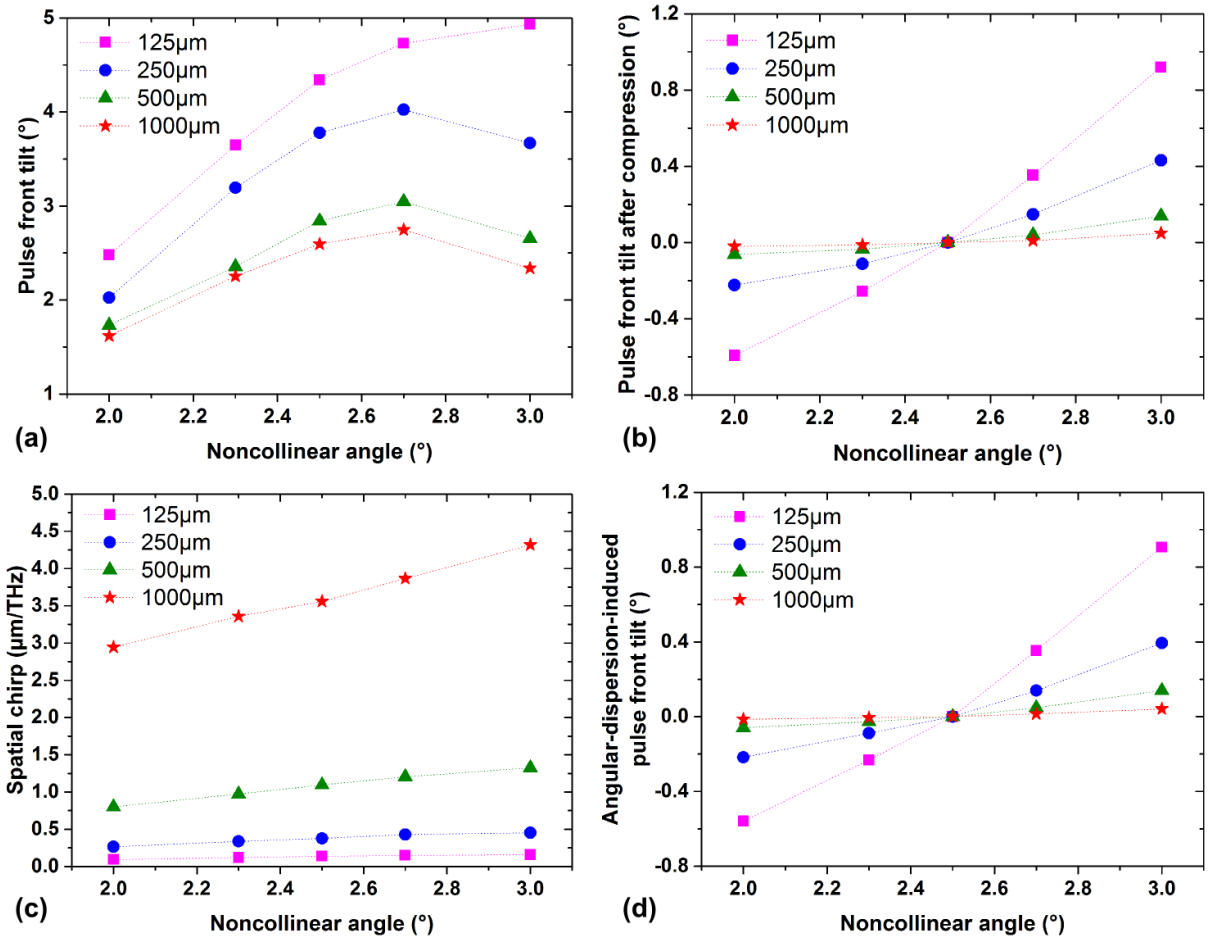

Figure 4.9: Variation of spatiotemporal distortions with noncollinear angle in the walk-off compensating (WOC) geometry for an unsaturated NOPCPA, for various beam waist values (c. f. Legend): (a) pulse front tilt before compression and (b) pulse front tilt after compression; (c) spatial chirp and (d) angular dispersion-induced pulse front tilt. At the magic angle (2.5°) both the pulse front tilt and the angular dispersion are zero after compression.

The angular dispersion vanishes at the magic angle for all beam sizes and is approximately proportional to the detuning from the magic angle [Fig. 4.9(d)]. The variation is stronger for small beam sizes, which is mainly due to their large angular spectrum. These results are in good agreement with those reported in [26, 27].

In order to understand the influence of the phase-matching geometry, this series of calculations was repeated for the NWOC configuration [see Fig. 4.1(b)]. The results are summarized in Fig. 4.10. Compared to the WOC configuration, a dramatic increase in the overall pulse front tilt is observed for small beam sizes [compare Figs. 4.9(a) and 4.10(a)]. This is mainly due to the larger spatial walk-off of the pump with respect to the signal, which increases the spatial chirp [compare Figs. 4.9(c) and 4.10(c)]. Nevertheless, after pulse compression the pulse front tilt is – as before – fully determined by angular dispersion

[compare Figs. 4.10(b) and 4.10(d)]. However, away from the magic angle, the magnitude of the residual pulse front tilt due to angular dispersion is higher in the NWOC configuration than in the WOC configuration.

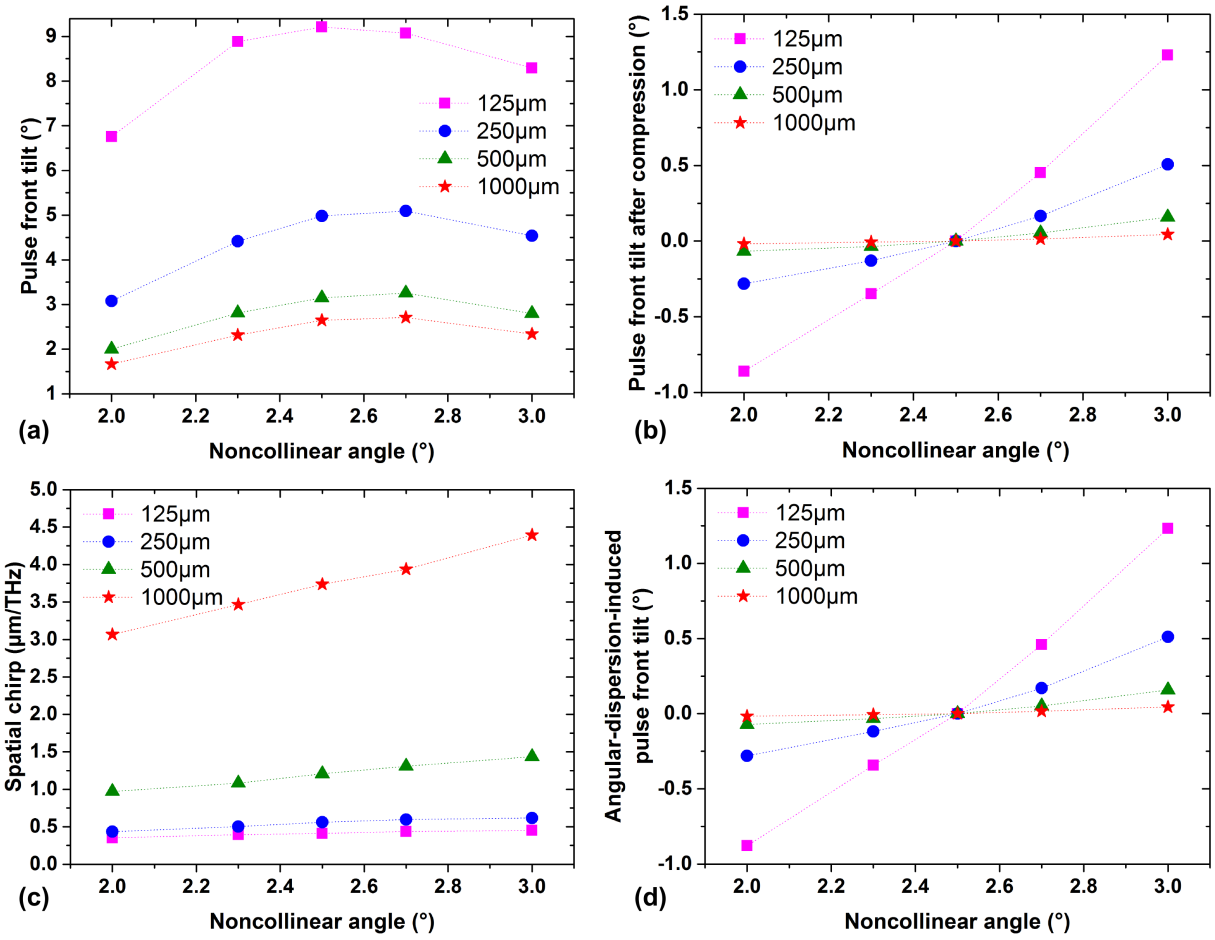

Figure 4.10: Variation of spatiotemporal distortions with noncollinear angle in the non-walk-off compensating (NWOC) geometry for an unsaturated NOPCPA, for various beam waist values (cf. Legend): (a) pulse front tilt before compression and (b) pulse front tilt after compression; (c) spatial chirp and (d) angular dispersion-induced pulse front tilt. At the magic angle (2.5°) both the pulse front tilt and the angular dispersion are zero after compression. Away from the magic angle, the pulse front tilt and the angular dispersion increase more rapidly than in the WOC case [see Fig. 4.9].

Impact of pulse-front matching

In addition to the group-velocity matching of the signal and the idler, pulse-front matching has been used in experiments to achieve tilt-free, spatially unchirped signal pulses from a noncollinear OPA [142]. Furthermore, numerical calculations show that matching the pulse fronts of the pump and the signal at the magic angle configuration minimizes the first-order

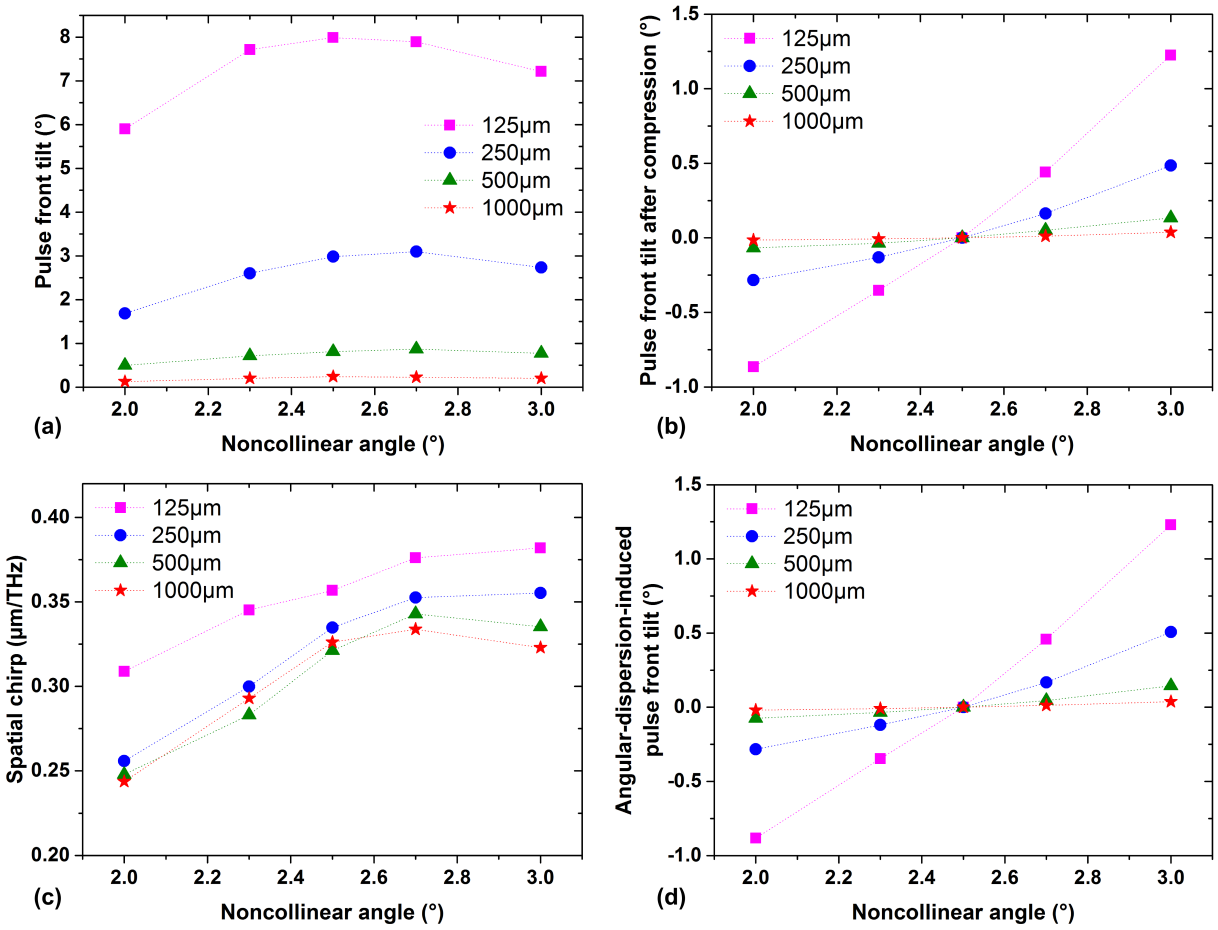

Figure 4.11: Impact of pulse-front matching on linear distortions in an unsaturated NOPCPA in non-walk-off compensating (NWOC) geometry for various beam waist values (c. f. Legend): (a) pulse front tilt before compression and (b) pulse front tilt after compression; (c) spatial chirp and (d) angular dispersion-induced pulse front tilt, after pulse-front matching of the pump and the signal.

distortions [27]. However, this has only been discussed for a particular set of parameters. In order to investigate the impact of pulse-front matching, simulations were performed by matching the pump and the signal pulse fronts in both phase-matching configurations.

First-order distortions, for the case of matched pulse fronts are shown in Fig. 4.11 for the case of a NWOC configuration. It is found that matching the pulse fronts of the pump and the signal reduces the overall pulse front tilt [Fig. 4.11(a)]. This decrease in tilt is most significant for beam waists >250 µm, due to the strongly reduced spatial chirp, as can be seen in Fig. 4.11(c) compared to Fig. 4.10(c). In all cases, the overall pulse front tilt is only due to angular dispersion once the pulses are compressed [Fig. 4.11(b)], as seen in the previous calculations. However, there are no changes in the angular dispersion due to the pulse-front matching [compare Fig. 4.10(d) and 4.11(d)]. This is not surprising since the pump bandwidth is much smaller than the signal bandwidth, and the influence

of angular dispersion introduced to the pump due to the tilted pulse fronts has negligible effect on the angular dispersion of the signal. Similar results were found in the case of WOC configuration (not shown). These results suggest that pulse-front matching is important only for beam waists >250 µm and in general, for beam sizes considerably larger than the physical extension of the pump pulse. Of course, this only applies to the present analysis of linear distortions in unsaturated amplifiers.

Influence of gain saturation

The amplification conditions that have been considered so far did not include gain saturation. Amplifiers with gain saturation may introduce high order couplings. Still, this situation is of high practical interest since most amplifiers are operated in saturation. Gain saturation was simulated for both the WOC and NWOC configurations in two different approaches. In one case, the pump intensity was increased keeping all other parameters constant until the gain saturated and back conversion from the signal to the pump occurred, while in the other case, the length of the crystal was increased stepwise in order to saturate the gain at fixed pump intensity.

In the first approach, the crystal length was kept constant at 3 mm and the pump intensity was varied from 5 GW/cm^2 to 100 GW/cm^2 by increasing the pulse energy and keeping the beam waist constant at 500 µm. The rest of the parameters were identical to those used in the single stage NOPCPA modeled in section A. The impact of different degrees of saturation on spatiotemporal distortions was characterized by calculating the Strehl ratio as described in section 4.4.2. Figure 4.12(a) depicts the evolution of the Strehl ratio and the conversion efficiency as a function of pump intensity in both the WOC and NWOC configurations. Gain saturation is clearly visible in the conversion efficiency in both configurations, whereas back conversion from the signal to the pump beam is visible in the NWOC configuration but not in the WOC configuration. Nevertheless, back conversion effects are observed in the WOC case in the temporal and spatial profiles of the pump and the signal. Additional simulations were also performed without considering parasitic effects. These calculations confirmed that strong parasitic second harmonic generation of the idler beam considerably reduces the back conversion from the signal to the pump in the WOC configuration. The degradation of the Strehl ratio when the gain saturates, indicates that the impact of gain saturation on distortions is severe. This is all the more true in the regime where back conversion occurs. Even though the increase in pump intensity increases the conversion efficiency, the peak power that can be achieved is significantly reduced due to the distortions.

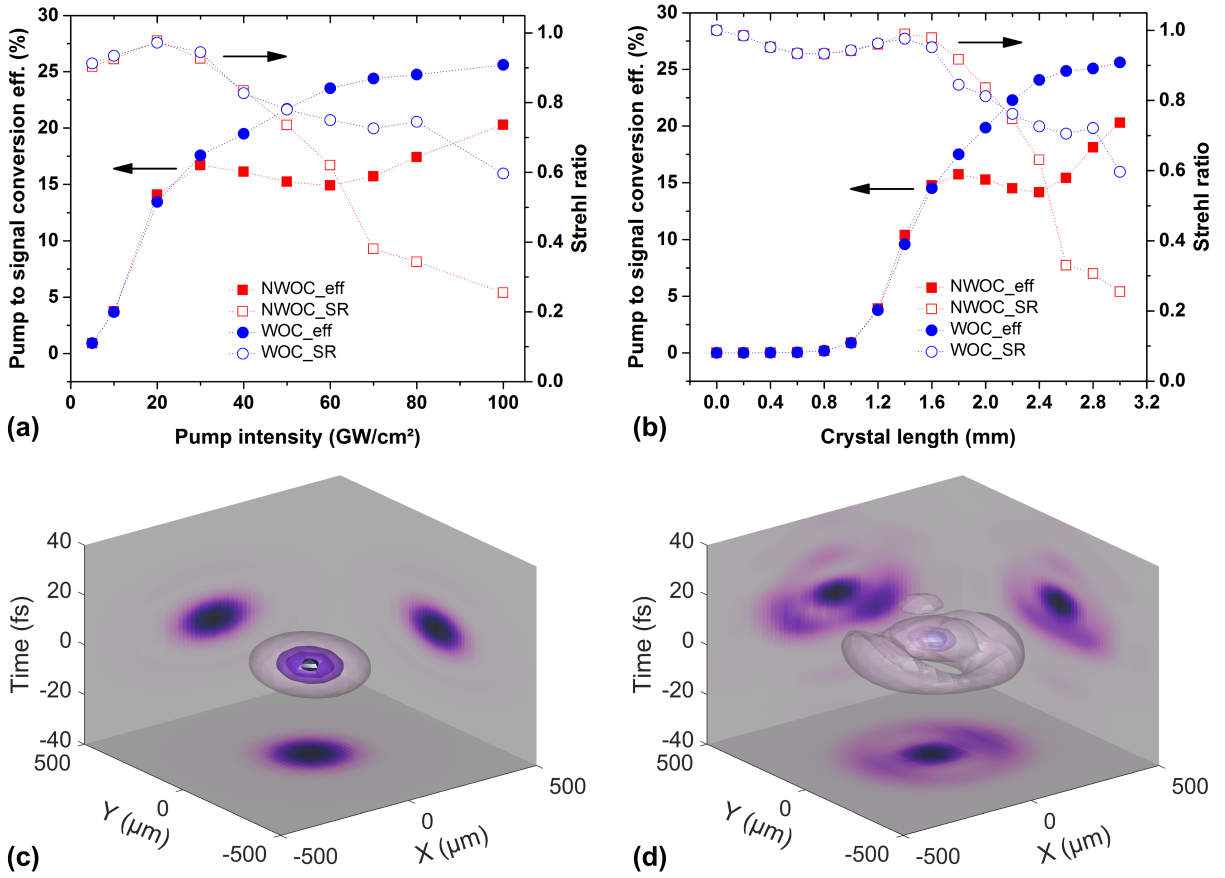

Figure 4.12: The impact of gain saturation on spatiotemporal distortions in the walk-off compensating (WOC) and non-walk-off compensating (NWOC) configurations: (a) when the pump intensity is increased for a crystal length of 3 mm, and (b) when crystal length is increased keeping the pump intensity constant at 100 GW/cm^2. The conversion efficiency is shown on the left (solid blue circles for the WOC configuration and solid red squares for the NWOC configuration), revealing gain saturation for higher pump intensities (a) and longer crystal lengths (b). The accompanying Strehl ratios are shown on the right (open blue circles for the WOC configuration and open red squares for the NWOC configuration), revealing that the onset of gain saturation is accompanied by a significant reduction in the Strehl ratio. 'SR' and 'eff' refer to the Strehl ratio and the conversion efficiency respectively. Parts (c, d) illustrate the 3D spatiotemporal distribution after compression and focusing for crystal lengths of 1.8 mm (c) and 2.8 mm (d), both in NWOC configuration and for a pump intensity of 100 GW/cm^2.

In the second calculation, the pump intensity was kept constant at 100 GW/cm^2 (with a pulse energy of 418 µJ and beam waist of 500 µm) and the crystal length was increased from 0 to 3 mm in steps of 0.2 mm [Fig. 4.12(b)]. As was the case in Fig. 4.12(a), for increased crystal lengths the increase in conversion efficiency goes at the expense of a significant reduction of the Strehl ratio. In addition, Figs. 4.12(c) and 4.12(d) show the 3D spatiotemporal distribution after compression and focusing, for crystal lengths of 1.8 mm and 2.8 mm respectively, both in the NWOC case. The 3D objects in the figures were

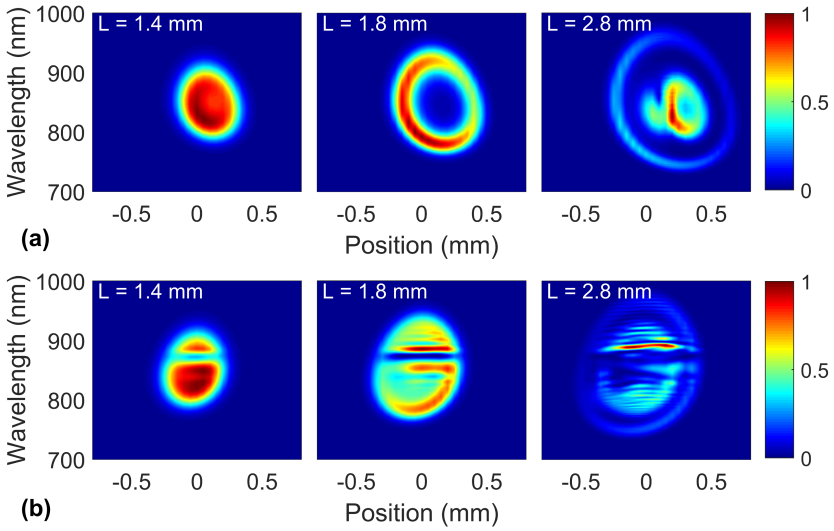

Figure 4.13: Spatio-spectral profiles in the walk-off plane for three different conversion efficiencies corresponding to the crystal lengths (L) of 1.4 mm, 1.8 mm and 2.8 mm [see Fig. 4.12(b)] in the NWOC (a) and WOC (b) phase-matching configuration.

constructed by plotting surfaces of constant intensity. The panels at the planes $x = 500\,\mu\text{m}$, $y = 500\,\mu\text{m}$ and $t = -40\,\text{fs}$ show 2D projections of the 3D distribution. The comparison between Figs. 4.12(c) and 4.12(d) illustrates how the spatiotemporal distribution, and hence the Strehl ratio, degrades when the crystal is longer than optimal.

Figure 4.12(b) indicates that at a pump intensity of $100\,\text{GW/cm}^2$, a Strehl ratio close to 1 can be maintained for crystal lengths shorter than 1.6 mm, which corresponds to conversion efficiency around 15 % for both WOC and NWOC configurations. Up to a crystal length of 2 mm, there is a reasonable compromise between conversion efficiency and Strehl ratio. Beyond 2 mm, the Strehl ratio further degrades. The degradation is much more pronounced in the NWOC case while the conversion efficiency is higher in the WOC case. However, in the latter case, the amplified spectrum suffers from modulations due to the parasitic second harmonics. The evolution of the spatiotemporal couplings as the conversion efficiency increases can be illustrated also, by analyzing how the amplified spectrum varies within the beam profile along the walk-off coordinate. Figure 4.13 shows the spatio-spectral profiles for three different conversion efficiencies corresponding to crystal lengths of 1.4 mm, 1.8 mm and 2.8 mm [see Fig. 4.12(b)] and for both the NWOC and WOC configurations. In the NWOC case, the spectral modulations are mainly due to back conversion and more pronounced as the propagation length increases, while there is a strong dependence of the spectral shape on the spatial coordinate, as shown in Fig. 4.13(a). Furthermore, the amplified spectrum in the WOC case is modulated due to both back conversion and the parasitic second harmonics. As can be seen in Fig. 4.13(b), the variation of the spectrum within the beam profile is larger for higher conversion efficiency.

In addition, it is important to check whether the pulse is compressible. In order to compare the spectrum and the spectral phase in both configurations, a particular crystal

length of 1.8 mm was chosen, for which the gain was already saturated but the Strehl ratio was better than 0.8 [Fig. 4.12(b)]. The complex electric field of the output signal at that crystal length was used to extract the spectrum and the spectral phase. First, a second-order polynomial was fitted to the spectral phase at the center of the beam. The fitted phase $\varphi_f(\omega)$ was then subtracted from the total phase as,

$$\varphi(\omega) = \varphi(x_{max}, y_{max}, \omega) - \varphi_f(\omega), \tag{4.6}$$

$$\varphi_f(\omega) = a_0 + a_1\omega + a_2\omega^2, \tag{4.7}$$

where $\varphi(\omega)$ refers to the residual phase and a_0, a_1 and a_2 are the polynomial coefficients. Thus, only higher-order residual phase terms that need to be compensated to achieve the Fourier transform-limited pulse duration are left. The spectrum and the residual spectral phase at the center of the beam profile and the average spectrum are shown in Fig. 4.14(a) and 4.14(b) for the NWOC and WOC configuration, respectively. The spectral phase at the center of the beam profile in the NWOC case seems well-behaved [Fig. 4.14(a)] and can readily be compensated, whereas the phase-jump resulting from the parasitic second harmonic in the WOC case [Fig. 4.14(b)] is challenging to compensate experimentally. This suggests that the NWOC configuration is more favorable for pulse compression. The pulses corresponding to the spectra at the center of the beam profile and the residual spectral phase, along with the Fourier transform-limited pulses as well as the near field beam profiles are shown in Figs. 4.14(c) and 4.14(d) for NWOC and WOC configuration, respectively. The near field beam profile is less distorted in the WOC case as expected, however, a strong post pulse appears in the temporal profile. In the NWOC case, the pulse is close to being Fourier transform-limited.

From a practical point of view, these results point out that a conversion efficiency of 15 - 18 % will ensure saturation, while keeping the Strehl ratio at acceptable values. Moreover, the NWOC configuration is the geometry of choice for better pulse compression, unless the walk-off effects degrade the beam quality.

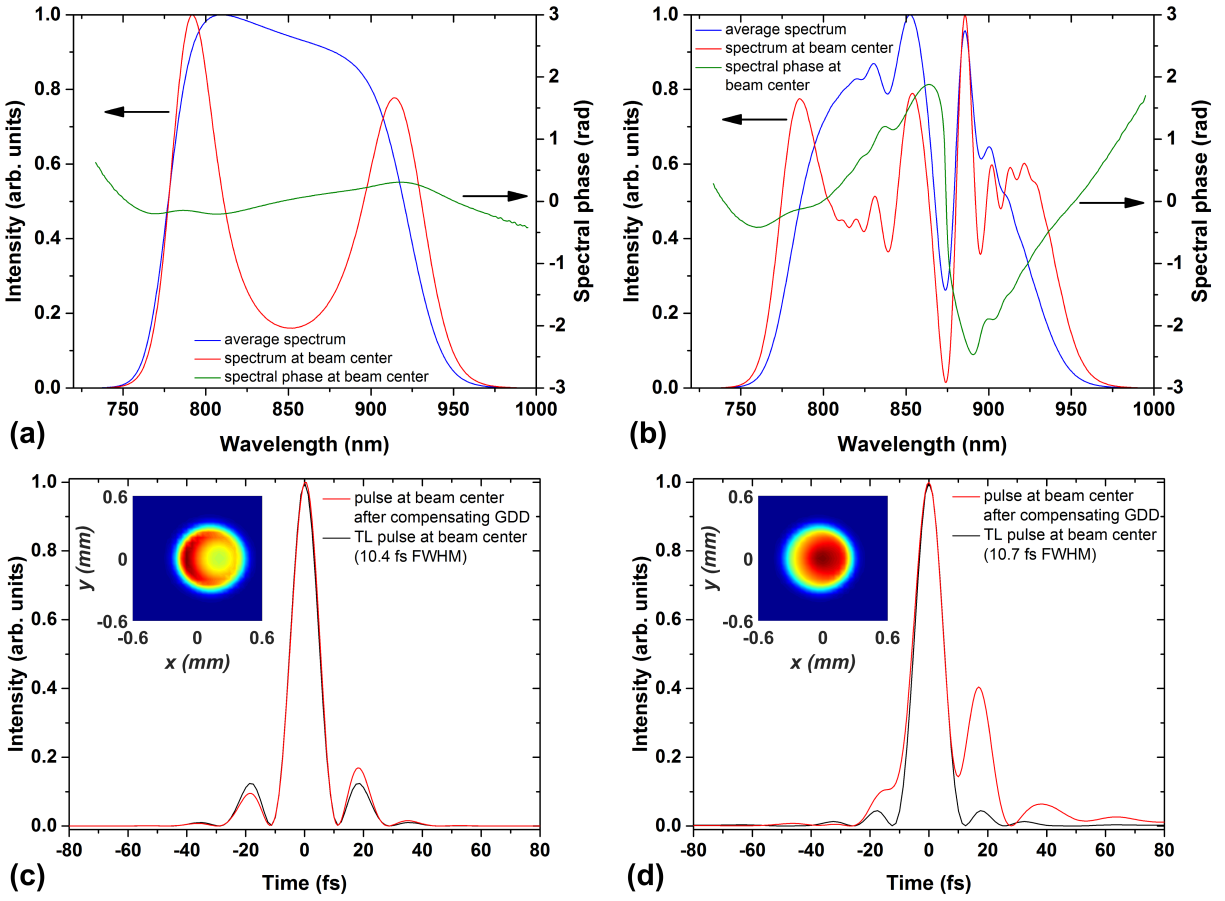

Figure 4.14: Spectral and temporal characterization of the amplified signal beam, for a crystal length of 1.8 mm, and a pump intensity of 100 GW/cm^2 [a conversion efficiency over 15 %, see Fig. 4.12(b)]: (a) Spectrum and spectral phase in the case of the NWOC and (b) the WOC configuration, (c, d) Temporal profiles corresponding to the spectrum at the center of the beam profile and the residual spectral phase (along with the Fourier transform-limited pulse) as well as the near field beam profile in the inset for (c) the NWOC and (d) the WOC configuration. The spectral phases in (a) and (b) correspond to higher-order dispersion terms, where the group delay dispersion has been removed.

Influence of beam/pulse shapes

So far only Gaussian beams and Gaussian spectral (and temporal) shapes have been considered for the seed and the pump pulses. From a practical point of view it is interesting to study how saturation effects change with different beam shapes or spectral profiles. For example, the output of laser systems used to pump parametric amplifiers have, in some cases, flat-top beam profiles (see for example [143]). In addition, the spectrum of broadband pulses is not Gaussian and it is often strongly modulated.

In order to study the impact of a modulated seed spectrum, a Gaussian spectral profile with a dip in the center was chosen which still supports Fourier transform-limited pulses of

10 fs (FWHM). The pulses were then chirped to 600 fs (FWHM). The beam shape of the seed was chosen to be Gaussian and the pulse energy was 8.4 nJ. The pump parameters were kept the same as in the previous section: Gaussian temporal shape with a duration of 1 ps (FWHM), pulse energy of 418 µJ and Gaussian beam profile focused to an intensity of 100 GW/cm^2 (beam waist of 500 µm). Figure 4.15 compares the conversion efficiency and Strehl ratio as a function of crystal length for three different seed spectra: 90 % modulation depth, 50 % modulation depth and no modulation (Gaussian shape), for the WOC and NWOC configuration. As can be clearly seen, there is very little influence of the spectral shape on the conversion efficiency and the Strehl ratio. On the one hand, these results imply that the conclusions from the previous section apply in general to more realistic spectral shapes. On the other hand, the implementation of existing techniques for spectral shaping would not have a strong impact in minimizing spatiotemporal couplings originated in saturated amplifiers.

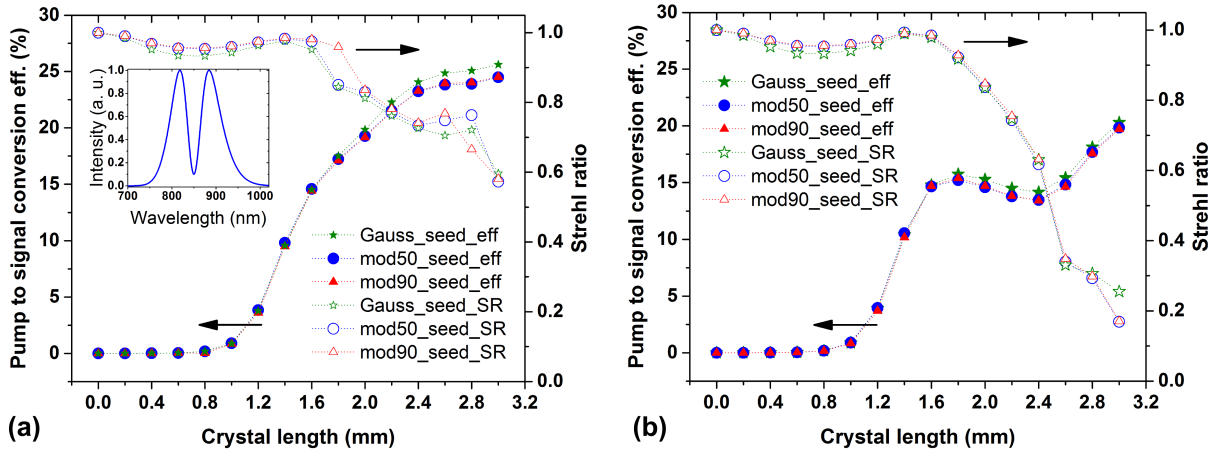

Figure 4.15: Impact of gain saturation on conversion efficiency and Strehl ratio for three different seed spectra in the case of (a) WOC and (b) NWOC configuration. The inset shows a seed spectrum with 90 % modulation depth. 'SR' and 'eff' refer to Strehl ratio and conversion efficiency, while 'Gauss_seed', 'mod50_seed' and 'mod90_seed' refer to the seed spectra without modulation, with 50 % and 90 % modulation depth respectively.

For the next set of simulations, the seed spectrum was Gaussian and all other seed parameters remained unchanged. Meanwhile the pump beam was changed to a supergaussian of order 10 with the aim of studying the impact of flat-top pump beam profiles. The pump pulse had a Gaussian temporal shape with pulse duration of 1 ps (FWHM) and the energy was increased to 668 µJ to keep the peak intensity constant at 100 GW/cm^2. Once again, the conversion efficiency and the Strehl ratio were calculated at each step along the crystal length and the results compared with those for a Gaussian pump beam as shown in Fig. 4.16. The homogenous gain across the seed beam due to the supergaussian pump beam profile allows a more efficient amplification for a given crystal length as compared to the Gaussian pump beam. Since the gain is relatively constant across the entire pump beam the energy transfer from pump to seed is spatially homogenous. That means that

before reaching the back conversion regime, a significant amount of energy is transferred to the signal from the whole pump beam and not only from the center. As a result, a high conversion efficiency of around 25 % can be achieved in both the WOC and NWOC configurations, while keeping a Strehl ratio higher than 0.9. The conversion efficiency can be increased even to more than 30 % in the WOC case [Fig. 4.16(a)] without significant degradation of the Strehl ratio (higher than 0.85 for a crystal length of 2.2 mm). In the NWOC case however, the Strehl ratio degrades faster in the back conversion regime [Fig. 4.16(b)].

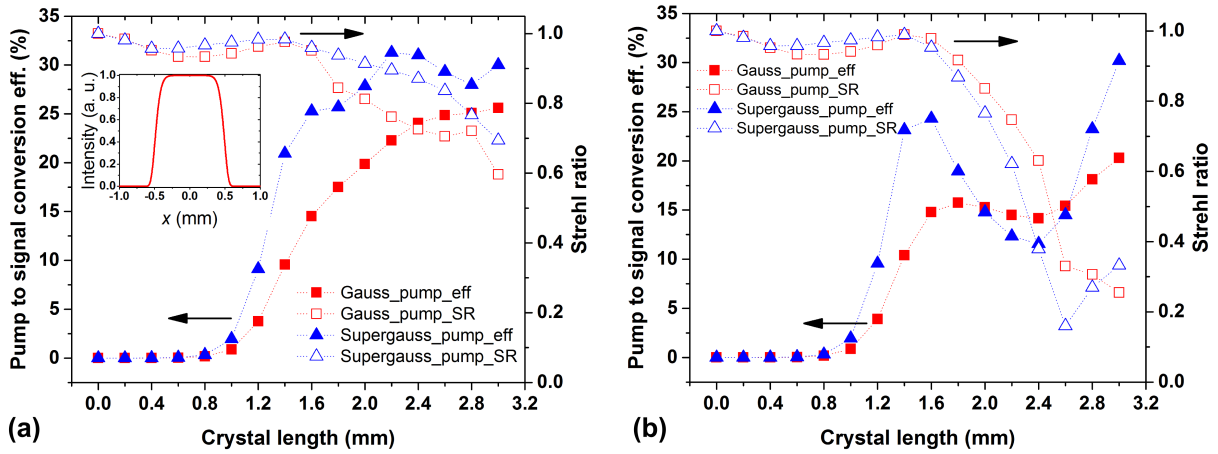

Figure 4.16: Impact of gain saturation on conversion efficiency and Strehl ratio in the case of Gaussian and supergaussian pump beam of order 10 with a peak intensity of 100 GW/cm^2 in the (a) WOC configuration and (b) NWOC configuration. The inset shows a supergaussian pump beam profile. 'SR' and 'eff' refer to Strehl ratio and conversion efficiency, while 'Gauss_pump' and 'Supergauss_pump' refer to the Gaussian and supergaussian pump beam profile respectively.

B. Double stage NOPCPA

NOPCPAs with output energy exceeding a few microjoules are mostly designed in a multi-stage scheme, therefore it is important to understand how the distortions carried over from one stage to the next affect the performance of the amplifier, in terms of spatiotemporal distortions. A double stage NOPCPA was modelled with the simulation parameters shown in Tab. 4.1. The pulse and beam shapes for the signal and pump were Gaussian. A pump intensity of 45 GW/cm^2 was used in both stages with the pump beam waists of 200 µm and 800 µm in the first and second stage respectively. An appropriate crystal length was chosen in order to investigate both unsaturated and saturated gain regimes. The primary focus is on the spatiotemporal distortions of the signal at the output of the second stage.

At first, stage 1 was simulated as an unsaturated amplifier with a 1.8 mm long crystal so that the distortions at the output signal are almost linear. The output signal after beam magnification seeds the second stage which consists of a 2.5 mm long crystal. This crystal length ensures that the second amplifier is saturated, which allows the study of

Table 4.1: Parameters for two-stage NOPCPA simulations

	Parameter	Stage 1	Stage 2	
Signal	Center wavelength	850 nm	Output signal from stage 1 after magnification	
	Pulse energy	1 nJ		
	Pulse duration (FWHM)	600 fs chirped		
	Bandwidth (FWHM)	106 nm		
	Beam waist	200 µm		
	Pulse and beam shapes	Gaussian		
Pump	Center wavelength	515 nm		
	Pulse energy	30 µJ	480 µJ	
	Pulse duration (FWHM)	1 ps (transform-limited)		
	Beam waist	200 µm	800 µm	
	Pulse and beam shapes	Gaussian		
BBO crystal	Length	1.8 mm	2.5 mm	
	d_{eff}	2 pm/V		
Phase-matching (PM) parameters	PM configuration	WOC	WOC	NWOC
	PM angle	26.95°	26.95°	21.95°
	Noncollinear angle	2.5°		

both unsaturated and saturated amplification by retrieving data from different positions along the crystal. Additionally, both WOC and NWOC configurations were considered in the second stage whereas the first stage was always in WOC configuration. Next, the length of the crystal in stage 1 was increased to 2.5 mm to saturate the gain and the output signal was used as the seed for the second stage.

Impact of distortions from the unsaturated first stage

A crystal length of 1.8 mm in stage 1 ensured that the gain is not saturated as shown in Fig. 4.17(a). The pulse front tilt of the output signal after the first stage was $\sim$ 232.7 fs/mm (4°) whereas the Strehl ratio was 0.97. After a magnification factor of 6, the output signal seeded the second stage under three different input cases and for both the WOC and NWOC configurations. For each case, the evolution of the Strehl ratio and the conversion efficiency are shown as a function of crystal length [Figs. 4.17(b) and 4.17(c)].

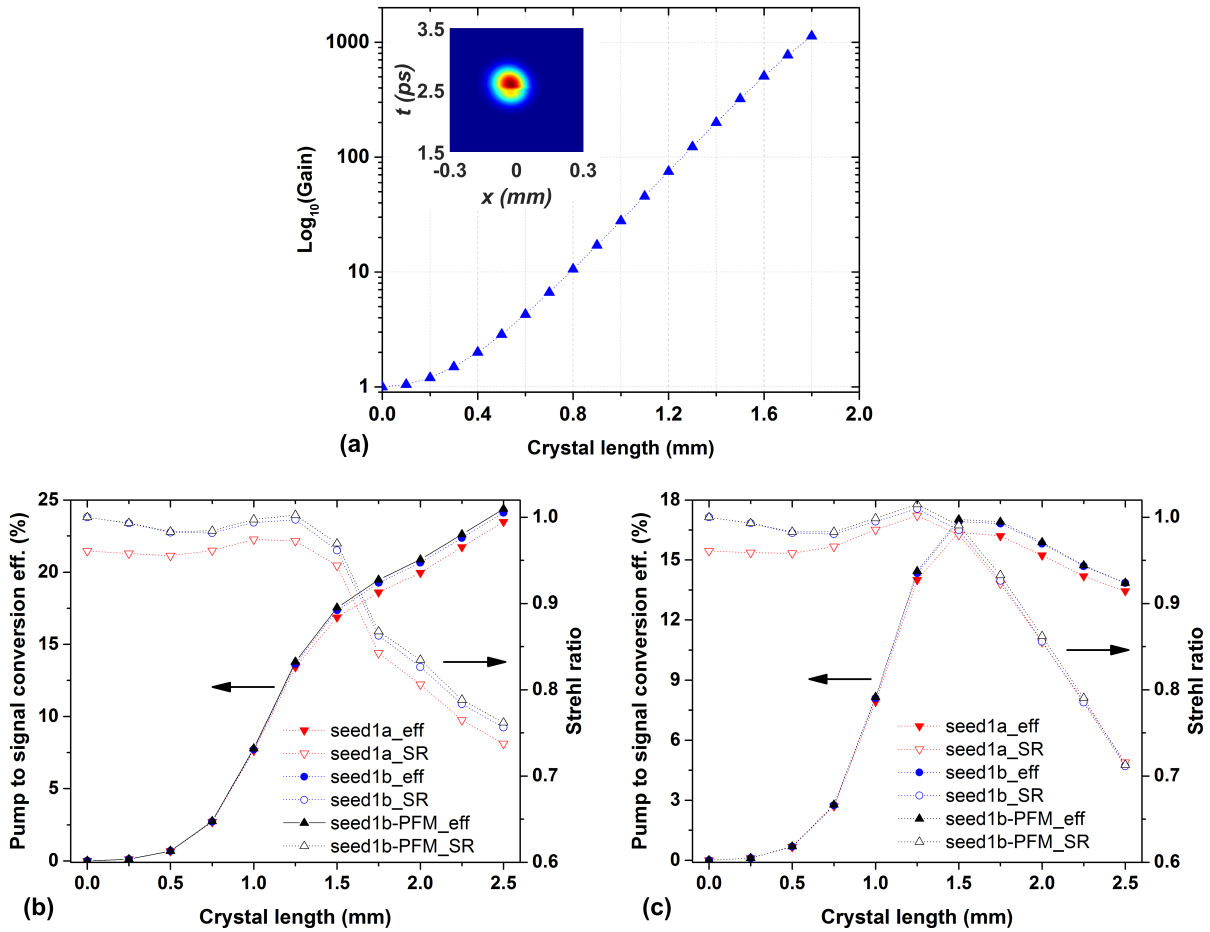

Figure 4.17: Investigation of the impact of distortions from an unsaturated first amplification stage on the amplification and the output characteristics in a second stage: (a) gain of the first stage as a function of the crystal length, for a pump intensity of 45 GW/cm^2; the inset shows the time-position profile of the output signal; (b) evolution of the Strehl ratio and the conversion efficiency in the second stage, for three input signal conditions (seed1a, seed1b and seed1b-PFM) in the WOC configuration and (c) in the NWOC configuration. The three input conditions for the second stage are given in the main text. 'SR', 'eff' and 'PFM' refer to the Strehl ratio, pump-to-signal energy conversion efficiency and pulse-front matching.

The three different input conditions were the following: (1) The output signal from the first stage seeded the second stage without any modifications (seed1a); (2) the distortions in the output signal from the first stage were removed [cf. Eq. 4.5] before seeding the second stage (seed1b); and (3) the distortions were removed from the seed and the pulse fronts of the seed and the pump were matched in the second stage (seed1b-PFM). For all crystal lengths of the second stage and for both configurations, the distortion-free seed performs slightly better than the distorted seed. The pulse-front matching of the pump and the distortion-free seed improves the conversion efficiency and the Strehl ratio even further, especially in the WOC case [Fig. 4.17(b)]. However, the effects of linear distortions in the

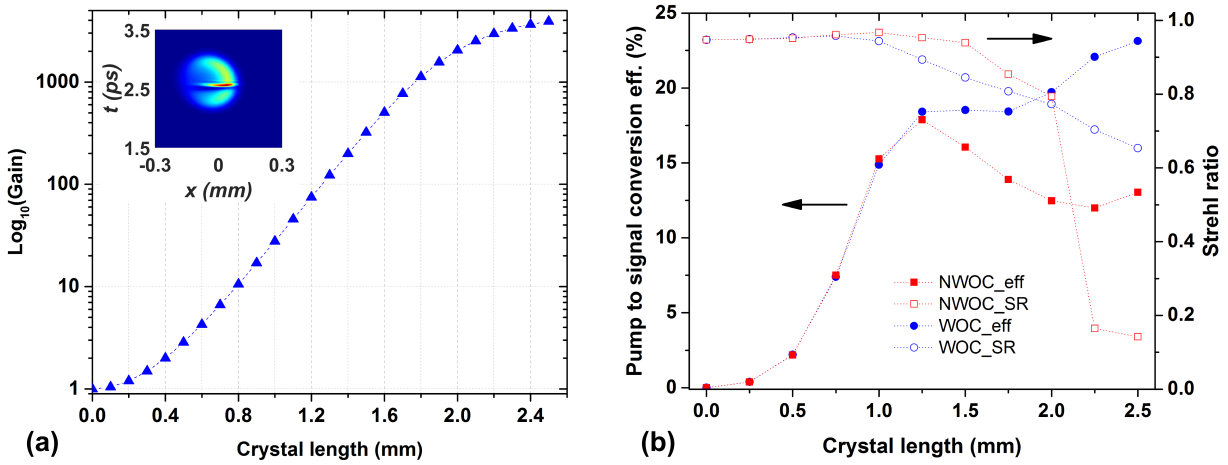

Figure 4.18: (a) Evolution of gain with the crystal length in the saturated first stage; inset: time-position profile of the signal at the output of the 2.5 mm long crystal; (b) evolution of the Strehl ratio and the conversion efficiency of the output of the second stage in the WOC and NWOC configurations when the second stage is seeded with a distorted signal.

seed are essentially negligible compared to the distortions introduced by gain saturation in the second stage. Since the degradation of Strehl ratio due to saturation dominates, pulse-front matching is not particularly useful in the case of saturated amplifiers.

Influence of distortions from the saturated first stage

The calculations in the previous section were repeated for the case where gain saturation also occurs in the first stage. The length of the crystal in the first stage was increased to 2.5 mm, so that the gain saturates without obvious back conversion as shown in Fig. 4.18(a). As mentioned in section A., under these conditions there are higher-order distortions present in the output signal of the first stage and the Strehl ratio drops to 0.95.

The distorted output signal was used to seed the second amplification stage. As expected, the gain now saturates at a shorter crystal length compared to the results of Fig. 4.17, given that the seed level is higher by a factor of 3.5. For longer crystal lengths, the Strehl ratio drops rapidly following the saturation behavior of conversion efficiency in both configurations [Fig. 4.18(b)]. In the unsaturated regime, the distortions in the output of the second stage are equivalent to the distortions in the seed as the Strehl ratio remains ~ 0.95 up to a conversion efficiency of $\sim 15\,\%$. Once the gain saturates, the Strehl ratio with the saturated seed is slightly lower than the Strehl ratio for an unsaturated seed at the same conversion efficiency. The degradation of the Strehl ratio becomes worse when the back conversion to the pump is strong, clearly visible in the NWOC configuration. It should be noted that in the second stage the spatial and temporal profiles of the signal beyond a 2 mm crystal length are strongly modulated due to back conversion. Furthermore, the output spectrum in the WOC configuration is heavily modulated due to parasitic second

harmonics.

It is clear that gain saturation dominates and degrades the Strehl ratio significantly. Additional simulations have shown that pulse-front matching doesn't improve the Strehl ratio despite minimizing the first-order distortions.

4.5 Summary

To summarize, a three-stage high energy NOPCPA has been modeled using 3D numerical code. The simulation results suggest that the broadband pulses (sub-6 fs) from a Ti:Sapphire oscillator can be amplified directly achieving an amplified bandwidth that supports sub-7 fs Fourier transform-limited pulses with a moderate conversion efficiency of $\sim$15 %. Utilizing pump pulse energy of ~ 1.1 mJ, few-cycle pulses with energy > 145 µJ can be achieved at a pulse repetition rate of 100 kHz which corresponds to an average power > 14.5 W.

In addition, a detailed numerical study of spatiotemporal distortions in BBO-based noncollinear optical parametric chirped-pulse amplifiers has been presented. Single stage and double stage amplifiers have been modeled under different amplification conditions and the spatiotemporal distortions in the amplified signal pulses have been characterized. As long as the amplifier is not saturated, the distortions at the output that are confined to the walk-off plane, are almost linear, and can be characterized by well-known parameters such as the pulse-front tilt angle, and constant spatial chirp and angular dispersion values. When the gain saturates, the distortions are no longer linear.

In amplifiers without strong gain saturation, angular dispersion vanishes at the magic noncollinear angle and increases with angular detuning, with a more pronounced effect for narrow beams. Pulse front tilt is significant for all noncollinear angles and pump beam sizes, but when the pulses are compressed the contribution from spatial chirp vanishes and only the contribution due to angular dispersion remains. Moreover, spatial chirp is always present for temporally chirped pulses, unless the pulse fronts of the pump and the signal are matched. Spatial chirp is particularly important for the case of a relatively large beam size. When the pulse is ideally compressed, the degradation of the Strehl ratio due to the first-order spatiotemporal distortions is not significant. However, gain saturation and particularly back conversion introduce strong higher-order distortions and degrade the Strehl ratio of the amplified signal beam. When the amplifier is deep into the back conversion regime, a situation arises where the peak intensity will be far from the maximum possible. If the amplifier gain is saturated, matching the pulse fronts of the pump and the signal does not appear to be important, for the particular range of beam waists and pulse duration used in this work.

If there are two amplification stages, the distortions from the unsaturated first stage play a minor role if the second stage is saturated. We conclude that it is convenient to build the first amplifier (or the first few amplifiers) in the WOC configuration and to operate them without strong saturation, so that the intensity of the amplified signal beam is not strong enough to drive efficient second harmonic generation, which degrades the spectral phase.

On the other hand, a power (or last) amplifier should be built in the NWOC configuration if the best possible pulse compression is desired, whereas the WOC configuration should be chosen if the beam quality is more important. In both scenarios, the pump to signal energy conversion efficiency for Gaussian beams should be kept around 15 % avoiding the back conversion regime if a degradation of the peak intensity higher than 10-20 % due to spatiotemporal distortions is to be avoided. This scenario can be highly improved if a pump beam with flat-top profile is implemented. In that case conversion efficiencies as high as 25 % can be achieved in both WOC and NWOC configuration, while keeping a Strehl ratio better than 0.9.

These results can be viewed as general guidelines for the development of BBO-based NOPCPAs with minimum spatiotemporal distortions. Furthermore, the described behavior can be qualitatively expected in any uniaxial crystal with dispersion properties similar to BBO.

5 Application of few-cycle pulses in strong field physics: electron interferometry

In the last decade, applications of ultrafast lasers in fundamental scientific research have been significantly boosted by remarkable developments in terms of output characteristics of the lasers, in particular, scaling of the peak power to petawatt level [144] and shortening of the pulse duration towards a single optical cycle [69]. Laser sources with few-cycle pulses and gigawatt peak power are routinely available in laboratories, and can be focused to achieve peak intensities in the range of $10^{14}\,\mathrm{W/cm^2}$. The interaction of the focused laser beam with matter triggers several strong field-induced physical processes. It is widely understood that the term 'strong field' refers to the external electromagnetic field that is on the order of the electric field experienced by the electron in the first Bohr orbit of the hydrogen atom ($\sim 5.1 \times 10^9\,\mathrm{V/cm}$). This level of field strength, accessible by focusing ultrashort pulses to high peak intensities has led to very diverse strong field physics experiments. In addition, the experimental findings have been supported to a large extent by complex quantum mechanical simulations. In most of these studies, the photoionization of atoms/molecules by strong laser fields and the detection of charged particles (photoelectrons or photoions) with various detector technologies have become key aspects. Indeed, strong field photoionization has been established as an essential tool to study the nuclear and electronic dynamics of atomic and molecular systems. Moreover, few-cycle pulses have enabled time-resolved studies of ultrafast processes in atoms and molecules on femtosecond and sub-femtosecond time scales.

Extreme nonlinear processes accessible with ultrashort laser pulses allow high harmonic generation and the generation of attosecond pulse trains [5]. Extremely short pulses, ideally with few optical cycles, are favorable for the generation of isolated attosecond pulses [6]. In this regard, energetic, high peak power, few-cycle laser pulses have become a backbone of strong field physics and attosecond science. Note that the stability of carrier envelope phase[1] of few-cycle laser pulses plays an important role in attosecond experiments.

This chapter presents an application of few-cycle, near-infrared pulses in strong field atomic physics: electron interferometry. The concept of attosecond electron interferometry has recently been demonstrated using an XUV-IR pump-probe scheme [145, 146]. In this work, the interferometric pump-probe technique is demonstrated experimentally with single color IR pulses only. A proof-of-principle IR-IR pump-probe experiment is carried out to characterize the bound states of strong field-excited Argon. The idea is to study the possibility of the characterization of bound electron wave packets with high spectral and temporal resolution using only few-cycle IR pulses, thereby reducing the complexity of the

[1]The phase between the peak of the envelope of the pulse and the nearest peak of the carrier wave.

experiment.

The chapter is organized as follows. The interferometric IR-IR pump-probe technique is briefly introduced in the first section, followed by a short background on electron interferometry. Then, the methods to retrieve the amplitudes and phases of excited bound states in an atomic system are reviewed. The IR-IR pump-probe experiment with Argon atoms is presented in section 5.3 and the results are reported in section 5.4. Issues in the retrieval of the amplitudes and phases of excited states are discussed and further analyzed with the support of numerical calculations performed by solving the time-dependent Schrödinger equation [section 5.6].

5.1 Introduction

Strong field ionization is one of the dominant responses of atoms and molecules in the presence of strong laser fields. Depending upon the laser intensity that atoms are exposed to, ionization mechanisms are classified into different categories such as multiphoton ionization, tunneling ionization and over the barrier ionization. If the energy of the laser photon is lower than the ionization potential of the atoms, single photon ionization is ruled out. That means the electron in an atom has to absorb more than one photon to overcome the Coulomb potential, and the mechanism is known as multiphoton ionization. The electron may absorb a larger number of photons than the minimum required to overcome the ionization potential, which is called above threshold ionization (ATI). If the laser intensity is large enough such that the Coulomb potential is distorted by the strong laser field reducing the width of the potential barrier, the electron can leave the atom via tunneling and the process is called tunnel ionization. It is worth to mention that multiphoton and tunnel ionization may occur together in experiments because of the different peak intensities encountered in the interaction volume. If the laser intensities are even higher, the barrier potential is completely suppressed so that the electron is free to leave the Coulomb potential. This mechanism is called over the barrier ionization and often happens at laser intensities $\gg 10^{16}\,\mathrm{W/cm^2}$. In the last decades, strong field ionization of atoms (and molecules) has been extensively studied and considered as the basis of various research areas such as high harmonic generation and spectroscopy, laser-induced diffraction imaging, and in general attosecond science.

In addition to the strong field ionization, strong field excitation of atoms has also been studied, where the excitation of bound states was initially explained by a multiphoton picture [147]. Multiphoton excitation is typically described in the frequency domain by simultaneous absorption of several photons populating high-lying Rydberg states. Recently, strong field excitation in the tunneling regime has been observed experimentally and explained by so-called frustrated tunneling ionization (FTI) [148], which is pictured in the time domain. If the drift energy gained by an electron after tunneling is not sufficient for ionization, the electron can be re-captured by the parent atom due to its Coulomb field. There is a possibility that the electron is captured into excited states of the neutral atom without emitting any radiation. The experiments on strong field excitation of

rare gas atoms in both the multiphoton and tunneling regime, along with an extensive analysis supported by quantum mechanical calculations have been discussed in Ref. [149]. The yield of strong field-excited atoms was experimentally measured (in contrast to the measurement of electrons/ions in common strong field experiments) and the distribution of the population of the excited states was calculated at a given laser intensity. This is indeed a very useful technique to find the population (amplitudes) of the excited states of a neutral atom after it is exposed to strong laser fields. However, the information about relative phases of the excited states is missing.

This chapter combines both strong field ionization and excitation in an interferometric pump-probe experiment by using near-infrared (IR) few-cycle pulses, with the aim of characterizing the excited bound states of the atom i.e. retrieving both amplitudes and phases of the excited states. A schematic picture of such an interferometric pump-probe technique is shown in Fig. 5.1. The idea is to ionize an atom by a few-cycle IR pump pulse, thereby creating an electron wave packet in the continuum and at the same time, exciting several bound states of the atom. Depending upon the intensity of the pump pulse, the excitation can be either by multiphoton or by frustrated tunneling ionization or by both as discussed earlier. After a certain time delay, a weaker probe pulse ionizes the excited states promoting electrons into the continuum. The continuum electrons ionized by the pump pulse (direct) serve as a 'reference' while the electrons from the excited bound states, which may form a bound wave packet, are ionized by the probe pulse (indirect) and are considered as 'unknown'. The electrons that reach the continuum via the two different paths (direct and indirect) interfere. The interference signal can be recorded by a standard two-dimensional detector such as a velocity map imaging spectrometer [see section 5.3]. As the interferometric signal contains both amplitude and phase information, the amplitudes and phases of the unknown bound wave packet i.e. of the excited bound states, can be retrieved from time-resolved photoelectron spectra that are measured for a set of pump-probe time delays.

Argon was chosen as gas target. The low ionization potential, easy availability and well-known spectroscopy of argon are the main reasons behind the choice of the target. Even though the bound states or high-lying Rydberg states of argon are well understood in strong field atomic physics, this will be used as a benchmark for the proof of principle experiment. As both the reference and unknown wave packets are created by strong field ionization and excitation, a peak intensity in the range of 10^{13} - 10^{14} W/cm^2 is sufficient for the experiment. The interferometric pump-probe technique can be used for the complete characterization of bound states, irrespective of the excitation mechanism that has excited them. Therefore, the technique can be applied to other similar quantum systems. In particular, the retrieved phase information about the excited states may provide more insights into the excitation processes. Moreover, the use of ultrashort, IR pulses significantly reduces the complexity of the experiment.

Interferometric techniques are well-known in the field of pump-probe spectroscopy. In particular, wave-packet interferometry [151] can be illustrated by an analogy to a pump-probe scheme in which pump and probe laser pulses create a pair of wave packets in atoms or molecules. The time delay between the pulses and thus the relative phase can

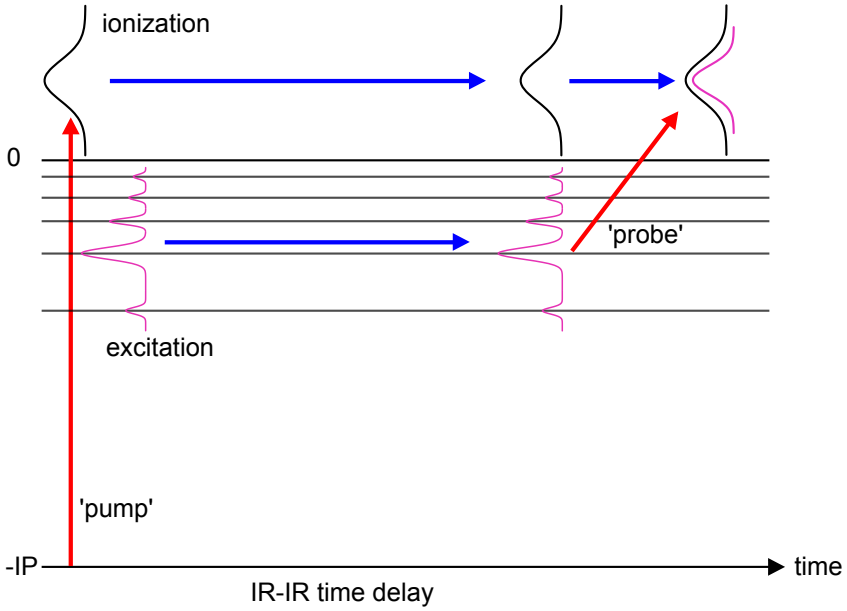

Figure 5.1: Quantum state holographic approach for the complete characterization of excited bound states. IP: ionization potential, WP: wave packet, IR: infrared. Strong field ionization of an atom by the IR pump pulse creates a continuum wave packet (reference) and simultaneously excites a bound wave packet (which is considered as unknown). After a certain time delay, the IR probe pulse ionizes the unknown bound wave packet which interferes with the previously created reference wave packet. By recording the photoelectron spectrum as a function of IR-IR delay, interference fringes can be observed and utilized to retrieve the energies, amplitudes and phases of the excited states that form the unknown bound wave packet. Figure adapted from [150].

be controlled to induce interference between the two wave packets. The interference will be either constructive or destructive depending upon the time delay between the pump and the probe pulse. The measurement of an interferogram allows the retrieval of quantum amplitudes and phases of the eigenstates that are superposed to form the wave packets. This approach, similar to optical holography, was described as quantum state holography [152]. Quantum state holography in attosecond science has recently been demonstrated by characterizing an attosecond electron wave packet in an interferometric XUV-IR pump-probe experiment [146]. In that experiment, a free and a bound wave packet were created simultaneously by exciting helium atoms with an attosecond pump pulse. For a certain pump-probe time delay, the bound wave packet evolves freely before being ionized by the IR pulse. The interference between the free wave packet ionized by the XUV pump pulse and the bound wave packet ionized by the IR probe pulse was observed in photoelectron spectra measured with a velocity map imaging spectrometer. Later, the technique was numerically studied for a so-called attosecond electron interferometer and a method for complete reconstruction of the attosecond electron wave packets was proposed by Klünder *et al.* [153]. In particular, retrieval of the relative phases of the excited bound states was demonstrated by introducing a phase retrieval algorithm. The concept of the attosecond

electron interferometer is the basis of the work presented in this chapter, however, utilizing few-cycle IR pulses instead of the isolated attosecond pulses as a pump.

5.2 Theoretical background

When an atom is exposed to a strong laser pulse, electron wave packets are created in the continuum by strong field ionization. At the same time, bound states of the atom are populated as mentioned in the previous section. In analogy to the previously mentioned electron interferometer, the wave packet created in the continuum serves as a reference whereas the excited bound wave packet is considered as unknown. The reference wave packet that is created at a time t_0 can be written as,

$$\Psi_c(r,t) = \int \mathrm{d}E \; c_E \exp[-i(Et/\hbar - \gamma_1(E))] \; \varphi_E(r), \tag{5.1}$$

where c_E, E and φ_E refer to the amplitudes, energies and wave functions of the continuum states. γ_1 represents an additional phase that may come from the ionization process. Similarly, the unknown wave packet, which is the coherent superposition of several bound states of excited argon, can be represented as,

$$\Psi_b(r, t > t_0) = \sum_n c_n \exp -i[E_n(t-t_0)/\hbar - \phi_n - \gamma_2(E_n)] \; \varphi_n(r), \tag{5.2}$$

where c_n and ϕ_n are the amplitudes and phases of the bound states, and φ_n and E_n are bound state wave functions and energies respectively. γ_2 corresponds to a phase that might be introduced due to the strong field excitation process.

At a time $t > t_0$, an IR probe pulse that is weaker and phase-locked with the IR pump pulse excites the electrons from the excited bound states thereby promoting a part of the bound wave packet into the continuum. This part of the unknown wave packet at energy E interferes with the reference wave packet at the same energy that is already created by the pump pulse. The phase difference $\Delta\phi(E,t)$ between the two wave packets is given by,

$$\Delta\phi(E,t) = (E - E_n)(t - t_0)/\hbar + \phi_n + (\gamma_2 - \gamma_1). \tag{5.3}$$

For simplicity, the energy and state dependence of γ_1 and γ_2 are neglected and the difference is considered as a constant and negligible phase offset. This is a good approximation when the pump and probe pulses are Fourier transform-limited [153].

As the wave-packet interference is governed by $\Delta\phi(E,t)$, ϕ_n determines when it is constructive or destructive. The energy at which a constructive interference occurs can be obtained from the Eq. 5.3 with $\Delta\phi(E,t) = 2m\pi$ as,

$$E = E_n + \frac{(2m\pi - \phi_n)\hbar}{(t - t_0)}, \tag{5.4}$$

where m is an integer. This means that in the time-resolved photoelectron spectra, the in-

terference fringes are hyperbolic curves. Furthermore, the photoelectron signal at an energy E oscillates with a frequency, given by $(E - E_n)/\hbar$. As the oscillation frequency is a linear function of energy E, Fourier transformation of the time-resolved photoelectron spectra along the time delay axis (i.e. a 2D map of the photoelectron kinetic energy vs. Fourier frequency) shows tilted lines of unity slope [see below]. The intercepts of these lines with the Fourier frequency axis provide the bound state energies E_n. In addition, the relative phases of the bound states can be retrieved from the measurement data as described in the Ref. [153].

In his PhD thesis, Sascha Birkner has discussed the interferometric XUV-IR pump-probe experiment that is mentioned in the previous section and numerically studied the possibility of replacing the XUV pump pulse by an IR pulse [24] while choosing an argon atom as the target. In this case, both the continuum and the bound wave packet will be created by an IR laser field. Similar numerical simulations have been performed in this work in order to complement the experimental results. The numerical procedure along with the approximations used in the calculations are briefly discussed here.

The most general form of the TDSE that is used to describe a quantum system evolving with time is written as,

$$i\hbar\frac{\partial}{\partial t}\Psi(r,t) = \hat{H}\Psi(r,t), \tag{5.5}$$

where $\Psi(r,t)$ is the time-dependent wave function of the quantum system and $\hat{H}$ is the Hamiltonian operator, which takes different forms depending upon the system. Its expectation value ($\langle|\Psi|\rangle$) provides the total energy of the system. For a particle e.g. an electron in a potential $V(r)$, $\hat{H}$ is given by,

$$\hat{H} = \frac{\hat{p}^2}{2m_e} + V(r), \tag{5.6}$$

where $\hat{p}$ is the momentum operator and m_e is the mass of the electron. In the presence of a laser field with vector potential $A(r,t)$, the momentum operator in Eq. 5.6 has to be replaced by $\hat{p} + eA(r,t)$, where e is the electron charge.

If there are more than two particles, the Hamiltonian is the sum of each single particle Hamiltonian including the resultant potential due to the interaction of all particles. In such a case, the TDSE can not be solved analytically without any approximations. Therefore, numerical methods have to be used following several assumptions/approximations. One of the widely used assumptions in strong field ionization is the so-called Single Active Electron (SAE) approximation in which only one electron is supposed to interact with the external laser field while the rest of the electrons create an effective potential.

In the case of argon in the SAE approximation, the potential is given by [154],

$$V(r) = [1 + Ae^{-Br} + (17 - A)e^{-Cr}]/r, \tag{5.7}$$

where $A = 5.4$, $B = 1$ and $C = 3.682$ are constants, with all values given in atomic units.

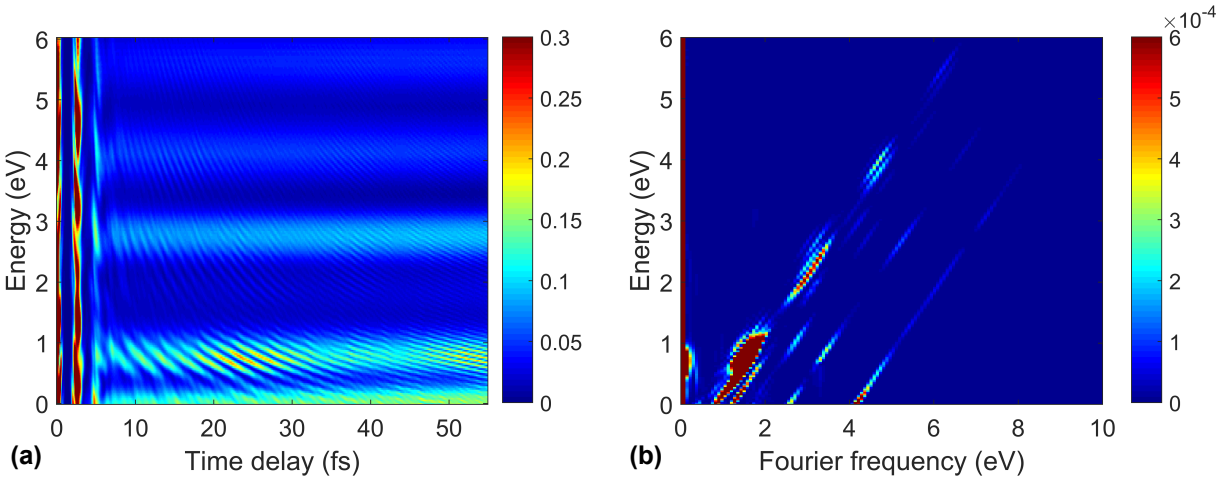

Figure 5.2: (a) Calculated photoelectron spectra in argon as a function of pump-probe time delay with pump and probe peak intensities of 5.6×10^{13} and $3.5 \times 10^{12}\,\mathrm{W/cm^2}$ respectively. For a zero time delay, the overlap of the IR pump and the IR probe pulse leads to a strong signal. When the pump pulse precedes the probe pulse, interference fringes appear. (b) Corresponding Fourier transform along the delay axis. The tilted lines correspond to the bound states of strong-field excited argon (see text for details). Simulation data was used from the Ref. [24].

The numerical program, originally written by H. G. Muller [154] was used to solve the TDSE on a space-time grid. Because of the spherically symmetric potential [Eq. 5.7], spherical coordinates were used for the space grid. For numerical simplicity, pulses with cosine-squared envelope were used, which can be written as,

$$E(t) = E_0 \cos^2\left(\frac{\omega_0}{2n_c}t\right)\cos(\omega_0 t), \qquad \text{for} \qquad -\pi n_c/\omega_0 \leq t \leq \pi n_c/\omega_0, \tag{5.8}$$

where $E(t)$ is the electric field of the pulse, E_0 is peak amplitude, ω_0 is the center frequency and n_c is the number of optical cycles within the pulse envelope. The calculations are carried out for a single intensity (no focal volume averaging) and the carrier envelope phase is assumed to be zero[2]. The details of the procedure along with all the necessary approximations used in the calculations can be found in the thesis of Sascha Birkner (see Ref. [24] and references therein).

Figure 5.2(a) shows calculated photoelectron spectra as a function of pump-probe time delay. The pump and probe pulses were centered at 800 nm with peak intensities of $5.6 \times 10^{13}\,\mathrm{W/cm^2}$ and $3.5 \times 10^{12}\,\mathrm{W/cm^2}$, respectively. The pulse shapes were assumed to be cosine-squared, with 5 optical cycles within the envelope (corresponds to a FWHM pulse duration of 6.6 fs). The probe pulse was delayed with respect to the pump pulse over a range of −5 fs to 55 fs with a time step of 0.1 fs.

For zero time delay, a strong signal is observed due to the overlap of the pump and

[2]In his thesis, Sascha showed more calculations, reporting that the interference effect is robust against focal volume and carrier envelope phase averaging [24].

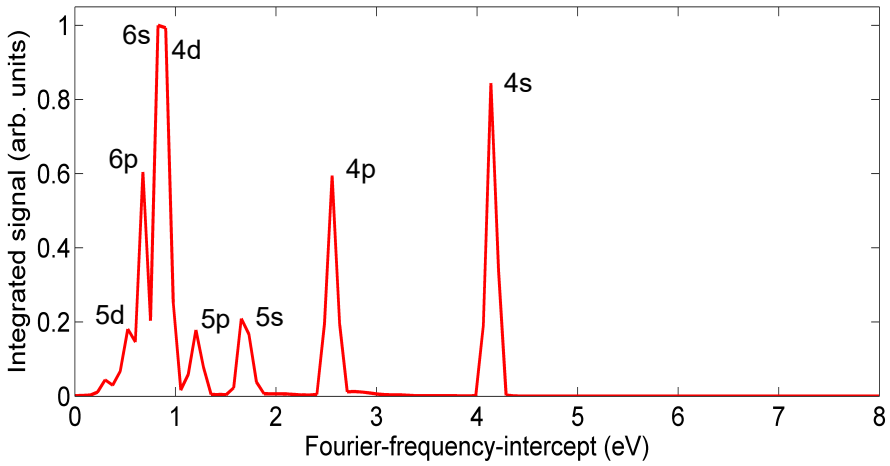

Figure 5.3: Signal integrated along the tilted lines in the 2D Fourier map [Fig. 5.2(b)].

the probe pulses. When the pump pulse precedes the probe pulse, interference structures appear over the whole range of pump-probe delays, which are a series of hyperbolas as discussed before. When a Fourier transform is performed along the time delay axis, a set of tilted lines at 45° are obtained which allow identifying the bound states of strong-field excited argon. As mentioned earlier, the bound state energies can be retrieved from the intersection of the tilted lines with the horizontal axis.

The 2D Fourier map [Fig. 5.2(b)] is integrated along the direction of the tilted lines and the resulting signal is plotted against the intercept of the tilted lines with the Fourier frequency axis. For clarity, the strong signals below a Fourier frequency of 2 eV are skipped during the integration. The peaks observed in the integrated signal, as shown in Fig. 5.3 provide the bound state energies of strong-field excited argon. The retrieved bound state energies are found to agree well with the energies used in the TDSE simulation (except for the higher-lying Rydberg states, which is mainly due to lower resolution), as compared in Tab. 5.1.

Table 5.1: Retrieved energies of the bound states of strong-field excited argon from the 2D Fourier map, along with the energies used in the TDSE simulation.

Bound state	Energy used in the simulation (eV)	Energy retrieved from the 2D Fourier map (eV)
4s	4.151	4.137
4p	2.563	2.558
5s	1.676	1.655
5p	1.224	1.204
4d	0.971	0.978
6s	0.914	0.828
6p	0.721	0.677
5d	0.610	0.527

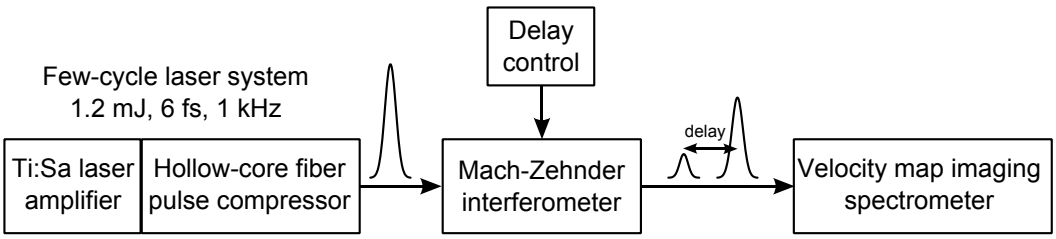

Figure 5.4: Schematic block diagram of the experimental scheme. Each pulse in the train of few-cycle near-infrared laser pulses is split into a pump and a probe pulse in a Mach-Zehnder interferometer. The pump and probe pulses are delayed with respect to each other and focused into the vacuum chamber of the velocity map imaging spectrometer where the pulses encounter an atomic beam. See text for details.

In addition, the intensity of each line provides the relative population of the corresponding bound state after the pump excitation. Furthermore, the relative phase of each bound state for a given photoelectron energy can be retrieved by following a retrieval procedure that was proposed for similar photoelectron spectra in Ref. [153]. The retrieval method is based on the separation of each bound state contribution from the photoelectron Fourier spectrum [Fig. 5.2(b)]. The corresponding amplitude and phase in the time domain can be obtained by using an inverse Fourier transform, which leads to the phase spectra $\Delta\phi(E,t)$ given by Eq. 5.3. From the phase spectra, the phases ϕ_n can be extracted as a function of energy (see Ref. [153] for the complete description of the retrieval algorithm).

The phase information retrieved in this way may provide interesting insight into the excitation mechanism. In the case of XUV excitation, the relative phase of the excited states are expected to be similar for all states. The situation will be different under the influence of strong IR pump, where excited states can be populated by different mechanisms such as direct photo-excitation and frustrated tunnel ionization (at higher intensities) as discussed in section 5.1. It would be very helpful to study if there exists a non-trivial dependence of the phase on the bound state that is excited by a strong IR laser field.

5.3 Experimental details

A schematic block diagram of the experiment is shown in Fig. 5.4. Few-cycle pulses from the laser system were sent to a home-built Mach-Zehnder interferometer. The laser pulse was divided into two pulses- a pump and a probe that are delayed with respect to each other in time. The output beam from the interferometer was focused into a velocity map imaging spectrometer, where the pulses were overlapped with a pulsed atomic beam at the position of laser beam focus. Each block of the schematic is briefly presented in the following subsections.

5.3.1 Laser system

The few-cycle laser system used in this experiment was based on nonlinear compression of pulses from a Ti:Sapphire amplifier in a hollow core fiber [155]. A commercially available Ti:Sapphire based regenerative amplifier (Spectra Physics Spitfire Pro) provides 35 fs (FWHM) pulses at 1 kHz with 3 mJ energy per pulse and a spectrum centered at 800 nm. A 2 mJ fraction of the output was focused into a gas-filled, differentially pumped hollow core fiber for spectral broadening. The spectral chirp of the spectrally-broadened pulses (due to self-phase modulation) was compensated by using a set of chirped mirrors. Pulses with more than 1.2 mJ energy at a repetition rate of 1 kHz were available after compression. The pulses were characterized using a commercially available SPIDER (Spectral Phase Interferometry for Direct Electric-field Reconstruction) device [APE GmbH, FC Spider]. Figure 5.5(a) shows the spectrum and spectral phase. The spectrum supports sub-5 fs Fourier transform-limited pulses. The pulses were compressed close to the Fourier limit with $\sim$ 6 fs (FWHM) pulse duration [Fig. 5.5(b)]. As can be seen clearly, pre- and post-pulse pedestals are present, extending beyond $\pm$30 fs. This is due to uncompensated spectral phase and spectral modulations.

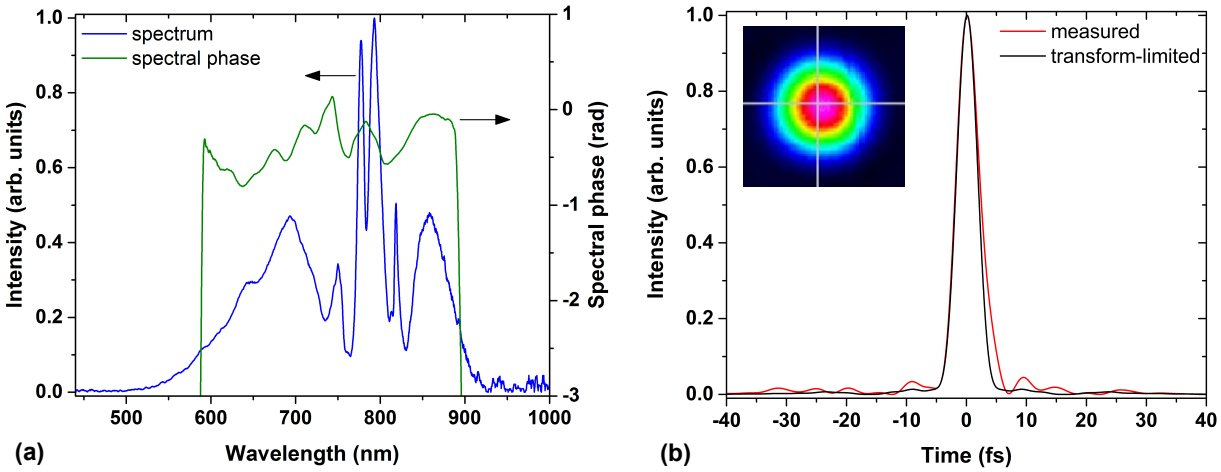

Figure 5.5: Characteristics of the few-cycle laser pulses used in the experiment. (a) Spectrum and spectral phase, and (b) measured temporal profile, after compressing with a set of chirped mirrors, along with the Fourier transform-limited temporal profile. Pre- and post-pulse pedestals are present in the measured profile, which are due to uncompensated spectral phase in combination with the spectral modulations. Inset: Far field beam profile recorded at the focus of a spherical mirror with 75 cm focal length. The spot size was 230 µm (full width at $1/e^2$ of peak intensity).

5.3.2 Pump-probe interferometer

The pump and probe pulses were derived from the same near-infrared laser pulse. A beam splitter of 1 mm thickness was used to divide the laser pulse into the pump and probe pulses, which were combined with another similar beam splitter. The reflectivity of the beam splitters were chosen in such a way that the ratio of the pump to probe intensity

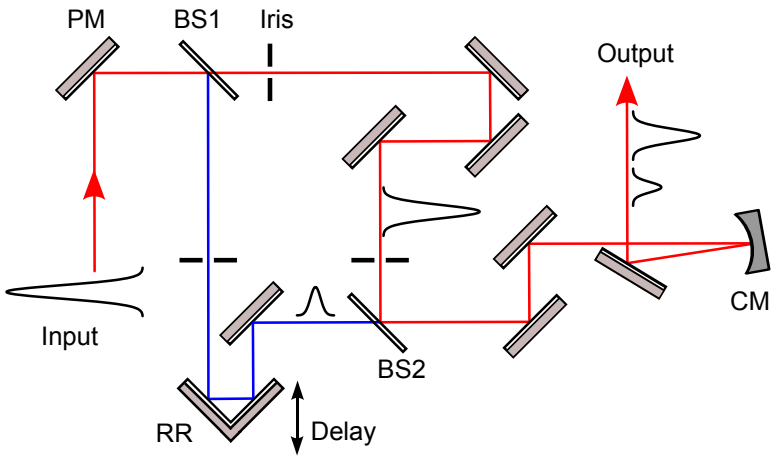

Figure 5.6: Optical layout of the Mach-Zehnder-type pump-probe interferometer. BS: beam splitter, PM: plane mirror, RR: retro-reflector, CM: curved mirror. The retro-reflector mounted on a translation stage is controlled by a LabVIEW-based program to introduce a variable delay of the probe pulse with respect to the pump pulse. The reflectivities of the beam splitters BS1 and BS2 were 37 % and 75 % respectively, which sets a pump-to-probe intensity ratio of ≈ 5:1.

was ≈ 5:1. The optical layout of the Mach-Zehnder type interferometer setup is shown in Fig. 5.6. After the first beam splitter BS1, the transmitted laser pulse travels to the second beam splitter BS2 and acts as a pump pulse. The reflected pulse acts as a probe and travels through a retro-reflector RR, mounted on a piezo-driven translation stage, which was used to control the time delay with respect to the pump pulse. The second beam splitter BS2 combines both the pump and the probe pulse. Depending upon the optical path difference, the pulses interfere with each other once the beams are overlapped spatially. At the output of the interferometer, a spherical mirror CM of 75 cm focal length was used to focus the beam inside the vacuum chamber of the velocity map imaging spectrometer.

The linear translation stage for the delay control was from Physik Instrumente (PI). An open-loop travel up to 120 µm could be achieved with a resolution of 0.2 nm, which corresponds to sub-5 as time resolution. The stage was calibrated for the weight of the mirror-mount including the retro-reflector. An interface program was developed using LabVIEW in order to control and scan the time delay between the pump and the probe pulse. The interference between the pump and the probe pulse was characterized by measuring an intensity autocorrelation signal with a photodiode. The vibrations from the optical table and the air fluctuations in the laboratory were found to introduce instabilities in the interferometric output signal. The disturbances related to vibrations were considerably minimized by positioning the interferometric setup on a separate optical breadboard which stands freely on the optical table and mounting it on o-rings (any kind of rubber pieces could have been used). In addition, a 'housing' was built to cover the interferometer to avoid perturbations introduced by air flow.

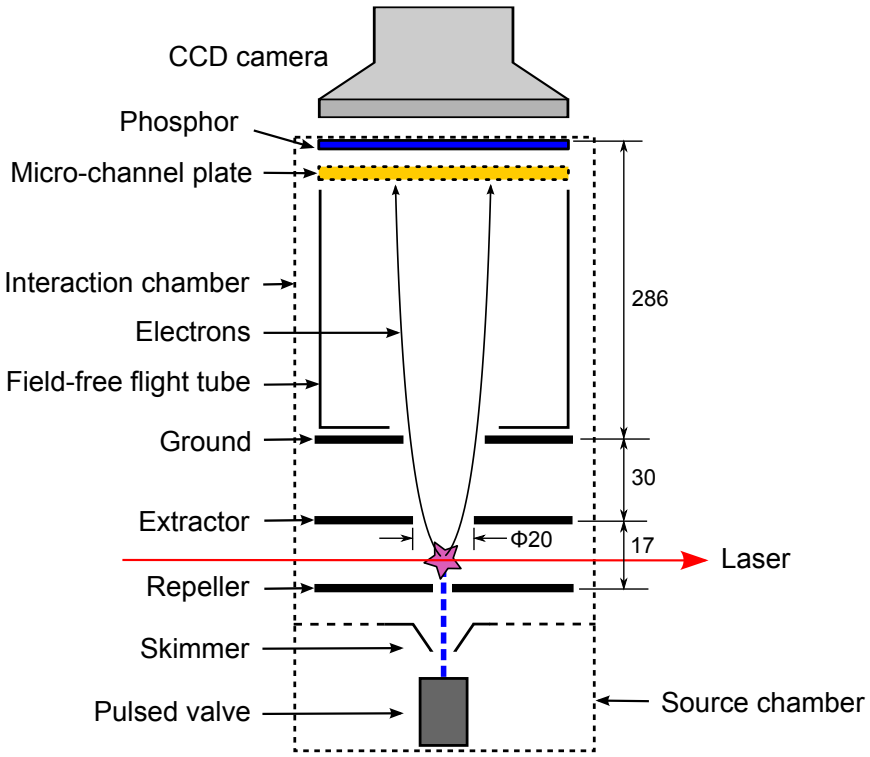

Figure 5.7: Schematic layout of the velocity map imaging spectrometer used in this experiment. Photoelectrons are accelerated towards a micro-channel plate (MCP) detector by applying high voltages to the repeller and extractor electrodes. By using a phosphor screen behind the micro-channel plate (MCP), two-dimensional images can be recorded by a CCD camera. The laser polarization lies in a plane parallel to the MCP detector. See Ref. [157] for the details of the design and practical implementation of a VMI spectrometer.

5.3.3 Velocity map imaging detector

The laser beam from the pump-probe interferometer intersects the atomic beam at the center of a velocity map imaging (VMI) spectrometer. The VMI spectrometer used for this experiment is based on the initial design of Eppink and Parker [156]. The spectrometer is composed of three electrodes, namely repeller, extractor and ground, as can be seen in the schematic layout shown in Fig. 5.7. With these electrodes, an electrostatic field can be applied in the interaction region in order to accelerate the electrons that result from the photoionization of atoms by the IR pump-probe laser pulses. The ratio of the high voltages applied to the extractor (V_E) and the repeller (V_R) has to be fixed in order to map the velocity distribution of the charged particles onto the two dimensional detector. The particular value of this ratio depends on the geometry of the spectrometer (e.g. the distance between the repeller and the extractor, and the distance between the repeller and the interaction volume). The electric field strength at the interaction region can be changed by changing the voltages V_E and V_R, keeping the ratio constant.

A piezo-driven pulsed valve was used to introduce the atomic beam into the spectrometer. The valve was operated at a repetition rate of 100 Hz. The use of the pulsed valve helps to maintain a high vacuum (while still accessing high densities in the interaction region) and accordingly to get a better signal-to-noise ratio. However, the low repetition rate of the valve did not exploit all the laser pulses available at a repetition rate of 1 kHz. The pulsed atomic beam passes through a skimmer and reaches the interaction region between the repeller and the extractor electrodes. There it encounters the laser beam that propagates along an orthogonal direction. In the interaction volume, electrons and ions are produced by photoionization. By applying proper high voltages to the electrodes, electrons are accelerated towards the detector. The electrodes act as an electrostatic lens, focusing photoelectrons with the same velocity that are originated at different positions within the interaction volume to one spot at the detector. The detector consists of a micro-channel plate (MCP) followed by a phosphor screen. The signal on the phosphor screen is recorded by a CCD camera and transferred to a computer using a LabVIEW-based data acquisition program.

The plane of the detector is parallel to the plane containing the atomic beam and the laser beam. The projection of the velocity distribution of the photoelectrons in the plane of the detector leads to a two-dimensional (2D) image in which each point corresponds to a particular initial velocity of the photoelectrons irrespective of the initial spatial distribution. The size of the velocity-map image depends on the repeller voltage whereas the focusing can be optimized by setting the extractor voltage. Following the optimization of the focusing, the repeller voltage can be adjusted to keep the voltage ratio constant.

It should be noted that the 2D velocity-map image is sufficient to extract both the kinetic energy and the angular distributions if the 3D momentum distribution has an axis of cylindrical symmetry in the plane of the detector. This is often the case in photoionization experiments [158], where the axis of symmetry is the laser polarization. An inverse Abel transform is used to retrieve the 3D momentum distribution from the 2D projection. The details of the design and practical implementation of a VMI spectrometer along with the data acquisition can be found in Ref. [157].

5.4 Experimental results

At first, the measurement conditions of the VMI spectrometer were optimized at a fixed time delay between the pump and the probe pulse. A high vacuum pressure of 10^{-7} mbar was achieved with the combination of a scroll pump and two turbo pumps (500 l/ sec). The focused laser beam was aligned to overlap with the atomic beam. The proper position of the atomic beam could be selected with a manipulator. High voltages were applied to the repeller and the extractor electrodes as well as to the MCP detector and the phosphor screen. First, the repeller voltage was set to 4 kV, choosing a proper size of the 2D velocity-map image. Then, the extractor voltage was scanned to optimize the focusing of the photoelectrons at the detector and set to 3.14 kV. At the same time, the phosphor screen was set to $\sim$ 3 kV and the voltage applied to the MCP was adjusted to 1.93 kV,

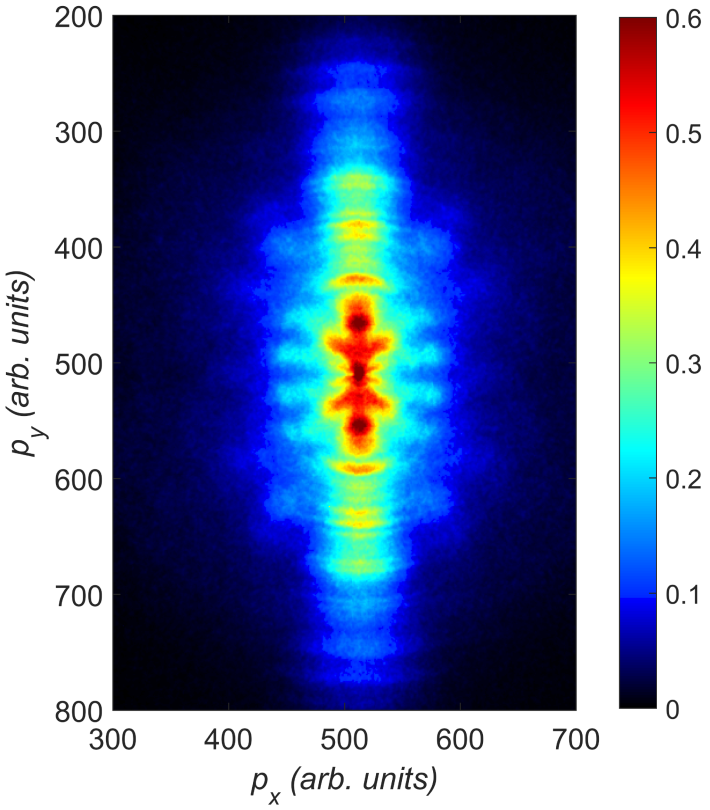

Figure 5.8: Experimental photoelectron image obtained after photoionization of argon by a sequence of two few-cycle near-infrared laser pulses at a time delay of 10 fs between the pump and the probe pulse. The laser polarization was along the vertical axis, which is the axis of symmetry of the 3D momentum distribution.

which were optimum to acquire 2D images of good quality. During the acquisition of the photoelectron signal, the MCP detector was gated for a time window of 200 ns, synchronized with the laser pulses and the pulsed valve. The valve was operated at a repetition rate of 100 Hz. Under these conditions, the pressure in the interaction chamber was around 1.1×10^{-5} mbar.

A typical raw image measured with the VMI spectrometer at a pump-probe time delay of 10 fs is shown in Fig. 5.8. The laser was polarized along the vertical axis, which is the axis of cylindrical symmetry of the 3D momentum distribution as discussed earlier. The projected velocity distribution is symmetric around the vertical axis, as can be seen in the raw image. A ring of constant radius corresponds to the photoelectrons with same magnitude of the initial velocity.

5.4.1 Abel inversion of 2D VMI images

The velocity map imaging technique requires the use of an Abel inversion method to obtain 3D momentum distributions from the measured 2D projections. The only necessary condi-

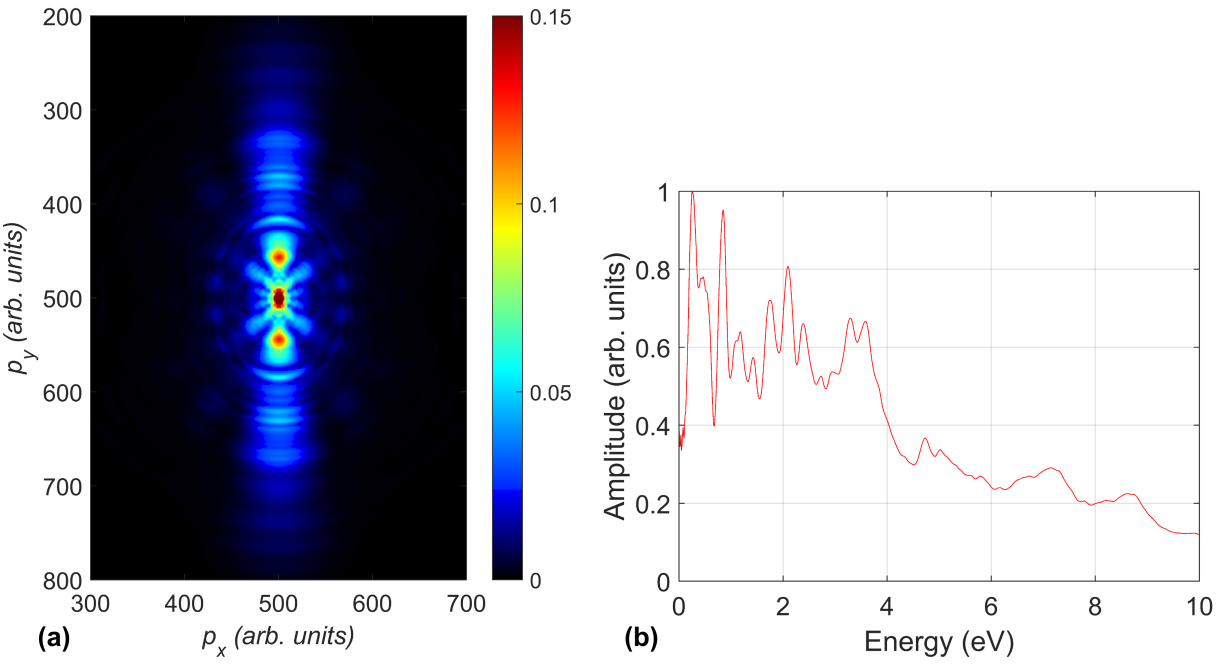

Figure 5.9: (a) A slice through the 3D momentum distribution obtained by applying an inversion procedure based on a Legendre polynomial expansion to the raw image shown in Fig. 5.8 and (b) Photoelectron kinetic energy distribution obtained by integrating the slice of the 3D distribution within a narrow cone (8°) along the polarization axis. Several peaks in the low energy region indicate electron interferences while ATI peaks in the high energy region are smeared out due to the broad bandwidth of few-cycle laser pulses.

tion for the Abel inversion is that the detector plane should contain an axis of cylindrical symmetry, which is often the case in photoionization experiments as mentioned earlier. A number of inversion procedures [158–162] exist to reconstruct the initial 3D momentum distribution from the 2D distribution measured using the MCP detector. In this work, an inversion procedure based on a Legendre polynomial expansion was utilized to perform the inverse Abel transform.

Figure 5.9(a) shows a slice through the 3D momentum distribution that was obtained by applying an inverse Abel transform on the raw image shown in Fig. 5.8. The 2D slice was integrated within a narrow cone (8°) along the laser polarization axis [i.e. the y-axis of the slice through 3D distribution shown in Fig. 5.9(a)]. The resulting distribution as a function of radial coordinate i.e. photoelectron kinetic energy is shown in Fig. 5.9(b). Several peaks appearing in the radial distribution reflect the electron interferences as discussed in section 5.1 and above-threshold ionization (ATI). The ATI peaks, which mostly smear out due to the broad bandwidth of the laser pulses can also be seen in both the 2D raw image and the slice of 3D distribution, especially in the region of large initial velocities.

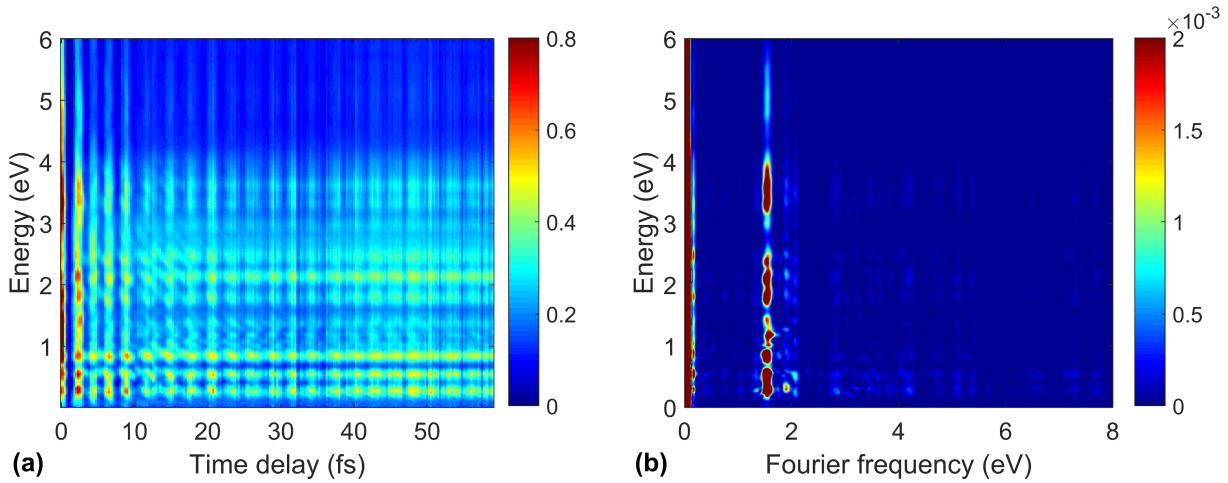

Figure 5.10: (a) Experimentally measured photoelectron spectra in argon as a function of the pump-probe time delay for pump and probe peak intensities of $\sim 2 \times 10^{14}\,\mathrm{W/cm^2}$ and $\sim 1.6 \times 10^{13}\,\mathrm{W/cm^2}$. For energies below 2 eV, the hyperbolic interference fringes are slightly visible. But strong oscillations that appear on the background overshadow the fringes, leading to a low signal-to-noise ratio. (b) Fourier transform of the photoelectron spectra along the delay axis. A strong signal at a Fourier frequency of $\sim 1.55\,\mathrm{eV}$ dominates over the delay-dependent lines that are expected to appear, as in the TDSE calculation [cf. Fig. 5.2(b)].

5.4.2 Pump-probe scan

Once the VMI spectrometer was optimized to acquire 2D momentum distributions at a particular pump-probe delay, the translation stage in the probe arm was controlled by an interface software to delay the probe pulse with respect to the pump pulse, in the range of $-20\,\mathrm{fs}$ to $60\,\mathrm{fs}$ with a resolution of $0.25\,\mathrm{fs}$. For each time delay, a 2D momentum distribution was recorded by integrating over 200 acquisitions. The 3D momentum distribution corresponding to each 2D image was reconstructed by using an inverse Abel transform, and a kinetic energy distribution was calculated by integrating the momentum of the photoelectrons emitted within a narrow cone around the laser polarization axis as described in the previous subsection.

The peak intensities of the pump and the probe pulses were calculated based on a measurement of the average power and the pulse duration before the spectrometer, and the focused beam size at the focus of the spherical mirror. For the experimental data presented below, the pump and probe peak intensities were estimated to be $2 \times 10^{14}\,\mathrm{W/cm^2}$ and $1.6 \times 10^{13}\,\mathrm{W/cm^2}$ respectively.

Figure 5.10(a) shows the experimentally measured photoelectron kinetic energy distribution along the laser polarization axis as a function of pump-probe time delay. At a zero time delay, the pump and the probe pulses are overlapped both in time and space, and their interference leads to a strong signal. At positive time delays where the pump pulse precedes the probe pulse, the hyperbolic interference fringes are observed predominantly at low kinetic energies. However, the hyperbolic interference pattern is overshadowed by a

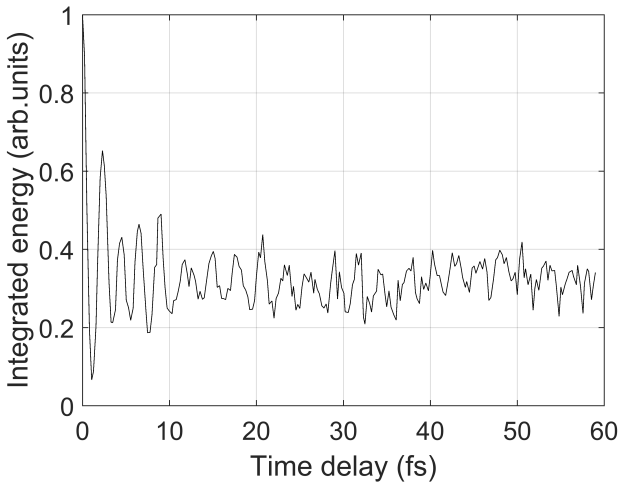

Figure 5.11: (a) Signal integrated along the energy axis of the photoelectron spectra as a function of the delay. Besides the strong interference signal around zero time delay, there is a periodic oscillation with a time period of ~ 2.5 fs.

strong background that is periodic and that appears over the whole range of pump-probe time delays. Indeed, the Fourier transform of the photoelectron spectra along the time delay axis, as shown in Fig. 5.10(b) shows a strong signal at a Fourier frequency of $\sim$ 1.55 eV. In Fig. 5.11, the photoelectron signal is integrated over all kinetic energies. As can be clearly seen, the oscillation is present for all time delays with an approximate period of 2.5 fs.

These background oscillations are attributed to the pedestals present in the IR pulses from the laser system. This has been confirmed by calculating optical interferences between the pump and the probe pulses at different time delays. The ratio of the pump and probe intensities is arbitrarily chosen to be 16:1 and the optical fields are calculated utilizing the spectrum and spectral phase measured by the SPIDER. Figure 5.12(a) shows the electric fields of both the pump and the probe pulses. As compared to the optical fields of Gaussian-shaped pump and probe pulses with 6 fs FWHM pulse duration, as shown in Fig. 5.12(d), the long pedestals are clearly visible in the experimental laser pulse. The optical interferences between the pump and the probe pulses are calculated for both cases at pump-probe time delays of 20 fs [see Figs. 5.12(b) and (e)] and 50 fs [see Figs. 5.12(c) and (f)]. The comparison suggests that the long pedestals present in the experimental laser pulses introduced the periodic oscillation signal on top of the hyperbolic fringes in the experimentally measured photoelectron spectra.

Additional pump-probe scans were also recorded for slightly different experimental conditions (e.g. for a different peak intensity of the probe pulse). In all experimentally measured photoelectron spectra, the strong oscillation pattern dominates over the hyperbolic interference fringes as discussed earlier. This suggests that the calculation of amplitudes from the 2D Fourier map that will ultimately determine the population of the bound states of strong-field excited argon is hindered by the background oscillation pattern. Therefore,

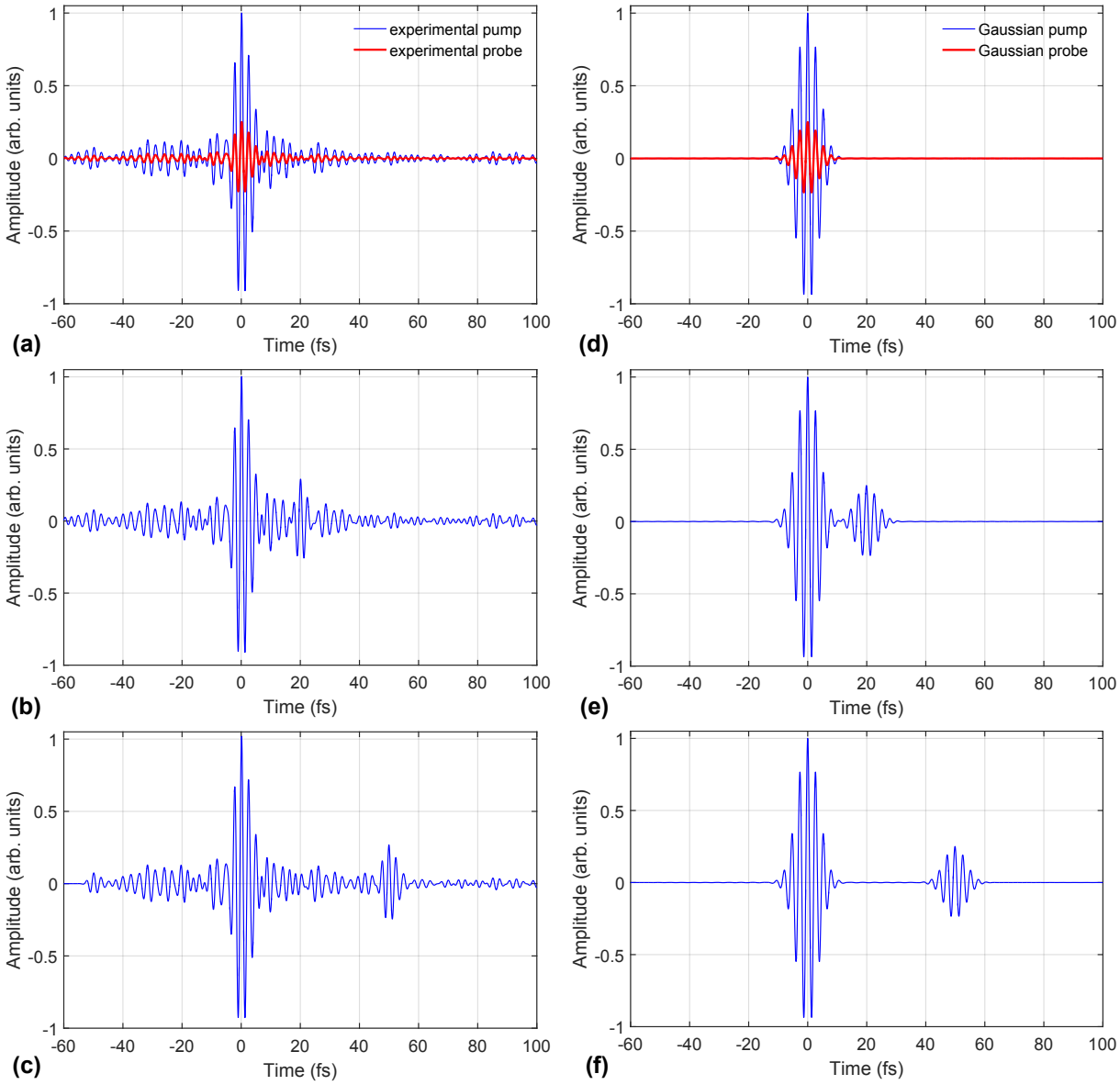

Figure 5.12: Calculation of optical interferences between the experimental pump and probe pulses, as compared to Gaussian-shaped pump and probe pulses. Panels (a) and (d) shows the electric fields of the pump and probe pulses that corresponds to the experimental and a Gaussian-shaped pulse, respectively [for a pump-probe intensity ratio of 16:1]. When the probe pulse is delayed with respect to the pump by 20 fs, the optical interferences for both sets of pulses are compared in panels (b) and (e). A similar comparison for a time delay of 50 fs is shown in panels (c) and (f). This indicates that the long pedestals of the experimental laser pulses, which are significant even for a large time delay, are the origin of the strong oscillations observed in the experimentally measured photoelectron spectra.

understanding the characteristics and the origin of the unwanted oscillations is critically important. At first, a numerical method of singular value decomposition was utilized in the experimental photoelectron spectra in order to decouple the oscillation pattern from the delay- and energy-dependent hyperbolic signal. Later, numerical simulations were performed by solving the time-dependent Schrödinger equation utilizing the experimentally measured temporal shape of the laser pulses [cf. Fig. 5.5(b)]. The outcomes of both approaches are described in the following sections.

5.5 Singular value decomposition

5.5.1 Introduction

In linear algebra, singular value decomposition (SVD) is a mathematical operation on a matrix which decomposes the matrix into three different matrices. A matrix M of size $m \times n$ can be factored into three matrices U, S and V of size $m \times m$, $m \times n$ and $n \times n$ respectively as follows:

$$M = USV^T \tag{5.9}$$

where U and V are unitary matrices and S is a rectangular diagonal matrix. The diagonal elements of S are known as singular values of the matrix M and typically arranged in descending order from the upper left to the lower right. The singular values are often called SVD components. Equation 5.9 can be expressed as [163],

$$M = \sum_{i}^{n} s_i \mathbf{u_i} \mathbf{v_i^T}, \tag{5.10}$$

which means that the matrix M is decomposed into a weighted sum of outer products ($\mathbf{u_i} \mathbf{v_i^T}$) of vectors. The vectors u_i and v_i^T are the column and row vectors of the matrices U and V^T respectively. s_i is the singular value which represents the weight of the i^{th} component of the sum.

SVD has been widely used for data analysis in many areas including time-resolved spectroscopy [164]. In the analysis of spectroscopic data, SVD allows the differentiation of noise and signal, thus offering a possibility to decouple noise from signal. As mentioned earlier, the 2D data matrix can be represented by two sets of linearly independent vectors weighted by singular values. If only a subset of singular values and the corresponding vectors are chosen appropriately, the noise in the data matrix is significantly reduced. The individual contribution of noise and the signal of interest in the data set can be estimated based on the magnitude of the singular values.

As previously mentioned, the experimentally measured photoelectron spectra [Fig. 5.10(a)] contains, in addition to the signal, a strong oscillation pattern that appear for all photoelectron energies. The energy and time dependencies of the unwanted oscillations are separable and can be approximated by a bilinear model. This means the oscillation at a given photoelectron energy changes only as a function of pump-probe delay while the oscillation along

the energy axis is independent of time. The bilinear approximation allows to decompose the data matrix M into a product of linearly independent vectors according to,

$$M = ED^T \tag{5.11}$$

where M_{ij} represents the signal at the time-delay i and energy j. The $m \times r$ matrix E contains a set of column vectors that correspond to a time-independent part of the oscillation pattern. Similarly, the $n \times r$ matrix D consists of a delay-dependent part in its rows. However, the signal of interest and background noise in the data don't fulfill the bilinear assumption.

If the SVD method is utilized for the data matrix, the large singular values or SVD components represent the unwanted oscillation pattern whereas the information about the signal of interest including the background noise is carried by the smaller singular values. If the oscillation is constant along the energy axis, the largest SVD component along with the corresponding set of vectors is enough to extract the contribution of the oscillation pattern to the data matrix. Otherwise, more than one SVD components have to be set zero to minimize the oscillations. The number of SVD components that represents the oscillation pattern can be determined by removing their cumulative contribution from the data set based on their singular values. This largely depends on the strength of the oscillations compared to the signal of interest, and their relative phase along the energy axis. In this work, the exact number of SVD components that needs to be removed has been checked qualitatively by setting the strong singular values to zero, and looking at the reconstructed data matrix and its 2D Fourier map.

5.5.2 Analysis of experimental data with SVD

The experimentally measured photoelectron spectra as a function of time delay is a rectangular matrix containing the kinetic energy distribution as column vectors for a set of time delays. According to Eq. 5.10, the data matrix can be decomposed into a sum where each SVD component is the weight of the outer product of the energy and time-delay vectors. It is clear that the contribution of the i^{th} SVD component in the photoelectron spectra is determined by the singular value s_i. While removing the unwanted oscillation pattern corresponding to the large singular values, the number of SVD components has to be appropriately chosen so that the hyperbolic interference fringes carrying the information of the bound electron wave packet are not affected.

The SVD was utilized for the experimentally measured photoelectron spectra shown in Fig. 5.10(a). The experimental data matrix (M) was decomposed into three matrices- U, S and V according to Eq. 5.9. The dominant SVD components were checked looking at the singular values of the matrix S. Figure 5.13(a) shows the normalized singular values corresponding to the first 50 SVD components. As can be seen clearly, the first few components are much stronger than the rest. These are the components corresponding to the strong background oscillations. The contribution of the background oscillations to the data matrix can be observed by setting the weak singular values in the diagonal of the matrix

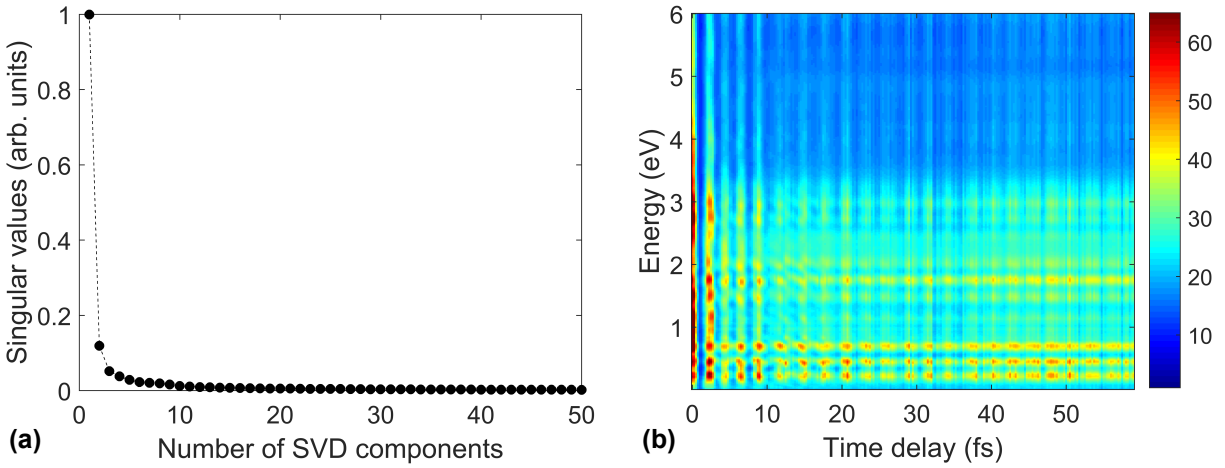

Figure 5.13: (a) The first 50 singular values of the data matrix corresponding to the experimental photoelectron spectra as a function of the number of SVD components. (b) The cumulative contribution due to the first 10 SVD components to the photoelectron spectra. The 10 SVD components were found to be optimum to decouple the unwanted oscillation pattern and were removed from the data matrix.

S to zero. As an example, the first 10 singular values of the matrix S are kept unchanged and the rest is set to zero, resulting in the matrix S'. Then, the original data matrix is reconstructed using the matrices U, S' and V, according to

$$M' = US'V^T. \tag{5.12}$$

The new data matrix M' is shown in Fig. 5.13(b), which contains the contribution of the first 10 components to the measured photoelectron spectra. This reflects the dominance of the oscillations in the data matrix over the interference fringes.

When the background oscillations are removed from the data matrix i.e. M' is subtracted from M, the interference fringes are better visible. The first 10 components with normalized singular value higher than 0.05 were found to be optimum to decouple the significant part of the oscillation pattern. As can be clearly seen in Fig. 5.14(a), hyperbolic fringes appear in the photoelectron spectra for energies below 3 eV. But the hyperbolas are slightly distorted and suffer from a very low signal-to-noise ratio. Nevertheless, Fourier transformation along the delay axis gives a clear indication of tilted lines as a function of Fourier frequency [5.14(b)]. With the advantage of having preliminary TDSE calculations [Fig. 5.2], several excited states of argon can be approximately assigned to the tilted lines as indicated by the arrows. However, the quantitative analysis, in particular the retrieval of amplitudes and phases of the wave packet components is difficult and requires an improvement of the signal-to-noise ratio.

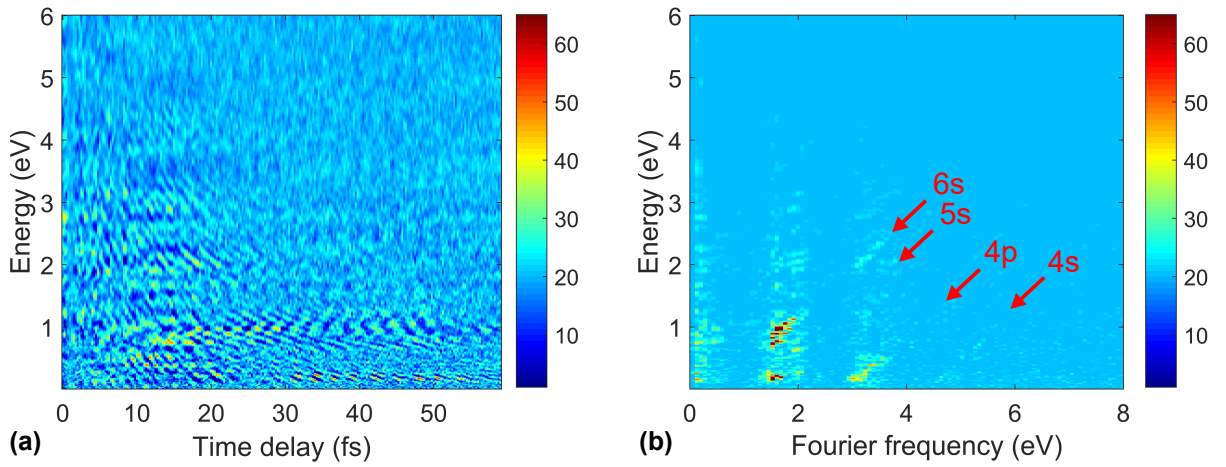

Figure 5.14: (a) Experimentally measured photoelectron spectra as a function of time delay after removing the first 10 SVD components. The hyperbolic fringes are now better visible compared to the original data set [see Fig. 5.10]. (b) Fourier transform of the photoelectron spectra shown on the left, which clearly indicates the possibility of identifying the excited states of argon that form the bound wave packet. However, the low signal-to-noise ratio hinders a complete characterization of the bound wave packets. Keeping the preliminary TDSE simulation in mind [Fig. 5.2], several tilted lines are approximately assigned to 4s, 4p, 5s and 6s states as indicated by the arrows.

5.6 TDSE calculations

The comparison between the preliminary TDSE calculations performed by Sascha Birkner [24], which were presented in section 5.2 and the experimental results shown in section 5.4 reveals that there is no indication of the background oscillation pattern in the photoelectron spectra simulated by the TDSE. It is worth noting that there were two differences between the preliminary simulation and the experiment. First, the temporal shape of the pulses were cosine-squared in the above-mentioned simulation which was not exactly the case in the experiment. In addition, the pump and probe peak intensities used in that simulation were slightly lower than those used in this experiment. These situations were investigated systematically in a new set of TDSE calculations, utilizing the experimentally characterized pulse profiles and corresponding peak intensities for the pump and the probe pulses.

5.6.1 Calculations using experimental pulse profiles

The TDSE calculation was extended by using the experimental pulse profiles that were retrieved from the SPIDER measurement [see Fig. 5.5(b)]. As can be seen in the figure, the main lobe in the experimental pulse profile was accompanied by pre- and post-pedestals extending up to a temporal window of 80 fs. These pulse pedestals with an extended background are the result of uncompensated spectral phase and sharp peaks in the spectrum as seen in Fig. 5.5(a). The pump and probe peak intensities were chosen to be $1 \times 10^{14}\,\mathrm{W/cm^2}$ and $2.5 \times 10^{13}\,\mathrm{W/cm^2}$ respectively, close to the estimated intensities in the experiment. The

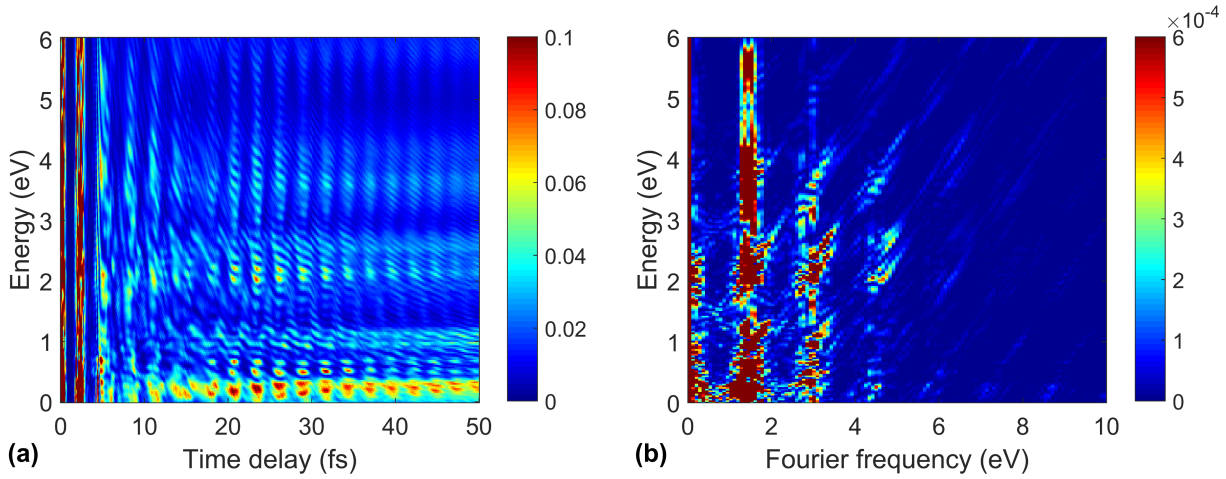

Figure 5.15: (a) Calculated photoelectron spectra (along the laser polarization axis) as a function of pump-probe delay for pump and probe peak intensities of $1 \times 10^{14}\,\mathrm{W/cm^2}$ and $2.5 \times 10^{13}\,\mathrm{W/cm^2}$, respectively. The hyperbolic fringes are visible when the pump pulse precedes the probe pulse. As in the experimental photoelectron spectra, an unwanted periodic oscillation appears in this case too, reducing the signal-to-noise ratio. (b) Corresponding 2D Fourier map, obtained by Fourier transformation of the photoelectron spectra along the time delay axis. As expected, several tilted lines are observed as a result of the interference between the reference and the unknown electron wave functions as discussed earlier. Moreover, additional lines appear compared to the calculation [Fig. 5.2(b)] using pedestal-free (cosine-squared pulse shape) pump and probe pulses. See the text for details.

probe pulse was delayed with respect to the pump pulse from 0 fs to 50 fs in steps of 0.1 fs.

The calculated photoelectron spectra (along laser polarization axis) as a function of pump-probe time delay are shown in Fig. 5.15(a). As expected, a strong signal appears around small time delay due to the overlap of the pump and probe pulses, and the hyperbolic interference fringes are visible in the region where the probe pulse is further delayed with respect to the pump pulse. As in the experimental photoelectron spectra [Fig. 5.10(a)], the oscillation pattern appears on top of the interference fringes in this case. Nevertheless, the hyperbolas are better visible with reduced noise background compared to the experimental photoelectron spectra. Furthermore, the 2D Fourier map, obtained by Fourier transformation of the spectra along the delay axis, as shown in Fig. 5.15(b), shows three noticeable features:

1. A vertical line at a Fourier frequency of ∼1.54 eV is observed which corresponds to the oscillation pattern in the photoelectron spectra as seen in the experimental data [Fig. 5.10(a)]. The pattern was not present in the photoelectron spectra obtained from the preliminary TDSE calculation using cosine-squared, pedestal-free pulses [Fig. 5.2(a)]. This clearly indicates that the unwanted periodic oscillation is due to the pulse pedestals present in the experimental laser pulses.

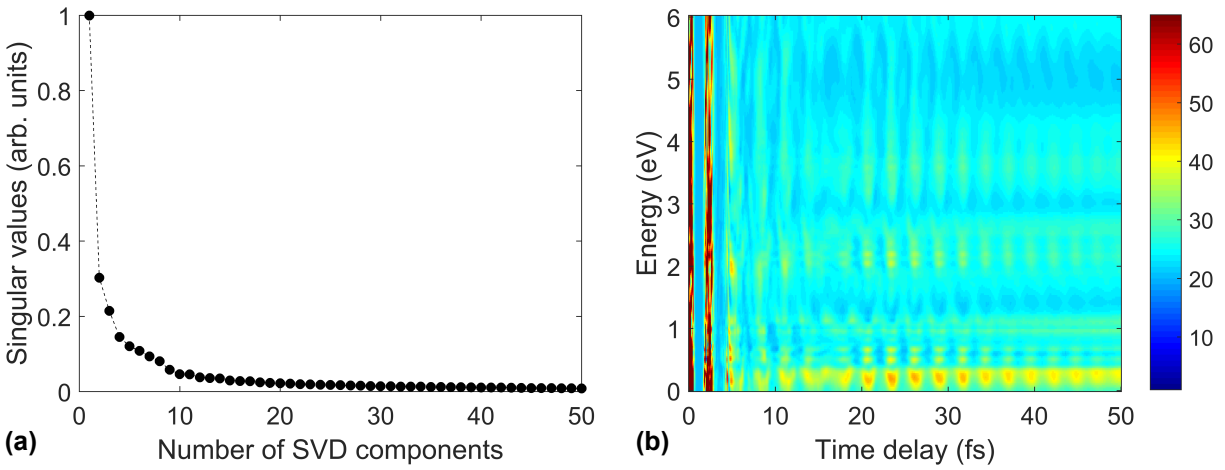

Figure 5.16: (a) The first 50 singular values of the data matrix corresponding to the calculated photoelectron spectra [Fig. 5.15(a)] as a function of the number of SVD components. (b) The cumulative contribution of the first 9 SVD components to the calculated photoelectron spectra. The first 9 SVD components with normalized singular values higher than 0.05 were removed from the data matrix which was found to be optimal for decoupling the oscillation pattern from the signal.

2. There are a series of tilted lines with an inclination angle of $\sim 45°$. Compared to the results for the TDSE calculation with pedestal-free cosine-squared pulses [Fig. 5.2(b)], additional lines appear that suggest a splitting of the tilted lines corresponding to the bound states of the strong-field excited argon.

3. The tilted lines intersect the horizontal axis for both negative and large positive Fourier frequencies. The latter lines at large positive frequencies intersect the horizontal axis at frequencies higher than 5 eV. But there are no excited states with binding energies >5 eV in the case of strong-field excited argon. The former lines pointing towards negative Fourier frequencies are even more difficult to interpret.

The above mentioned features raise some interesting questions. Does the probe peak intensity have any influence on these features? Is the background oscillation pattern due to the pedestals in the pump pulse or in the probe pulse, or in both? What causes the additional tilted lines to appear and why do they intersect the horizontal axis for both negative and large positive Fourier frequencies? In order to look for the answers of these questions, additional TDSE calculations were performed, reducing the probe peak intensity and using a cosine-squared pulse shape either for the pump pulse only, or for the probe pulse only. The outcomes of the calculations are discussed in the following subsections.

Analysis using SVD

Before going into a further discussion of the characteristics of the 2D Fourier map shown in Fig. 5.15(b), the SVD method was used to decouple the hyperbolic fringes and the un-

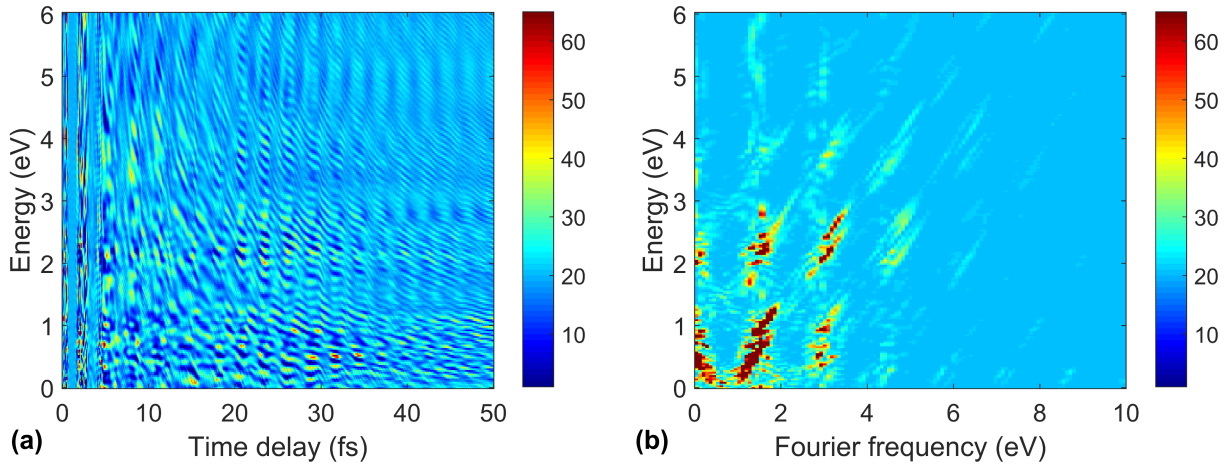

Figure 5.17: (a) The calculated photoelectron spectra (for pump and probe peak intensities of $1 \times 10^{14}\,\mathrm{W/cm^2}$ and $2.5 \times 10^{13}\,\mathrm{W/cm^2}$ respectively) as a function of time delay after removing the first 9 SVD components. The background oscillation is reduced and the visibility of the interference fringes is slightly better compared to Fig. 5.15(a). The hyperbolic oscillation pattern still remains on the top of the vertical interference fringes. (b) Corresponding Fourier transform along the delay axis. The characteristics of the 2D Fourier map, in particular the tilted lines (as described in the previous case without SVD) remains unchanged, but the signal-to-noise ratio is enhanced due to the use of the SVD method.

wanted oscillation pattern as in the case of the experimental data. Figure 5.16(a) shows the first 50 singular values of the calculated data matrix as a function of the number of SVD components, which indicates that the weight of the first few components in the decomposition is much larger than that of the rest. The SVD components with normalized singular value higher than 0.05 were found to dominate the vertical interference fringes. Their contribution to the calculated photoelectron spectra is shown in Fig. 5.16(b), which, as expected, displays an oscillation pattern over the whole range of pump-probe time delay. The reconstructed photoelectron spectra resulting from the subtraction of that contribution from the original data matrix is shown in Fig. 5.17(a). As can be seen clearly, the oscillation pattern is still hindering the observation of the interference fringes. The Fourier transformation of the spectra along the delay axis, as shown in Fig. 5.17(b) shows that all the features, which are discussed in the case of Fig. 5.15(b), are still present except that the vertical line corresponding to the unwanted oscillation pattern is much weaker. These observations imply that the SVD method, as expected, has reduced the background oscillation thereby enhancing the signal-to-noise ratio.

5.6.2 Influence of the probe intensity

The intensity of the probe pulse was reduced from $2.5 \times 10^{13}\,\mathrm{W/cm^2}$ to $6.25 \times 10^{12}\,\mathrm{W/cm^2}$ so that the ratio of the pump-to-probe peak intensity is 16:1, the ratio used in the preliminary TDSE calculations with pedestal-free, cosine-squared pulses. The rest of the parameters

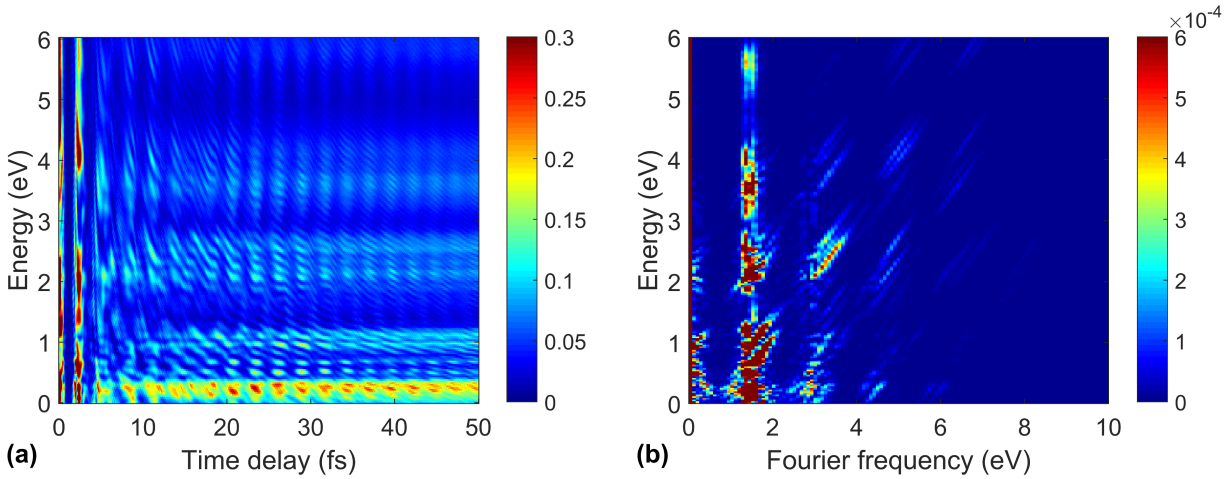

Figure 5.18: (a) Calculated photoelectron spectra as a function of pump-probe delay for pump and probe peak intensities of $1 \times 10^{14}\,\mathrm{W/cm^2}$ and $6.25 \times 10^{12}\,\mathrm{W/cm^2}$, respectively. As was the case for the higher probe peak intensity, electron interferences are visible when the pump pulse precedes the probe pulse. However, the signal-to-noise ratio is low due to background oscillations. (b) Corresponding Fourier transform along the delay axis. Several tilted lines appear in the Fourier domain, which were observed in the previous TDSE calculations already. Compared to the previously observed 2D Fourier maps, a slight change in the distribution of the tilted lines (with weaker signal) are visible due to the reduced probe peak intensity.

including the experimentally measured pulses shapes for both the pump and probe pulses were kept constant and the photoelectron spectra thus obtained were analyzed following the same procedure as used in the case of the higher probe intensity.

Figure 5.18(a) and (b) show the photoelectron spectra and the corresponding Fourier transform along the time-delay axis, respectively. Similar to the photoelectron spectra observed for higher probe intensity [see Fig. 5.15], hyperbolic interference fringes are visible, slightly distorted and shadowed by periodic oscillations also in this case. Similarly, the 2D Fourier map is comparable to that observed for higher probe intensity. The signal in the 2D Fourier map is integrated along the tilted lines and plotted as a function of the intercept of the tilted lines with the Fourier frequency axis, as shown in Fig. 5.19 (see blue curve). Compared to the case of higher probe intensity (red curve), most of the peaks are observed almost at the same Fourier frequencies and the signal in some regions is slightly stronger for higher probe intensity. As the lines are split and closely spaced in each case, it is unclear how the lines can be associated with the excited states of argon. Altogether, it can be concluded that reducing the probe peak intensity (within the range of intensities considered here) has almost no influence on the characteristics of the tilted lines.

For completeness, the SVD method was also utilized for this data matrix. The contribution of the unwanted oscillation pattern to the photoelectron spectra was removed by setting the first 7 SVD components to zero, which were found to be dominant. The reconstructed spectra and the corresponding Fourier transform along the delay axis, as shown in Fig. 5.20(a) and (b) respectively, display all the features that were observed in the case

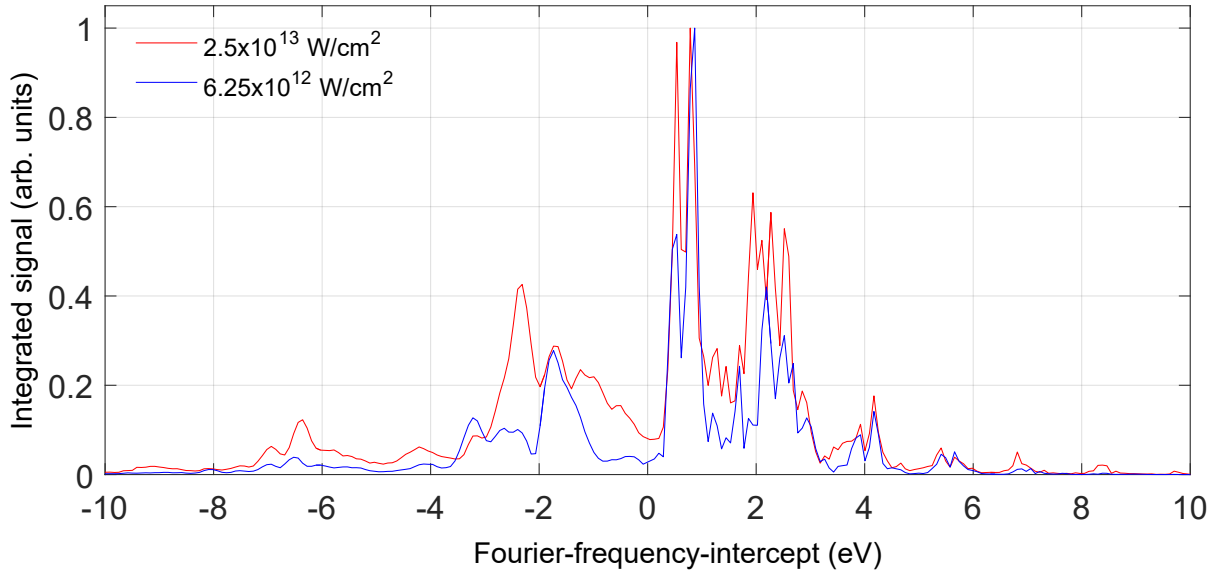

Figure 5.19: Signals integrated along the tilted lines in the 2D Fourier maps corresponding to probe peak intensities of $2.5 \times 10^{13}\,\mathrm{W/cm^2}$ (red curve) and $6.25 \times 10^{12}\,\mathrm{W/cm^2}$ (blue curve).

of a higher probe intensity. Therefore, it is concluded that the peak intensity of the probe pulse has no significant influence on the characteristics observed in the 2D Fourier map of the photoelectron spectra.

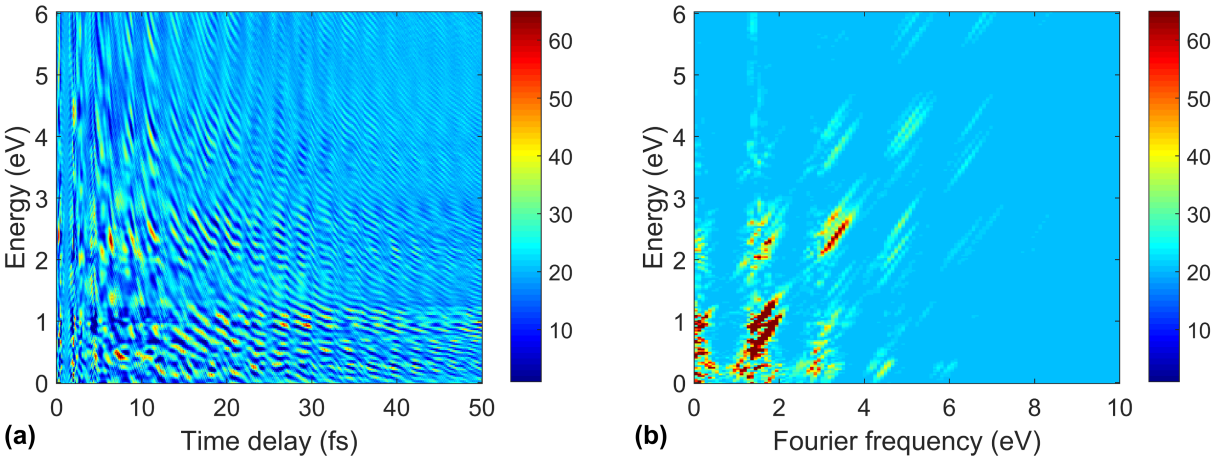

Figure 5.20: (a) Calulated photoelectron spectra as a function of time delay (for pump and probe peak intensities of $1 \times 10^{14}\,\mathrm{W/cm^2}$ and $6.25 \times 10^{12}\,\mathrm{W/cm^2}$ respectively) after removing the first 7 SVD components. The interference fringes are better visible due to the reduced noise background. (b) Corresponding Fourier transform along the delay axis. Compared to the 2D Fourier map without using SVD [Fig. 5.18(b)], the vertical line corresponding to the background oscillation is significantly reduced and all the other characteristics remains visible as expected.

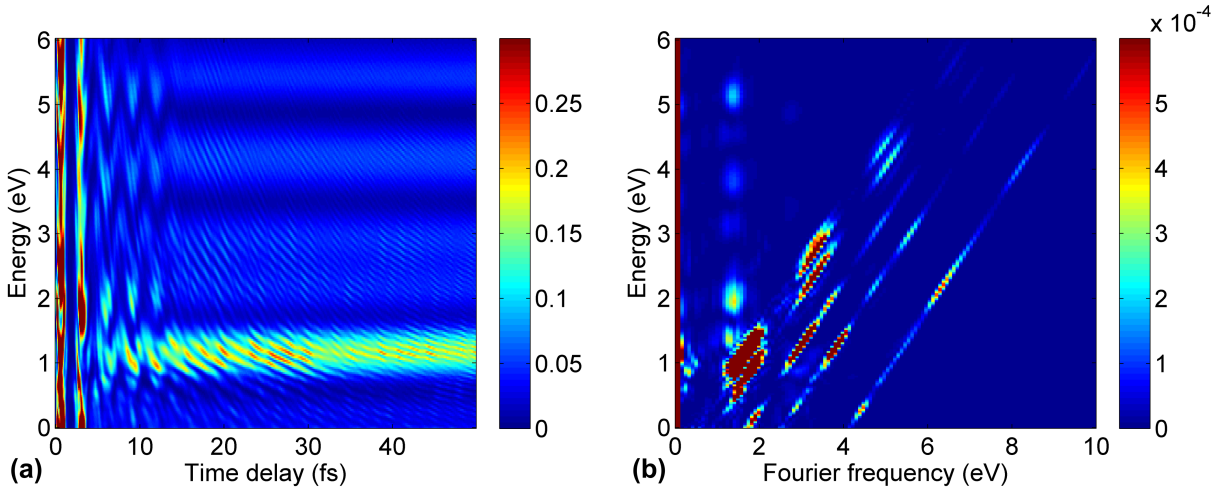

Figure 5.21: (a) Calculated photoelectron spectra as a function of pump-probe delay for a pump with a cosine-squared pulse shape and a probe with the experimentally measured temporal shape, with peak intensities of $8.4 \times 10^{13}\,\mathrm{W/cm^2}$ and $5.6 \times 10^{12}\,\mathrm{W/cm^2}$ respectively. Interestingly, there are no vertical oscillation patterns visible, while the interference fringes are much clearer, especially after the pump-probe delay >10 fs. (b) Corresponding Fourier transform along the delay axis. The tilted lines due to the interference between the reference and the unknown electron wave packets are clear without splitting and without intersecting the horizontal axis at negative Fourier frequencies. The photoelectron spectra and the corresponding Fourier map are very similar to the ones obtained from the preliminary TDSE simulation using cosine-squared pump and cosine-squared probe pulses [see Fig. 5.2(a)].

5.6.3 Impact of pulse pedestals

It is clear from the previous discussion that pulse pedestals present in the experimental laser pulses are responsible for the strong background oscillations in the photoelectron spectra and accordingly for the unwanted features observed in the Fourier domain. It is important to figure out if the unwanted characteristics observed in the 2D Fourier map depend on the pulse pedestals of either the pump and the probe pulses, or both. In order to distinguish the individual contribution of the pedestals in the pump and the probe pulses, TDSE calculations were repeated under two different conditions as follows:

Pedestal-free cosine-squared pump and experimental probe pulses

In the first TDSE calculation, a cosine-squared shape for the pump pulse and the experimentally measured temporal shape for the probe pulse were used. The peak intensities of the pump and the probe pulse were set to $8.4 \times 10^{13}\,\mathrm{W/cm^2}$ and $5.6 \times 10^{12}\,\mathrm{W/cm^2}$ respectively. The pulse duration of the pump pulse was 6 fs (FWHM) and rest of the parameters were kept constant.

As can be seen clearly in the calculated photoelectron spectra shown in Fig. 5.21(a), the hyperbolic fringes are much clearer with largely improved signal-to-noise ratio and

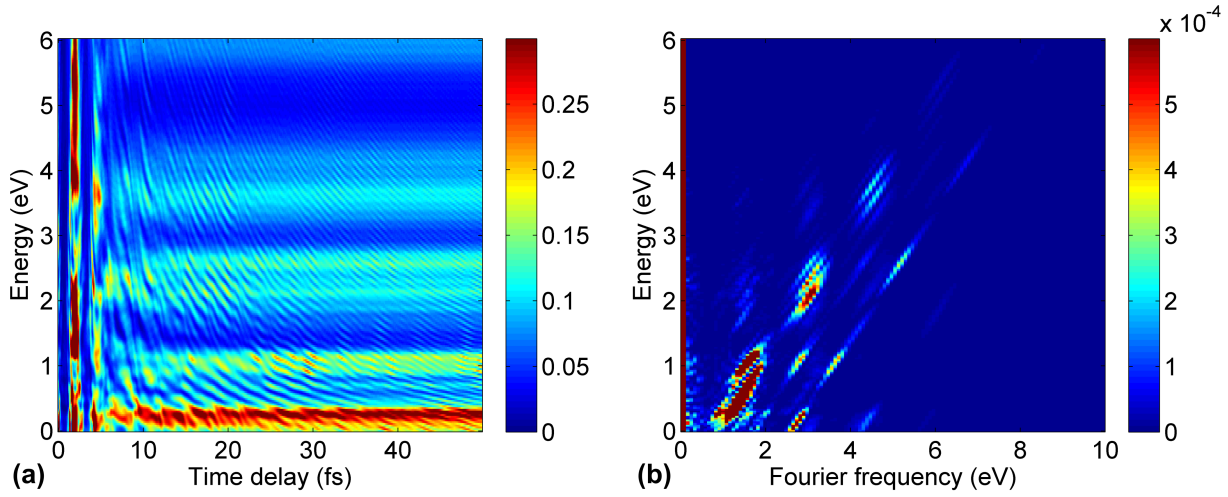

Figure 5.22: (a) Calculated photoelectron spectra as a function of pump-probe delay for the experimental pump and a cosine-squared probe pulse with peak intensities of $8.4 \times 10^{13}\,\mathrm{W/cm^2}$ and $5.6 \times 10^{12}\,\mathrm{W/cm^2}$ respectively. There are no vertical oscillation patterns, but the hyperbolic interference fringes are slightly distorted compared to the previous case [see Fig. 5.21]. (b) Corresponding Fourier transform along the delay axis. The tilted lines due to the interference between the reference and the unknown electron wave packets are accompanied by additional lines including the lines that intersect the horizontal axis at negative Fourier frequencies. The photoelectron spectra is not far from that obtained with the experimental pulse shape for both pump and probe pulses [see Fig. 5.18(a)] except that there are dominant vertical oscillations in the latter case.

there are almost no background oscillations visible. Indeed, the photoelectron spectra look quite similar to those obtained in the calculation using cosine-squared pump and cosine-squared probe pulses [see Fig. 5.2(a)]. The Fourier transformation along the delay axis, as shown in Fig. 5.21(b) produces tilted lines at an inclination angle of 45° in the 2D Fourier map. There are no splittings of the lines and no additional lines are present at higher Fourier frequencies. Similarly, tilted lines that intersect the horizontal axis at negative frequencies are absent. These observations suggest that pulse pedestals in the pump pulse are responsible for the splitting of the tilted lines and the lines intersecting the horizontal axis at negative frequencies, and accordingly hindering the retrieval of amplitudes and phases of the excited states of the strong-field excited argon.

Experimental pump and pedestal-free cosine-squared probe pulses

The previous TDSE calculation was repeated by switching the temporal shape of the pump and the probe pulse. The shape of the probe pulse was cosine-squared with a peak intensity of $5.6 \times 10^{12}\,\mathrm{W/cm^2}$ and a pulse duration of 6 fs (FWHM), whereas the pump pulse was the experimentally measured laser pulse with a peak intensity of $8.4 \times 10^{13}\,\mathrm{W/cm^2}$.

Figure 5.22(a) shows calculated photoelectron spectra for the given set of parameters as a function of the IR-IR pump-probe delay. The hyperbolic fringes are slightly distorted

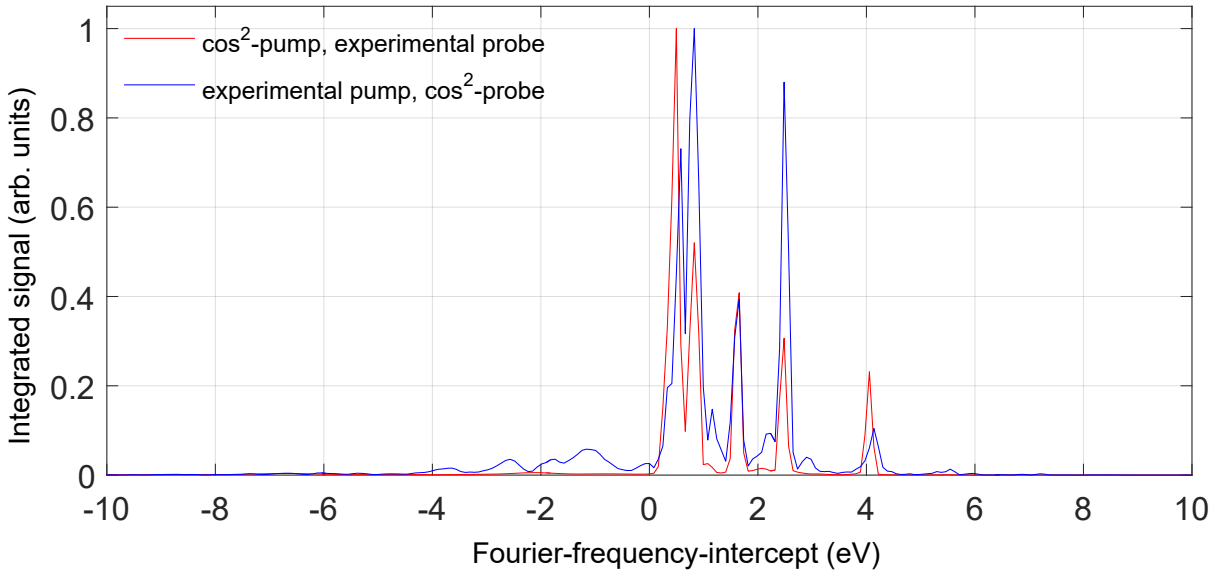

Figure 5.23: Signals integrated along the tilted lines in the 2D Fourier maps: the red curve corresponds to the case of a pedestal-free cosine-squared pump and the experimental probe pulse shape, whereas the blue curve corresponds to the experimental pump pulse and pedestal-free cosine-squared probe pulses.

compared to the previous simulation. Interestingly, there is no vertical oscillation pattern in the photoelectron spectra as in the previous case, which is further confirmed by the absence of the corresponding vertical line at a fixed Fourier frequency in the corresponding Fourier map [see Fig. 5.22(b)]. However, the splitting of the tilted lines is observed with a few lines that intersect the negative frequency axis as previously seen in the simulation with the experimental pulse shapes for both pump and probe pulses [see Fig. 5.18(b)]. The impact of pulse pedestals present in either the pump or the probe pulses can be compared by integrating the 2D Fourier maps along the tilted lines. Figure 5.23 shows the signals obtained from the integration of the 2D Fourier maps shown in Figs. 5.21(b) and 5.22(b). As mentioned earlier, the few tilted lines that intersect the negative frequency axis appear only when the pump pulse has a pedestal [see the blue curve in the negative frequency axis]. Moreover, a few additional peaks, which are due to the splitting of the main peaks, can be seen in the region of positive frequencies compared to the case where the pump pulse has a cosine-squared shape. Note that the peaks observed in the case of the pedestal-free cosine-squared pump (red curve) are very similar to those observed in the 2D Fourier map corresponding to the cosine-squared pump and cosine-squared probe [see Fig. 5.3].

In addition, the disappeared background oscillation pattern in both sets of pump-probe pulses suggests that the strong background oscillation and the very low signal-to-noise ratio in the experimentally measured photoelectron spectra originates from the long pedestals present in both the pump and probe pulses. The pedestals in the pump pulse are only responsible for the splitting of the tilted lines and for the lines that intersect the negative

frequency axis, however, the physical meaning of the negative intercepts is not clear yet.

Altogether, the TDSE simulations suggest that the pedestals in the pump and/or probe pulses have to be suppressed in order to avoid the background oscillation, thereby enhancing the signal-to-noise ratio in the photoelectron spectra. Furthermore, the pedestals in the pump pulses should strongly be minimized in order to avoid the splitting of the tilted lines in the corresponding Fourier map.

5.7 Summary

Electron interferometry has been demonstrated by performing an IR-IR pump probe experiment in which few-cycle laser pulses excite and ionize Argon atoms. Both continuum and bound wave packets were prepared by strong field ionization and excitation respectively, using an IR pump pulse. After a certain time delay, the bound wave packets were ionized by an IR probe pulse, leading to their interference with the continuum wave packets. The wave-packet interference was observed in experimentally measured photoelectron spectra acquired with a velocity map imaging spectrometer.

Analysis of the measured photoelectron spectra as a function of time delay revealed that there is a possibility to characterize the bound states of strong field excited Argon if the signal-to-noise ratio is enhanced. The measurement reflected most of the features that were expected from the simulation except that periodic oscillations shadowed the signal of interest and degraded the signal-to-noise ratio. The strong background was attributed to the pulse pedestals which were present in the pump and probe pulses. TDSE calculations showed that the pedestals in the pump pulse were mainly responsible for the unwanted features observed in the 2D Fourier map of the photoelectron spectra.

As the background periodic oscillations dominate over the hyperbolic interference fringes, pedestals in the few-cycle IR pulses have to be suppressed in order to improve the signal-to-noise ratio and accordingly to be able to retrieve the amplitudes and phases of the bound wave packet components. This can be done for example, by generating the second harmonic of the pump pulse. Experiments with few-cycle pulses with reduced pedestals have been planned in the near future and are expected to ease the characterization of the bound states of strong field excited Argon. Such experiments will bring the electron wave packet interferometry within the reach of few-femtosecond laser pulses, enabling the complete characterization of bound electron wave packets created by strong field excitation.

6 Summary and outlook

This thesis presents scientific research works, which were carried out during a PhD project within the framework of the European Industrial Doctorate (EID) program. The research was focused on the generation of few-cycle pulses along with the study of their spatiotemporal characteristics, and their applications in strong field physics.

The first part of the thesis focuses on the necessity of a high peak power, high energy pump laser for the generation of few-cycle pulses. For some applications e.g. in attosecond experiments using electron-ion coincidence detectors, scaling of the pulse repetition rate is important in order to speed up the data acquisition and to increase the signal-to-noise ratio. A brief review of laser technologies has revealed that thin-disk technology has been recognized as the most suitable configuration for scaling pulse energy and average power simultaneously. A pump laser based on a Yb:YAG thin-disk regenerative amplifier has been developed utilizing chirped-pulse amplification. Pulse energies >1 mJ were obtained at a pulse repetition rate of 25 kHz with sub-picosecond pulse duration in a table-top, compact setup. After the compressor, a maximum average power of 35 W was produced at 100 kHz whereas a maximum pulse energy of 1.6 mJ was extracted at 10 kHz with excellent pulse-to-pulse stability. The amplified beam profiles were close to the diffraction limit over a wide range of repetition rates. Further scaling of the average power keeping the pulse energy at millijoule-level can be foreseen if a multipass amplifier is used as a power booster. Indeed, kilowatt-level average power with >1 mJ pulse energy has already been demonstrated by using a multipass thin-disk amplifier following the regenerative amplifier.

Additionally, second and third harmonics of the amplified pulses were generated in BBO crystals. High conversion efficiencies $\sim 70\,\%$ are possible in the second harmonic generation leading to 16 W average power at 100 kHz with good beam quality. In third harmonic generation, a conversion efficiency up to 50 % has been achieved with excellent average power stability and good beam quality. These results strongly indicate that the laser system is ideal for pumping OPCPA in the visible and near-infrared spectral range.

Since the amplification of very short pulses is limited by the gain bandwidth of the laser medium and the gain narrowing effect, nonlinear pulse compression has been established as a route to reduce the pulse duration of high energy, high power ultrafast amplifiers. In this thesis, sub-picosecond pulses from the regenerative amplifier were compressed in a hollow-core Kagome fiber. As a first step, spectral broadening was performed in an air-filled Kagome fiber at atmospheric pressure, which shows the possibility of generating Fourier transform-limited pulses shorter than 100 fs. After the compensation of nonlinear chirp due to self-phase modulation, pulses as short as 130 fs with pulse energy >50 µJ (before the compressor) were achieved. Further scaling of the pulse energy was hindered by the ionization of air due to the high peak intensity. This limitation can be minimized by using

larger core fibers. Further spectral broadening that is necessary to support few-cycle pulses is possible by using either an additional spectral broadening stage or a gas-filled fiber along with the optimization of fiber parameters.

The second part of the thesis deals with spatiotemporal characteristics of a noncollinear OPCPA, where the spatiotemporal quality of the output pulses is an important factor that may limit the achievable peak intensity at focus. A high energy, few-cycle OPCPA system that is under development at the Max-Born-Institute has been modeled using a three-dimensional numerical code. In addition, spatiotemporal couplings in a noncollinear OPCPA have been studied, in general for a wide range of design parameters such as pump beam sizes, noncollinear angle and phase-matching geometry under different amplification conditions like pulse front matching, gain saturation and back conversion. In the case of unsaturated amplifiers, linear spatiotemporal distortions are always present except that angular dispersion vanishes at a noncollinear angle for which the gain bandwidth is maximum. In this case, pulse front tilt due to spatial chirp and temporal chirp also disappears if the pulses are compressed. when gain strongly saturates and back conversion from the signal to the pump occurs, nonlinear distortions dominate and the spatiotemporal quality of the amplified pulses is significantly deteriorated thereby strongly reducing the peak intensity. For a BBO-based noncollinear OPCPA pumped by the second harmonic of Yb-based amplifiers (with Gaussian pulse and beam shapes), it has been observed that the conversion efficiency has to be limited to $<20\,\%$ in order to minimize degradation of the peak intensity due to spatiotemporal distortions [106]. These numerical results will be very helpful to optimize OPCPAs ensuring better spatiotemporal quality of few-cycle pulses ultimately minimizing degradation of the peak intensity at focus. These simulations can be easily extended to experimental beam and pulse shapes and also to the mid-infrared spectral range. Recently, few-cycle pulses from the experimental OPCPAs were characterized by using a spatiotemporal characterization tool such as SEA-SPIDER (spatially encoded arrangement- spectral phase interferometry for direct electric field reconstruction) [25]. The simulation results can, in principle be complemented with those experimental observations extending the analysis further.

The last part of the thesis utilizes few-cycle, near-infrared pulses in electron interferometry. In a proof-of-principle interferometric, IR-IR pump-probe experiment using argon as a target, the excited states of strong field-excited argon, which may form a bound wave packet, were partially characterized by interfering the wave packet (considered as unknown) with a reference continuum wave packet. Electrons in the continuum were created by strong field ionization of argon atoms with a pump pulse. At the same time, the excited or bound states were populated by strong field excitation and frustrated-tunnel ionization. A time-delayed probe pulse ionizes the excited states introducing the electrons in the continuum. The electrons ionized by the pump pulse and the probe pulse interfere with each other depending upon the phase difference. The photoelectrons were detected using a velocity map imaging spectrometer. The experimentally measured photoelectron spectra suffered from low signal-to-noise ratio and a strong background oscillation as a function of pump-probe time delay. This hindered the retrieval of both the amplitudes and the phases of the excited states. Nevertheless, the analysis of the experimental observations was extended by using

simulation results obtained from time-dependent Schrödinger equation in the single active electron approximation. The unwanted background oscillation observed in the experimental data was attributed to the pulse pedestals present in the few-cycle IR pulses. Therefore, suppressing the pulse pedestals is necessary to reduce the background oscillation and to enhance the signal-to-noise ratio, which is expected to allow the complete characterization of excited states of strong field excited argon. One of the options to minimize the impact of pulse pedestals is to perform a two-color IR or IR-UV pump-probe experiment, where the second harmonic of the few-cycle pulses with reduced pulse pedestals can be used as either the pump or the probe. Numerical results suggested that pump pulses without pulse pedestals will be optimum to enhance the signal-to-noise ratio by suppressing the unwanted background oscillation. Such a proof of principle experiment with few-cycle IR pulses may bring electron wave packet interferometry within the reach of femtosecond pulses.

Bibliography

[1] L. E. Hargrove, R. L. Fork, and M. A. Pollack. Locking of He-Ne laser modes induced by synchronous intercavity modulation. *Applied Physics Letters*, 5(1):4, 1964.

[2] R. Ell, U. Morgner, F. X. Kärtner, J. G. Fujimoto, E. P. Ippen, V. Scheuer, G. Angelow, T. Tschudi, M. J. Lederer, A. Boiko, and B. Luther-Davies. Generation of 5-fs pulses and octave-spanning spectra directly from a Ti:sapphire laser. *Optics Letters*, 26(6):373, 2001.

[3] D. Strickland and G. Mourou. Compression of amplified chirped optical pulses. *Optics communications*, 56(3):219–221, 1985.

[4] A. Dubietis, G. Jonušauskas, A. Piskarskas, G. Jonu, and A. Piskarskas. Powerful femtosecond pulse generation by chirped and stretched pulse parametric amplification in BBO crystal. *Optics Communications*, 88(4-6):437–440, 1992.

[5] P. M. Paul, E. S. Toma, P. Breger, G. Mullot, F. Augé, P. Balcou, H. G. Muller, and P. Agostini. Observation of a Train of Attosecond Pulses from High Harmonic Generation. *Science*, 292(5522), 2001.

[6] K. Zhao, Q. Zhang, M. Chini, Y. Wu, X. Wang, and Z. Chang. Tailoring a 67 attosecond pulse through advantageous phase mismatch. *Optics Letters*, 37(18):3891–3893, 2012.

[7] F. Calegari, G. Sansone, S. Stagira, C. Vozzi, and M. Nisoli. Advances in attosecond science. *J. Phys. B: At. Mol. Opt. Phys.*, 49(6):062001, 2016.

[8] P. B. Corkum and F. Krausz. Attosecond science. *Nature Physics*, 3(6):381–387, 2007.

[9] F. Krausz and M. Ivanov. Attosecond physics. *Reviews of Modern Physics*, 81(1):163–234, 2009.

[10] M. Nisoli, S. De Silvestri, O. Svelto, R. Szipöcs, K. Ferencz, C. Spielmann, S. Sartania, and F. Krausz. Compression of high-energy laser pulses below 5 fs. *Optics letters*, 22(8):522–524, 1997.

[11] S. Bohman, A. Suda, T. Kanai, S. Yamaguchi, and K. Midorikawa. Generation of 5 fs, 50 mJ pulses at 1 kHz using hollow-fiber pulse compression. *Optics Letters*, 35(11):1887, 2010.

[12] X. Chen, A. Malvache, A. Ricci, A. Jullien, and R. Lopez-Martens. Efficient hollow fiber compression scheme for generating multi-mJ, carrier-envelope phase stable, sub-5 fs pulses. *Laser Physics*, 21(1):198–201, 2011.

[13] F. Böhle, M. Kretschmar, A. Jullien, M. Kovacs, M. Miranda, R. Romero, H. Crespo, U. Morgner, P. Simon, R. Lopez-Martens, and T. Nagy. Compression of CEP-stable multi-mJ laser pulses down to 4 fs in long hollow fibers. *Laser Physics Letters*, 11(9):095401, 2014.

[14] S. Hädrich, M. Kienel, M. Müller, A. Klenke, J. Rothhardt, R. Klas, T. Gottschall, T. Eidam, A. Drozdy, P. Jójárt, Z. Várallyay, E. Cormier, K. Osvay, A. Tünnermann, and J. Limpert. Energetic sub-2-cycle laser with 216 W average power. *Optics Letters*, 41(18):4332, 2016.

[15] J. Rothhardt, S. Demmler, S. Hädrich, J. Limpert, and A. Tünnermann. Octave-spanning OPCPA system delivering CEP-stable few-cycle pulses and 22 W of average power at 1 MHz repetition rate. *Optics express*, 20(10):10870–8, 2012.

[16] S. Prinz, M. Haefner, C. Y. Teisset, R. Bessing, K. Michel, Y. Lee, X. T. Geng, S. Kim, D. E. Kim, T. Metzger, and M. Schultze. CEP-stable, sub-6 fs, 300-kHz OPCPA system with more than 15 W of average power. *Optics Express*, 23(2):1388, 2015.

[17] F. J. Furch, A. Giree, F. Morales, A. Anderson, Y. Wang, C. P. Schulz, and M. J. J. Vrakking. Close to transform-limited, few-cycle 12 μJ pulses at 400 kHz for applications in ultrafast spectroscopy. *Optics Express*, 24(17):19293, 2016.

[18] A. Dubietis, R. Butkus, and A. Piskarskas. Trends in chirped pulse optical parametric amplification. *IEEE Journal of Selected Topics in Quantum Electronics*, 12(2):163–172, 2006.

[19] A. Baltuška, T. Fuji, and T. Kobayashi. Visible pulse compression to 4 fs by optical parametric amplification and programmable dispersion control. *Optics letters*, 27(5):306–308, 2002.

[20] G. Cirmi, C. Manzoni, D. Brida, S. De Silvestri, and G. Cerullo. Carrier-envelope phase stable, few-optical-cycle pulses tunable from visible to near IR. *Journal of the Optical Society of America B*, 25(7):B62, 2008.

[21] J. Nillon, O. Crégut, C. Bressler, and S. Haacke. Two MHz tunable non collinear optical parametric amplifiers with pulse durations down to 6 fs. *Optics express*, 22(12):14964–14974, 2014.

[22] T. Stanislauskas, R. Budriūnas, R. Antipenkov, A. Zaukevičius, J. Adamonis, A. Michailovas, L. Giniūnas, R. Danielius, A. Piskarskas, and A. Varanavičius. Table top TW-class OPCPA system driven by tandem femtosecond Yb:KGW and picosecond Nd:YAG lasers. *Optics Express*, 22(2):1865, 2014.

[23] F. J. Furch, S. Birkner, F. Kelkensberg, A. Giree, A. Anderson, C. P. Schulz, and M. J. J. Vrakking. Carrier-envelope phase stable few-cycle pulses at 400 kHz for electron-ion coincidence experiments. *Optics Express*, 21(19):274–276, 2013.

[24] S. Birkner. *Strong Field Ionization of Atoms and Molecules : Electron-Ion Coincidence Measurements at High Repetition Rate*. PhD thesis, Freie Universität Berlin, 2015.

[25] F. J. Furch, T. Witting, A. Giree, C. Luan, F. Schell, G. Arisholm, C. P. Schulz, and M. J. J. Vrakking. CEP-stable few-cycle pulses with more than 190 μJ of energy at 100 kHz from a noncollinear optical parametric amplifier. *Optics Letters*, 42(13):2495, 2017.

[26] J. Bromage, C. Dorrer, and J. D. Zuegel. Angular-dispersion-induced spatiotemporal aberrations in noncollinear optical parametric amplifiers. *Optics letters*, 35(13):2251–3, 2010.

[27] A. Zaukevičius, V. Jukna, R. Antipenkov, V. Martinėnaitė, A. Varanavičius, A. P. Piskarskas, and G. Valiulis. Manifestation of spatial chirp in femtosecond noncollinear optical parametric chirped-pulse amplifier. *Journal of the Optical Society of America B*, 28(12):2902, 2011.

[28] P. Di Trapani, A. Andreoni, G. P. Banfi, C. Solcia, R. Danielius, A. Piskarskas, P. Foggi, M. Monguzzi, and C. Sozzi. Group-velocity self-matching of femtosecond pulses in noncollinear parametric generation. *Physical Review A*, 51(4):3164–3168, 1995.

[29] G. Arisholm. General numerical methods for simulating second-order nonlinear interactions in birefringent media. *Journal of the Optical Society of America B*, 14(10):2543–2549, 1997.

[30] W. Koechner. *Solid-state laser engineering*. Springer, 2006.

[31] A. E. Siegman. *Lasers*. University Science Books, 1986.

[32] William T. Silfvast. *Laser Fundamentals*. Cambridge University Press, 1996.

[33] R. W. Boyd. *Nonlinear Optics*. Academic Press, third edition, 2007.

[34] C. Rulliere. *Femtosecond laser pulses Principles and Experiments*. Springer, second edition, 2003.

[35] A. M. Weiner. *Ultrafast optics*. Wiley, 2009.

[36] O. Svelto. *Principles of Lasers*. Springer US, fifth edition, 2010.

[37] M. Grishin, V. Gulbinas, and A. Michailovas. Dynamics of high repetition rate regenerative amplifiers. *Optics express*, 15(15):9434–9443, 2007.

[38] J. Dörring, A. Killi, U. Morgner, A. Lang, M. Lederer, and D. Kopf. Period doubling and deterministic chaos in continuously pumped regenerative amplifiers. *Optics express*, 12(8):1759–68, 2004.

[39] T. Metzger, A. Schwarz, C. Y. Teisset, D. Sutter, A. Killi, R. Kienberger, and F. Krausz. High-repetition-rate picosecond pump laser based on a Yb:YAG disk amplifier for optical parametric amplification. *Optics letters*, 34(14):2123–5, 2009.

[40] M. Grishin, V. Gulbinas, and A. Michailovas. Bifurcation suppression for stability improvement in Nd: YVO 4 regenerative amplifier. *Optics express*, 17(18):15700–15708, 2009.

[41] L. von Grafenstein, M. Bock, D. Ueberschaer, U. Griebner, and T. Elsaesser. Picosecond 34 mJ pulses at kHz repetition rates from a Ho:YLF amplifier at 2 µm wavelength. *Optics Express*, 23(26):33142–33149, 2015.

[42] P. Kroetz, A. Ruehl, G. Chatterjee, A. L. Calendron, K. Murari, H. Cankaya, P. Li, F. X. Kärtner, I. Hartl, and R. J. Dwayne Miller. Overcoming bifurcation instability in high- repetition-rate Ho : YLF regenerative amplifiers. *Optics letters*, 40(23), 2015.

[43] P. Gao, H. Lin, J. Li, J. Guo, H. Yu, H. Zhang, and X. Liang. Megahertz-level, high-power picosecond Nd:LuVO_4 regenerative amplifier free of period doubling. *Optics Express*, 24(13):13963, 2016.

[44] J. Speiser. Scaling of thin-disk lasers–influence of amplified spontaneous emission. *Journal of the Optical Society of America B*, 26(1):26, 2009.

[45] O. E. Martinez, J. P. Gordon, and R. L. Fork. Negative group-velocity dispersion using refraction. *Journal of the Optical Society of America A*, 1(10):1003, 1984.

[46] G. Imeshev, I. Hartl, and M. E. Fermann. Chirped pulse amplification with a nonlinearly chirped fiber Bragg grating matched to the Treacy compressor. *Optics letters*, 29(7):679–681, 2004.

[47] K.-H. Liao, M.-Y. Cheng, E. Flecher, V. I. Smirnov, L. B. Glebov, and A. Galvanauskas. Large-aperture chirped volume Bragg grating based fiber CPA system. *Optics Express*, 15(8):4876, 2007.

[48] S. Antipov, M. Ams, R. J. Williams, E. Magi, M. J. Withford, and A. Fuerbach. Direct infrared femtosecond laser inscription of chirped fiber Bragg gratings. *Optics Express*, 24(1):30, 2016.

[49] E. B. Treacy. Optical pulse compression with diffraction gratings. *IEEE Journal of Quantum Electronics*, 5(9):454–458, 1969.

[50] L. Walmsley, L. Waxer, and C. Dorrer. The role of dispersion in ultrafast optics. *Review of Scientific Instruments*, 72(1 I):1–29, 2001.

[51] L. McDonagh. *888 nm pumping of Nd:YVO4 for high-power TEM00 lasers*. PhD thesis, Technical University of Kaiserslautern, 2007.

[52] R. Eckardt and J. Reintjes. Phase matching limitations of high efficiency second harmonic generation. *Journal of Quantum Electronics*, 20(10):1178–1187, 1984.

[53] G. Cerullo and S. De Silvestri. Ultrafast optical parametric amplifiers. *Review of Scientific Instruments*, 74(1):1, 2003.

[54] S. Witte, R. Zinkstok, W. Hogervorst, and K. Eikema. Numerical simulations for performance optimization of a few-cycle terawatt NOPCPA system. *Applied Physics B*, 87(4):677–684, 2007.

[55] C. Manzoni and G. Cerullo. Design criteria for ultrafast optical parametric amplifiers. *Journal of Optics*, 18(10):1–33, 2016.

[56] fiberdesk software © 2002-2017 Thomas Schreiber. https://www.fiberdesk.com/.

[57] G. P. Agrawal. *Nonlinear Fiber Optics*. Academic Press, fourth edition, 2007.

[58] C. V. Shank, R. L. Fork, R. Yen, R. H. Stolen, and W. J. Tomlinson. Compression of femtosecond optical pulses. *Applied Physics Letters*, 40(9):761–763, 1982.

[59] W. Tomlinson, R. Stolen, and C. Shank. Compression of optical pulses chirped by self-phase modulation in fibers. *Journal of the Optical Society of America B*, 1(2):139–149, 1984.

[60] C. Rolland and P. B. Corkum. Compression of high-power optical pulses. *Journal of the Optical Society of America B*, 5(3):641, 1988.

[61] M. Nisoli, S. De Silvestri, and O. Svelto. Generation of high energy 10 fs pulses by a new pulse compression technique. *Applied Physics Letters*, 68(20):2793, 1996.

[62] F. Couny, F. Benabid, P. J. Roberts, P. S. Light, and M. G. Raymer. Generation and photonic guidance of multi-octave optical-frequency combs. *Science*, 318(2007):1118–1121, 2007.

[63] Y. Y. Wang, N. V. Wheeler, F. Couny, P. J. Roberts, and F. Benabid. Low loss broadband transmission in hypocycloid-core Kagome hollow-core photonic crystal fiber. *Optics letters*, 36(5):669–71, 2011.

[64] B. Debord, M. Alharbi, T. Bradley, C. Fourcade-Dutin, Y. Y. Wang, L. Vincetti, F. Gérôme, and F. Benabid. Hypocycloid-shaped hollow-core photonic crystal fiber Part I: Arc curvature effect on confinement loss. *Optics express*, 21(23):28597–21, 2013.

[65] M. Alharbi, T. Bradley, B. Debord, C. Fourcade-Dutin, D. Ghosh, L. Vincetti, F. Gérôme, and F. Benabid. Hypocycloid-shaped hollow-core photonic crystal fiber Part II: cladding effect on confinement and bend loss. *Optics express*, 21(23):28609–16, 2013.

[66] O. H. Heckl, C. J. Saraceno, C. R. E. Baer, T. Südmeyer, Y. Y. Wang, Y. Cheng, F. Benabid, and U. Keller. Temporal pulse compression in a xenon-filled Kagome-type hollow-core photonic crystal fiber at high average power. *Optics Express*, 19(20):19142, 2011.

[67] F. Emaury, C. F. Dutin, C. J. Saraceno, M. Trant, O. H. Heckl, Y. Y. Wang, C. Schriber, F. Gerome, T. Südmeyer, F. Benabid, and U. Keller. Beam delivery and pulse compression to sub-50 fs of a modelocked thin-disk laser in a gas-filled Kagome-type HC-PCF fiber. *Optics Express*, 21(4):4986–4994, 2013.

[68] F. Emaury, C. J. Saraceno, B. Debord, D. Ghosh, A. Diebold, F. Gèrôme, T. Südmeyer, F. Benabid, and U. Keller. Efficient spectral broadening in the 100-W average power regime using gas-filled kagome HC-PCF and pulse compression. *Optics letters*, 39(24):6843–6, 2014.

[69] T. Balciunas, C. Fourcade-Dutin, G. Fan, T. Witting, a. a. Voronin, a. M. Zheltikov, F. Gerome, G. G. Paulus, a. Baltuska, and F. Benabid. A strong-field driver in the single-cycle regime based on self-compression in a kagome fibre. *Nature communications*, 6(May 2014):6117, 2015.

[70] F. Guichard, A. Giree, Y. Zaouter, M. Hanna, G. Machinet, B. Debord, F. Gérôme, P. Dupriez, F. Druon, C. Hönninger, E. Mottay, F. Benabid, and P. Georges. Nonlinear compression of high energy fiber amplifier pulses in air-filled hypocycloid-core Kagome fiber. *Optics Express*, 23(6):7416–7423, 2015.

[71] S. Hädrich, M. Krebs, A. Hoffmann, A. Klenke, J. Rothhardt, J. Limpert, and A. Tünnermann. Exploring new avenues in high repetition rate table-top coherent extreme ultraviolet sources. *Light: Science & Applications*, 4(October 2014):e320, 2015.

[72] K. Murari, G. J. Stein, H. Cankaya, B. Debord, F. Gérôme, G. Cirmi, O. D. Mücke, P. Li, A. Ruehl, I. Hartl, K.-H. Hong, F. Benabid, and F. X. Kärtner. Kagome-fiber-based pulse compression of mid-infrared picosecond pulses from a Ho:YLF amplifier. *Optica*, 3(8):816, 2016.

[73] K. F. Mak, J. C. Travers, N. Y. Joly, A. Abdolvand, and P. S. J. Russell. Two techniques for temporal pulse compression in gas-filled hollow-core kagomé photonic crystal fiber. *Optics letters*, 38(18):3592–5, 2013.

[74] M. C. Funck, B. Wedel, I. Kayander, and J. Niemeyer. Industrial beam delivery system for ultra-short pulsed laser. *Proc. of SPIE*, 9356:935603–1, 2015.

[75] B. Debord, M. Alharbi, L. Vincetti, A. Husakou, C. Fourcade-Dutin, C. Hoenninger, E. Mottay, F. Gérôme, and F. Benabid. Multi-meter fiber-delivery and pulse self-compression of milli-Joule femtosecond laser and fiber-aided laser-micromachining. *Optics express*, 22(9):10735–46, 2014.

[76] P. Russbueldt, T. Mans, G. Rotarius, J. Weitenberg, H. D. Hoffmann, and R. Poprawe. 400W Yb:YAG Innoslab fs-Amplifier. *Optics express*, 17(15):12230–45, 2009.

[77] W. S. Brocklesby. Progress in high average power ultrafast lasers. *The European Physical Journal Special Topics*, 224(13):2529–2543, 2015.

[78] C. Teisset, M. Schultze, R. Bessing, M. Haefner, S. Prinz, D. Sutter, and T. Metzger. 300 W Picosecond Thin-Disk Regenerative Amplifier at 10 kHz Repetition Rate. *Advanced Solid-State Lasers Congress Postdeadline*, page JTh5A.1, 2013.

[79] T. Nubbemeyer, M. Kaumanns, M. Ueffing, M. Gorjan, A. Alismail, H. Fattahi, J. Brons, O. Pronin, H. G. Barros, Z. Major, T. Metzger, D. Sutter, and F. Krausz. 1 kW , 200 mJ picosecond thin-disk laser system. *Optics Letters*, 42(7):1–5, 2017.

[80] J. P. Negel, A. Loescher, D. Bauer, D. Sutter, A. Killi, M. Abdou, and T. Graf. Second Generation Thin-Disk Multipass Amplifier Delivering Picosecond Pulses with 2 kW of Average Output Power. In *Proceedings of Advanced Solid State Lasers (ASSL) 2016*, volume ATu4A.5, page ATu4A.5, Washington, D.C., 2016. OSA.

[81] J. P. Negel, A. Loescher, A. Voss, D. Bauer, D. Sutter, A. Killi, M. A. Ahmed, and T. Graf. Ultrafast thin-disk multipass laser amplifier delivering 1.4 kW (47 mJ, 1030 nm) average power converted to 820 W at 515 nm and 234 W at 343 nm. *Optics Express*, 23(16):21064, 2015.

[82] D. C. Brown and V. A. Vitali. Yb:YAG kinetics model including saturation and power conservation. *IEEE Journal of Quantum Electronics*, 47(1):3–12, 2011.

[83] Amplitude Systèmes, 2015.

[84] T. Fan. Heat generation in Nd:YAG and Yb:YAG. *IEEE Journal of Quantum Electronics*, 29(6):1457–1459, 1993.

[85] J. Dong, M. Bass, Y. Mao, P. Deng, and F. Gan. Dependence of the Yb 3+ emission cross section and lifetime on temperature and concentration in yttrium aluminum garnet. *JOSA B*, 20(9):1975–1979, 2003.

[86] C. Hönninger, I. Johannsen, M. Moser, G. Zhang, A. Giesen, and U. Keller. Diode-pumped thin-disk Yb:YAG regenerative amplifier. *Applied Physics B-Lasers and Optics*, 65(3):423–426, 1997.

[87] M. Delaigue. *Study and realization of high average power femtosecond systems.* PhD thesis, University of Bordeaux 1, 2006.

[88] J. E. Murray and W. H. Lowdermilk. ND : YAG regenerative amplifier. *Journal of Applied Physics*, 51(7):3548, 1980.

[89] W. H. Lowdermilk and J. E. Murray. The multipass amplifier: Theory and numerical analysis. *Journal of Applied Physics*, 51(5):2436–2444, 1980.

[90] S. Biswal, J. Itatani, J. Nees, and G. Mourou. Efficient energy extraction below the saturation fluence in a low-gain low-loss regenerative chirped-pulse amplifier. *IEEE Journal of Selected Topics in Quantum Electronics*, 4(2):421–425, 1998.

[91] Y. Takeuchi, J. Kawanaka, and M. Fujita. Nonlinear refractive index of a YAG crystal at low temperature. In *CLEO/Europe - EQEC 2009 - European Conference on Lasers and Electro-Optics and the European Quantum Electronics Conference*, pages 1–1. IEEE, 2009.

[92] M. Bache, H. Guo, B. Zhou, and X. Zeng. The anisotropic Kerr nonlinear refractive index of the beta-barium borate (β-BaB_2O_4) nonlinear crystal. *Optical Materials Express*, 3(3):357, 2013.

[93] O. Novák, T. Miura, M. Smrž, M. Chyla, S. Nagisetty, J. Mužík, J. Linnemann, H. Turčičová, V. Jambunathan, O. Slezák, M. Sawicka-Chyla, J. Pilař, S. Bonora, M. Divoký, J. Měsíček, A. Pranovich, P. Sikocinski, J. Huynh, P. Severová, P. Navrátil, D. Vojna, L. Horáčková, K. Mann, A. Lucianetti, A. Endo, D. Rostohar, and T. Mocek. Status of the High Average Power Diode-Pumped Solid State Laser Development at HiLASE. *Applied Sciences*, 5(4):637–665, 2015.

[94] C. L. Chang, P. Krogen, K.-H. Hong, L. E. Zapata, J. Moses, A.-L. Calendron, H. Liang, C.-J. Lai, G. J. Stein, P. D. Keathley, G. Laurent, and F. X. Kärtner. High-energy, kHz, picosecond hybrid Yb-doped chirped-pulse amplifier. *Optics Express*, 23(8):10132–44, 2015.

[95] J. Fischer, A. C. Heinrich, S. Maier, J. Jungwirth, D. Brida, and A. Leitenstorfer. 615 fs pulses with 17 mJ energy generated by an Yb:thin-disk amplifier at 3 kHz repetition rate. *Optics Letters*, 41(2):246, 2016.

[96] H. Fattahi, A. Alismail, H. Wang, J. Brons, O. Pronin, T. Buberl, L. Vámos, G. Arisholm, A. M. Azzeer, and F. Krausz. High-power, 1-ps, all-Yb:YAG thin-disk regenerative amplifier. *Opt. Lett.*, 41(6):1126–1129, 2016.

[97] W. Schneider, A. Ryabov, C. Lombosi, T. Metzger, Z. Major, J. A. Fülöp, and P. Baum. 800-fs, 330-μJ pulses from a 100-W regenerative Yb:YAG thin-disk amplifier at 300 kHz and THz generation in LiNbO3. *Optics Letters*, 39(23):6604, 2014.

[98] O. H. Heckl, S. Weiler, R. Fleischhaker, R. Gebs, A. Budnicki, M. Wolf, J. Kleinbauer, S. Russ, M. Kumkar, and D. H. Sutter. Industry-grade high average power femtosecond light source. In A. Heisterkamp, P. R. Herman, M. Meunier, and S.

Nolte, editors, *Frontiers in Ultrafast Optics: Biomedical, Scientific, and Industrial Applications XIV*, volume 8972, pages 89720P–7, 2014.

[99] M. Puppin, Y. Deng, O. Prochnow, J. Ahrens, T. Binhammer, U. Morgner, M. Krenz, M. Wolf, and R. Ernstorfer. 500 kHz OPCPA delivering tunable sub-20 fs pulses with 15 W average power based on an all-ytterbium laser. *Optics Express*, 23(2):1491–1497, 2015.

[100] M. Mero, F. Noack, F. Bach, V. Petrov, and M. J. J. Vrakking. High-average-power, 50-fs parametric amplifier front-end at 155 μm. *Optics Express*, 23(26):33157, 2015.

[101] H. Höppner, A. Hage, T. Tanikawa, M. Schulz, R. Riedel, U. Teubner, and M. J. Prandolini. An optical parametric chirped-pulse amplifier for seeding high repetition rate free-electron lasers. *New Journal of Physics*, 17(5):053020, 2015.

[102] J. Ahrens, O. Prochnow, T. Binhammer, T. Lang, B. Schulz, M. Frede, and U. Morgner. Multipass OPCPA system at 100 kHz pumped by a CPA-free solid-state amplifier. *Optics Express*, 24(8):8074, 2016.

[103] G. Pariente, V. Gallet, a. Borot, O. Gobert, and F. Quéré. Space–time characterization of ultra-intense femtosecond laser beams. *Nature Photonics*, 10(8):547–553, 2016.

[104] J. A. Armstrong, N. Bloembergen, J. Ducuing, and P. S. Pershan. Interactions between light waves in a nonlinear dielectric. *Physical Review*, 127(6):1918–1939, 1962.

[105] R. Baumgartner and R. Byer. Optical parametric amplification. *IEEE Journal of Quantum Electronics*, 15(6):432–444, 1979.

[106] A. Giree, M. Mero, G. Arisholm, M. J. J. Vrakking, and F. J. Furch. Numerical study of spatiotemporal distortions in noncollinear optical parametric chirped-pulse amplifiers. *Optics Express*, 25(4):3104, 2017.

[107] I. N. Ross, P. Matousek, G. H. C. New, and K. Osvay. Analysis and optimization of optical parametric chirped pulse amplification. *J. Opt. Soc. Am. B*, 19(12):2945–2956, 2002.

[108] F. Tavella, A. Marcinkevičius, and F. Krausz. Investigation of the superfluorescence and signal amplification in an ultrabroadband multiterawatt optical parametric chirped pulse amplifier system. *New Journal of Physics*, 8(10):219–219, 2006.

[109] M. Nieto-Vesperinas and G. Lera. Solution to non-linear optical mixing equations with depletion and diffraction. *Optics Communications*, 69(3):329–333, 1989.

[110] A. V. Smith and M. S. Bowers. Phase distortions in sum- and difference-frequency mixing in crystals. *Journal of the Optical Society of America B*, 12(1):49, 1995.

[111] B. Zhao, Y. Jiang, K. Sueda, N. Miyanaga, and T. Kobayashi. Ultrabroadband noncollinear optical parametric amplification with LBO crystal. *Optics express*, 16(23):18863–18868, 2008.

[112] N. Ishii, K. Kaneshima, K. Kitano, T. Kanai, S. Watanabe, and J. Itatani. Sub-two-cycle, carrier-envelope phase-stable, intense optical pulses at 1.6 μm from a BiB3O6 optical parametric chirped-pulse amplifier. *Optics letters*, 37(20):4182–4, 2012.

[113] C. Skrobol, I. Ahmad, S. Klingebiel, C. Wandt, S. A. Trushin, Z. Major, F. Krausz, and S. Karsch. Broadband amplification by picosecond OPCPA in DKDP pumped at 515 nm. *Optics Express*, 20(4):4619, 2012.

[114] D. Sanchez, M. Hemmer, M. Baudisch, S. L. Cousin, K. Zawilski, P. Schunemann, O. Chalus, C. Simon-Boisson, and J. Biegert. 7 μm, ultrafast, sub-millijoule-level mid-infrared optical parametric chirped pulse amplifier pumped at 2 μm. *Optica*, 3(2):147, 2016.

[115] J. Bromage, J. Rothhardt, S. Hädrich, C. Dorrer, C. Jocher, S. Demmler, J. Limpert, A. Tünnermann, and J. D. Zuegel. Analysis and suppression of parasitic processes in noncollinear optical parametric amplifiers. *Optics express*, 19(18):16797–808, 2011.

[116] G. Arisholm, J. Bieger, P. Schlup, C. P. Hauri, and U. Keller. Ultra-broadband chirped-pulse optical parametric amplifier with angularly dispersed beams. *Optics Express*, 12(3):518, 2004.

[117] K. Yamane, T. Tanigawa, T. Sekikawa, and M. Yamashita. Angularly-dispersed optical parametric amplification of optical pulses with one-octave bandwidth toward monocycle regime. *Optics Express*, 16(22):18345–18353, 2008.

[118] F. Tavella. *Multiterawatt few-cycle pulse OPCPA for applications in high-field physics*. PhD thesis, Ludwig-Maximilans University, 2007.

[119] D. Herrmann, C. Homann, R. Tautz, M. Scharrer, P. S. J. Russell, F. Krausz, L. Veisz, and E. Riedle. Approaching the full octave: noncollinear optical parametric chirped pulse amplification with two-color pumping. *Optics express*, 18(18):18752–18762, 2010.

[120] H. Fattahi. *Third-generation femtosecond technology*. PhD thesis, Ludwig-Maximilans University, 2015.

[121] N. Ishii, L. Turi, V. S. Yakovlev, T. Fuji, F. Krausz, A. Baltuska, R. Butkus, G. Veitas, V. Smilgevicius, R. Danielius, and A. Piskarskas. Multimillijoule chirped parametric amplification of few-cycle pulses. *Optics Letters*, 30(5):567, 2005.

[122] R. T. Zinkstok, S. Witte, W. Hogervorst, and K. S. E. Eikema. High-power parametric amplification of 118-fs laser pulses with carrier-envelope phase control. *Optics Letters*, 30(1):78, 2005.

[123] D. A. Kleinman. Theory of optical parametric noise. *Physical Review*, 174(3):1027–1041, 1968.

[124] J. Moses, C. Manzoni, S. Huang, G. Cerullo, and F. X. Kärtner. Temporal optimization of ultrabroadband high-energy OPCPA. *Optics Express*, 17(7):5540, 2009.

[125] J. Rothhardt, S. Demmler, S. Hädrich, T. Peschel, J. Limpert, and A. Tünnermann. Thermal effects in high average power optical parametric amplifiers. *Optics letters*, 38(5):763–5, 2013.

[126] M. J. Prandolini, R. Riedel, M. Schulz, A. Hage, H. Höppner, and F. Tavella. Design considerations for a high power, ultrabroadband optical parametric chirped-pulse amplifier. *Optics express*, 22(2):1594–607, 2014.

[127] P. Di Trapani, A. Andreoni, P. Foggi, C. Solcia, R. Danielius, and A. Piskarskas. Efficient conversion of femtosecond blue pulses by travelling-wave parametric generation in non-collinear phase matching. *Optics Communications*, 119(3-4):327–332, 1995.

[128] G. Arisholm. Quantum noise initiation and macroscopic fluctuations in optical parametric oscillators. *Journal of the Optical Society of America B*, 16(1):117, 1999.

[129] P. Schlup, J. Biegert, C. P. Hauri, G. Arisholm, and U. Keller. Design of a sub-13-fs, multi-gigawatt chirped pulse optical parametric amplification system. *Applied Physics B: Lasers and Optics*, 79(3):285–288, 2004.

[130] O. Chalus, P. K. Bates, and J. Biegert. Design and simulation of few-cycle optical parametric chirped pulse amplification at mid-IR wavelengths. *Optics express*, 16(26):21297–21304, 2008.

[131] M. W. Haakestad, H. Fonnum, and E. Lippert. Mid-infrared source with 02 J pulse energy based on nonlinear conversion of Q-switched pulses in ZnGeP_2. *Optics Express*, 22(7):8556, 2014.

[132] S. Prinz, M. Häfner, M. Schultze, C. Y. Teisset, R. Bessing, K. Michel, R. Kienberger, and T. Metzger. Active pump-seed-pulse synchronization for OPCPA with sub-2-fs residual timing jitter. *Optics Express*, 22(25):31050, 2014.

[133] S. Akturk, X. Gu, P. Bowlan, and R. Trebino. Spatio-temporal couplings in ultrashort laser pulses. *Journal of Optics*, 12(9):093001, 2010.

[134] I. P. Christov. Propagation of femtosecond light pulses. *Optics Communications*, 53(6):364–366, 1985.

[135] S. Akturk, X. Gu, P. Gabolde, and R. Trebino. The general theory of first-order spatio-temporal distortions of Gaussian pulses and beams. *Optics Express*, 13(21):8642, 2005.

[136] D. N. Schimpf, J. Rothhardt, J. Limpert, A. Tünnermann, and D. C. Hanna. Theoretical analysis of the gain bandwidth for noncollinear parametric amplification of ultrafast pulses. *JOSA B*, 24(11):2837, 2007.

[137] A. Shirakawa, I. Sakane, and T. Kobayashi. Pulse-front-matched optical parametric amplification for sub-10-fs pulse generation tunable in the visible and near infrared. *Optics Letters*, 23(16):1292–1294, 1998.

[138] O. Isaienko and E. Borguet. Pulse-front matching of ultrabroadband near-infrared noncollinear optical parametric amplified pulses. *Journal of the Optical Society of America B*, 26(5):965, 2009.

[139] Z. Bor and B. Racz. Group velocity dispersion in prisms and its application to pulse compression and travelling-wave excitation. *Optics Communications*, 54(3):165–170, 1985.

[140] X. Gu, S. Akturk, and R. Trebino. Spatial chirp in ultrafast optics. *Optics Communications*, 242(4-6):599–604, 2004.

[141] S. Akturk, X. Gu, E. Zeek, and R. Trebino. Pulse-front tilt caused by spatial and temporal chirp. *Optics Express*, 12(19):4399–4410, 2004.

[142] T. Kobayashi and A. Baltuska. Sub-5 fs pulse generation from a noncollinear optical parametric amplifier. *Measurement Science and Technology*, 13(11):1671–1682, 2002.

[143] V. Bagnoud, I. A. Begishev, M. J. Guardalben, J. Puth, and J. D. Zuegel. 5 Hz, $>$ 250 mJ optical parametric chirped-pulse amplifier at 1053 nm. *Optics letters*, 30(14):1843–1845, 2005.

[144] Z. Wang, C. Liu, Z. Shen, Q. Zhang, H. Teng, and Z. Wei. High-contrast 1.16 PW Ti:sapphire laser system combined with a doubled chirped-pulse amplification scheme and a femtosecond optical-parametric amplifier. *Optics letters*, 36(16):3194–3196, 2011.

[145] T. Remetter, P. Johnsson, J. Mauritsson, K. Varjú, Y. Ni, F. Lépine, E. Gustafsson, M. Kling, J. Khan, R. López-Martens, K. J. Schafer, M. J. J. Vrakking, and A. L'Huillier. Attosecond electron wave packet interferometry. *Nature Physics*, 2(5):323–326, 2006.

[146] J. Mauritsson, T. Remetter, M. Swoboda, K. Klünder, A. L'Huillier, K. J. Schafer, O. Ghafur, F. Kelkensberg, W. Siu, P. Johnsson, M. J. J. Vrakking, I. Znakovskaya, T. Uphues, S. Zherebtsov, M. F. Kling, F. Lépine, E. Benedetti, F. Ferrari, G. Sansone, and M. Nisoli. Attosecond Electron Spectroscopy Using a Novel Interferometric Pump-Probe Technique. *Physical Review Letters*, 105(5):053001, 2010.

[147] M. P. de Boer and H. G. Muller. Observation of Large Populations in Excited-States after Short-Pulse Multiphoton Ionization. *Physical Review Letters*, 68(18):2747, 1992.

[148] T. Nubbemeyer, K. Gorling, A. Saenz, U. Eichmann, and W. Sandner. Strong-field tunneling without ionization. *Physical Review Letters*, 101(23):1–4, 2008.

[149] H. Zimmermann, S. Patchkovskii, M. Ivanov, and U. Eichmann. Unified Time and Frequency Picture of Ultrafast Atomic Excitation in Strong Laser Fields. *Physical Review Letters*, 013003(January):1–5, 2017.

[150] M. J. J. Vrakking. Attosecond imaging. *Physical Chemistry Chemical Physics*, 16(7):2775, 2014.

[151] K. Ohmori. Wave-Packet and Coherent Control Dynamics. *Annual Review of Physical Chemistry*, 60(1):487–511, 2009.

[152] C. Leichtle, W. Schleich, I. Averbukh, and M. Shapiro. Quantum State Holography. *Physical Review Letters*, 80(7):1418–1421, 1998.

[153] K. Klünder, P. Johnsson, M. Swoboda, A. L'Huillier, G. Sansone, M. Nisoli, M. J. J. Vrakking, K. J. Schafer, and J. Mauritsson. Reconstruction of attosecond electron wave packets using quantum state holography. *Physical Review A - Atomic, Molecular, and Optical Physics*, 88(3):1–6, 2013.

[154] H. G. Muller and F. Kooiman. Bunching and Focusing of Tunneling Wave Packets in Enhancement of High-Order Above-Threshold Ionization. *Physical Review Letters*, 81:1207–1210, 1998.

[155] P. Froemel. Generation of few-cycle laser pulses by hollow-core fiber compression for high harmonic generation. Master's thesis, Humboldt University Berlin, 2014.

[156] A. T. J. B. Eppink and D. H. Parker. Velocity map imaging of ions and electrons using electrostatic lenses: Application in photoelectron and photofragment ion imaging of molecular oxygen. *Review of Scientific Instruments*, 68(9):3477–3484, 1997.

[157] F. R. Pruna. *Alignment of Diatomic Molecules Induced by Intense Laser Fields*. PhD thesis, Vrije Universiteit Amsterdam, 2001.

[158] M. J. J. Vrakking. An iterative procedure for the inversion of two-dimensional ion/photoelectron imaging experiments. *Review of scientific Instruments*, 72(11):4084, 2001.

[159] C. Bordas, F. Paulig, H. Helm, and D. L. Huestis. Photoelectron imaging spectrometry: Principle and inversion method. *Review of Scientific Instruments*, 67(6):2257, 1996.

[160] J. Winterhalter, D. Maier, J. Honerkamp, V. Schyja, and H. Helm. Imaging of charged atomic reaction products: Inversion by a two-dimensional regularization method. *The Journal of Chemical Physics*, 110(23):11187, 1999.

[161] V. Dribinski, A. Ossadtchi, V. A. Mandelshtam, and H. Reisler. Reconstruction of Abel-transformable images: The Gaussian basis-set expansion Abel transform method. *Review of Scientific Instruments*, 73(7):2634, 2002.

[162] G. A. Garcia, L. Nahon, and I. Powis. Two-dimensional charged particle image inversion using a polar basis function expansion. *Review of Scientific Instruments*, 75(11):4989–4996, 2004.

[163] M. R. Panman, P. Bodis, D. J. Shaw, B. H. Bakker, A. C. Newton, E. R. Kay, D. A. Leigh, W. J. Buma, A. M. Brouwer, and S. Woutersen. Time-resolved vibrational spectroscopy of a molecular shuttle. *Physical Chemistry Chemical Physics*, 14(6):1865–1875, 2012.

[164] M. Schmidt, S. Rajagopal, Z. Ren, and K. Moffat. Application of Singular Value Decomposition to the Analysis of Time-Resolved Macromolecular X-Ray Data. *Biophysical Journal*, 84(3):2112–2129, 2003.

[165] R. Paschotta. article on 'Faraday isolators' in the Encyclopedia of Laser Physics and Technology, https://www.rp-photonics.com/faraday_isolators.html, accessed on 2017-06-18.

[166] Swamp Optics, Introduction to pulse measurement, http: www.swampoptics.com/intro.html, accessed on 2017-06-18.

List of publications

Peer-reviewed journal papers

[1] A. Giree, M. Mero, G. Arisholm, M. J. J. Vrakking, and F. J. Furch. Numerical study of spatiotemporal distortions in noncollinear optical parametric chirped-pulse amplifiers. *Optics Express*, 25(4):3104–3121, 2017.

[2] F. J. Furch, T. Witting, A. Giree, C. Luan, F. Schell, G. Arisholm, C. P. Schulz, M. J. J. Vrakking. CEP-stable few-cycle pulses with more than 190 µJ of energy at 100 kHz from a noncollinear optical parametric amplifier. *Optics Letters*, 42(13):2495-2498, 2017.

[3] F. J. Furch, A. Giree, F. Morales, A. Anderson, Y. Wang, C. P. Schulz, and M. J. J. Vrakking. Close to transform-limited, few-cycle 12 µJ pulses at 400 kHz for applications in ultrafast spectroscopy. *Optics Express* 24(17):19293, 2016.

[4] F. Guichard, A. Giree, Y. Zaouter, M. Hanna, G. Machinet, B. Debord, F. Gérôme, P. Dupriez, F. Druon, C. Hönninger, E. Mottay, F. Benabid, and P. Georges. Nonlinear compression of high energy fiber amplifier pulses in air-filled hypocycloid-core Kagome fiber. *Optics Express*, 23(6):7416–7423, 2015.

[5] F. J. Furch, S. Birkner, F. Kelkensberg, A. Giree, A. Anderson, C. P. Schulz, and M. J. J. Vrakking. Carrier-envelope phase stable few-cycle pulses at 400 kHz for electron-ion coincidence experiments. *Optics Express*, 21(19):274–276, 2013.

Conference contributions

[1] A. Giree, F. J. Furch, M. Mero, G. Arisholm, and M. J. Vrakking. Analysis of Spatiotemporal Couplings in Noncollinear Optical Parametric Chirped-Pulse Amplifiers. In Conference on Lasers and Electro-Optics, OSA Technical Digest (2016) (OSA, 2016), p. SF2I.7.

[2] A. Giree, F. J. Furch, M. Mero, and M. J. J. Vrakking. Spatiotemporal distortions in noncollinear optical parametric chirped-pulse amplifiers. In Proceedings - 2016 International Conference Laser Optics, LO 2016 (IEEE, 2016), p. R117.

[3] A. Giree, F. Guichard, G. Machinet, Y. Zaouter, Y. Hagen, B. Debords, P. Dupriez, F. Gérôme, M. Hanna, F. Benabid, C. Hönninger, P. Georges, and E. Mottay. Nonlinear compression of ultrafast industrial lasers in hypocyloid-core Kagome hollow-core fiber.

In Proc. SPIE 9355, Frontiers in Ultrafast Optics: Biomedical, Scientific, and Industrial Applications XV (2015), p. 93550I.

[4] F. J. Furch, A. Anderson, S. Birkner, Y. Wang, A. Giree, C. P. Schulz, and M. Vrakking. Improved Characteristics of High Repetition Rate Non-Collinear Optical Parametric Amplifiers for Electron-Ion Coincidence Spectroscopy. In CLEO:2015, OSA Technical Digest (online) (OSA, 2015), p. SF1M.5.

[5] A. Giree, F. Guichard, Y. Zaouter, M. Hanna, G. Machinet, B. Debord, F. Gérôme, P. Dupriez, C. Hoenninger, E. Mottay, F. Benabid, and P. Georges. High-energy, 34 fs, fiber source via nonlinear compression in hypocycloid-core Kagome fiber. In CLEO:2015, OSA Technical Digest (online) (OSA, 2015), p. ATu4M.3.

[6] F. J. Furch, S. Birkner, F. Kelkensberg, A. Giree, A. Anderson, C. P. Schulz, and M. J. Vrakking. Few-cycle pulses at 400 kHz for electron-ion coincidence experiments. In Research in Optical Sciences, OSA Technical Digest (online) (OSA, 2014), p. HTh3B.2.

A Appendix

A.1 Faraday rotator and isolator

A Faraday rotator is a magneto-optic device, based on the Faraday effect (an interaction between the light and the magnetic field in a medium), that rotates the polarization direction of linearly polarized light. When the linearly polarized light is transmitted through a transparent medium that is under the influence of a magnetic field with flux density along the propagation axis, the plane of polarization is continuously rotated during propagation. The total angle of rotation β is given by the equation,

$$\beta = VBd, \tag{A.1}$$

where V is the Verdet constant of the medium, B is the magnetic flux density in the direction of light propagation, d is the interaction length. The desired characteristics of a material to be used in a Faraday rotator include a high Verdet constant, low nonlinear refractive index, low absorption coefficient and high damage threshold.

The most important characteristic of a Faraday rotator is the non-reciprocal behavior i.e. if linearly polarized light that passes through a Faraday rotator is counter-propagated after reflected by a mirror, the polarization rotation sum up, rather than canceling each other. In a proper combination with waveplates and polarizers, Faraday rotators can be used as a directional gate i.e. beams propagating in one direction are transmitted by a polarizer while beams propagating in the opposite direction are reflected. This arrangement, schematically shown in Fig. A.1(taken from Ref. [165]) is usually called Faraday isolator.

A.2 Pockels cell

Pockels cell is an electro-optic device, with which a phase difference between the two orthogonal polarization components of the light propagating through it can be introduced by applying an electric voltage. For this reason, Pockels cells are also called voltage-controlled wave plates. The device is based on Pockels effect or linear electro-optic effect, where the refractive index of the medium can be altered by a high-voltage field. The difference in refractive index for two orthogonal polarization components corresponding to the waves polarized in two orthogonal axes is given by,

$$\Delta n = n_0^3 r_{ij} E, \tag{A.2}$$

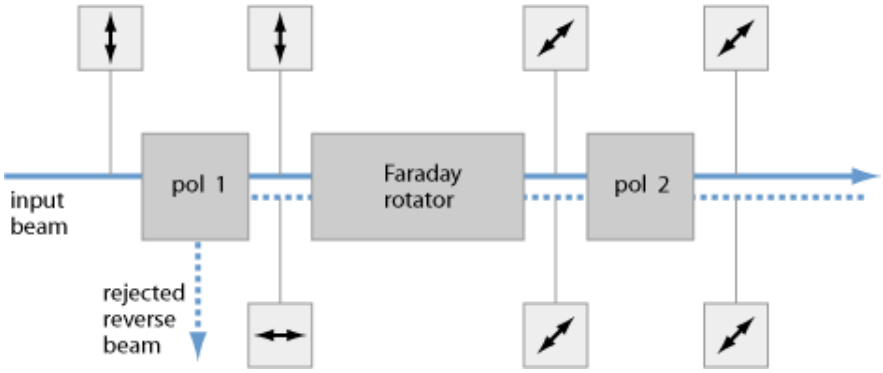

Figure A.1: Schematic picture of a Faraday isolator (taken from Ref. [165]). 'pol' refers to polarizer and the double arrows represent the polarization directions of propagating beams. The arrangement of the polarizers (pol 1 and pol 2) and the Faraday isolator rotates the polarization direction of incident beam by 45°. If the light is reflected back to the isolator with the same polarization direction, it will be blocked by the pol 1. This is mainly due to the non-reciprocal behavior of the Faraday rotator as described in text. If the beam propagating in backward direction is polarized in a different direction, the polarizer 'pol 2' reflects, only transmitting the light polarized along its transmission axis.

where n_0 is the ordinary index of refraction, E is the electric field in the direction of beam propagation and r_{ij} is one of the 18 electro-optic coefficients that belong to the electro-optic tensor of rank 3. The indices ij depends on crystal symmetry. For example, $r_{ij} = r_{63}$ for a potassium dihydrogen phosphate (KDP, KH_2PO_4) and r_{22} for a beta barium borate (BBO, BaB_2O_4) crystal.

Depending upon the direction of the applied electric field with respect to the direction of beam propagation, Pockels cell can be classified into two categories [30] as follows:

1) **Pockels cell with longitudinal field**: The electric field is applied in the direction of beam propagation and parallel to the optical axis of the crystal. A non-zero electric field introduces changes in refractive indices of the medium along two orthogonal axes. For a crystal of length L, the difference of refractive index causes a phase difference of $\Delta\phi = 2\pi\Delta nL/\lambda$. For an applied electric voltage $V = EL$, the phase difference becomes,

$$\Delta\phi = \frac{2\pi}{\lambda} n_0^3 r_{63} V. \tag{A.3}$$

This means the voltage required to induce a phase difference of $\pi/2$, which is often called quarter-wave voltage is given by,

$$V_{\lambda/4} = \frac{\lambda}{4n_0^3 r_{63}}. \tag{A.4}$$

2) **Pockels cell with transverse fields**: The electric field is applied perpendicular to the direction of the beam propagation. For a crystal of thickness d and an applied

electric voltage $V = Ed$, the quarter-wave voltage is given by,

$$V_{\lambda/4} = \frac{\lambda d}{4 n_0^3 r_{63} L}. \tag{A.5}$$

Unlike the Pockels cell with longitudinal field, the voltage required to introduce phase difference in the case of transverse fields depends on the ratio of thickness to length of the crystal. This indicates that a proper choice of crystal geometry allows to use relatively lower voltage.

For high repetition rate, high average power amplifiers, Pockels cells with BBO crystals are preferred due to its high damage threshold compared to KDP and lithium niobate ($LiNbO_3$). As an example, at a given wavelength of 1030 nm, the ordinary refractive index of BBO is 1.655 and $r_{22} = 2.7$ pm V. The quarter-wave voltage for a crystal size of 5 mm × 5 mm × 30 mm is estimated to be 3.51 kV using Eq. A.5.

A.3 Intensity autocorrelation

The intensity autocorrelation is a technique, which can be used to measure a time-dependent intensity profile of an ultrashort pulse. It is typically realized by splitting a pulse into two replicas, delaying one with respect to each other with variable time delays, and superimposing the two beams in a nonlinear medium with $\chi^{(2)}$ nonlinearity, as schematically shown in Fig. A.2 (taken from Ref. [166]).

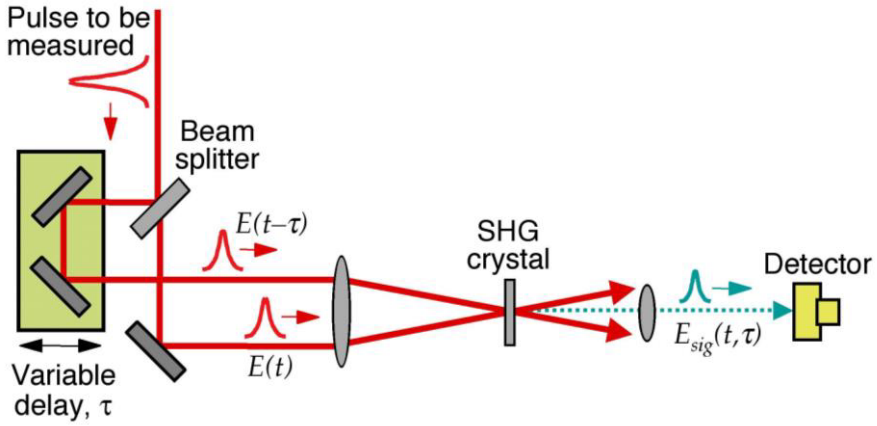

Figure A.2: Optical layout of an intensity autocorrelator based on second harmonic generation (taken from Ref. [166]). An input pulse to be measured is split into two by using a beam splitter. One arm is time-delayed with respect to other. Both beams are crossed into a second harmonic crystal, generating second harmonic signal when the two pulses are temporally overlapped. The signal is then measured with a detector as a function of time delay, which provides the pulse duration if the pulse shape is known.

If $I(t)$ is the intensity of the input pulse and $I(t-\tau)$ is the time-delayed replica, the autocorrelation signal $A(\tau)$ measured with detectors is given by,

$$A(\tau) = \int_{-\infty}^{+\infty} I(t)I(t-\tau)dt, \tag{A.6}$$

The signal measured as a function of time delay provides the pulse duration of the input pulse, given that the input pulse shape is known. For a Gaussian pulse shape, the FWHM pulse duration of the autocorrelation pulse is 1.414 times longer than the FWHM pulse duration of the input pulse. The conversion factor depends on the pulse shape, for example, 1.543 in the case of sech^2-shaped pulses [34].

Short summary

In the last decade, the sources of carrier envelope phase-stable few-cycle, high energy laser pulses have become the backbone of attosecond science. To date, energetic, few-cycle pulses are mostly generated via either nonlinear pulse compression of Ti:Sa amplifiers or noncollinear optical parametric chirped-pulse amplifiers (OPCPAs). Both approaches demand high energy, ultrafast laser amplifiers. In contrast to the nonlinear compression of Ti:Sa amplifiers that are limited in average power and pulse repetition rates ($< 10\,\mathrm{kHz}$), OPCPAs offer high repetition rate that is only limited by pump lasers. Few-cycle pulses at high repetition rates ($> 100\,\mathrm{kHz}$) are desirable for electron-ion coincidence detector to increase data acquisition speed and signal-to-noise ratio. In this respect, this thesis focuses on generation of energetic, few-cycle pulses at high repetition rates based on noncollinear OPCPAs, emphasizing on high energy and high peak power ultrafast pump laser, and on spatiotemporal quality of the amplified pulses.

The first part of the thesis presents a mJ-level, sub-ps laser based on thin-disk technology. The chirped pulse amplification technique is utilized to amplify ultrashort pulses from a fiber oscillator using an Yb:YAG thin-disk regenerative amplifier, along with a chirped-fiber Bragg grating stretcher and a grating compressor. After compression, $\sim 1\,\mathrm{ps}$ pulses with an average power of 35 W at 100 kHz, and pulse energy of 1.6 mJ at 10 kHz or 1.1 mJ at 25 kHz are achieved. The long term power stability, pulse-to-pulse stability and close to diffraction-limited beam quality, in combination with the highly efficient second and third harmonic generation have been demonstrated, showing the suitability of the laser system for pumping optical parametric amplifiers. In addition, the pulses are compressed down to 130 fs using an air-filled hollow core Kagome fiber.

In the second part, spatiotemporal distortions in noncollinear OPCPAs are numerically studied. A modeling of BBO-based amplifiers reveal that high pump-to-signal energy conversion efficiency comes at a cost of degraded spatiotemporal quality of few-cycle pulses, which reduces the peak power when the pulses are focused. The numerical results suggest to limit the conversion efficiency below 20 % if the degradation of peak power due to spatiotemporal distortions is to be avoided.

The last part concentrates on application of few-cycle pulses in strong field atomic physics. A proof-of-principle IR pump-IR probe electron interferometry experiment is presented, where Argon is used as a target and a velocity map imaging spectrometer is used to detect electrons after photoionization. The aim is to characterize the bound states of strong-field excited Argon. The complete characterization of the excited states is hindered by low signal-to-noise ratio of the experimentally measured photoelectron spectra, which is discussed with the help of numerical results that are obtained by solving time-dependent Schrödinger equation in the single active electron approximation.

Deutsche Kurzfassung

Während der letzten zehn Jahre haben sich Lasersysteme, die phasenstabile Pulse mit einer Dauer von wenigen optischen Zyklen und hoher Pulsenergie erzeugen, als Grundlage der Attosekundenforschung etabliert. Diese intensiven, ultrakurzen Pulse werden vorwiegend durch nichtlineare Pulskompression nach einem Ti:Sa-Verstärker oder mit Hilfe nichtkollinearer optisch-parametrischer Verstärkung gechirpter Pulse (OPCPAs) erzeugt. Für beide Ansätze werden ultraschnelle Pumplaser mit hoher Energie benötigt. Im Gegensatz zur nichtlinearen Kompression von Ti:Sa-Verstärkern, die nur eine begrenzte Durchschnittsleistung und Repetitionsrate erlaubt (<10 kHz), ermöglichen OPCPAs hohe Repetitionsraten, die nur durch die Pump-Laser beschränkt sind. Wenig-Zyklen-Pulse bei hohen Repetitionsraten (>100 kHz) sind für Elektron-Ion-Koinzidenzmessungen wünschenswert, um die Datenaufnahmegeschwindigkeit und somit das Signal-Rausch-Verhältnis zu erhöhen. Daher liegt der Schwerpunkt der vorliegenden Arbeit auf der Erzeugung von intensiven Wenig-Zyklen-Pulsen bei hohen Repetitionsraten mit Hilfe von OPCPAs. Insbesondere werden die Bedeutung von ultraschnellen Pumplasern mit hoher Pulsenergie und hoher Durchschnittsleistung sowie die räumlich-zeitlichen Eigenschaften der verstärkten Pulse hervorgehoben.

Im ersten Teil der Arbeit wird ein auf der Scheiben-Technologie basierender Laser vorgestellt, der Pulse mit mJ-Energien und sub-ps-Dauer liefert. Die Technik der Verstärkung gechirpter Pulse wird dazu verwendet, die Pulse von einem Faser-Oszillator mit Hilfe eines regenerativen Yb:YAG-Scheiben-Verstärkers sowie eines Bragg-Gitter-Stretchers mit gechirpter Faser und eines Gitterkompressors zu verstärken. Nach der Kompression konnten so Pulse mit einer Dauer von 1 ps bei einer Durchschnittsleistung von 35 W bei 100 kHz sowie Pulsenergien von 1.6 mJ bei 10 kHz oder 1.1 mJ bei 25 kHz erzeugt werden. Außerdem wurden die Langzeitstabilität der Leistung, die Puls-zu-Puls-Stabilität und ein nahezu beugungsbegrenztes Strahlprofil demonstriert, was zusammen mit der sehr effizienten zweiten und dritten Harmonischen-Erzeugung die Eignung des Lasersystems für das Pumpen von optisch-parametrischen Verstärkern zeigt. Schließlich wurden die Pulse mit einer luftgefüllten Kagome-Hohlfaser auf 130 fs komprimiert.

Im zweiten Teil wurde die räumlich-zeitliche Verzerrung von Laserpulsen in nichtkollinearen OPCPAs numerisch untersucht. Die Modellierung von Verstärkern auf BBO-Basis zeigt, dass hohe Konversionseffizienzen schlechte räumlich-zeitliche Eigenschaften des Pulses nach sich ziehen, welche bei der Fokussierung der Pulse die Spitzenleistung verringern. Demnach sollte die Konversionseffizienz auf unter 20 % begrenzt werden, um eine Verringerung der Spitzenleistung infolge räumlich-zeitlicher Verzerrungen zu vermeiden.

Der letzte Teil konzentriert sich auf die Anwendung von Wenig-Zyklen-Pulsen in Starkfeld-Atomphysik-Experimenten. Ein grundlegendes IR-Pump-IR-Probe-Elektroneninterferometrie-Experiment mit Argon-Atomen wurde durchgeführt. Ziel war die Charakterisierung von gebundenen Zuständen in den durch das starke Feld angeregten Argon-Atomen. Allerdings gelingt die vollständige Charakterisierung der experimentell gemessenen Photoelektronenspektren wegen des geringen Signal-Rausch-Verhältnisses nicht vollständig. Dies wird mit Hilfe numerischer Ergebnisse aus der Lösung der zeitabhängigen Schrödinger-Gleichung erörtert.

Acknowledgements

Besides the efforts of myself, there are encouragements, support and guidelines of many others behind the success of this thesis work. I am truly indebted and thankful to Prof. Marc J. J. Vrakking for giving me the opportunity of doing the thesis under the European Industrial Doctorate fellowship program so-called JMAP (Joint Max Born Institute Amplitude PhD Program) and for supervising.

I would like to thank Prof. Jens Limpert for co-refreeing my thesis.

Further, I would like to gratefully acknowledge and extend my heartfelt gratitude to my direct supervisor Dr. Federico J. Furch for his continuous guidance, fruitful discussions and very impressive suggestions during the whole work. This work would not have been possible without his strong knowledge, positive attitude and significant contributions.

I express my sincerest gratitude to Dr. Clemens Hönninger for providing an opportunity to carry out the laser development works at the research and development department of Amplitude Systèmes in Bordeaux, France. Many thanks to Eric Mottay, the CEO of Amplitude Systèmes for everything that I have during my stay in France. In addition, thanks goes to the people in Amplitude Technologies, Paris for their administrative support during the fellowship program.

Special thanks goes to my daily supervisor Dr. Claus Peter Schulz for teaching me the atomic and molecular physics. Without his patience and experience on experimental physics, the pump-probe interferometric experiment would not have been possible. At the same time, I am grateful to the help of Dr. Arnoud Rouzée and Dr. Mikalai Zhavoronkov for their efforts to make the experiment successful. Many thanks to Dr. Felipe Morales for his valuable support for the simulations presented in chapter 5.

The greatest appreciation and heartily thanks to my seniors Martin Delaigue, Yoann Zaouter and Florent Guichard for their logical suggestions and answers of many questions during the experiments. Thanks to the JMAP fellows for scientific discussions and lots of fun during the project.

I would also like to mention very friendly colleagues in Amplitude Systèmes: Benoît, Birgit, Areti, Guillaume, François, Frank, Magali, Alizée, Amélie, Antoine, Julien, Cécile, Yvon and Damien for the encouragement, scientific discussions and fun outside the work. Similarly, my thanks also goes to the colleagues at Max Born Institute: Oleg, Felix, Florian, Martin, Katrin, Peter, Johan, Yicheng, Lorenz and Geert for creating a nice working environment with lots of fun.

Finally, I am forever indebted to my parents and my wife Pabitra Kandel for their understanding, patience and endless love. I would like to dedicate the whole work to my lovely kids Adeep and Prahit. Love you boys!

Erklärung der Selbstständigkeit

Hiermit versichere ich, dass ich die vorliegende Dissertation selbstständig und nur unter Verwendung der angegebenen Literatur und Hilfsmittel verfasst habe. Die Arbeit ist weder in einem früheren Promotionsverfahren angenommen noch als ungenügend beurteilt worden.

Berlin, den 26. Februar 2018 Achut Giree